One-dimensional Hybrid Nanomaterials Based on Cylindrical Polymer Brushes

DISSERTATION

zur Erlangung des akademischen Grades eines
Doktors der Naturwissenschaften (Dr. rer. nat.)
im Fach Chemie der Fakultät für Biologie, Chemie und
Geowissenschaften der Universität Bayreuth

vorgelegt von

Jiayin Yuan

Geboren in Anhui / China

Bayreuth, 2009

Die vorliegende Arbeit wurde in der Zeit von März 2005 bis September 2008 in Bayreuth am Lehrstuhl Makromolekulare Chemie II unter Betreuung von Herrn Prof. Dr. Axel H. E. Müller angefertigt.

Vollständiger Abdruck der von Fakultät für Biologie, Chemie und Geowissenschaften der Universität Bayreuth genehmigten Dissertation zur Erlangung des akademischen Grades eines Doktors der Naturwissenschaften (Dr. rer. Nat.).

Dissertation eingereicht am:	12.01.2009
Zulassung durch die Promotionskommission:	14.01.2009
Wissenschaftliches Kolloquium:	02.04.2009

Amtierender Dekan: Prof. Dr. Axel H. E. Müller

Prüfungsausschuss:

Prof. Dr. A. H. E. Müller (Erstgutachter)

Prof. Dr. M. Ballauff (Zweitgutachter)

Prof.. Dr. K. Seifert (Vorsitzender)

Prof. Dr. J. Breu

To my wife Yan

You never know what you can do till you try.

Table of contents

Chapter 1 Introduction

The development of novel materials with new properties and improved performance is a continually expanding research area, which covers subjects ranging from chemistry, physics, biology, to material science. The largest activity in this field currently is the generation and the study of nanomaterials where the constructing units have at least one dimension between 1 and 100 nm. The interest in such structures mainly originates from the fact that novel properties are only acquired at this dimension scale, and equally important, that these properties change with their size or shape, which is not a result of scaling factors.

Among various reported structures, one-dimensional (1-D) materials such as wires, rods, tubes, etc., are expected to play an important role as both building blocks, interconnects, and functional units in fabricating nanoscale devices.

Exemplarily, polymer-inorganic 1-D hybrid nanomaterials are of considerable interest because of their wide-spread applications in fields like electronics, optics, catalysis, and sensors.[1, 2] They combine the intrinsic properties of 1-D inorganic nanostructures with very desirable characteristics of polymers, for instance, processability, dispersibility and solubility. The recent advances in "living" / controlled radical polymerization (CRP) techniques have provided plenty of opportunities to design and construct numerous functional polymers with rising complexity concerning their structures and components. This paths the way to meet the increasing requirements in the field of material science. In this thesis, different types of cylindrical polymer brushes with well-defined structure and controlled dimensions were prepared via the combination of anionic polymerization and atom transfer radical poylmerization; these polymers were further used as templates and supporting agent for the controlled fabrication of 1-D hybrid nanomaterials.

1.1 Cylindrical polymer brushes

Cylindrical polymer brushes (CPBs), i.e. "molecular bottlebrushes", which possess linear side chains or high-generation dendritic side groups densely grafted from a linear main chain (ideally every monomer unit of the main chain carries one side chain), have attracted considerable attention over the past decade.[3] These polymeric cylinders are architecturally interesting for both

experimental and theoretical chemists, owing to their unique properties in solution, bulk and thin films, especially the possibility of forming extended chain conformations based on the intramolecular excluded-volume interactions between densely grafted side chains. Moreover, their hyperbranched structure leads to very compact molecular dimensions in comparison with the corresponding linear polymers with a comparable molecular weight.

In the last two decades, advances in "living" / controlled radical polymerization (CRP) techniques like atom transfer radical polymerization (ATRP)[4], reversible addition-fragmentation chain transfer (RAFT),[5] and nitroxide-mediated radical polymerization (NMP)[6] have greatly facilitated the design, preparation and functionalization of CPBs. These techniques act as powerful tools and permit an unprecedented opportunity in the control and construction of macromolecules with a variety of monomers under mild conditions. Accordingly, many CPBs with diverse new architectures have been synthesized and studied to understand their properties. Furthermore, due to their anisotropic nature CPBs have successfully been employed as "soft" 1-D templates to direct the synthesis of inorganic 1-D nanostructures.[7, 8]

1.1.1 Synthesis of CPBs

Three basic methods, the "grafting through"[9-11], "grafting onto"[12-14], and "grafting from"[15-18] strategies, have been mainly used in the synthesis of CPBs. These brushes possess enough linear or dendritic side chains covalently bonded to a linear backbone (i.e. main chain), and stretch it to achieve the cylindrical shape. In addition, noncovalent interactions, such as hydrogen bonding,[19] ionic interactions,[20] and coordination bonding[21] have also been reported to attach side-groups onto linear polymer chains. Moreover, such structures can be prepared through the self-assembly of block copolymers. For example, core-crosslinked cylindrical micelles of block copolymers in solution,[22] the crosslinking of cylindrical microdomains of microphase-separated block copolymers in the bulk,[23, 24] and core-shell wormlike polymeric cylinders with crystalline or semicrystalline cores[25] have been reported. In these cases, the side chains were covalently bound to a linear fixed microdomain instead of a linear polymer backbone. (Scheme 1-1)

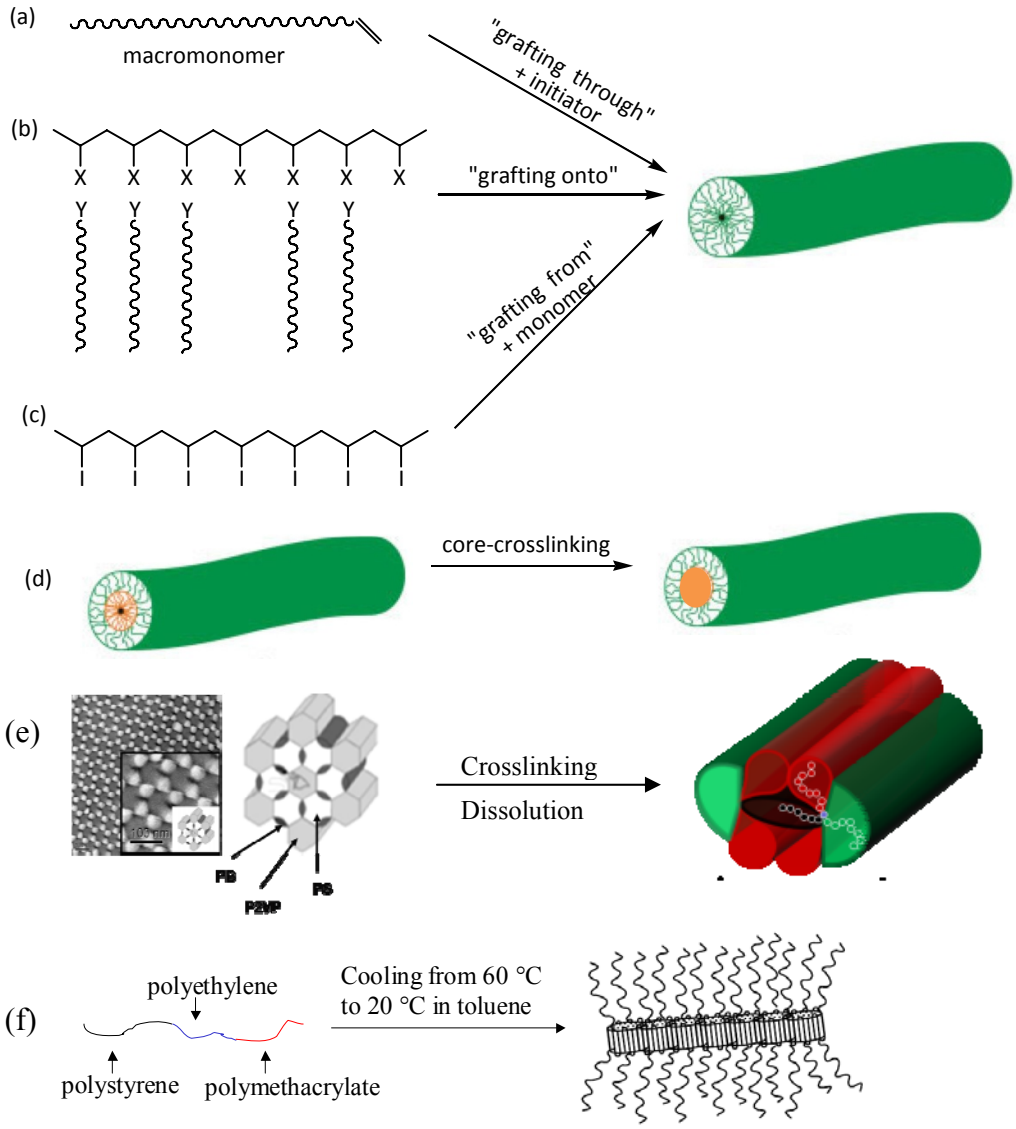

Scheme 1-1. Synthetic strategies for the preparation of CPBs and their analogues: (a) ‘‘grafting through’’, (b) ‘‘grafting onto’’ (X and Y are functional groups capable of coupling), (c) ‘‘grafting from’’ (I is an initiating group), (d) cross-linking of the core in cylindrical micelles, (e) multicompartment polymer cylinders by crosslinking the microphase-segregated bulk structure, and (f) triblock terpolymer cylindrical micelles with a crystalline middle block.

1.1.1.1 Grafting through

The “grafting through” method is the homo- or copolymerization of macromonomers with a polymerizable group (commonly double bond). The macromonomer chains are usually shorter than the backbone, but long enough to introduce the excluded-volume interactions to form the cylindrical morphology. It is the first method employed for the preparation of cylindrical polymer

brush as reported by Tsukahara et al. in 1989.[11] In this pioneering study, oligostyrene prepared via anionic polymerization was end-functionalized with a methacrylate moiety to create a macromonomer. Subsequently, the free radical polymerization of macromonomers led to CPBs with uniform side chains onto each repeating unit in the backbone.

However, the gel effect prevented the complete conversion of macromonomers, which causes difficulties in the separation of the polymer brushes from the residual unreacted macromonomers. Besides, this method typically creates brushes with rather broad distributions of the backbone length, owing to the uncontrolled free radical polymerization process. The brushes with a low degree of polymerization resemble granular stars rather than polymeric cylinders. Although living anionic polymerization,[26, 27] cationic polymerization,[28] group transfer polymerization,[29] ring-opening methathesis polymerization,[30, 31] and atom transfer radical polymerization[32-36] of macromonomers have been applied to increase the backbone length and decrease the polydispersity of the polymer brushes, high molecular weight CPBs with narrow molecular weight distribution have not yet been prepared by this approach.

1.1.1.2 Grafting onto

Within the "grafting onto" technique both the backbone and the side chains as the two basic building units, are separately prepared with "living" / controlled polymerization techniques. The construction of CPBs is then performed by grafting side chains onto a backbone via coupling reactions between pendant functional groups on the backbone and the end-functionalized side chains. Here, the grafting density (number-average ratio of side chains compared to backbone monomer units) is usually low, particularly for large rigid side chains, since the grafted side chains on the backbone introduce steric hindrance, preventing the ungrafted side chains from reaching the backbone.

Many efforts have been made to improve the grafting density. One attempt is the use of an excess of reactive side chains to favor the grafting reaction. However, it turned out to be not so easy to remove the ungrafted linear side chains from the final brush polymers. Another attempt is to perform more efficient organic coupling reactions to assure a fast coupling between reactive side chains and the backbone. One example is the "grafting onto" technique based on the termination of living anionic polymer chains with investigated polymer backbone carrying multiple electrophilic sites. The coupling of polystyryllithium with poly(2-chloroethyl vinyl ether) (PCEVE) resulted in a cylindrical brush with a PCEVE backbone and polystyrene (PS)

side chains.[37-40] Newly, a new type of highly efficient organic coupling reaction, the Cu(I)-catalyzed 1,3-dipolar cycloaddition reactions between an azide and an alkyne, i.e., "click reactions",[41] have been employed to construct CPBs, as shown in Scheme 1-2.[42] A poly(2-hydroxyethyl methacrylate) (PHEMA) backbone prepared via ATRP of 2-hydroxyethyl methacrylate (HEMA) was functionalized with an alkyne group at each monomer unit. Meanwhile, azido-terminated polymeric side chains, like poly(ethylene oxide) (PEO), polystyrene (PS), poly(*n*-butylacrylate) (PBA), or PS-*b*-PBA, were prepared via ATRP and then connected to the polymeric backbone via "click chemistry". Grafting efficiency reached ~90% for short "thin" PEO side chains, but was much smaller for longer PEO or "thicker" PS or PBA side chains. At present, insufficient grafting efficiency remains the insurmountable problem.

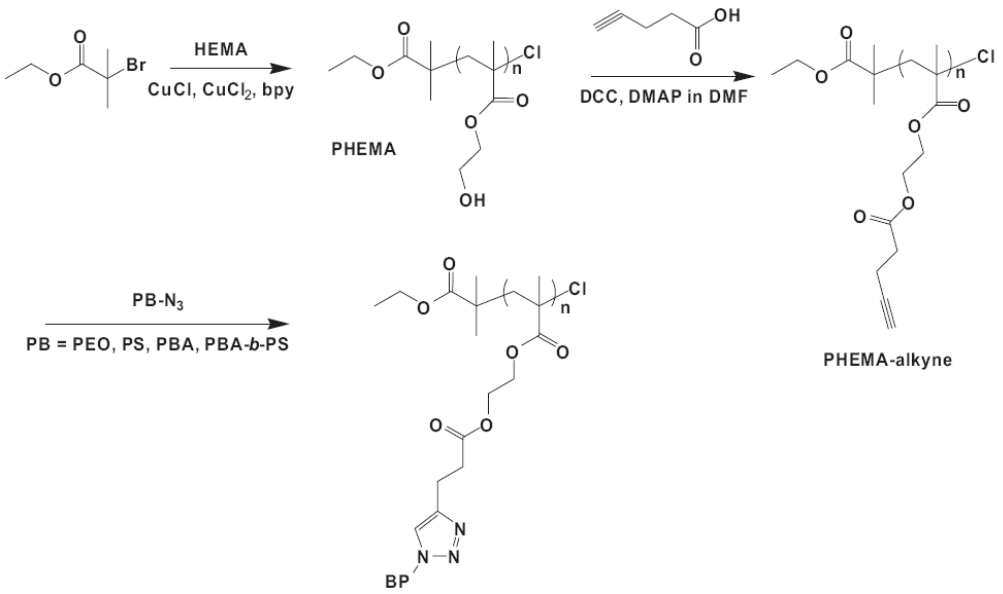

Scheme 1-2. Synthetic route of CPBs via a combination of ATRP and "click chemistry".

1.1.1.3 Grafting from

The "grafting from" method has received much attention as a new effective pathway to prepare well-defined CPBs.[43-49] Via this method a uniform backbone is first prepared via living polymerization techniques, followed by attaching initiating sites to each monomer unit. Side chains are then initiated from these pendant initiating sites along the backbone via living polymerization techniques, like ATRP,[17] ring opening polymerization (ROP),[46] and NMP.[49] Typically, a well-defined long backbone with a narrow molecular weight distribution (MWD) is crucial for the "grafting from" technique, because the length distribution of the CPBs is largely

dependent on the MWD of the backbone. Although "living" / controlled polymerization techniques like ATRP, RAFT and ROP can provide a quite good control over the polymerization of many monomers, typically anionic polymerization is still the better choice to obtain polymers with very narrow MWD, despite of its strict purification procedures for monomers, solvents and all additives.[16]

An apparent advantage of the "grafting from" approach in comparison with other methods is the simple purification, since the polymer brush is the only resulting product. Furthermore, both the backbone and the side chains are prepared via "living" / controlled polymerization techniques, so the obtained CPBs are well-defined. Moreover, a high grafting efficiency can be achieved, provided that the appropriate polymerization conditions for a given monomer are carefully selected. It was found that the growing of polybutylacrylate (PBA) side chains from a poly[2-(2-bromoisobutyryloxy)ethyl methacrylate] (PBIEM) backbone can reach a grafting efficiency of nearly 90% at 12% monomer conversion.[33] This is significantly higher than 20~30 %[42] of the usual "grafting onto" method obtained by "click chemistry". Here, the incomplete initiation in the "grafting from" method was attributed to slow initiation in comparison with propagation and slow deactivation due to the steric hindrance of neighboring side chains.

ATRP is among the most efficient used "living" / controlled polymerization techniques which has been widely applied to a large number of vinyl monomers, including styrenes, (meth)acrylates, and acrylonitrile.[50] So far, CPBs based on polymethacrylate or PS backbones and various polyacrylate,[15, 16, 44, 45, 47, 51] polymethacrylate,[52] PS,[47] poly(N-isopropylacrylamide),[53] and sugar[54] side chains have been prepared via ATRP. Due to its radical nature, ATRP is tolerant of many functional groups in monomers, enabling CPBs carrying different functionalities. Another unique advantage of ATRP in the "grafting from" techniques is that CPBs with various block copolymer side chains can be easily synthesized, for instance, core–shell (Scheme 1-3) or core-shell-corona CPBs.[16, 55]

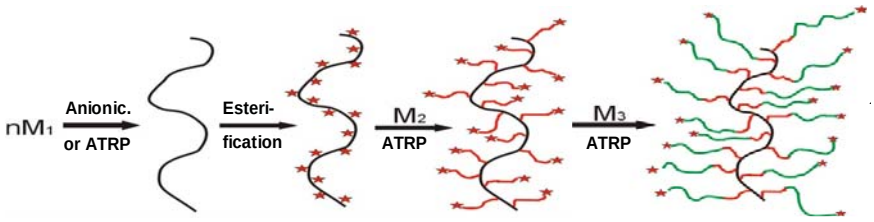

Scheme 1-3. Illustration for the synthesis of core-shell CPBs. (M_1: HEMA or trimethylsilyl protected HEMA; M_2 and M_3 are the monomer units in the diblock copolymer side chains.)

1.1.2 Properties of CPBs

Intensive studies have been performed on the unique properties of CPBs, focusing not only on their peculiar hyperbranched nature but also on the different types. It is widely accepted that in comparison with the corresponding linear polymers of the same molecular weight these polymer brushes are structurally more compact with a high density of chain-ends and high stiffness in the main chain. The conventional characterization techniques, like gel permeation chromatography, light scattering, and viscometry are often limited when applied to these complex macromolecules with branching and heterogeneous composition. In recent years, the visualization of individual macromolecules by scanning probe microscopes has become a powerful tool for the characterization of their molecular weight, size, conformation and even for the verification of the synthetic strategies that were followed.[56]

1.1.2.1 Solution properties

The elongated conformation of CPBs is a result of the competition between the long backbone and the short side chains. The densely grafted neighboring side chains repulse each other, but their mobility is hindered by the fixation of one chain end onto the backbone which locally confines the side chains into a cylindrical domain.[57] In solution, CPBs adopt a conformation of a wormlike object, which is characterized by the length per monomer (l_m), the brush diameter (D), and the persistence length (l_p). The cylindrical dimensions also depend on the degree of polymerization (DP) of the side chains and their grafting density. Despite the large number of experimental,[58-65] simulated,[66-74] and theoretical[75-79] studies dealing with the conformational properties of these cylindrical macromolecules in solutions, the effect of the side chain length is on the persistence length and on the overall brush structure is still not absolutely conclusive.. Predictions vary from a strong increase of the persistence length (backbone,[68] brush[63, 76, 78, 79]) over a slight increase (backbone,[60, 64, 68-70] brush[60, 64, 77]) down to almost no influence (backbone,[58, 61, 62, 65, 67] brush[58]). For flexible side chains, theory predicts that the stiffening of the backbone is not sufficient to cause the ordering of CPBs.[69] However, several experimental studies reported on the transition from flexible coils to stiff cylinders with increasing side chain length[80] and the hexagonal ordering of CPBs upon increasing the concentration in solution.[81]

For the formation of a lyotropic phase in solutions, the critical parameter is the ratio of l_p/D (aspect ratio). Predictions for semi-flexible cylinders with hard-core interaction revealed that the ratio l_p/D should be of the order of 10 in order to lead to lyotropic behavior at reasonable

concentrations.[81] The driving force for ordering phenomena in the brush solutions are the excluded volume interactions. In contrast to flexible cylinders with hard-core interactions, the CPBs, at least their side chains, start to interpenetrate when the threshold concentration, which can be rather low for brushes with long side chains, is exceeded. With further increase of the concentration above the threshold, excluded volume interactions will gradually diminish, thus lyotropic behavior is expected to disappear again at somewhat higher concentrations.[82]

Another solution property of CPBs is that the morphology as well as their flexibility is controlled by many factors like solvent quality, surfactants, temperature, pH, ionic strength.[18, 53, 60, 83-85] The ability to trigger the changes in the CPB´s conformation using various stimuli makes them promising candidates for many practical applications like, e.g., sensors. For instance, CPBs of poly(N-isopropylacrylamide) collapsed from an R_g of 61 nm at 20 °C to 25 nm at 32 °C,[53] poly(N,N-dimethylaminoethyl methacrylate) (PDMAEMA) CPBs were reported to be responsive to changes in pH.[18] The corresponding quaternized analogues, poly([2-(methacryloyloxy)ethyl] trimethylammonium iodide) (PMETAI) brushes collapsed into spheres in solutions with a high concentration of monovalent salt, as proven by dynamic light scattering (DLS) and atomic force microscopy (AFM) (Fig. 1-1).

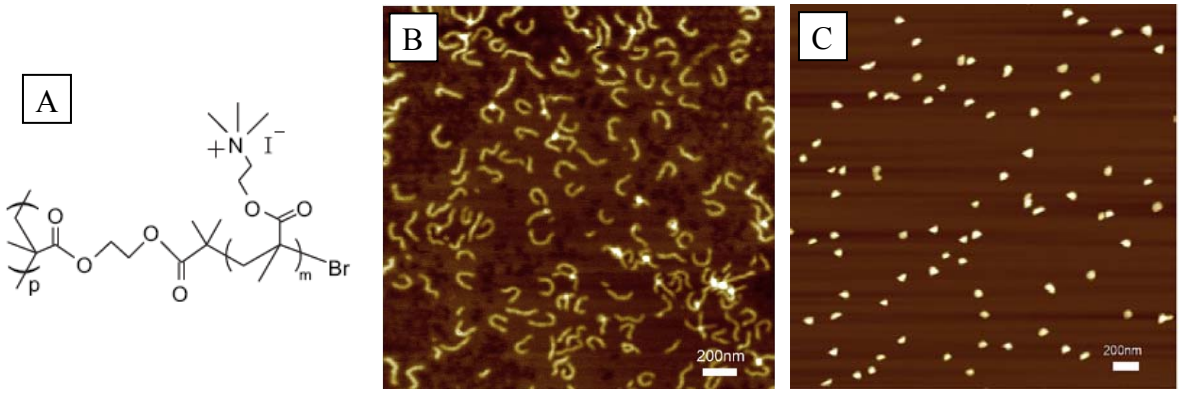

Figure 1-1. (A) Molecular structure of PMETAI CPBs, (B) their AFM height image on mica (Z range 7 nm) spin-coated from their aqueous solution, (C) AFM height image of PMETAI brushes on mica spin-coated from 0.5 M sodium bromide solution (Z range 12 nm).

Recently, more complex cylindrical polymer architectures with various copolymer structures have been prepared.. For example, a core-shell structured amphiphilic CPBs demonstrated structural collapse of the interior PS block in pure methanol; through the addition of chloroform

to reach a volume ratio of 1:1 the PS chains were solvated again and adopted an extended conformation;[3] a copolymer with a linear PS block and a brush block with PAA side chains showed unusual association in selective solvents, e.g. it aggregated into a star-like micelles in aqueous solution.[86]

1.1.2.2 Properties in the bulk

The high density and proportion of relatively short side chains present in molecular brushes has an important effect on their resulting bulk properties. Due to the radial distribution and extended nature of the backbone, chain packing can be significantly hindered, leading to morphologies different from those expected for simple linear polymers with the same identity as the side chains. Wesslen et al. found that CPBs with short PEO side chains (DP = 9 or 23) were amorphous with a glass-transition temperature of –55 to –60°C, and crystalline only when the PEO side chains were sufficiently long (e.g, DP = 45) with a melting point of 38-44°C.[87]

In the bulk phase, the entanglement of the backbone can be largely limited due to its small volume fraction compared to the side chains. This self-disentangled behavior results in unique viscoelastic properties dependant on the length of the side chains as well as on the backbone. For long CPBs, two rubbery plateaus at 10^5 Pa for the relaxation of side chains, and 10^3 Pa for the entire brush molecule could be detected in the master curves for the dynamic storage modulus.[88-90] Moreover, X-ray measurements revealed that CPBs extruded from the melt state show a macroscopic orientation. The effect is attributed to occurring backbone-backbone correlation of neighboring brushes.[91]

1.1.2.3 CPBs in thin-films on different substrates

On solid substrates, the extension of the backbone due to steric repulsion of the adsorbed side chains results in a rod-like conformation. This gives a nanometer-sized building block with well-defined shape and multiple chemical functionalities. Depending on the strength of adsorption and the brush architecture, brush molecules may undergo both association and dissociation upon their adsorption onto surfaces. It has been reported that PBA CPBs with two linear poly(oxtadecyl methacrylate) chains on both ends can associate into multimers such as long blocks and branches due to the crystallization of the octadecyl tail segments.[44]

Through recent advances in environmentally controlled AFM, the in-situ monitoring of conformational changes of single brush molecules could show the reversible transformation from

an extended wormlike to a compact globular structure upon changing the relative vapor pressure of water and ethanol in the surrounding atmosphere.[92] The adsorption of water and ethanol changed the surface properties of the mica substrate and thus the attraction of the side chains towards the substrate. Another interesting phenomenon of CPBs on solid substrates is the scission of the polymer backbone(Fig. 1-2).[93]The experiment was performed by recording a series of AFM images obtained for different incubation times of a brush with particularly long side chain on a surface of a water/propanol substrate. The scission of the backbone was verified by observing the shortening of the brush and, alongside with that, an increase in the amount of brushes in the probing range.

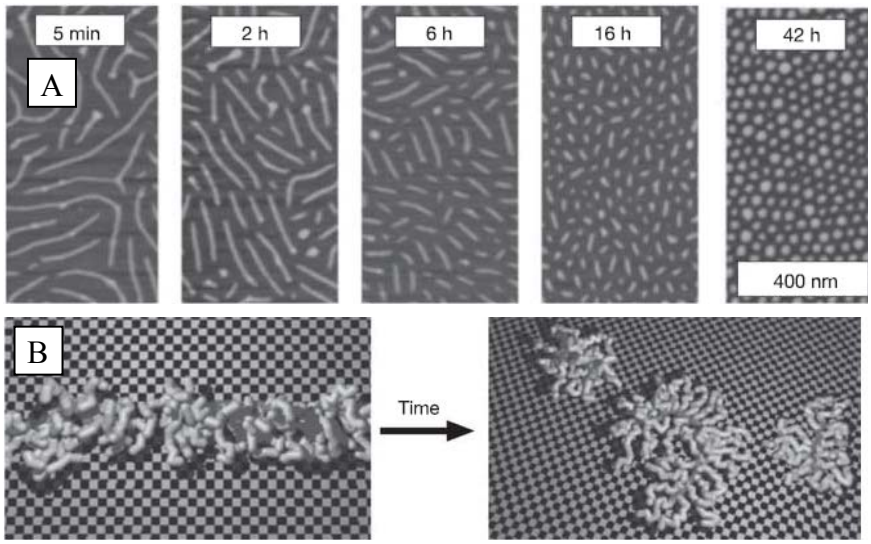

Figure 1-2. (A) Degradation of CPBs on mica by AFM height imaging after exposure for different time periods to a water/propanol (99.8/0.2 wt/wt%) substrate. (B) Schematics of an adsorbed brush (left) which undergoes spontaneous scission of the covalent backbone (right). Side chains are shown in light grey, the backbone in dark grey.

The unusual properties of brush macromolecules on surfaces arise from their ability to change their conformation in response to variations of the surface energy of the substrate and lateral compression. By monitoring the conformational changes of CPBs one could use them as sensors to measure the local pressure within precursor films of polymer drops spreading on a solid substrate.[94] The friction coefficient of the molecules depending on the substrate can be deduced from the measured pressure gradient. This method offers a facile and straightforward alternative technique to diffusion measurements for determining molecular friction on surfaces.

Another recent achievement shows the enhanced alignment of polymer cylinders during spreading on the surface of highly oriented-pyrolytic-graphite.[95] Unlike conventional flow-induced orientation of anisotropic objects, e.g. rod-like particles, the observed molecular orientation is not coupled with the direction of flow (Fig. 1-3). This suggests that the role of flow is merely to enhance diffusion and thus facilitate epitaxial ordering of the large macromolecules, while the direction of orientation was independent on the flow direction, instead solely determined by the underlying crystallographic lattice of the graphite surface.

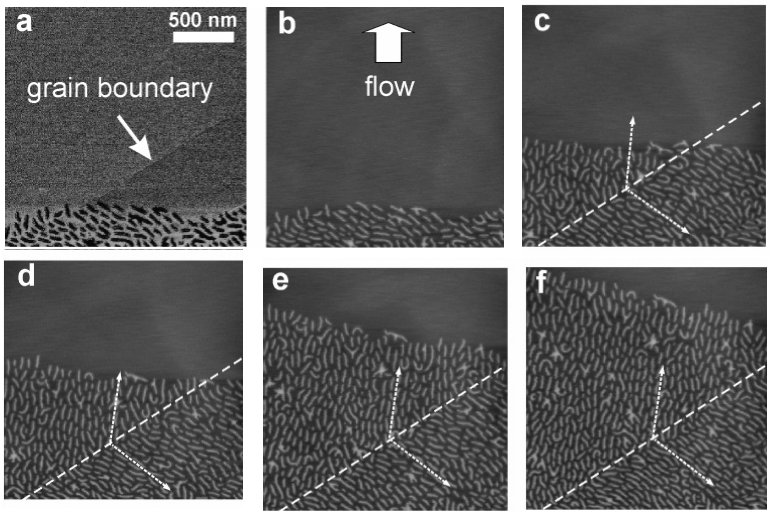

Figure 1-3. AFM real-time imaging of the shift in molecular orientation upon crossing a grain boundary during the spreading of PBA CPBs on graphite. The images (a) and (b) represent phase and height AFM images from the same sample area in order to visualize the grain boundary (indicated by a white arrow and dashed lines later). The arrow with dotted lines in images (b-f) indicates the average molecular orientation within the two domains.

1.1.3 Structure of CPBs

In terms of chemical compositions and architectures, CPBs with linear side chains can be classified into 8 main structures.(Scheme 1-4) The most common and basic structure is the homopolymer CPB (Scheme 1-6a). Based on this simple model, more complex and functional CPBs have been designed and synthesized, aiming at new structures, properties and applications. So far, core-shell-type, core-shell-corona-type, Janus-type, block-type, statistical-type, gradient-type and macrocyclic-type homo/copolymer CPBs have been successfully prepared. They can be employed as building blocks to construct brush superstructures.

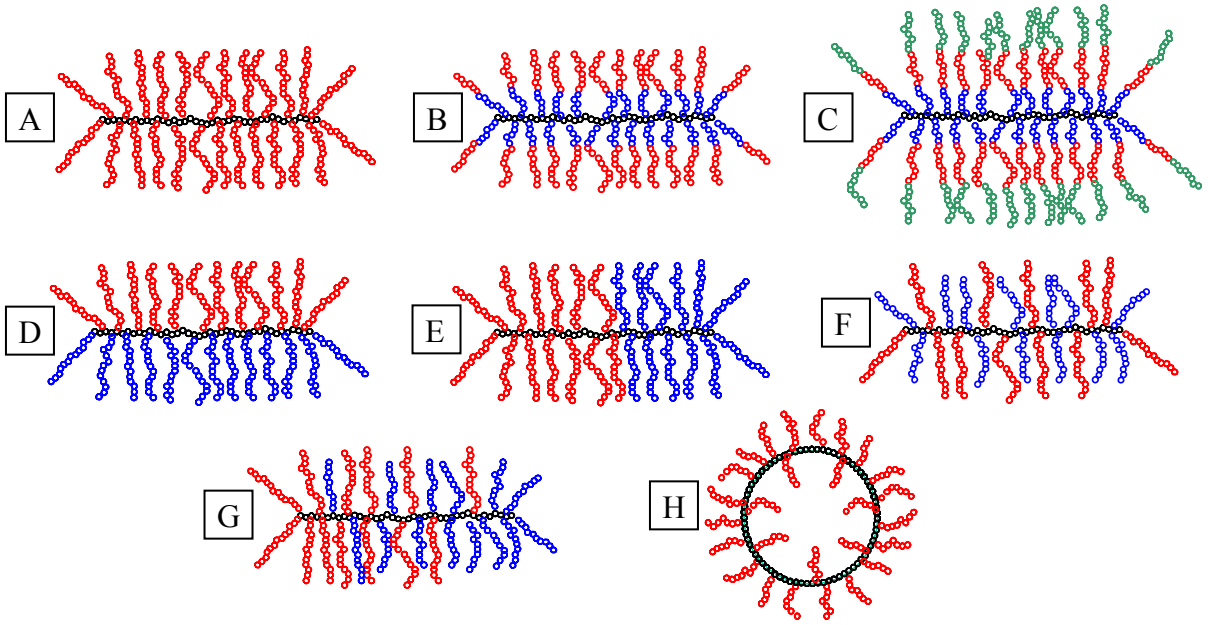

Scheme 1-4. Various structures of CPBs: (A) a homopolymer brush, (B) a core–shell brush, (C) a core-shell-corona brush, (D) a Janus-type brush, (E) a block-type brush, (F) a statistical brush, (G) a gradient brush, and (H) a macrocylic brush.

1.1.3.1 Core-shell and core-shell-corona CPBs

If side chains are built from diblock copolymers or triblock terpolymers, CPBs will exhibit a core–shell or core-shell-corona type structure. So far, core–shell CPBs have been synthesized by ‘‘grafting through’’,[9, 96, 97] and ‘‘grafting from’’ methods.[16, 45-47, 49, 52] In the “grafting through” method, the conventional radical polymerization of diblock macromonomers with end-functionalized vinyl group is a straightforward route, for example, the radical polymerization of poly(2-vinylpyridine)-*b*-polystyrene (P2VP-*b*-PS) macromonomers.[9] However, the inherent disadvantages associated with the ‘‘grafting through’’ technique are also valid here. A further difficulty lies in the preparation of the diblock macromonomers. Compared with “grafting through” method, “grafting from” is more favored to achieve well-defined core–shell structures. Very often, diblock copolymer side chains were grafted from a polymethacrylate-based backbone, like PBIEM, via sequential ATRP of two monomers from the pendant initiating groups on the backbone. The length as well as the functional groups can be readily tuned by ATRP through varying conversion and monomers. Besides ATRP, ROP and NMP polymerization have also been reported to enable the growth of diblock copolymer side chains. For example, Wooley et al. reported a tandem synthetic strategy, by which the polymeric backbone with pendant NMP

initiating groups was prepared by ROP. The sequential polymerizations of isoprene and *tert*-butyl acrylate followed by hydrolysis of the P*t*BA block resulted in an amphiphilic core-shell copolymer cylindrical brush.[49]

The multiblock side chains increase not only the structural components, but also introduce new morphology and properties. AB-type diblock side chains may include block segment combinations of soft-hard, hydrophilic-hydrophobic and crystalline-amorphous, and therefore the entire brushes then resemble intramolecularly phase-separated cylindrical micelles. For example, in CPBs with poly(ε-caprolactone)-*b*-poly(*n*-butyl acrylate) (PCL-*b*-PBA) side chains, the cylindrical microphase separation of the crystalline PCL core and the amorphous PBA shell block resulted in a distinct stripe morphology.[46] The hydrophilic-hydrophobic microphase separation within individual CPBs is extremely useful for the template-directed synthesis of one-dimensional hybrid nanostructures which will be described in more details in chapter 1.3.

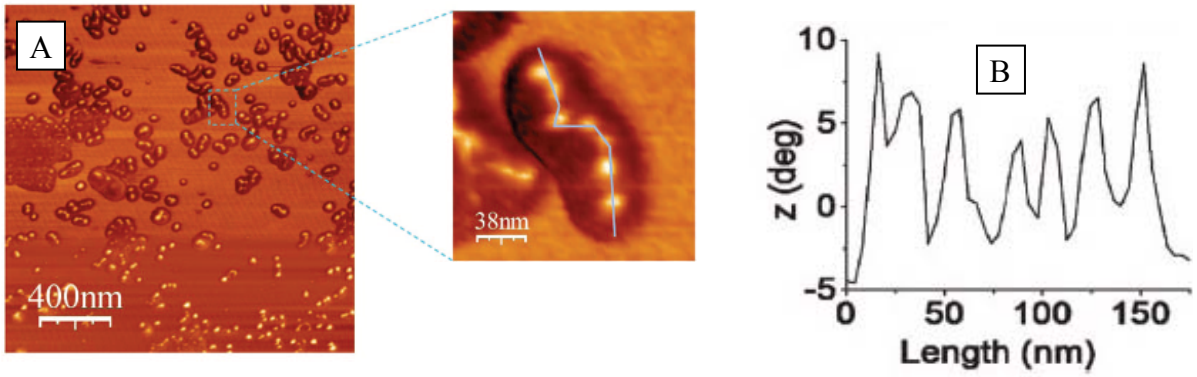

Figure 1-4. AFM height images (A) and section analysis (B) of core-shell cylindrical polymer brush with PAA-*b*-PBA block copolymer side chains dip-coated onto mica from toluene.

Besides the formation of hybrid nanowires, the core-shell CPBs may also show responses to environmental changes (e.g., solvent and metal ions) in an anisotropic way due to the block copolymer character of the side chains. For example, by simply changing the solvent quality, one can easily adjust the thickness of the core or the shell of amphiphilic brushes. Amphiphilic core-shell CPBs with poly(acrylic acid)-*b*-poly(*n*-butylacrylate) (PAA-*b*-PBA) side chains exhibited a regular wormlike morphology in a mixture of chloroform/methanol (1:1). Through the addition of divalent (Cd^{2+}) or trivalent (Fe^{3+}) metal ions the core turned into pearl-necklace-like structures. Even without the addition of metal ions, the pearl-necklace-like morphology appeared simply by

changing the solvent to pure toluene, a non-solvent for the PAA core.[98] (Fig. 1-4)

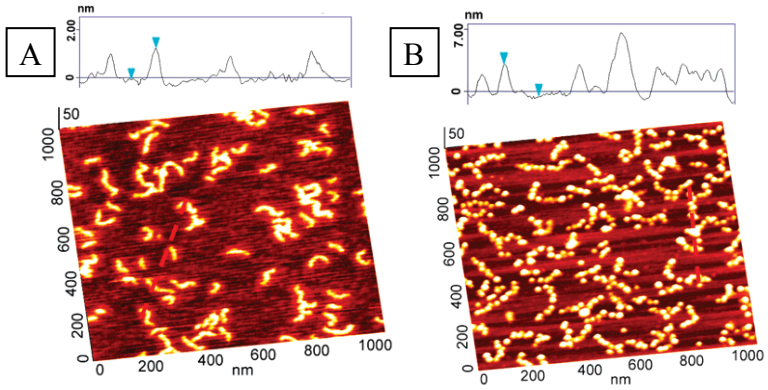

Figure 1-5. AFM height images and cross-section analysis of CPBs with PBA-*b*-PAN diblock copolymer (A) and PBA-*b*-PAN-*b*-P*t*BA triblock terpolymer side chains (B).

It is well-known that the phase diagram of ABC triblock terpolymers is much more complex compared to AB diblock copolymers. For core-shell-corona structured CPBs, the third block in the side chains additionally influences the solution conformation and the behavior on substrates through microphase separation effects. The preparation of CPBs with triblock terpolymer side chains has been rarely reported due to the complex synthetic process. Considering the steric triblock terpolymer side chains and the difficulty in purification, Matyjaszewski[55] et al. first reported the successful preparation of core-shell-corona CPBs with poly(*n*-butyl acrylate)-*b*-polyacrylonitrile-*b*-poly(t-butyl acrylate) (PBA-*b*-PAN-P*t*BA) triblock terpolymer side chains via the "grafting from" approach. AFM showed that a pearl-necklace morphology instead of a wormlike shape was observed after the introduction of the PAN block.(Fig.1-5) This morphology changes could be ascribed to the avoidance of the rather hydrophilic mica surface through the hydrophobic P*t*BA segments and, further, the partial miscibility of PBA and P*t*BA.

1.1.3.2 Statistical and Janus-type CPBs

Two types of chemically different homopolymer side chains can be tethered to the same backbone. Depending on their distribution along the backbone (random or alternating), their interaction parameters, and the nature of the solvent, side chains of these brushes can have a mixed structure or segregate into two different hemicylinders, also called a Janus cylinder.[23]

Statistical copolymer brushes consist of two statistically arranged different side chains, for

instance, poly(2-vinylpyridine) (P2VP) and poly(methyl methacrylate) (PMMA), [99] prepared through the random copolymerization of their corresponding macromonomers. These copolymer brushes showed a normal wormlike morphology when spin-cast from chloroform onto mica. However, quaternization of the P2VP with ethyl bromide raised the incompatibility between the different side chains and induced intramolecular phase separation. Depending on the solvent for spin casting, these statistical copolymer brushes adopted peculiar shapes such as horseshoe or meander-like structures on mica substrates.

Up to now, reported janus-type cylindrical polymeric micelles possess a linear fixed core instead of a linear backbone via the selective crosslinking of the central block of a cylindrical bulk morphology.[23] By S_2Cl_2 crosslinking (cold vulcanization) of the polybutadiene (PB) block in the lamella–cylinder bulk morphology of PS-*b*-PB-*b*-PMMA triblock terpolymers, Janus cylinders consisting of a crosslinked PB core and two hemicylinders of PS and PMMA were obtained after sonication assisted dissolution. The lack of centrosymmetry in the Janus cylinders has led to their interesting aggregation behavior into superstructures on different length scales, and has opened up a wide field of conceivable applications, ranging from medicine, biochemistry, and physics to colloidal chemistry.

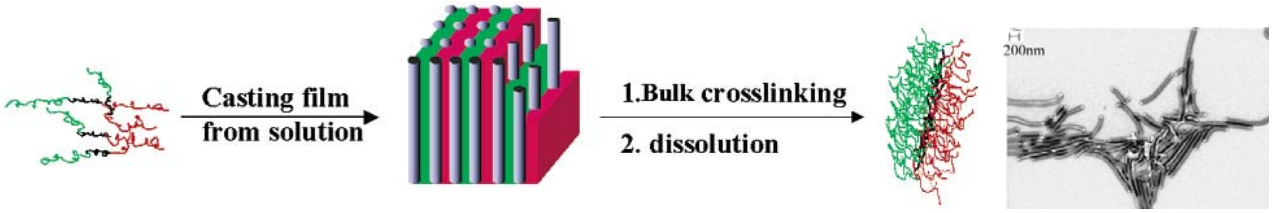

Scheme 1-5. Illustration of the synthesis of core-crosslinked Janus cylinders (left). The SEM image of Janus cylinders on a silicon wafer is shown on the right.

1.1.3.3 Hetero-grafted block-type CPBs

Among the architectural possibilities for CPBs, AB-type hetero-grafted block brushes have not been studied extensively due to limited synthetic approaches. The first example was reported by Ishizu et al. by the combination of "grafting through" and "grafting from" techniques.[100] In their work, ATRP of a macromonomer oligo(ethylene glycol) methacrylate (OEGMA) was first conducted to form the first brush block (A block). It was further used as macroinitiator for the subsequent ATRP of HEMA. The esterification of the PHEMA block to yield a PBIEM macroinitiator followed by the grafting of PHEMA from PBIEM resulted in the second brush

block (B block) with PHEMA side chains. However, this pioneering approach has some limitations. First, it was difficult to achieve a high DP during the polymerization of the OEGMA macromonomer due to steric hindrance. Second, the removal of excess macromonomers from the brushes was challenging, as already mentioned earlier. Third, the chain extension of the POEGMA brush macroinitiator to form brush-block-coil was inefficient owing to the rather low accessibility of the initiating site for monomers.

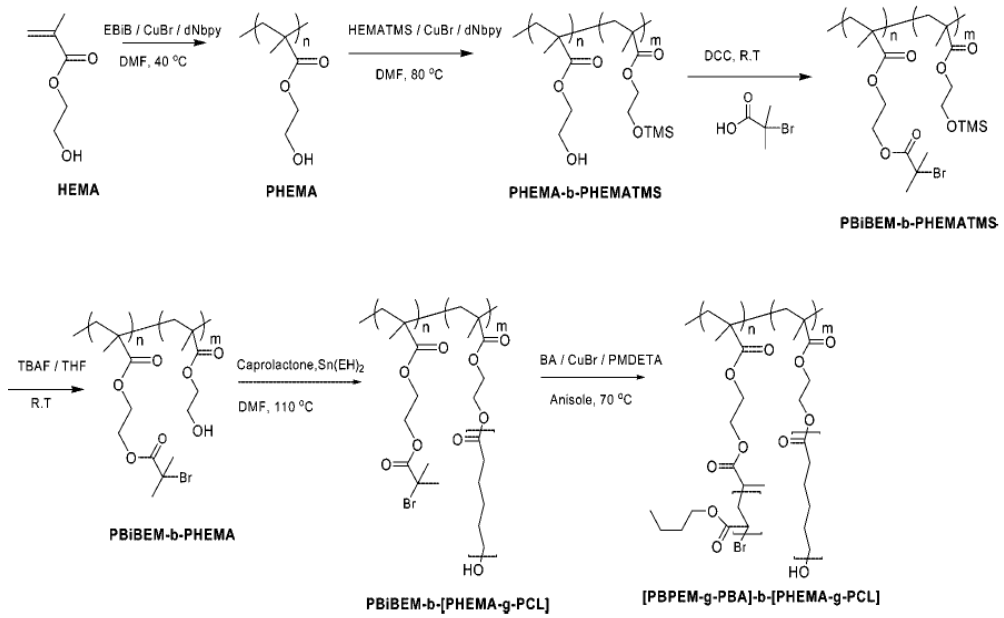

Scheme 1-6. Synthesis of hetero-grafted CPBs containing PCL and PBA side chains.

Very recently, the first successful synthesis of hetero-grafted block brushes with PCL and PBA side chains using only the "grafting from" technique has been reported (Scheme 1-6).[101] The crystalline PCL was synthesized by ROP from a PBIEM-*b*-PHEMA diblock copolymer backbone. Then, the amorphous PBA segments were synthesized by ATRP to form the hetero-grafted block brush. The success of the synthetic strategy was verified through imaging of individual brushes by AFM.

1.1.3.4 Gradient CPBs

CPBs with a gradient of grafting density in the side chains along the backbone have been synthesized via the ''grafting from'' and "grafting through" techniques with ATRP.[36, 51] Via the "grafting from" technique, a macroinitiator, poly(methyl methacrylate-graft-2-(2-bromopropionyloxy)ethyl methacrylate) [poly(MMA-*g*-BPEM)], was prepared via a gradient

copolymerization of MMA and TMS-HEMA and the following attachment of an ATRP initiator. Side chains were then grafted only from the pendant initiating groups in the BPEM unit in the poly(MMA-*g*-BPEM) backbone, leaving the MMA units untouched. Interestingly, it is found that upon the compression of a monolayer of these CPBs on the air/water interface followed by transfer to mica, these gradient brushes underwent asymmetric changes in their molecular conformation: the rod–globule transition occurred only at the end where the brush was densely grafted, leaving a molecule with a globular head and an extended tail, a so-called tadpole conformation.[51]

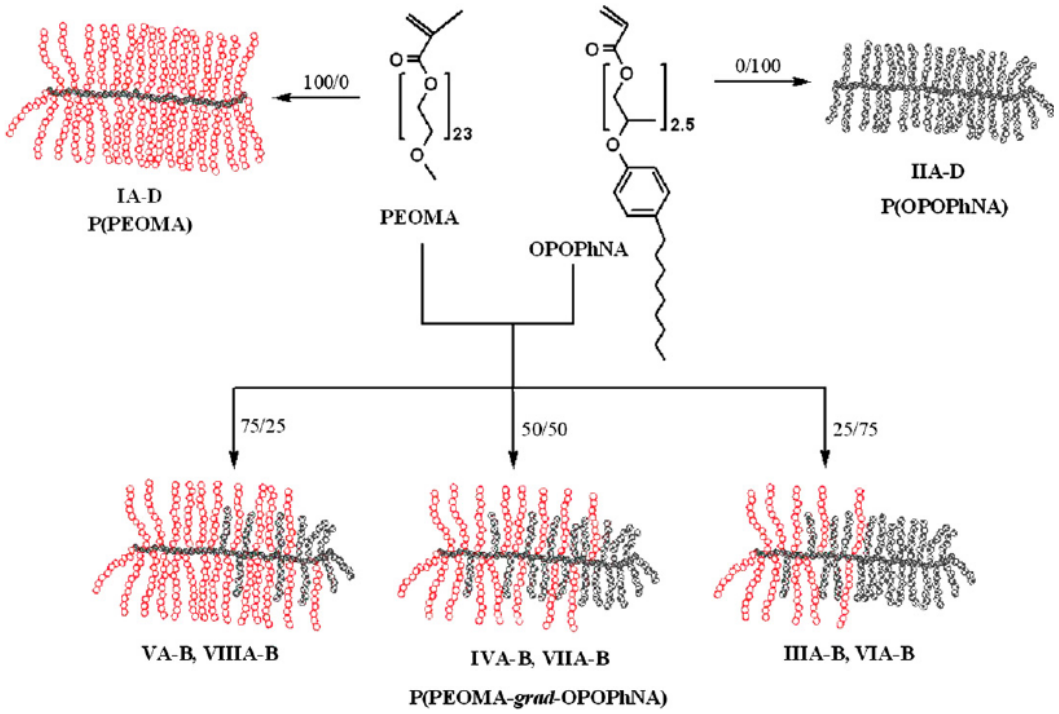

Scheme 1-7. Structures of OEGMA, OPOPhN, and their (co)polymers.

In the "grafting through" approach, the ATRP copolymerization of an OEGMA macromonomer with a hydrophobic (oligo(propylene glycol)-4-nonylphenyl ether acrylate; OPOPhNA) was described (Scheme 1-7).[36] The one-pot procedure using various ratios of comonomers resulted in amphiphilic graft copolymers with a differential distribution of OEGMA and OPOPhNA grafts. Due to the higher reactivity of OEGMA than OPOPhNA, copolymer brushes with a spontaneous gradient composition starting from the grafted segment of POEGMA were obtained. Because of their amphiphilic character, they can exhibit phase-separation of

hydrophobic and hydrophilic domains depending on the environmental conditions (temperature, surface, and solvent).

1.1.3.5 Macrocyclic polymer brushes

Macrocyclic polymer brushes can be considered as special CPBs, in which the two ends of the brushes meet each other by a coupling reaction. Although macrocyclic polymers were first obtained 40 years ago,[102] the preparation of large macrocyclic (co)polymer brushes is limited by (i) the difficulty to get pure α,ω-difunctional high molar mass precursors, (ii) the drastic decrease of the end-to-end ring closing efficiency when increasing the distance between the chain ends, and (iii) the separation from linear contaminants of comparable molar mass.

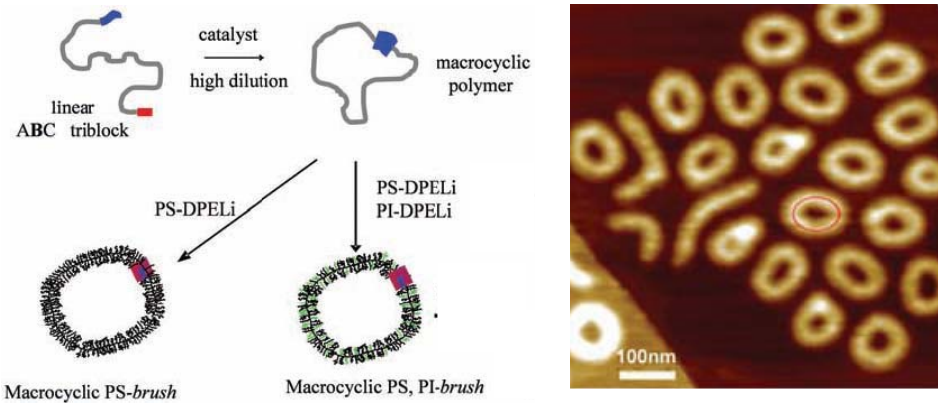

Figure 1-6. Left: strategy for the synthesis of macrocyclic copolymer brushes. PS-DPELi, (1,1-diphenylethylene) end-capped polystyryllithium; PI-DPELi, (1,1-diphenylethylene) end-capped polyisoprenyllithium. Right: AFM image of macrocyclic PS brushes with PS branch after fractionation by precipitation.

Very recently, Deffieux el at. have developed a new strategy to synthesize large polymer macrocycles based on an ABC triblock terpolymer by sequential living cationic polymerization of three different vinyl ethers(Fig. 1-6).[103] In the triblock terpolymer, the long central B block is extended by two short A and C sequences bearing monomer units with reactive antagonist functions. The external blocks are then selectively activated under dilute conditions to allow intramolecular coupling between the A and C blocks to form the macrocyclic polymers, with further functionalization to form the corresponding brush polymers with PS or randomly distributed PS and polyisoprene (PS/PI) branches. These macrocylic polymer brushes were readily visualized by AFM.

1.1.3.6 Superstructures from CPBs.

CPBs have been used as building blocks to construct more complex polymer architectures for star-shaped brushes,[40, 104] double-grafted (graft-on-graft) brushes,[17, 90] cylindrical tubes,[103] flower-like or dumbbell-like structures[101] and others[86].

Star-shaped brushes have been prepared via three strategies, "grafting onto", "grafting from" and self-assembly processes, respectively. In the "grafting onto" process, star-shaped brushes with four or five arms composed of CPBs have been synthesized via the coupling reaction of living polystyryllithium onto starlike PCEVE main chains.[40] In the "grafting from" strategy, three or four-arm brushes were prepared by the grafting of PBA side chains from a star-shaped backbone prepared by ATRP.[104] Concerning the self-assembly process, rod–coil amphiphilic brushes consisting of a stiff PAA cylindrical brush and a linear coil PS chain attached to the backbone, have been synthesized via the metallocene-catalyzed sequential polymerizations of PS macromonomer and *t*BA followed by hydrolysis of the P*t*BA block. They were shown to form giant, spherical micelles in selective solvents like THF or water.[86]

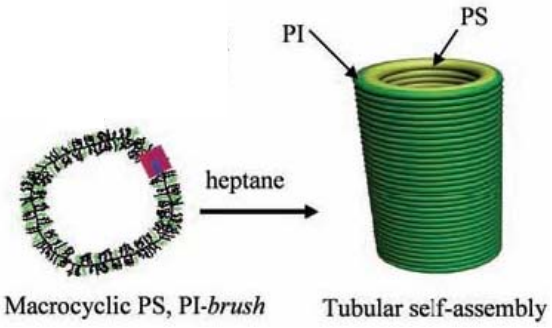

Figure 1-7. Self-assembly of macrocyclic brushes into cylindrical tubes in heptane.

In a selective solvent for the PI branches, macrocyclic PS/PI brushes self-assembled into submicron-sized cylindrical tubes (Fig. 1-7), indicated by dynamic light scattering (DLS) and AFM on solid substrates.[103] In heptane, the cyclic PS/PI brush copolymer self-assembles, forming a single population of large cylindrical objects with an average hydrodynamic radius of 200 nm. AFM analysis showed that these tubular objects exhibit section diameters of about 100 nm, corresponding to elementary macrocyclic PS/PI brushes, and lengths of up to 700 nm.

Double-grafted CPBs have been prepared via the ''grafting from'' method, via the growth of a macromonomer instead of a normal monomer from the linear long backbone. These

macromonomers consists of either a long linear alkyl chain or PEO oligomer. The resulting polymer has a very high density of grafted chains with rather strong repulsion among them.[17, 90]

1.1.4 Hybrid nanostructures templated by CPBs

Contrary to the comprehensive research concerning the synthesis and properties of CPBs, the investigation of their application potential has only started several years ago. Among the different structures, core–shell CPBs are of special interest because they can lead to cylindrical hybrid nanostructures, such as nanowires, with interesting properties after metallization or other modifications.

As a first attempt, core-shell CPBs with a P2VP core and a PS shell have been successfully employed as templates to prepare a linear array of gold nanoclusters and nanowires.[105] The P2VP domains were one-dimensionally confined by the PS corona and complexed with negatively charged $AuCl_4^-$ ions. After reduction with $NaBH_4$, gold nanoparticles were in-situ generated exclusively within the core and aligned in a linear manner. In another attempt by Ishizu, a poly(α-methylstyrene) (PMS) shell as an insulating layer confines a cylindrical P2VP core, in which then polypyrrole was synthesized, aiming at the preparation of highly conducting molecular wires.[106] However, in these two templates, the length distribution was broad because they were synthesized by the "grafting through" method. Without additional purification of the templates, like precipitation fractionation, the length of the fabricated nanowires was not well controlled.

Müller et al. have synthesized uniform core–shell CPBs with a PAA core and a PBA shell via a combination of anionic polymerization (of the backbone) and ATRP (side chain), using the ''grafting from'' technique.[7, 8] They were used as single molecular nanoreactors and cylindrical templates for the generation of inorganic nanoparticles. Wirelike assemblies of semiconducting (CdS) and superparamagnetic (iron oxide) nanoparticles within these amphiphilic CPBs have been prepared.(Fig. 1-8) The synthetic strategy takes advantages of each of the unique aspects of the CPBs. First, the core of the polymer brush possesses carboxylate groups capable of undergoing coordination chemistry with metal ions and works as a nanoreactor for the nanoparticle formation. Furthermore, it directs the particle distribution along the brush backbone. Second, the shell of the polymer brush protects the fabricated nanoparticles from aggregation and provides the solubility of the hybrid cylinders in organic solvents.

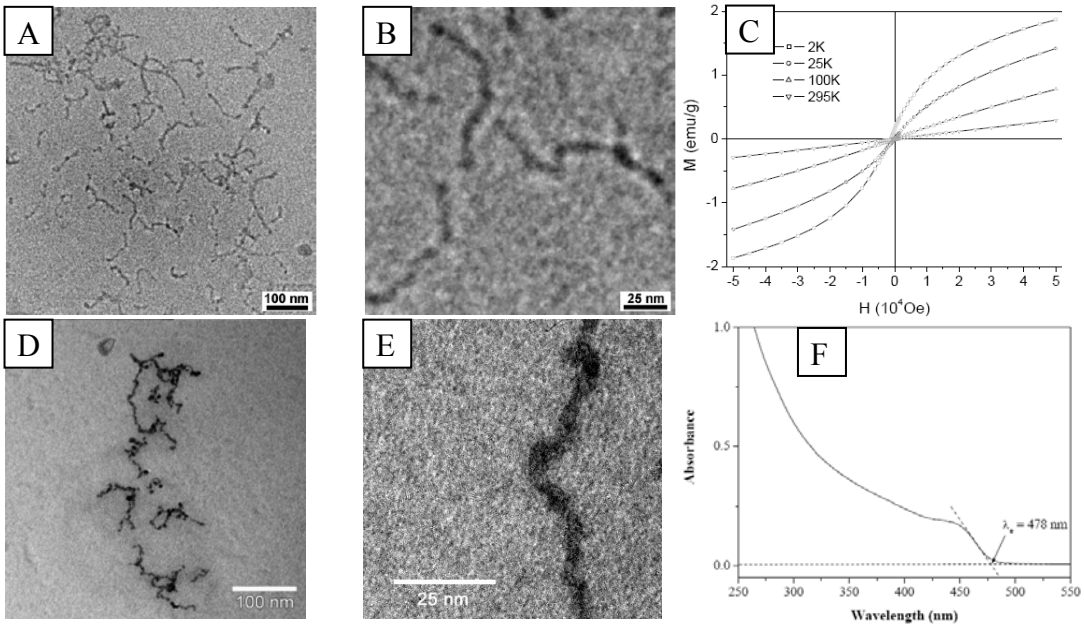

Figure 1-8 (A) Non-stained TEM image of γ-Fe_2O_3 nanowires templated by CPBs with a PAA core and a PBA shell, (B) is the enlarged view, and (C) is the corresponding magnetization curve of the hybrid. (D) Non-stained TEM image of CdS nanowires templated by CPBs with a PAA core and a PBA shell, (E) is the enlarged view, and (F) is the corresponding UV-vis spectrum of the hybrid solution.

1.2 One-dimensional hybrid organic-inorganic nanostructures

Compared to bulk materials, low-dimensional nanomaterials, especially 1-D nanomaterials, have attracted increasing research attention in the last decade, due to their superior properties, which strongly depend on size and geometry.[107-113] Compared to their 0-D and 2-D counterparts, the creation of one-dimensional (1-D) nanostructures (nanowires, nanorods, nanobelts and nanotubes) has been hampered by the difficulties associated with the synthesis. Modern application requires nanostructures with well-controlled dimensions, morphology, phase purity, and chemical composition. In general, 1-D nanostructures provide good model systems for the investigation of the dependence of electrical, optical, mechanical and thermal properties on the materials dimensions and size reduction (or quantum confinement). They are also expected to play an important role as both interconnects and functional units for electronic, optoelectronic, electrochemical, and electromechanical nanodevices.[107, 114] Various methods and techniques have been exploited for their fabrication, and the development of new techniques is still required to enable their production in larger quantities from a broad range of materials, rapidly, and at reasonable costs.

1.2.1 1-D hybrid organic-inorganic nanostructures

The combination at the nanosize level of active inorganic and organic components in a 1-D manner paths the way to an immense new area of materials science has and is supposed to have tremendous effects on the development of multi-functional materials. These functional hybrids are considered as innovative advanced materials with promising applications in many fields: optics, electronics, energy storage and conversion, mechanics, membranes, catalysis, sensors, biology, etc.[115] It is usually believed that the introduction of the organic phase into the 1-D systems has several advantages. First, it can improve the stability of the inorganic nanostructures by passivating their surface and reducing the surface tension. Second, the covering of the 1-D inorganic nanostructures by organic materials enables the fabrication of nanodevices from individual 1-D inorganic nanostructures since the inorganic objects are separated from each other. Third, the organic phase, in this particular case the polymers, can solubilize the hybrid nanostructures in solution and prevent the inorganic particles from sedimentation. Finally, the organic phase-based synthesis of 1-D hybrid nanomaterials is a low-cost production and can be

easily scaled up for potential applications.

The properties of such 1-D hybrid nanomaterials often originate from a combination of the single building blocks. In most cases, organic components are introduced at the beginning simply as a template to fabricate inorganic 1-D nanostructures. The template remains together with the inorganic part after the preparation process to achieve a specific aim, for example avoiding the agglomeration of the 1-D inorganic nanostructures due to their rather high surface energy[7, 8, 105] or to tune the physical properties (electronic, optic, et al.) of the inorganic nanostructures in a facile manner. On the other hand, inorganic moieties, like nanoparticles, are embedded into polymeric 1-D matrix to introduce special properties (optical, catalytic, magnetic, et al) to the polymer nanostructures.

So far, the most useful and powerful methods for the preparation of 1-D hybrid organic-inorganic nanomaterials are the template-directed synthesis and electrospining techniques.[115] Various nanostructures and unique functions have been realized in the 1-D hybrid nanostructures obtained by these two methods.

1.2.2 Template-directed synthesis

Template-directed synthesis represents a conceptually simple, intuitive, straightforward, and versatile route to 1-D hybrid nanostructures. A number of templates, mostly organic ones, have been used as a scaffold, including mesoscale structures self-assembled from surfactants or block copolymers, channels within porous polymeric or inorganic materials, natural 1-D macromolecules such as DNA, or rod-shaped viruses. Generally, template-directed synthesis provides a simple, high-through-put, and cost-effective procedure that also allows the transfer of a complex topology present on the surface of a template.

1.2.2.1 Self-assembled molecular structures

Mesophase structures self-assembled from surfactants and peptides create a wide class of useful and versatile templates for generating 1-D hybrid nanostructures in relatively large quantities. It is well-known that surfactant molecules may spontaneously organize into rod-shaped micelles (or inverse micelles) when their concentration reaches a critical value. These anisotropic structures can be immediately, or after the fixation of the structure, used as soft templates to promote the formation of nanowires, nanorods or nanotubes when coupled with an

appropriate chemical or electrochemical reaction. This route is especially useful to prepare metal nanorods from solution, like gold nanorods. Murphy and co-worker demonstrated the seed-mediated growth of gold nanorods in a solution that contained rod-like micelles assembled from cetyltrimethylammonium bromide (CTAB).[116, 117] The lateral dimensions and aspect ratios of these nanorods could be controlled by varying the ratio of seeds relative to the metal precursors. Besides metal, metal oxide nanorods have also been synthesized by this method. For example, α-FeOOH nanorods with diameters of 170–210 nm and lengths up to 3–5 μm were synthesized in a high yield via hydrothermal methods using wormlike micelles from sodium dodecyl sulphate as templates.[118]

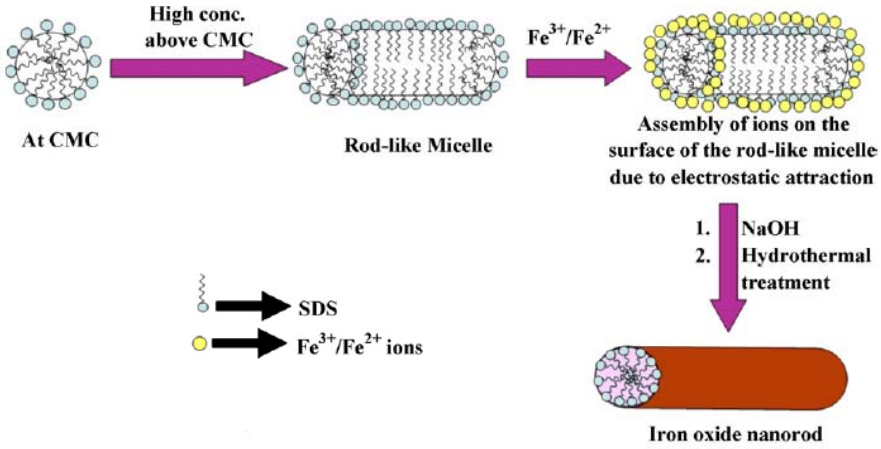

Scheme 1-8. Illustration of the synthesis of α-FeOOH nanorods in aqueous SDS solution.

Comparing with small organic molecules, block copolymers are the most widely used soft template for the fabrication of 1-D hybrid nanomaterials. When chemically distinct polymer chains are immiscible, these block copolymers will phase separate in solution or in the bulk. By means of self-assembly, either concentration driven or induced by solvent selectivity, block copolymers with suitable volume fractions will undergo microphase segregation and form a regular arrays of cylinders.[24, 119] Due to the unlike properties, the compartments can be individually addressed and decorated with inorganic precursor materials through physical adsorption or chemical coordination. Quite often, the crosslinking of one domain in the self-assembled structures (cylinders or tubes) is performed to improve the stability during the fabrication process. Liu and co-workers synthesized cross-linked cylindrical assemblies starting from a triblock copolymer in the solid state (Scheme 1-9).[120] The triblock copolymer was initially

self-assembled into an array of cylinders crosslinked in bulk. Upon interaction with a good solvent for the polymer, the crosslinked fibers were dispersed into solution, which were further converted into nanotubes with interior carboxylic acid groups by selective core degradation. By encapsulation of inorganic nanoparticles such as γ-Fe_2O_3 inside polymeric nanotubes, well-defined 1-D magnetic hybrids were obtained.

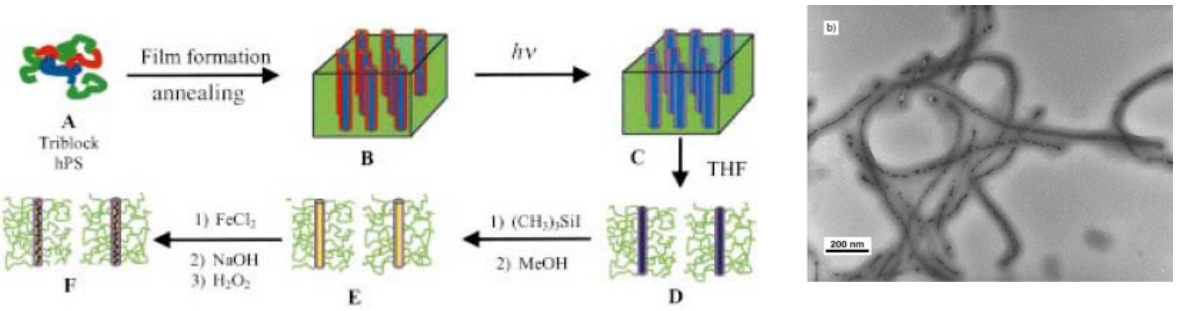

Scheme 1-9. Synthetic strategy (left) and TEM image (right) of the triblock copolymer/γ-Fe_2O_3 hybrid nanofibers.

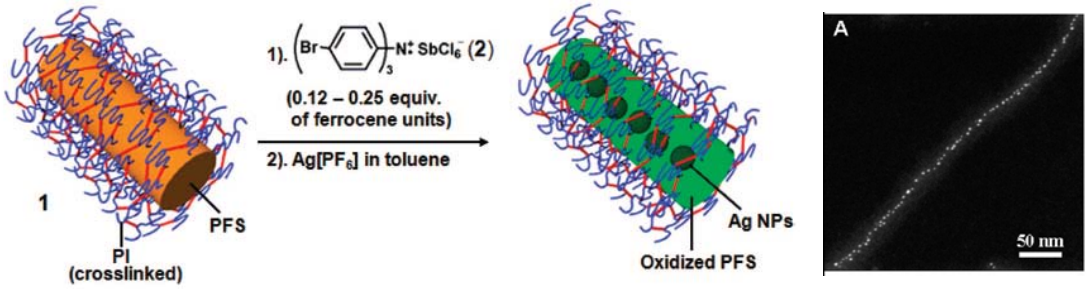

Scheme 1-10. Synthetic strategy (left) and TEM image (right) of the encapsulation of silver nanoparticles in shell-cross-linked hybrid cylinders.

In some block copolymers the building units, already contain inorganic precursors. In this manner, the self-assembly process is completed simultaneous with the 1-D alignment of the inorganic moieties. For instance, Winnik and Manners have reported the preparation of colloidally stable shell-cross-linked cylindrical organometallic block copolymer micelles with adjustable length and swellablity (Scheme 1-10).[121] The core is made up of semicrystalline polyferrocenyldimethylsilane (PFS), which contains Fe and Si in the backbone. The self-assembled cylindrical micelles themselves are 1-D hybrid nanomaterials. They can further act as templates for the introduction of inorganic nanoparticles. In situ redox reactions between the

remaining Fe (II) centers in the PFS core and Ag^+ cations in solution lead to the formation of silver-nanoparticle-encapsulated shell-cross-linked hybrid cylinders.

1.2.2.2 Natural 1-D structures

Nature offers plenty of existing organic nanostructures, in which the building blocks are combined preferentially into a 1-D manner. Typical examples include cellulose,[122] collagen,[123, 124] DNA,[125-128] and the tobacco mosaic virus (TMV).[129-133] These originally elongated nanostructures can be harvested directly from plants or animals for the localization and conversion of inorganic precursors to nanostructures on their surface.

Among them, DNA is the most frequently employed natural 1-D template. Usually the coating with metal nanoparticles, so-called metallization, is a sequence of three main steps. The first step is binding of metal ions or metal complexes to DNA strands to create reactive metal sites. This step is usually called the activation step and is based either on exchanging ions with the DNA backbone, or the insertion of metal complexes between the DNA bases. In the second step, the reactive metal sites are usually treated with a reducing agent. This converts the metal ions or metal complexes into metal nanoclusters fixed onto the DNA strand. The third step of the metallization process then is the autocatalytic growth of these affixed metal nanoclusters, which are now able to act as seeds because of the simultaneous presence of both metal-ions/metalcomplexes as well as reducing agents in the growth solution. In this step, even a second metal ion could be deposited on the DNA scaffold. For example, Co nanoparticles could grow on the Pt nanoseeds in the third step to form Co nanowires within the DNA instead of Pt nanowires.[127] (Fig. 1-9)

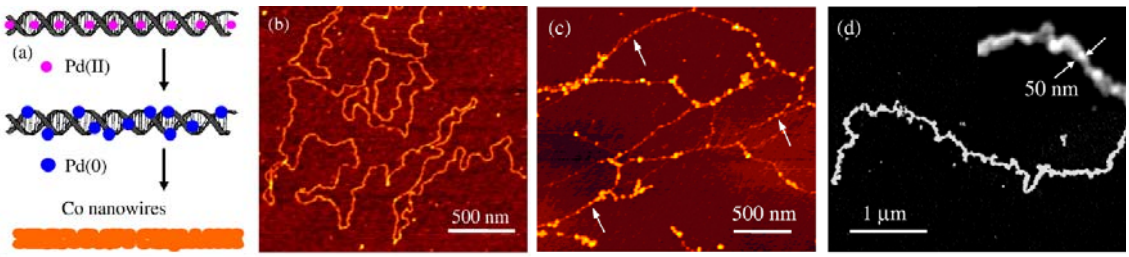

Figure 1-9. (a) Schematic illustration of Pd nanoparticle-controlled Co nanowire growth, (b) AFM image of an unmodified DNA molecule (Z range: 0.98 nm), (c) AFM image of Pd seeds (1-3 nm) coated DNA (Z range: 3.5 nm), and (d) SEM image of a single continuous Co nanowire.

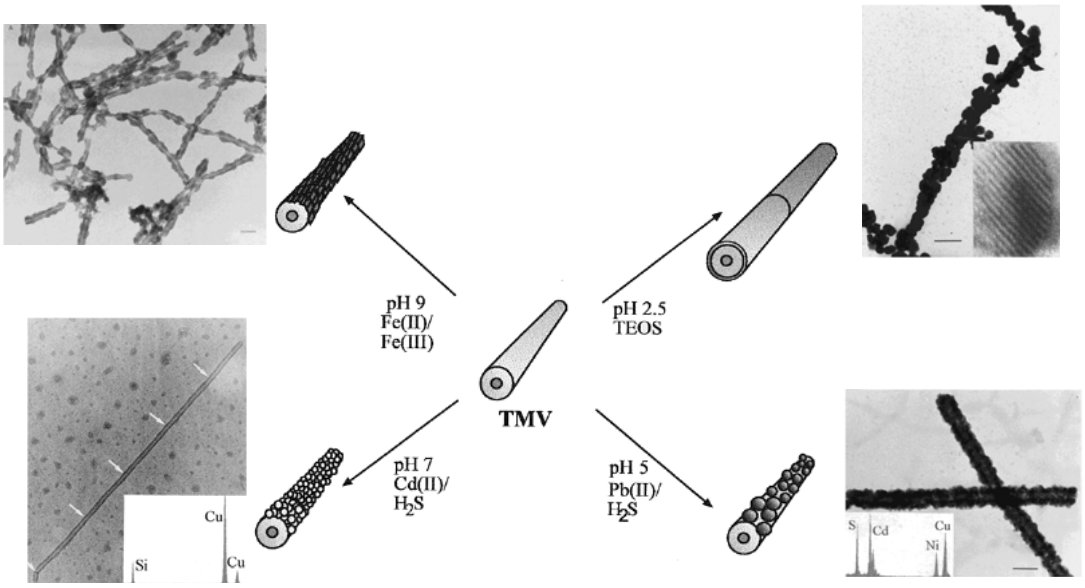

Figure 1-10. Synthetic routes for nanotube hybrids using TMV templates. Clockwise from top right: sol-gel condensation (silica); coprecipitation (PbS and CdS nanocrystals); oxidative hydrolysis (iron oxide).

The TMV is another natural template for the fabrication of inorganic-organic hybrids. TMV is a remarkably stable virus, remaining intact at temperatures up to 60 °C and at pH values between 2 and 10. Each viral particle is 300 x 18 nm in size, with a 4 nm-wide central channel. The internal and external surfaces consist of repeated patterns of charged amino acid residues, such as glutamate, aspartate, arginine, and lysine. Mann et al demonstrated the versatility of TMV as a template for the fabrication of a range of nanotubular organic-inorganic hybrids, as shown inFig. 1-10.[131] In the case of silica mineralization from acidic (below pH 3) solutions, strong interactions are supposed to occur between the TMV particles and anionic silicate species formed by hydrolysis of TEOS, due to positive charges on the protein surface below the isoelectric point. In comparison, preferential deposition of CdS, PbS, and iron oxides on the TMV external surface can be achieved by specific metal-ion binding onto the numerous glutamate and aspartate surface groups.

1.2.2.3 Channels in porous materials

1-D Channels in porous membranes provide another class of templates for the synthesis of 1-D hybrid nanostructures. For this approach, the template contains very small cylindrical pores or voids within the host material, and the empty spaces are filled with the chosen material, which

adopts the pore morphology to form 1-D nanostructured systems. Various types of porous materials, including commercial available porous polymeric membrane[134-136] and alumina films,[137] have been used. Among these, the alumina films are the most promising materials due to their regular channels with little or no tilting with respect to the surface normal. They furthermore exhibit a high pore density. To create 1-D hybrid nanomaterials, inorganic and organic components were simply introduced into the channels either simultaneously or sequentially to achieve the spatial organization of dissimilar and commonly incompatible components. When the inorganic and organic precursors were introduced and treated sequentially, core-shell structured 1-D hybrid nanomaterials should be formed. For example, arrays of TiO_2 tubules were first synthesized within the pores of the alumina membrane via the sol–gel process.[134] After thermal treatment of the TiO_2 tubules, conductive polypyrrole nanowires were grown using the chemical polymerization method inside the semiconductor tubules. This core-shell hybrid structures possess both a high surface area of TiO_2 as well as a photocatalytic activity and a high electrical conductivity.[134] Employing the same strategy, more complicated structures like conductor–insulator–conductor concentric tubules, carbon–polyacrylonitrile–gold for example, have been fabricated.

1.2.3 Electrospinning techniques

Electrospinning, also known as electrostatic spinning, is a highly versatile method to process solutions or melts, mainly of polymers, into continuous fibers with diameters ranging from micro- to nanometers. This method gained substantial academic attention since the 1990s because of the close combination of both fundamental and application-oriented research combining scientific as well as engineering disciplines. Electrospinning is currently the only technique that allows the fabrication of continuous fibers with diameters down to a few nanometers. The method can be applied virtually to all soluble or fusible polymers, polymer alloys, and polymers loaded with various kinds of nanoparticles or active agents. Nanofibers with complex architectures, such as core–shell fibers or hollow fibers, can be produced by special electrospinning methods. The scope of applications, in fields as diverse as optoelectronics, sensor technology, catalysis, filtration, and medicine, is very broad.[115]

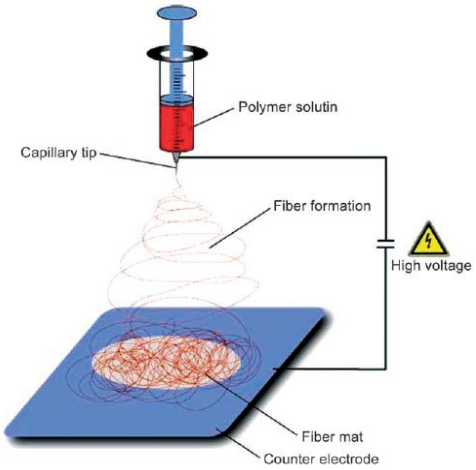

Scheme 1-11. Illustration of an electrospinning experiment.

A large number of reports describe the electrospinning of hybrid nanofibers based on polymeric and inorganic moieties. Due to the large number of suitable candidates in both fields, the combination of two ingredients results in a huge family of polymer-inorganic hybrid nanofibers. The incorporated inorganic components include montmorillonite, carbon nanotubes, metal, metal oxide or chalcogenide nanoparticles. Electrospinning hybrid fibers containing montmorillonite with polyamide 6,[138] polyamide 6,6, PVA,[139] PMMA,[140] and PU[141] as the carrier material have been described. Carbon nanotubes (CNTs) can be immobilized in electrospining polymer fibers for the functionalization of polymer nanofibers (electrical conductivity or mechanical strengthening) or the orientation of the CNTs along the fiber axis. Examples of polymers that were spun with CNTs into the corresponding hybrid fibers include PAN, PEO, PVA, PLA, PC, PS, PU, and PMMA.[142-147] Examples of electrospinning polymer-hybrid fibers containing noble metal nanoparticles include PPX/Pd (Fig. 1-11),[2] PAN-co-PAA/Pd (by reduction of Pb salts with hydrazine after electrospinning),[148] PEO/Au,[1] PVP/ Ag,[149] and PAN/Ag (by UV irradiation of $AgNO_3$).[150] The hybrid nanofibers loaded with monometallic or bimetallic nanoparticles are especially useful in the field of catalysis, for example, hydrogenation reactions. The immobilization of noble metal nanoparticles in nanofibers facilitates the removal and recycling of the catalysts after the reaction.

Combined with sol–gel processes, a large number of polymer-metal oxide (or metal chalcogenide) hybrid fibers have been produced by electrospinning, like PVP/TiO_2 or PVP/ZrO_2 hybrids.[151] Further examples of metal oxides and chalcogenides that have been incorporated into

polymer nanofibers are ZnO,[152] CdS,[153] PbS,[154] and NiO.[155]

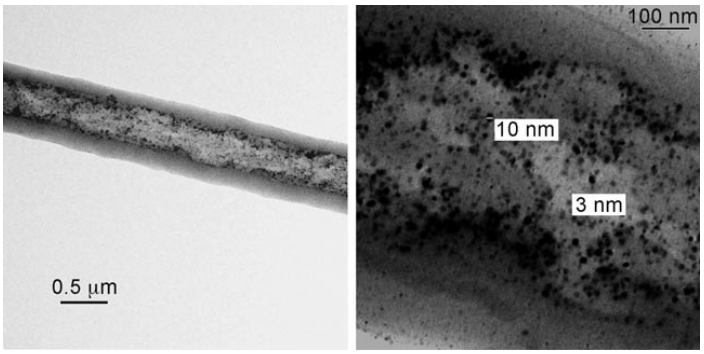

Figure 1-11. TEM image of a hollow PPX fiber with incorporated Pd nanoparticles (left) and an enlargement (right).

1.2.4 1-D hybrids prepared by other methods

Besides the methods mentioned above, there are also other alternatives. For example, a chain-like titanium glycolate complex obtained from the reflux of $Ti(OR)_4$ (with R ~ $–C_2H_5$, –iso-C_3H_7, or –n-C_4H_9) in ethylene glycol at 170°C, crystallized into uniform titanium glycolate hybrid nanowires. Moreover, gold nanorods were synthesized in the presence of CTAB surfactant. The two ends of the nanorods could be further tethered with thiol-terminated polystyrenes to form ABA-typed polymer-gold nanorod hybrid structures. The two polymeric phases at both ends of the inorganic nanorods act as a "glue" to connect the gold nanorods end-to-end into linear, ring-like, bundle or spherical hybrid superstructures. (Fig. 1-12)

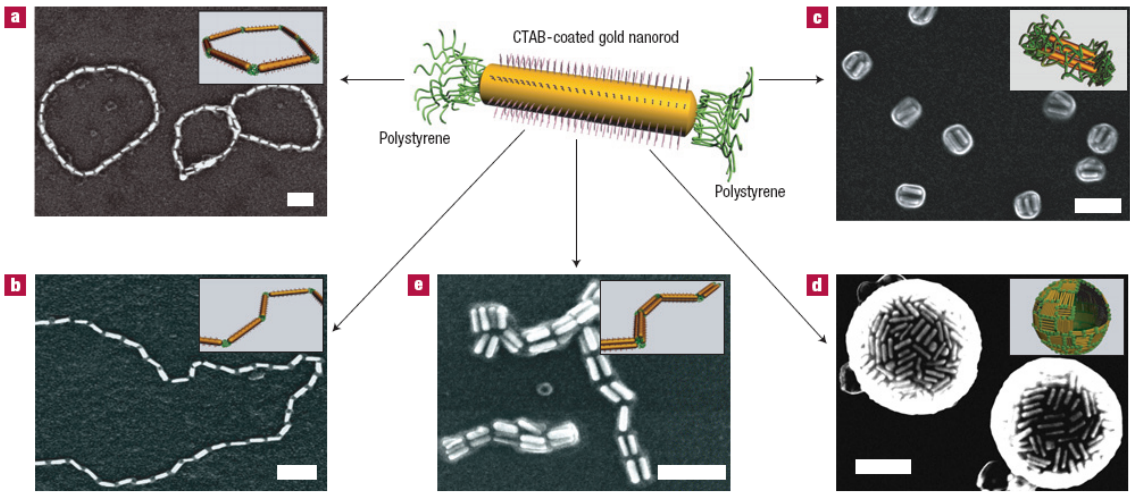

Figure 1-12. Self-assembly of polymer-tethered gold nanorods into (a) rings, (b) chains, (c) bundles, (d) nanospheres, and (e) bundled nanorod chains.

1.3 Objective of this thesis

The motivation of this work was to broaden the application range of cylindrical polymer brushes (CPBs) as templates to prepare new one-dimensional polymer-inorganic hybrid nanomaterials.

In the case of core-shell CPBs, the attempts were focused on three parts. a) A silicon-containing monomer should be used to build the brush core by ATRP, as ATRP is very tolerant to a variety of functional monomers. In this strategy, the introduction of inorganic silicon precursor and the construction of the CPB core could be achieved in one step. Meanwhile, the CPB shell could be constructed from a water-soluble block by ATRP in order to render the hybrid nanowires water-solubility. b) Although the multi-loading process of inorganic nanoparticles into core-shell CPBs with a poly(acrylic acid) core has been theoretically proven, there was yet no experimental investigation. In the scope of this thesis, a double-loading process of these brushes was performed to verify this strategy and compare the property and morphology of the hybrid nanowires before and after double-loading process. c) Besides quantum dots and magnetic nanoparticles, a widely used photocatalyst, TiO_2 nanoparticles, should be introduced and aligned in the CPB core to form hybrid titania nanowires.

In the case of homopolymer CPBs, their compact structures with high density of functional groups should be tested to assist the formation of one-dimensional inorganic nanostructures.

The as-prepared 1D hybrid materials should be characterized by various techniques (electron microscopies, spectroscopies, etc) to obtain information about the peculiar properties of the hybrids.

1.4 References

1. Kim, G. M.; Wutzler, A.; Radusch, H. J.; Michler, G. H.; Simon, P.; Sperling, R. A.; Parak, W. J. *Chem. Mater.* **2005,** 17, (20), 4949-4957.
2. Sun, Z.; Zeng, J.; Hou, H.; Wickel, H.; Wendorff, J. H.; Greiner, A., Preparation of poly(p-xylylene) TUFT-tubes containing Palladium, Silver, or Copper Nanoparticles. In *Scattering Methods and the Properties of Polymer Materials*, 2005; pp 15-19.
3. Zhang, M.; Müller, A. H. E. *J. Polym. Sci. Part A: Polym. Chem.* **2005,** 43, (16), 3461-3481.
4. Matyjaszewski, K.; Xia, J. *Chem. Rev.* **2001,** 101, (9), 2921-90.
5. Barner-Kowollik, C.; Davis, T. P.; Heuts, J. P. A.; Stenzel, M. H.; Vana, P.; Whittaker, M. *J. Polym. Sci. Part A: Polym. Chem.* **2003,** 41, (3), 365-375.
6. Yin, M.; Krause, T.; Messerschmidt, M.; Habicher, W. D.; Voit, B. *J. Polym. Sci. Part A: Polym. Chem.* **2005,** 43, (9), 1873-1882.
7. Zhang, M.; Drechsler, M.; Müller, A. H. E. *Chem. Mater.* **2004,** 16, (3), 537-543.
8. Zhang, M.; Estournes, C.; Bietsch, W.; Müller, A. H. E. *Adv. Funct. Mater.* **2004,** 14, (9), 871-882.
9. Djalali, R.; Hugenberg, N.; Fischer, K.; Schmidt, M. *Macromol. Rapid Comm.* **1999,** 20, (8), 444-449.
10. Tsukahara, Y.; Tsutsumi, K.; Yamashita, Y.; Shimada, S. *Macromolecules* **1990,** 23, (25), 5201-5208.
11. Tsukahara, Y.; Mizuno, K.; Segawa, A.; Yamashita, Y. *Macromolecules* **1989,** 22, (4), 1546-1552.
12. Deffieux, A.; Schappacher, M. *Macromolecules* **1999,** 32, (6), 1797-1802.
13. Lanson, D.; Schappacher, M.; Borsali, R.; Deffieux, A. *Macromolecules* **2007,** 40, (26), 9503-9509.
14. Lanson, D.; Schappacher, M.; Borsali, R.; Deffieux, A. *Polym. Prepr.* **2006,** 47, (1), 458-459.
15. Beers, K. L.; Gaynor, S. G.; Matyjaszewski, K.; Sheiko, S. S.; Moeller, M. *Macromolecules* **1998,** 31, (26), 9413-9415.
16. Zhang, M.; Breiner, T.; Mori, H.; Müller, A. H. E. *Polymer* **2003,** 44, (5), 1449-1458.
17. Xu, Y.; Becker, H.; Yuan, J.; Burkhardt, M.; Zhang, Y.; Walther, A.; Bolisetty, S.;

Ballauff, M.; Müller, A. H. E. *Macromol. Chem. Phys.* **2007,** 208, (15), 1666-1675.

18. Xu, Y.; Bolisetty, S.; Drechsler, M.; Fang, B.; Yuan, J.; Ballauff, M.; Müller, A. H. E. *Polymer* **2008,** 49, (18), 3957-3964.
19. Ruokolainen, J.; Torkkeli, M.; Serimaa, R.; Komanschek, E.; ten Brinke, G.; Ikkala, O. *Macromolecules* **1997,** 30, (7), 2002-2007.
20. Bazuin, C. G.; Tork, A. *Macromolecules* **1995,** 28, (26), 8877-8880.
21. Ruokolainen, J.; Tanner, J.; ten Brinke, G.; Ikkala, O.; Torkkeli, M.; Serimaa, R. *Macromolecules* **1995,** 28, (23), 7779-7784.
22. Liu, G.; Li, Z.; Yan, X. *Polymer* **2003,** 44, (25), 7721-7727.
23. Liu, Y. F.; Abetz, V.; Müller, A. H. E. *Macromolecules* **2003,** 36, (21), 7894-7898.
24. Liu, G. *Adv. Mater.* **1997,** 9, (5), 437-439.
25. Schmalz, H.; Schmelz, J.; Drechsler, M.; Yuan, J.; Walther, A.; Schweimer, K.; Mihut, A. M. *Macromolecules* **2008,** 41, (9), 3235-3242.
26. Ryu, S. W.; Hirao, A. *Macromolecules* **2000,** 33, (13), 4765-4771.
27. Pantazis, D.; Chalari, I.; Hadjichristidis, N. *Macromolecules* **2003,** 36, (11), 3783-3785.
28. Kanaoka, S.; Sueoka, M.; awamoto, M. S.; Higashimura, T. *J. Polym. Sci. Part A: Polym. Chem.* **1993,** 31, (10), 2513-2521.
29. Asami, R.; Takaki, M.; Moriyama, Y. *Polym. Bull.* **1986,** 16, (2), 125-130.
30. Nomura, K.; Takahashi, S.; Imanishi, Y. *Macromolecules* **2001,** 34, (14), 4712-4723.
31. Heroguez, V.; Gnanou, Y.; Fontanille, M. *Macromolecules* **1997,** 30, (17), 4791-4798.
32. Yamada, K.; Miyazaki, M.; Ohno, K.; Fukuda, T.; Minoda, M. *Macromolecules* **1999,** 32, (2), 290-293.
33. Neugebauer, D.; Sumerlin, B. S.; Matyjaszewski, K.; Goodhart, B.; Sheiko, S. S. *Polymer* **2004,** 45, (24), 8173-8179.
34. Neugebauer, D.; Zhang, Y.; Pakula, T.; Matyjaszewski, K. *Macromolecules* **2005,** 38, (21), 8687-8693.
35. Neugebauer, D.; Theis, M.; Pakula, T.; Wegner, G.; Matyjaszewski, K. *Macromolecules* **2006,** 39, (2), 584-593.
36. Neugebauer, D. *Polymer* **2007,** 48, (17), 4966-4973.
37. Schappacher, M.; Billaud, C.; Paulo, C.; Deffieux, A. *Macromol. Chem. Phys.* **1999,** 200, (10), 2377-2386.
38. Schappacher, M.; Deffieux, A. *Macromolecules* **2005,** 38, (11), 4942-4946.

39. Schappacher, M.; Deffieux, A. *Macromolecules* **2005,** 38, (17), 7209-7213.
40. Schappacher, M.; Deffieux, A. *Macromolecules* **2000,** 33, (20), 7371-7377.
41. Kolb, H. C.; Finn, M. G.; Sharpless, K. B. *Angew. Chem. Int. Ed.* **2001,** 40, (11), 2004-2021.
42. Gao, H.; Matyjaszewski, K. *J. Am. Chem. Soc.* **2007,** 129, (20), 6633-6639.
43. Boyce, J. R.; Lee, H.-i.; Matyjaszewski, K.; Sheiko, S. *Polym. Mater. Sci. Eng.* **2007,** 96, 864-865.
44. Qin, S.; Matyjaszewski, K.; Xu, H.; Sheiko, S. S. *Macromolecules* **2003,** 36, (3), 605-612.
45. Boerner, H. G.; Beers, K.; Matyjaszewski, K.; Sheiko, S. S.; Moeller, M. *Macromolecules* **2001,** 34, (13), 4375-4383.
46. Lee, H.; Jakubowski, W.; Matyjaszewski, K.; Yu, S.; Sheiko, S. S. *Macromolecules* **2006,** 39, (15), 4983-4989.
47. Cheng, G.; Boeker, A.; Zhang, M.; Krausch, G.; Müller, A. H. E. *Macromolecules* **2001,** 34, (20), 6883-6888.
48. Lee, H.-I.; Matyjaszewski, K.; Yu, S.; Sheiko, S. S. *Macromolecules* **2005,** 38, (20), 8264-8271.
49. Cheng, C.; Qi, K.; Khoshdel, E.; Wooley, K. L. *J. Am. Chem. Soc.* **2006,** 128, (21), 6808-6809.
50. Davis, K. A.; Matyjaszewski, K., Statistical, Gradient, Block, and Graft Copolymers by Controlled/Living Radical Polymerizations. In *Statistical, Gradient, Block and Graft Copolymers by Controlled/Living Radical Polymerizations*, 2002; pp 30-106.
51. Borner, H. G.; Duran, D.; Matyjaszewski, K.; da Silva, M.; Sheiko, S. S. *Macromolecules* **2002,** 35, (9), 3387-3394.
52. Koji Ishizu, H. K. *J. Polym. Sci. Part A: Polym. Chem* **2005,** 43, (1), 63-70.
53. Li, C.; Gunari, N.; Fischer, K.; Janshoff, A.; Schmidt, M. *Angew. Chem. Int. Ed.* **2004,** 43, (9), 1101-1104.
54. Muthukrishnan, S.; Zhang, M.; Burkhardt, M.; Drechsler, M.; Mori, H.; Müller, A. H. E. *Macromolecules* **2005,** 38, (19), 7926-7934.
55. Tang, C.; Dufour, B.; Kowalewski, T.; Matyjaszewski, K. *Macromolecules* **2007,** 40, (17), 6199-6205.
56. Sheiko, S. S.; da Silva, M.; Shirvaniants, D.; LaRue, I.; Prokhorova, S.; Moeller, M.; Beers, K.; Matyjaszewski, K. *J. Am. Chem. Soc.* **2003,** 125, (22), 6725-6728.

57. Sheiko, S. S.; Sumerlin, B. S.; Matyjaszewski, K. *Prog. Polym. Sci.* **2008,** 33, (7), 759-785.

58. Rathgeber, S.; Pakula, T.; Wilk, A.; Matyjaszewski, K.; Beers, K. L. *J. Chem. Phys.* **2005,** 122, (12), 124904-13.

59. Wataoka, I.; Urakawa, H.; Kajiwara, K.; Schmidt, M.; Wintermantel, M. *Polym. Int.* **1997,** 44, (3), 365-370.

60. Fischer, K.; Schmidt, M. *Macromol. Rapid Comm.* **2001,** 22, (10), 787-791.

61. Terao, K.; Nakamura, Y.; Norisuye, T. *Macromolecules* **1999,** 32, (3), 711-716.

62. Hokajo, T.; Terao, K.; Nakamura, Y.; Norisuye, T. *Polym. J.* **2001,** 33, (6), 481-485.

63. Wintermantel, M.; Gerle, M.; Fischer, K.; Schmidt, M.; Wataoka, I.; Urakawa, H.; Kajiwara, K.; Tsukahara, Y. *Macromolecules* **1996,** 29, (3), 978-983.

64. Gerle, M.; Fischer, K.; Roos, S.; Müller, A. H. E.; Schmidt, M.; Sheiko, S. S.; Prokhorova, S.; Moller, M. *Macromolecules* **1999,** 32, (8), 2629-2637.

65. Nemoto, N.; Nagai, M.; Koike, A.; Okada, S. *Macromolecules* **1995,** 28, (11), 3854-3859.

66. Murat, M.; Grest, G. S. *Macromolecules* **1991,** 24, (3), 704-708.

67. Gauger, A.; Pakula, T. *Macromolecules* **1995,** 28, (1), 190-196.

68. Rouault, Y.; Borisov, O. V. *Macromolecules* **1996,** 29, (7), 2605-2611.

69. Saariaho, M.; Ikkala, O.; Szleifer, I.; Erukhimovich, I.; ten Brinke, G. *J. Chem. Phys.* **1997,** 107, (8), 3267-3276.

70. Saariaho, M.; Szleifer, I.; Ikkala, O.; ten Brinke, G. *Macromol. Theory Simul.* **1998,** 7, (2), 211-216.

71. Saariaho, M.; Subbotin, A.; Szleifer, I.; Ikkala, O.; ten Brinke, G. *Macromolecules* **1999,** 32, (13), 4439-4443.

72. Saariaho, M.; Subbotin, A.; Ikkala, O.; ten Brinke, G. *Macromol. Rapid Comm.* **2000,** 21, (2), 110-115.

73. Shiokawa, K.; Itoh, K.; Nemoto, N. *J. Chem. Phys.* **1999,** 111, (17), 8165-8173.

74. Khalatur, P. G.; Shirvanyanz, D. G.; Starovoitova, N. Y.; Khokhlov, A. R. *Macromol. Theory Simul.* **2000,** 9, (3), 141-155.

75. Halperin, A.; Tirrell, M.; Lodge, T., Tethered chains in polymer microstructures. In *Macromolecules: Synthesis, Order and Advanced Properties*, 1992; pp 31-71.

76. Fredrickson, G. H. *Macromolecules* **1993,** 26, (11), 2825-2831.

77. Birshtein, T. M.; Borisov, O. V.; Zhulina, E. B.; Khokhlov, A. R.; Yurasova, T. A.

Vysokomolekulyarnye Soedineniya, Seriya A **1987,** 29, (6), 1169-74.

78. Subbotin, A.; Saariaho, M.; Ikkala, O.; ten Brinke, G. *Macromolecules* **2000,** 33, (9), 3447-3452.
79. Nakamura, Y.; Norisuye, T. *Polym. J.* **2001,** 33, (11), 874.
80. Zhang, B.; Groehn, F.; Pedersen, J. S.; Fischer, K.; Schmidt, M. *Macromolecules* **2006,** 39, (24), 8440-8450.
81. van der Schoot, P. *J. Chem. Phys.* **1996,** 104, (3), 1130-9.
82. Rathgeber, S.; Pakula, T.; Wilk, A.; Matyjaszewski, K.; Lee, H.-i.; Beers, K. L. *Polymer* **2006,** 47, (20), 7318-7327.
83. Yamamoto, S.-i.; Pietrasik, J.; Matyjaszewski, K. *Macromolecules* **2008,** 41, (19), 7013-7020.
84. Gunari, N.; Cong, Y.; Zhang, B.; Fischer, K.; Janshoff, A.; Schmidt, M. *Macromol. Rapid Comm.* **2008,** 29, (10), 821-825.
85. Yamamoto, S.-i.; Pietrasik, J.; Matyjaszewski, K. *Macromolecules* **2007,** 40, (26), 9348-9353.
86. Neiser, M. W.; Muth, S.; Kolb, U.; Harris, J. R.; Okuda, J.; Schmidt, M. *Angew. Chem. Int. Ed.* **2004,** 43, (24), 3192-3195.
87. Bo, G.; Wesslén, B.; Wessléen, K. B. *J. Polym. Sci. Part A: Polym. Chem.* **1992,** 30, (9), 1799-1808.
88. Pakula, T.; Zhang, Y.; Matyjaszewski, K.; Lee, H.-i.; Boerner, H.; Qin, S.; Berry, G. C. *Polymer* **2006,** 47, (20), 7198-7206.
89. Tsukahara, Y.; Namba, S.-i.; Iwasa, J.; Nakano, Y.; Kaeriyama, K.; Takahashi, M. *Macromolecules* **2001,** 34, (8), 2624-2629.
90. Neugebauer, D.; Zhang, Y.; Pakula, T.; Sheiko, S. S.; Matyjaszewski, K. *Macromolecules* **2003,** 36, (18), 6746-6755.
91. Zhang, B.; Zhang, S.; Okrasa, L.; Pakula, T.; Stephan, T.; Schmidt, M. *Polymer* **2004,** 45, (12), 4009-4015.
92. Gallyamov, M. O.; Tartsch, B.; Khokhlov, A. R.; Sheiko, S. S.; Boerner, H. G.; Matyjaszewski, K.; Moeller, M. *Chem. Eur. J.* **2004,** 10, (18), 4599-4605.
93. Sheiko, S. S.; Sun, F. C.; Randall, A.; Shirvanyants, D.; Rubinstein, M.; Lee, H.-i.; Matyjaszewski, K. *Nature* **2006,** 440, (7081), 191-194.
94. Xu, H.; Sun, F. C.; Shirvanyants, D. G.; Rubinstein, M.; Shabratov, D.; Beers, K. L.;

Matyjaszewski, K.; Sheiko, S. S. *Adv. Mater.* **2007,** 19, (19), 2930-2934.

95. Xu, H.; Sheiko, S. S.; Shirvanyants, D.; Rubinstein, M.; Beers, K. L.; Matyjaszewski, K. *Langmuir* **2006,** 22, (3), 1254-1259.
96. Ishizu, K.; Tsubaki, K.-i.; Ono, T. *Polymer* **1998,** 39, (13), 2935-2939.
97. Tsubaki, K.; Ishizu, K. *Polymer* **2001,** 42, (20), 8387-8393.
98. Polotsky, A.; Charlaganov, M.; Xu, Y.; Leermakers, F. A. M.; Daoud, M.; Müller, A. H. E.; Dotera, T.; Borisov, O. *Macromolecules* **2008,** 41, (11), 4020-4028.
99. Stephan, T.; Muth, S.; Schmidt, M. *Macromolecules* **2002,** 35, (27), 9857-9860.
100. Ishizu, K.; Satoh, J.; Sogabe, A. *J. Colloid Interface Sci.* **2004,** 274, (2), 472-479.
101. Lee, H.-i.; Matyjaszewski, K.; Yu-Su, S.; Sheiko, S. S. *Macromolecules* **2008,** 41, (16), 6073-6080.
102. Semlyen, J. A.; Walker, G. R. *Polymer* **1969,** 10, 597-601.
103. Schappacher, M.; Deffieux, A. *Science* **2008,** 319, (5869), 1512-1515.
104. Matyjaszewski, K.; Qin, S.; Boyce, J. R.; Shirvanyants, D.; Sheiko, S. S. *Macromolecules* **2003,** 36, (6), 1843-1849.
105. Djalali, R.; Li, S.-Y.; Schmidt, M. *Macromolecules* **2002,** 35, (11), 4282-4288.
106. Ishizu, K.; Tsubaki, K.; Uchida, S. *Macromolecules* **2002,** 35, (27), 10193-10197.
107. Chen, J.; Wiley, B. J.; Xia, Y. *Langmuir* **2007,** 23, (8), 4120-4129.
108. Teo, B. K.; Sun, X. H. *Chem. Rev.* **2007,** 107, (5), 1454-1532.
109. Lv, J.; Liu, H.; Li, Y. *Pure Appl. Chem.* **2008,** 80, (3), 639-658.
110. Cui, S.; Liu, H.; Gan, L.; Li, Y.; Zhu, D. *Adv. Mater.* **2008,** 20, (15), 2918-2925.
111. Zhao, Y. S.; Fu, H.; Peng, A.; Ma, Y.; Xiao, D.; Yao, J. *Adv. Mater.* **2008,** 20, (15), 2859-2876.
112. Ostrikov, K.; Levchenko, I.; Xu, S.; Huang, S. Y.; Cheng, Q. J.; Long, J. D.; Xu, M. *Thin Solid Films* **2008,** 516, (19), 6609-6615.
113. Yang, J.; Xiang, H., Low Dimensional Nanomaterials for Spintronics. In *One-Dimensional Nanostructures*, 2008; pp 247-271.
114. Xia, Y.; Yang, P.; Sun, Y.; Wu, Y.; Mayers, B.; Gates, B.; Yin, Y.; Kim, F.; Yan, H. *Adv. Mater.* **2003,** 15, (5), 353-389.
115. Greiner, A.; Wendorff, J. H. *Angew. Chem. Int. Ed.* **2007,** 46, (30), 5670-5703.
116. Jana, N. R.; Gearheart, L.; Murphy, C. J. *Adv. Mater.* **2001,** 13, (18), 1389-1393.
117. Murphy, C. J.; Jana, N. R. *Adv. Mater.* **2002,** 14, (1), 80-82.

118. Mandal, S.; Müller, A. H. E. *Mater. Chem. Phys.* **2008,** 111, (2-3), 438-443.
119. Sean Stewart, G. L. *Angew. Chem. Int. Ed.* **2000,** 39, (2), 340-344.
120. Yan, X.; Liu, G.; Liu, F.; Tang, B. Z.; Peng, H.; Pakhomov, A. B.; Wong, C. Y. *Angew. Chem. Int. Ed.* **2001,** 40, (19), 3593-3596.
121. Wang, H.; Wang, X.; Winnik, M. A.; Manners, I. *J. Am. Chem. Soc.* **2008,** 130, (39), 12921-12930.
122. Zollfrank, C.; Scheel, H.; Greil, P. *Adv. Mater.* **2007,** 19, (7), 984-987.
123. Bai, H.; Xu, K.; Xu, Y.; Matsui, H. *Angew. Chem. Int. Ed.* **2007,** 46, (18), 3319-3322.
124. Gottlieb, D.; Morin, S. A.; Jin, S.; Raines, R. T. *J. Mater. Chem.* **2008,** 18, (32), 3865-3870.
125. Richter, J.; Mertig, M.; Pompe, W.; Monch, I.; Schackert, H. K. *Appl. Phys. Lett.* **2001,** 78, (4), 536-538.
126. Kundu, S.; Liang, H. *Adv. Mater.* **2008,** 20, (4), 826-831.
127. Gu, Q.; Haynie, D. T. *Mater. Lett.* **2008,** 62, (17-18), 3047-3050.
128. Nguyen, K.; Monteverde, M.; Filoramo, A.; Goux-Capes, L.; Lyonnais, S.; Jegou, P.; Viel, P.; Goffman, M.; Bourgoin, J.-P. *Adv. Mater.* **2008,** 20, (6), 1099-1104.
129. Shenton, W.; Douglas, T.; Young, M.; Stubbs, G.; Mann, S. *Adv. Mater.* **1999,** 11, (3), 253-256.
130. Fonoberov, V. A.; Balandin, A. A. *Nano Lett.* **2005,** 5, (10), 1920-1923.
131. Liu, W. L.; Alim, K.; Balandin, A. A.; Mathews, D. M.; Dodds, J. A. *Appl. Phys. Lett.* **2005,** 86, (25), 253108-3.
132. Knez, M.; Sumser, M.; Bittner, A. M.; Wege, C.; Jeske, H.; Martin, T. P.; Kern, K. *Adv. Funct. Mater.* **2004,** 14, (2), 116-124.
133. Knez, M.; Kadri, A.; Wege, C.; Gosele, U.; Jeske, H.; Nielsch, K. *Nano Lett.* **2006,** 6, (6), 1172-1177.
134. Hulteen, J. C.; Martin, C. R. *J. Mater. Chem.* **1997,** 7, (7), 1075-1087.
135. Martin, C. R. *Acc. Chem. Res.* **1995,** 28, (2), 61-8.
136. Martin, C. R. *Science* **1994,** 266, (5193), 1961-1966.
137. Jagminas, A.; Valsiunas, I.; Veronese, G. P.; Juskenas, R.; Rutavicius, A. *J. Cryst. Growth* **2008,** 310, (2), 428-433.
138. Fong, H.; Liu, W.; Wang, C.-S.; Vaia, R. A. *Polymer* **2002,** 43, (3), 775-780.
139. Ristolainen, N.; Heikkilä, P.; Harlin, A.; Seppälä, J. *Macromol. Mater. Eng.* **2006,** 291,

(2), 114-122.

140. Kim, G.-M.; Lach, R.; Michler, G. H.; Chang, Y.-W. *Macromol. Rapid Comm.* **2005,** 26, (9), 728-733.

141. Hong, J. H.; Jeong, E. H.; Lee, H. S.; Baik, D. H.; Won, S.; Youk, S. J. H. *J. Polym. Sci. Part B: Polym. Phys.* **2005,** 43, (22), 3171-3177.

142. Ko, F.; Gogotsi, Y.; Ali, A.; Naguib, N.; Ye, H.; Yang, G. L.; Willis, C. L. P. *Adv. Mater.* **2003,** 15, (14), 1161-1165.

143. Liu, J.; Wang, T.; Uchida, T.; Kumar, S. *J. Appl. Polym. Sci.* **2005,** 96, (5), 1992-1995.

144. Dror, Y.; Salalha, W.; Khalfin, R. L.; Cohen, Y.; Yarin, A. L.; Zussman, E. *Langmuir* **2003,** 19, (17), 7012-7020.

145. Zhou, W.; Wu, Y.; Wei, F.; Luo, G.; Qian, W. *Polymer* **2005,** 46, (26), 12689-12695.

146. Kim, G. M.; Michler, G. H.; Pötschke, P. *Polymer* **2005,** 46, (18), 7346-7351.

147. Sen, R.; Zhao, B.; Perea, D.; Itkis, M. E.; Hu, H.; Love, J.; Bekyarova, E.; Haddon, R. C. *Nano Lett.* **2004,** 4, (3), 459-464.

148. Demir, M. M.; Gulgun, M. A.; Menceloglu, Y. Z.; Erman, B.; Abramchuk, S. S.; Makhaeva, E. E.; Khokhlov, A. R.; Matveeva, V. G.; Sulman, M. G. *Macromolecules* **2004,** 37, (5), 1787-1792.

149. Jin, W.-J.; Lee, H. K.; Jeong, E. H.; Park, W. H.; Youk, J. H. *Macromol. Rapid Comm.* **2005,** 26, (24), 1903-1907.

150. Li, Z.; Huang, H.; Shang, T.; Yang, F.; Zheng, W.; Wang, C.; Manohar, S. K. *Nanotechnology* **2006,** 17, (3), 917-920.

151. Li, D.; Xia, Y. *Nano Lett.* **2003,** 3, (4), 555-560.

152. Viswanathamurthi, P.; Bhattarai, N.; Kim, H. Y.; Lee, D. R. *Nanotechnology* **2004,** 15, (3), 320-323.

153. Lu, X.; Zhao, Y.; Wang, C.; Wei, Y. *Macromol. Rapid Comm.* **2005,** 26, (16), 1325-1329.

154. Lu, X.; Zhao, Y.; Wang, C. *Adv. Mater.* **2005,** 17, (20), 2485-2488.

155. Guan, H.; Shao, C.; Wen, S.; Chen, B.; Gong, J.; Yang, X. *Inorg. Chem. Commun.* **2003,** 6, (10), 1302-1303.

Chapter 2 Overview of the thesis

This thesis consists of nine chapters including five publications which are presented in Chapters 3 to 7.

Core-shell cylindrical polymer brushes (CPBs) with a poly(3-acryloylpropyl trimethoxysilane) core and a shell made up from oligo(ethylene glycol) methacrylate units were prepared via the combination of anionic polymerization and atom transfer radical polymerization. They were hydrolyzed into water-soluble organo-silica hybrid nanowires. These nanowires show lyotropic liquid-crystalline behavior and can be pyrolyzed to silica nanowires (Chapter 3).

Amphiphilic core-shell CPBs with a poly(acrylic acid) core and a poly(*n*-butyl acrylate) shell were used as cylindrical templates and nanoreactors to fabricate semiconductor CdSe nanowires. Since the chemical structure of the poly(acrylic acid) core was resumed after the formation of CdSe nanowires, a double-loading process with CdSe nanoparticles was conducted to study the morphological and optical change of the CdSe hybrid nanowires (Chapter 4).

Bishydrophilic core-shell CPBs with a poly(2-hydroxyethyl methacrylate) core and a poly(oligo(ethylene glycol) methacrylate) shell were prepared for the fabrication of titania hybrid nanowires, which contain a wormlike assembly of titania nanoparticles in the CPB core. They were successfully converted into anatase titania nanowires by pyrolysis at 550 °C (Chapter 5).

Poly(*tert*-butyl methacrylate) homopolymer CPBs were used to support the formation of uniform single-crystalline tellurium nanorods at room temperature in THF. These rods with polymer attached on their surface are well-dispersed and long-term stable in THF. They were able to assemble tellurium or Fe_3O_4 nanoparticles on their surface via hydrophobic interactions (Chapter 6).

Fe_3O_4-decorated Te nanorods prepared in the presence of linear poly(*tert*-methyl methacrylate) with high molecular weight are superparamagnetic. They were aligned when deposited from solution on a solid substrate in the presence of an external magnetic field, and were further demagnetized into tellurium nanorods. The population of magnetite nanoparticles per nanorod could be varied by the stoichiometric ratio of the two components (Chapter 7).

In the following, an overview of the main results is presented.

2.1 Water-soluble organo-silica hybrid nanowires

A common existing problem of using CPBs as template is the continuity and the structural control of the formed 1D inorganic nanostructures in the CPB core.[1] By constructing the CPBs themselves with a precursor-containing monomer, hybrid nanowires with a silsesquioxane core and a poly(oligo(ethylene glycol) methacrylate) (POEGMA) shell, have been successfully prepared.

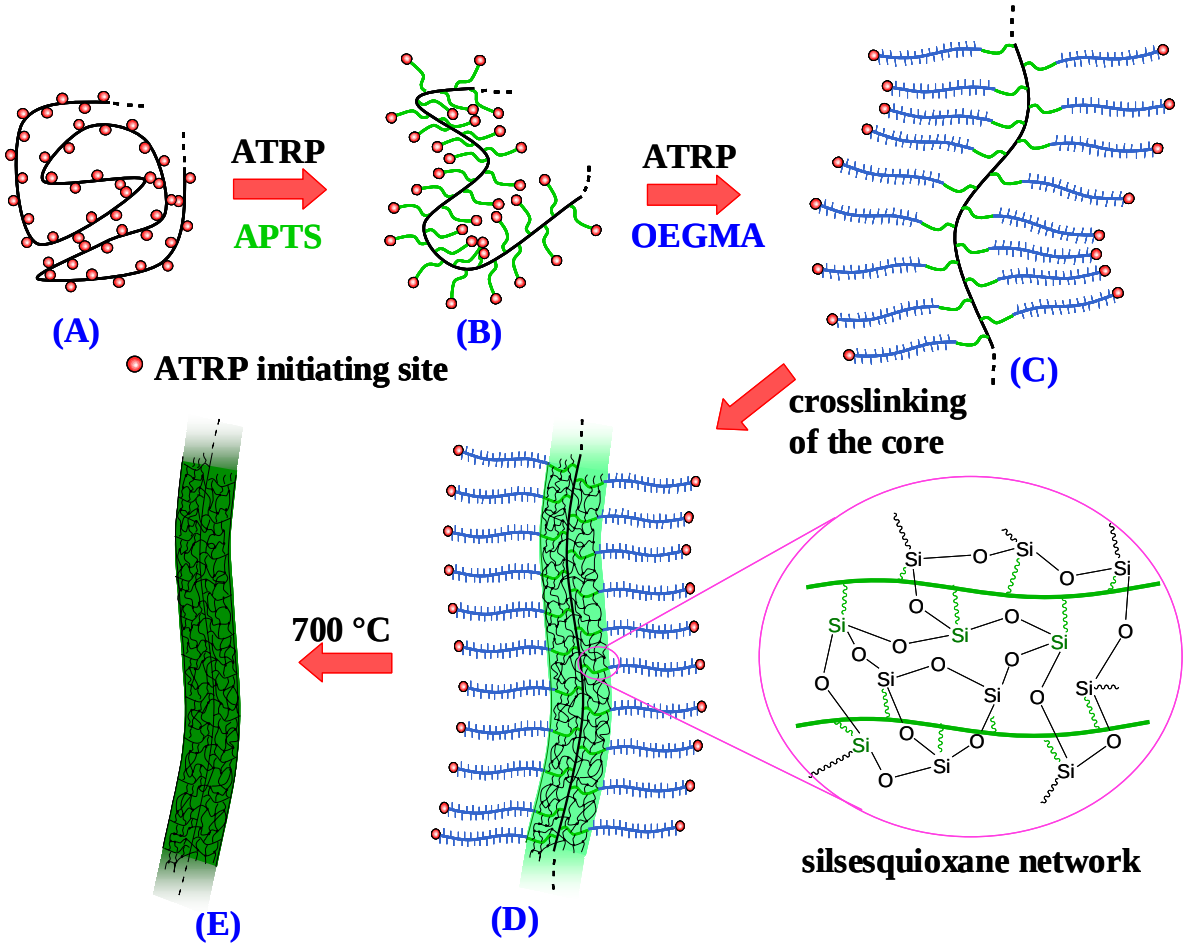

Scheme 2-1. Synthesis of soluble organo-silica and inorganic silica nanowires. A), ATRP polyinitiator PBIEM; B), CPB with side chains of 20 APTS units; C), core-shell CPB with additional 57 OEGMA units; D), soluble organo-silica hybrid nanowires with crosslinked silsesquioxane network in the core; E), inorganic silica nanowires after pyrolysis.

The synthetic strategy is illustrated in Scheme 2-1. Firstly, the poly(2-bromoisobutyryloxyethyl methacrylate) (PBIEM) backbone with DP = 3200 was obtained by anionic polymerization of 2-(trimethylsilyloxy)ethyl methacrylate (TMS-HEMA) followed by attaching ATRP initiating group along the backbone. This was used as a polyinitiator to grow block copolymer chains with 20 units of 3-acryloylpropyl trimethoxysilane (APTS) and 57 units of oligo(ethylene glycol) methacrylate (OEGMA), leading to a core-shell CPB, $[APTS_{20}$-*b*-$OEGMA_{57}]_{3200}$. Hydrolysis of the trimethoxysilyl moieties and subsequent condensation resulted in a cylindrical crosslinked silsesquioxane core, solubilized by POEGMA shell. These rigid and continuous hybrid nanowires are structurally tunable and can construct lyotropic phase. Pyrolysis at 700 °C can be used to convert the hybrid nanowires into inorganic silica nanowires.

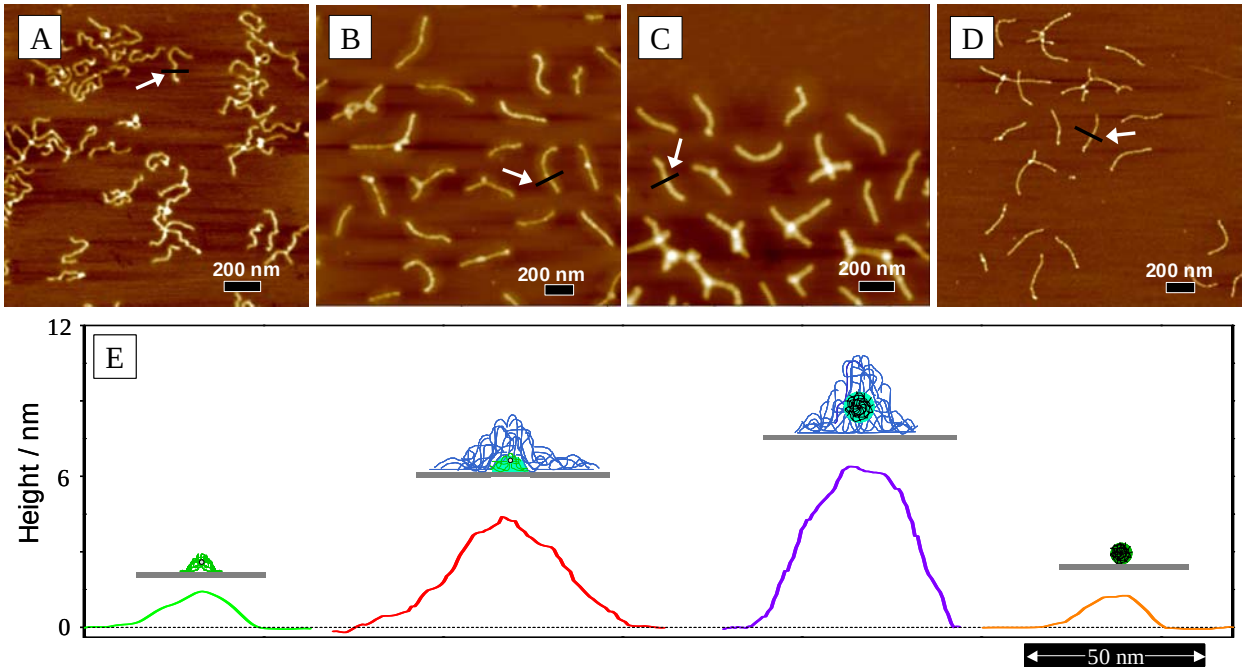

Figure 2-1. AFM height images on mica: A), $[APTS_{20}]_{3200}$ CPBs (z range, 4 nm); B), $[APTS_{20}$-*b*-$OEGMA_{57}]_{3200}$ core-shell CPBs (z range, 15 nm); C), soluble organo-silica hybrid nanowires $[(SiO_{1.5})_{20}$-*b*-$OEGMA_{57}]_{3200}$ (z range, 20 nm); D), inorganic silica nanowires (z range, 4 nm); E), cross-sectional analysis of objects marked with an arrow in each AFM image.

The successful synthetic strategy was verified by the molecular visualization with atomic force microscopy (AFM) of the products at each stage. In all cases, AFM revealed individual wormlike / wirelike structures lying flat on the substrate. The core-shell CPB $[APTS_{20}$-*b*-

$OEGMA_{57}]_{3200}$ (Fig. 2-1B) are much more stretched than the CPB $[APTS_{20}]_{3200}$ (Fig. 2-1A), since the repulsion among the side chains is enhanced due to the newly grown bulky POEGMA blocks. After the condensation of the APTS units, a continuous silsesquioxane network in the core was generated, forming soluble organo-silica hybrid nanowires $[(SiO_{1.5})_{20}$-*b*-$OEGMA_{57}]_{3200}$. Following the synthetic route, cross-section analysis of individual objects (indicated by white arrows) verifies an increase of the CPB height from A to C in Fig. 2-1E. This tendency results from the sequential growth of each block and the successful condensation. The hybrid nanowires were converted to inorganic silica nanowires by a pyrolysis process at 700 °C. They are uniform in dimension but "thinner" in the AFM characterization (Fig. 2-1D), since the POEGMA shell is lost during the pyrolysis. The silica content in the hybrid nanowires was determined to be 3.53% (theoretical amount: 3.95%) by thermogravimetric analysis (TGA), and the residue was proven to be pure silica by energy dispersive X-ray (EDX) analysis and Fourier transform infrared spectrum (FTIR).

The absolute dimensions of the organo-silica hybrid nanowires in the dry state and in solution were determined by scanning electron microscopy (SEM), transmission electron microscopy (TEM) and cryogenic TEM (cryo-TEM), respectively. The non-stained TEM image (Fig. 2-2A) indicates that the hybrid nanowires are 276 ± 29 nm in length and 9 nm in width, giving an aspect ratio of 30. The SEM image (Fig. 2-2B) shows the collapsed POEGMA shell. Here, L_n = 280 ± 30 nm and d = 21 ± 3 nm are observed, leading to an aspect ratio of 13. Thus, the thickness of POEGMA shell is 6~7 nm. The structure of the hybrid nanowires in water was identified by cryo-TEM measurements (Fig. 2-2C). The dark line represents the nanowire core, and the gray corona stands for the POEGMA shell. The size of the nanowire core (L_n = 285 ± 40 nm, d = 9.5 ± 1 nm) remains the same as that in Fig. 2-1A, while the diameter, including the solvent-swollen corona, has dramatically expanded to 45 ± 5 nm, leading to a thickness of the swollen corona of ~18 nm.

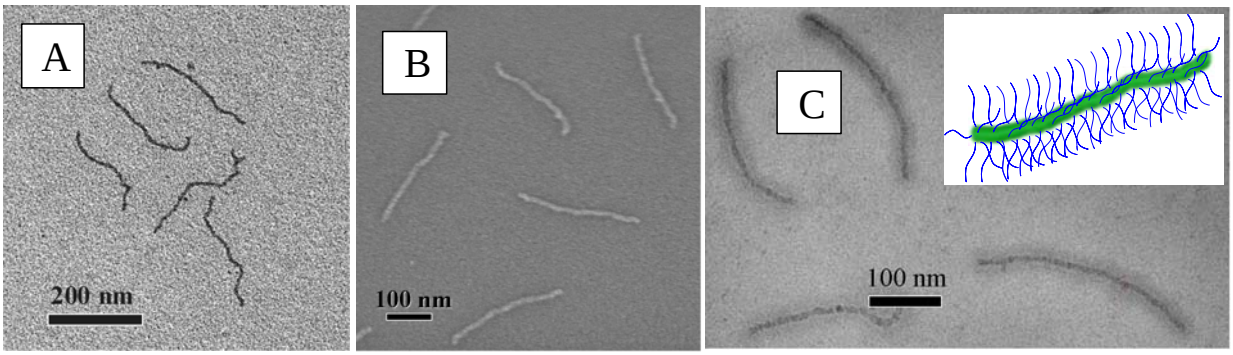

Figure 2-2. Electron microscopy characterization of soluble organo-silica hybrid nanowires. A), non-stained TEM image of $[(SiO_{1.5})_{20}$-*b*-$OEGMA_{57}]_{3200}$; B), its SEM image; C), its non-stained cryo-TEM image in water.

2.2 Cadmium selenide nanowires within core-shell CPBs: synthesis, characterization and the double-loading process

Wirelike CdS nanoparticle assemblies have previously been templated within core-shell CPBs with a poly(acrylic acid) (PAA) core and a poly(*n*-butyl acrylate) (P*n*BA) shell.[1] Formation of CdS nanoparticles inside the CPB was followed by the resume of the chemical structure of the PAA core. Theoretically, the CPB can be reused as template to reload more nanoparticles.

To demonstrate this strategy experimentally, we used the core-shell CPB $[AA_{25}$-*b*-*n*$BA_{61}]_{1500}$ as template for the fabrication of CdSe semiconductor nanowires via a double-loading process. The general approach includes three steps as shown in Scheme 2-2. In the first step (a to b), the carboxylic groups in the PAA core were neutralized by NaOH. Via ion exchange, Cd^{2+} ions replace Na^{+} ions (step 2: b to c), forming a CPB-Cd^{2+} polychelate. The purified polychelate solution reacted with H_2Se gas to generate CdSe nanoparticles aligned within the cylindrical core (step 3: c to d). Simultaneously, the PAA core resumes the initial chemical structure (i.e., carboxylic acid functions) which enables the double-loading process by repeating steps 1 to 3.

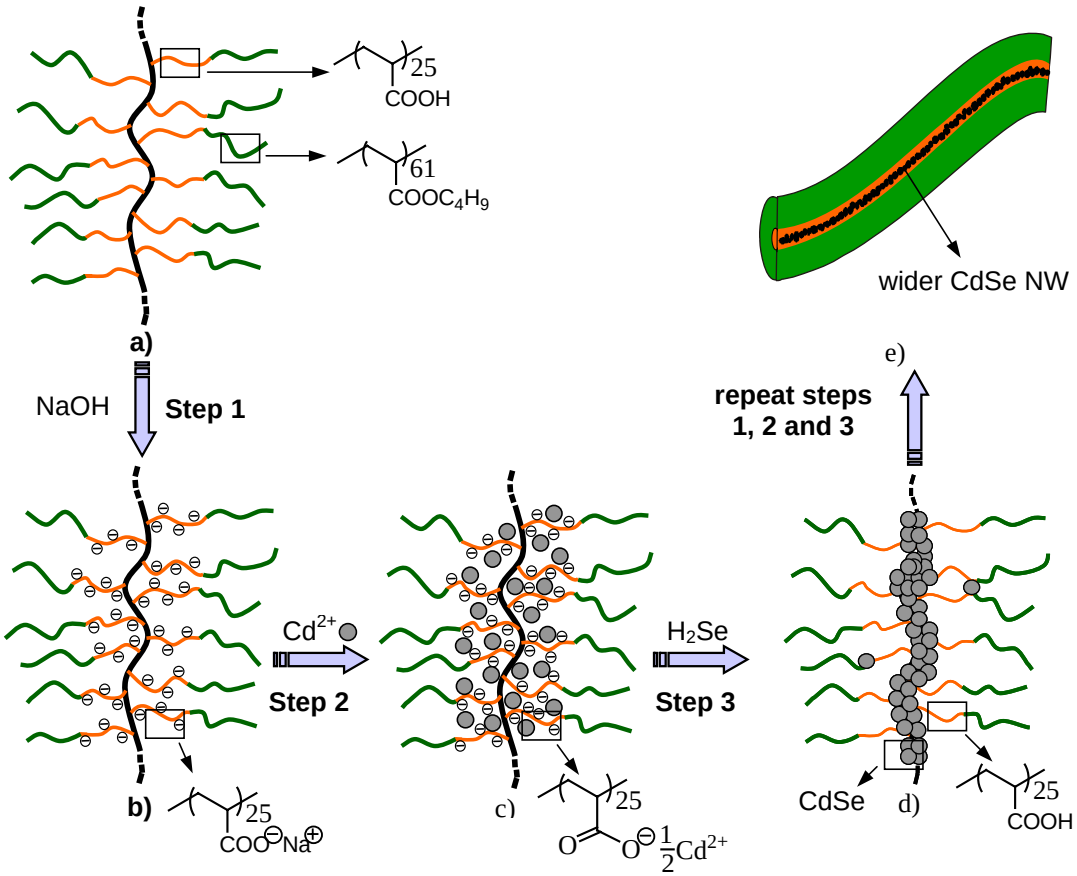

Scheme 2-2. Illustration of the CdSe nanowire synthesized inside the CPB via a double-loading process. a), the core-shell CPB $[AA_{25}\text{-}b\text{-}nBA_{61}]_{1500}$; b), neutralized CPB with poly(sodium acrylate) core; c), polychelate of the CPB and Cd^{2+}; d), 1st loaded hybrid of the CPB and CdSe nanowires; e), the 2nd loaded (double-loaded) hybrid of the CPB and CdSe nanowires.

The CPB $[AA_{25}\text{-}b\text{-}nBA_{61}]_{1500}$ is a unimolecular template with a low length polydispersity (L_w/L_n = 1.08), as revealed by the AFM characterization (Fig. 2-3A). They define both the dimension and solubility of the CdSe nanowires within the CPB core. The generation of CdSe nanoparticles into the CPB core was conducted by the sequential introduction of Cd^{2+} ions (excess Cd^{2+} ions were removed) and H_2Se gas. The CdSe-CPB hybrid nanowires show the similar wormlike morphology (Fig. 2-3B) as the pure CPB in the AFM image. However, there is significant increase of the average height from 0.71 nm (pure CPB) to 2.00 nm of the 1st loaded CdSe-CPB hybrid nanowires. Since the -COOH coordination sites after the formation of CdSe nanowires were resumed, the reloading of CdSe nanoparticles was carried out in the same manner. The height of the double-loaded CdSe-CPB hybrid nanowires (Fig. 2-3C) increases

further to 2.66 nm, insinuating a further size expansion of the nanoparticles during the double-loading process.

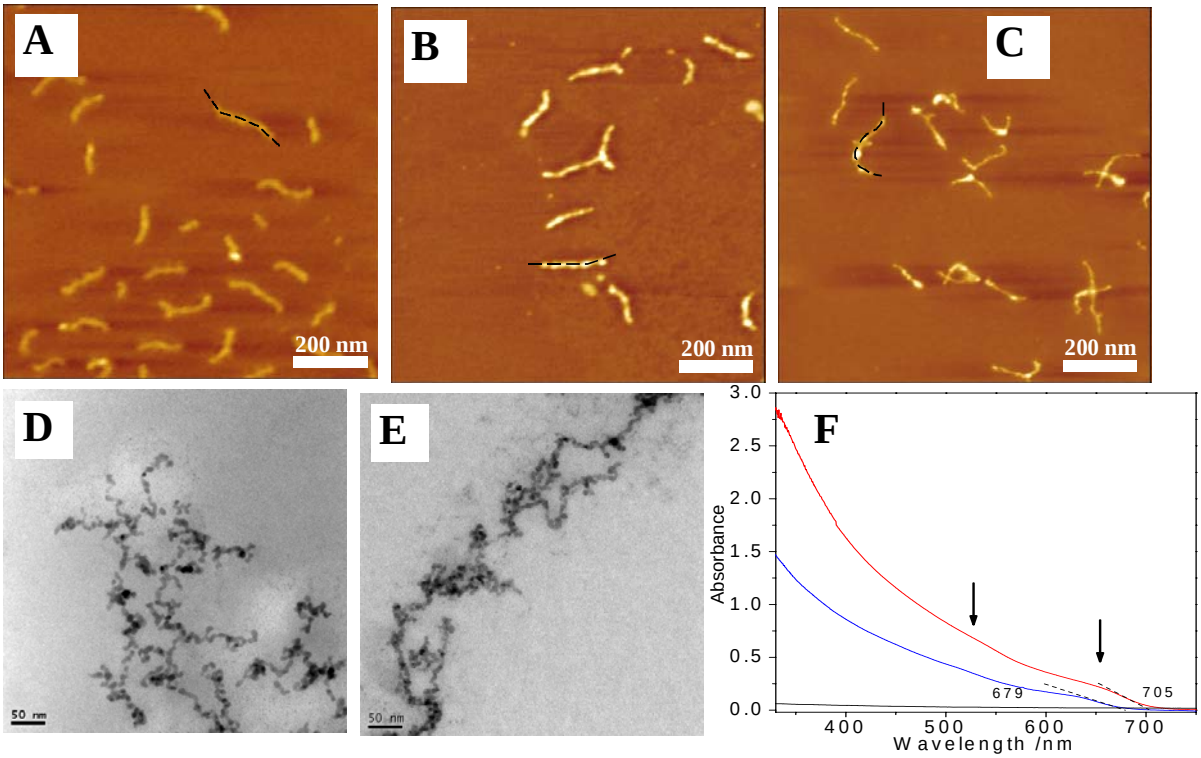

Figure 2-3. A-C) AFM height images of A) core-shell CPB $[AA_{25}$-*b*-*n*$BA_{61}]_{1500}$ (Z range : 3nm), B) the 1st loaded CdSe-CPB hybrid nanowires (Z range : 6 nm), and C) the double-loaded CdSe-CPB hybrid nanowires (Z range : 12 nm). D-E), the corresponding TEM images of 1st and double-loaded hybrids. F), UV–vis spectra of the polychelate (black line), 1st (blue line) and double-loaded (red line) hybrid nanowires, the concentration for all is 0.4 g/L (polymer content).

TEM characterization gives a deep view of the CdSe nanoparticles in the CPB core. The characteristic wormlike shapes of the 1st and double-loaded hybrid nanowires (Fig. 2-3D and 2-3E) clearly prove the success of this template-directed synthetic strategy. Statistical measurements of the nanowire width at different locations away from the distorted joins indicate that their diameters are 7.6 nm for the 1st loaded and 9.3 nm for the double-loaded hybrid nanowires. Selected area electron diffraction (SAED) of both hybrid nanowires proves the polycrystalline nature of CdSe nanowires, due to the random orientated crystalline CdSe nanoparticles in the nanowires.

Beside AFM and TEM characterizations, UV-vis spectra were also applied to verify the double-loading process. Since the polychelate solution gives almost no UV-vis absorption, the strong absorption bands (blue and red lines in Fig. 2-3F) come exclusively from the introduced CdSe nanowires. The double-loaded hybrid nanowires show stronger absorption than the 1st loaded hybrid, meaning more CdSe nanoparticles within the CPBs after the double-loading process. Furthermore, the threshold increases from 679 nm (1st loading) to 705 nm (double-loading), indicating the size expansion of nanoparticles from 7 nm (1st loading) to 10 nm (double-loading) according to Murray's empirical curve.[2] These values are close to the average width values of 7.6 nm (1st loading) and 9.3 nm (double-loading) of the CdSe nanowires obtained via TEM investigation.

2.3 Template-directed synthesis of titania hybrid nanowires within core-shell cylindrical polymer brushes

Titanium dioxide (titania) nanomaterials have tremendous practical applications in many different fields such as photocatalysis, gas sensors, dye-sensitized solar cells, optics, etc.[3-5] They are usually synthesized in templates assembled from small surfactants or amphiphilic block copolymers.[6, 7] However, the conventional micellar structures from the self-assembly of surfactants or block copolymers are dynamically unstable and sensitive to external environments such as solvent, temperature, concentration, or pH.[8] CPBs, as robust template, are tolerant to various conditions because of the covalent bond between the side chain and the backbone. We used bishydrophilic core-shell CPBs $[HEMA_{85}$-*b*-$OEGMA_{200}]_{3,200}$ with a poly(2-hydroxyethyl methacrylate) (PHEMA) core and a POEGMA shell to template linear assemblies of titania nanoparticles, forming a kind of titania-CPB hybrid nanowires. They were converted to inorganic crystalline titania nanowires via pyrolysis. As an example illustrated in Scheme 2-3, firstly, PTMS-HEMA-*b*-POEGMA diblock copolymer side chains were grafted from the PBIEM backbone polyinitiator via sequential ATRPs. After hydrolyzing the PTMS-HEMA block into PHEMA, the titania precursor, $Ti(OC_4H_9)_4$, were locally confined in the CPB core through a transalcoholysis reaction. Via hydrolysis, wormlike assemblies of titania nanoparticles were formed within the core-shell CPB, leading to soluble titania-CPB hybrid nanowires. At the end, uniform crystalline titania nanowires were obtained via pyrolysis at 550 °C.

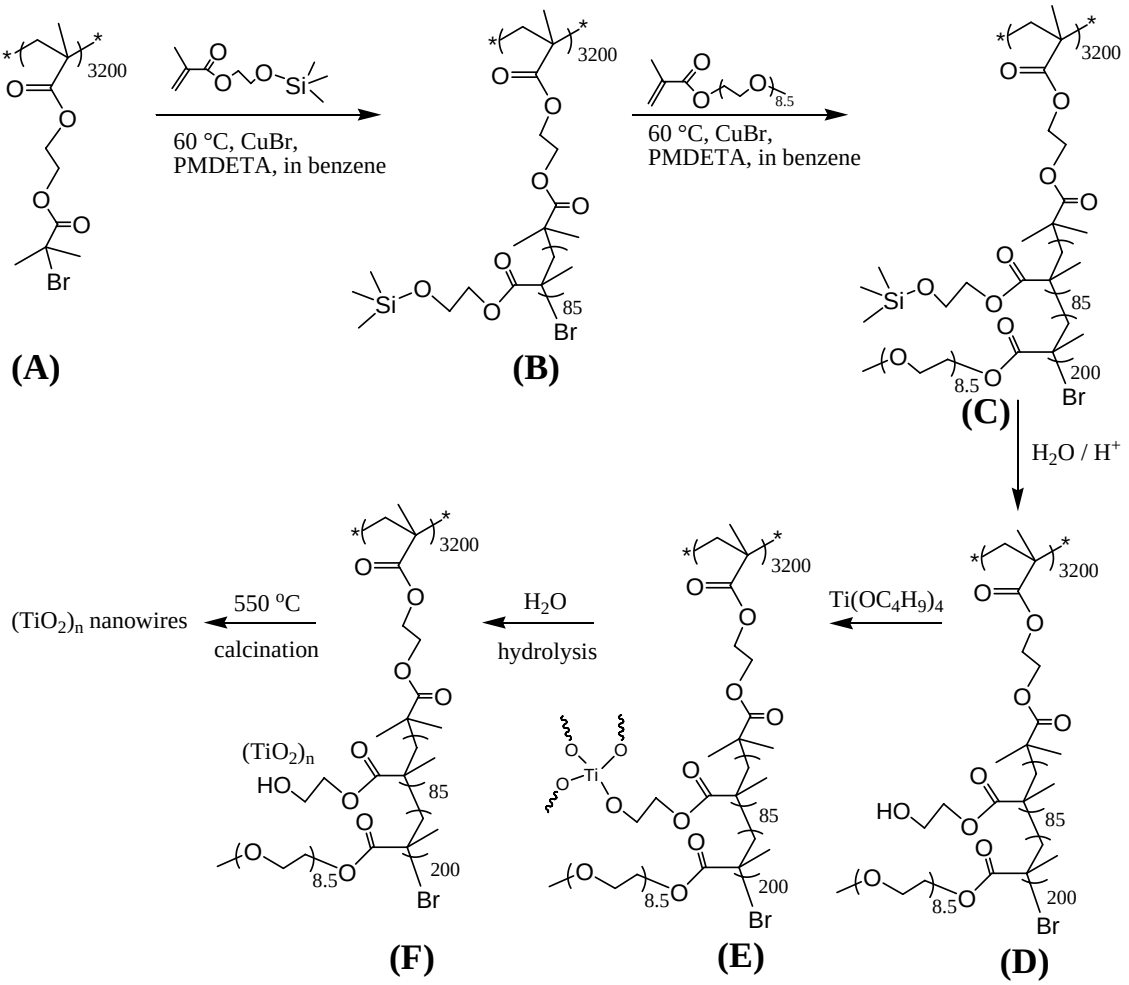

Scheme 2-3. Synthetic route for titania-CPB hybrid nanowires and inorganic titania nanowires. A), ATRP polyinitiator PBIEM; B), $[TMS\text{-}HEMA_{85}]_{3,200}$ CPB; C), $[TMS\text{-}HEMA_{85}\text{-}b\text{-}OEGMA_{200}]_{3,200}$ core–shell CPB; D), $[HEMA_{85}\text{-}b\text{-}OEGMA_{200}]_{3,200}$ core–shell CPB; E) Ti^{4+}-doped CPB hybrids $[(HEMA_{85}+n Ti^{4+})\text{-}b\text{-}OEGMA_{200}]_{3,200}$; F), titania-CPB hybrid nanowires $[(HEMA_{85}+n TiO_2)\text{-}b\text{-}OEGMA_{200}]_{3,200}$.

The successful preparation of the polymeric template was confirmed by the proton nuclear magnetic resonance (^{1}H-NMR) spectra and AFM characterization. The titania precursor, $Ti(OC_4H_9)_4$, attached to the PHEMA chains in the CPB core via a transalcoholysis reaction. The titania-CPB hybrid nanowires were generated when the Ti^{4+}-doped CPB hybrids reacted with water. The AFM image (Fig. 2-4A) of the titania-CPB hybrid nanowires shows the characteristic

wormlike shape of CPBs, demonstrating the high stability of the CPBs. Their height is 11.5 nm, according to the cross-section analysis, much higher than the pure core-shell CPB (~ 5 nm).

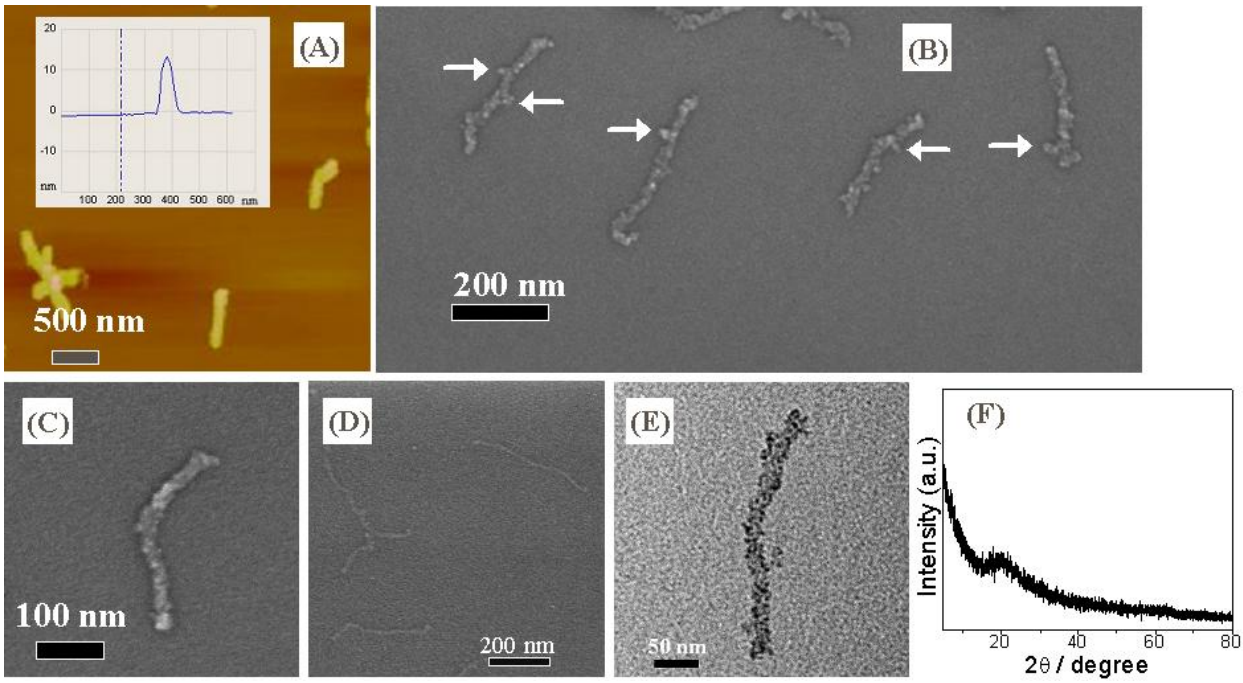

Figure 2-4. A), AFM height image of titania-CPB hybrid nanowires, the inset shows the cross-section analysis of a single hybrid nanowire; B-C), SEM images of titania-CPB hybrid nanowires; D), SEM image of pure CPBs as a comparison; E), TEM image of a single titania-CPB hybrid nanowire; F), XRD pattern of the obtained titania-CPB hybrid nanowires.

The absolute dimensions were obtained from the SEM characterization. The hybrid nanowires do not agglomerate into big objects and well-dispersed on mica (Fig. 2-4B). The high self-dispersibility of hybrid nanowires is rendered in fact by the large POEGMA shell, which screens the fusion and aggregation of the titania nanoparticles among different CPBs. The hybrid nanowires are 290 ± 36 nm in length and 29 ± 8 nm in diameter, giving an aspect ratio of 10. In the enlarged view of a single hybrid nanowire (Fig. 2-4C), the titania nanoparticles appear as bright dots distributed along the grey hybrid nanowire. They represent larger titania nanoparticles which can hardly be encapsulated within the CPB in the solid state (shrinking of the CPB during the drying process). In the TEM characterization (Fig. 2-4E), the black dots, namely titania nanoparticles with a diameter of 2-7 nm are confined into a linear manner. This is the solid proof

that the strategy of using CPB as cylindrical template to fabricate titania nanoparticles is successful. Here, the diameter of the hybrid nanowires is ~19 nm. The XRD pattern (Fig. 2-4F) indicates an amorphous phase of the titania in the hybrids nanowires. The crystallinity was improved by refluxing the hybrid nanowire solution in the mixture of water and dioxane for 5 days.

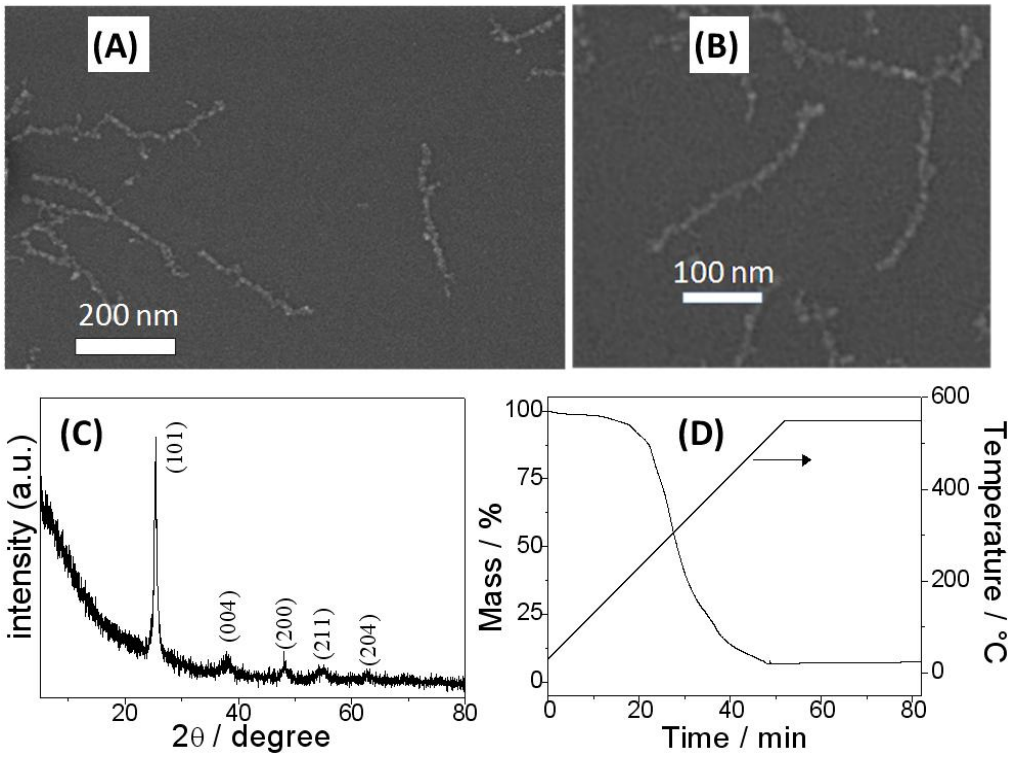

Figure 2-5. A-B), SEM image of titania nanowires after the calcination at 550 °C; C), XRD pattern of the titania nanowires; D), TGA curve of the titania-CPB hybrid nanowires.

The titania-CPB hybrid nanowires were converted into inorganic crystalline titania nanowires via pyrolysis at 550 °C. Compared to the hybrid nanowires, the titania nanowires appear thinner in the SEM image (Fig. 2-5A). The width shrinks from 29 nm of the hybrid nanowires to only 14 nm due to the decomposition of the CPB during the pyrolysis. A close view of these nanowires (Fig. 2-5B) further indicates that individual nanowires actually consist of the linearly aligned titania nanoparticles. The rough contour and the inhomogeneous brightness along the nanowires result from the nonuniformity of the nanoparticles´ size and the different contrast between the nanoparticle center and the boundary. The titania nanowires are crystalline according to XRD

measurement. The corresponding diffraction peaks (Fig. 2-5C) match well with that of anatase phase, confirming the phase transformation during the calcination. The complete removal of polymeric template is confirmed by EDX analysis; only oxygen and titanium signals were detected. The titania content in the hybrid nanowires was determined to be 8.05% by TGA (Fig. 2-5D). It is 34% higher than the theoretical amount (6.02%) when each HEMA unit in the core is considered to bind one titanium atom. The difference here is due to additional adsorption of Ti^{4+} ions in the POEGMA shell.

2.4 Room-temperature growth of uniform tellurium nanorods and the assembly of tellurium or Fe_3O_4 nanoparticles on the nanorods

The CPB is a hyperbranched compact polymeric superstructure, which confines a rather high local concentration of functional groups in a single macromolecule. Thus it can be powerful to control the preferential growth of a crystal and shape it into an elongated structure. Poly(*tert*-butyl methacrylate) homopolymer CPBs $[t\text{BMA}_{90}]_{3200}$ have been employed for the preparation of uniform and single-crystalline tellurium (Te) nanorods at room temperature. The reaction was performed simply by purging H_2Te gas into the CPB solution in organic solvents. The aspect ratio (AR) of the Te nanorods depends on the reaction medium.

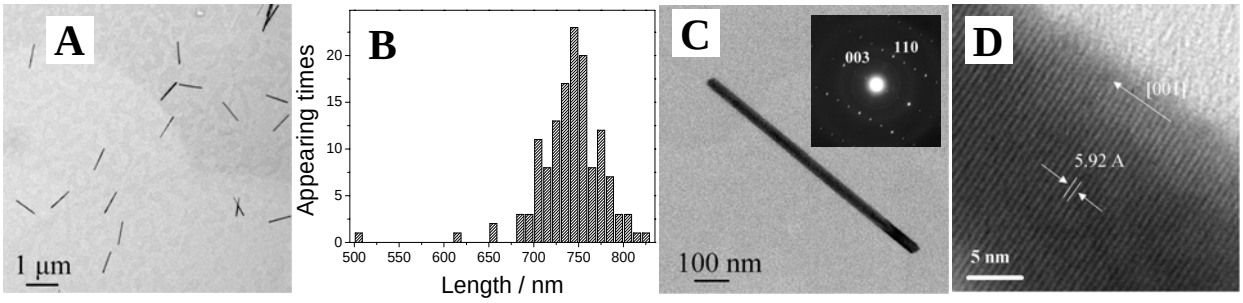

Figure 2-6. A), TEM image of Te nanorods synthesized by introducing H_2Te gas into a CPB $[t\text{BMA}_{90}]_{3200}$ solution in THF; B), the length distribution histogram of 137 Te nanorods; C), a single Te nanorod (inset is its electron diffraction pattern); D), its corresponding HRTEM image.

Te nanorods with high AR (>20) prepared in THF solution were quite uniform and well-dispersed, as identified from the TEM investigation (Fig. 2-6A). They are typically 741 ± 37.8

nm in length and 36.1 ± 7.9 nm in diameter, which gives an AR of 21. The length distribution histogram from 137 Te nanorods (Fig. 2-6B) shows an extremely low polydispersity (L_w/L_n = 1.003). The straight nanorod possesses a uniform diameter along its entire length (Fig. 2-6C). Its electron diffraction pattern (inset in Fig. 2-6C) confirms the hexagonal crystalline structure (space group: $P3_121$ (no.152)). The corresponding HRTEM image (Fig. 2-6D) proves that the Te nanorod is structurally single-crystalline with a periodic fringe spacing of 5.92 Å along the longitudinal axis (c axis), which corresponds to the interplanar spacing between the (001) planes of the hexagonal lattice of Te. The obtained Te nanorods are highly stable in solution under argon, due to the P*t*BMA CPB on the Te nanorod surface.

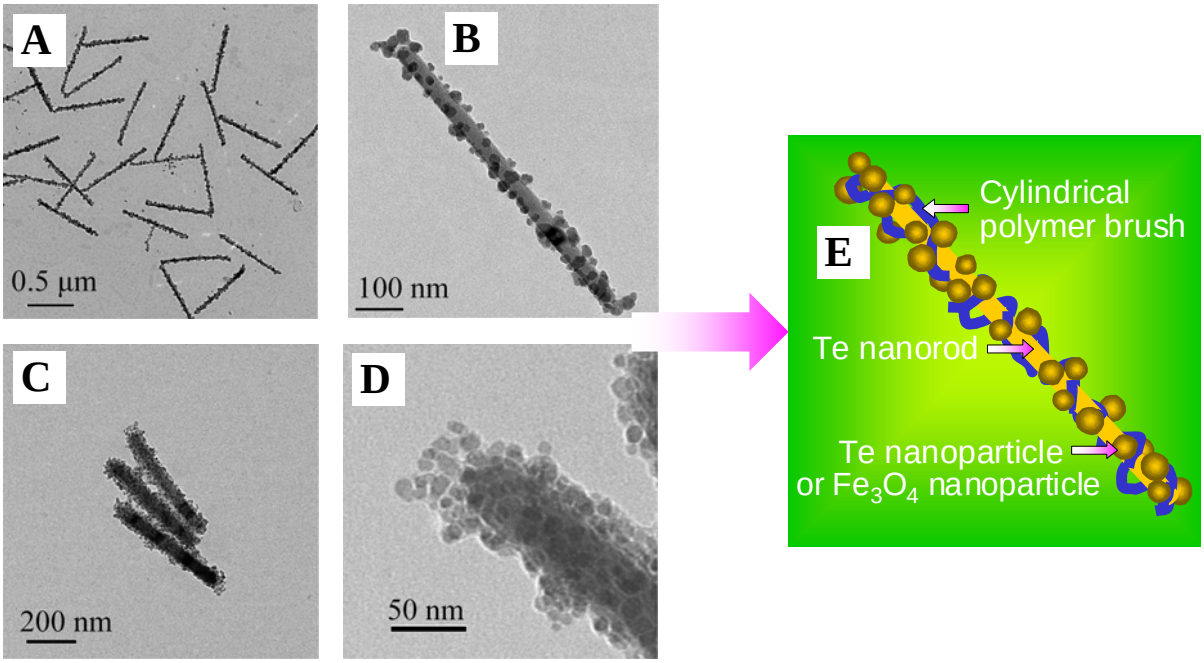

Figure 2-7. A-B), TEM images of Te nanorod/ Te nanoparticle complex; C-D), TEM images of Te nanorod/ Fe_3O_4 nanoparticle complex; and E), proposed model for Te nanorod/ (Te or Fe_3O_4) nanoparticle complex.

The as-prepared Te nanorods were able to assemble inorganic nanoparticles on their surface. Both Te and magnetite nanoparticles have been successfully attached onto Te nanorods respectively. The Te nanorod/Te nanoparticle complex (Fig. 2-7A and 2-7B) was prepared by in-situ oxidation of the H_2Te gas into Te nanoparticles in the presence of Te nanorods. The formed Te nanoparticles were enriched and assembled on the nanorod surface. The same phenomenon

was also found when oleic acid-capped Fe_3O_4 nanoparticles were added externally into Te nanorod solution in THF. The TEM images (Fig. 2-7C and 2-7D) prove that all Fe_3O_4 nanoparticles in solution stick to Te nanorods, which leaves a nanoparticle-free solution. The assembly of magnetite nanoparticles on Te nanorods generates a novel kind of Te nanorod-based magnetic nanocylinders (Te nanorod/Fe_3O_4 nanoparticle complex). The unique self-assembly behavior is related to the intrinsic hybrid structure of Te nanorods, whose surface were capped by hydrophobic P*t*BMA polymer. They preferentially interact with the hydrophobic polymer layers on Te nanoparticles or the long hydrophobic alkyl chains on Fe_3O_4 nanoparticles in THF.

2.5 Alignment of tellurium nanorods via a magnetization-alignment-demagnetization ("MAD") process assisted by an external magnetic field

We continued the research on the magnetic nanocylinders based on Te nanorods and magnetite nanoparticles. In this work, Te nanorods were prepared with the same strategy mentioned in Chapter 2.4 except using linear P*t*BMA polymer with high molecular weight instead of P*t*BMA CPBs due to its available large quantity. Table 2-1 summarizes the prepared Te nanorods with different lengths and aspect ratios.

Table 2-1. Te nanorods with different lengths and diameters obtained via TEM investigation.

Sample	Length /nm	Diameter /nm	Aspect ratio
Te (1)	422 ± 48	47 ±11	9
Te (2)	295 ± 47	21 ± 5	14
Te (3)	473 ± 46	155 ± 32	3

The magnetic nanocylinders were achieved by mixing the Te nanorod solution and magnetite nanoparticle solution in THF under strong mechanical shaking. The population of magnetite nanoparticles on individual Te nanorods could be controlled by the stoichiometric ratio of

nanoparticles to nanorods. Fig. 2-8 shows the various TEM images of the magnetic nanocylinders prepared with constant Te (1) nanorod concentration (60 mg/L) and decreasing concentration of nanoparticles in THF from 50.6 mg/L (Fig. 2-8A) to 1.87 mg/L (Fig. 2-8D). It is found that when the nanoparticle concentration was not above 5.2 mg/L, all nanoparticles adhered onto the nanorods rather than stayed in THF. No free nanoparticles could be detected in Fig. 2-8C ($C_{nanoparticles}$ = 5.2 mg/L) and Fig. 2-8D ($C_{nanoparticles}$ = 1.87 mg/L). Thus we define the concentration of the magnetite nanoparticles in Fig. 2-8C, 5.2 mg/L, as the critical concentration. Below it all nanoparticles will sit on the nanorods, leading to pure magnetic nanocylinders in THF. A calculation of the stoichiometric ratio of Fe_3O_4 nanoparticles to Te nanorods hints that each nanocylinder in Fig. 2-8C carries ca. 167 nanoparticles, and in Fig. 2-8D only 55. As the magnetic cylinders are based on the nanoparticles, their magnetic properties can be quantitatively tuned by loading different amount of nanoparticles below the critical concentration.

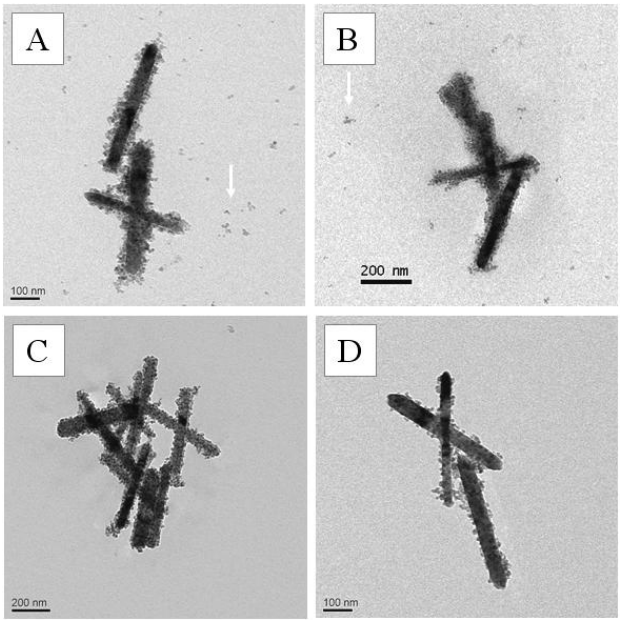

Figure 2-8. Magnetic Te (1) nanocylinders prepared from Te (1) nanorods (60 mg/L) and different concentrations of magnetite nanoparticles: (A) 50.6 mg/L, (B) 16.8 mg/L, (C) 5.2 mg/L, and (D) 1.87 mg/L in THF. The stoichiometric ratios (nanoparticles to nanorods) are (A) 1625, (B) 539, (C) 167 and (D) 55, respectively.

The magnetic Te (2) nanocylinders, prepared at the critical concentration, ($C_{nanoparticles}$ = 8.65 mg/L and $C_{nanorods}$ = 33.7 mg/L) were investigated with respect to their response to a magnetic

field. It was first visualized by responding to an external magnet, as shown in Fig. 2-9A-C. The responsive behavior was utilized to align the nanocylinders deposited from THF solution onto a solid substrate in the presence of an external magnetic field of 0.3 T. Due to the magnetite nanoparticles on the surface, the longitudinal axis of all Te nanorods are almost parallel to the magnetic field (Fig. 2-9D). Besides, a linear connection of the nanocylinders was often found (Fig. 2-9E). The elongated superstructure resembles that of macroscopic magnetic rods, which are connected at the ends via magnetic dipole interaction. The whole linear superstructure points to the same direction as the magnetic field.

The aligned magnetic nanocylinders on the solid substrate were further demagnetized by selectively dissolving the magnetite nanoparticles in an aqueous HCl solution, leaving Te nanorods in an aligned state. The methodology of decorating nanorods with magnetite nanoparticles, aligning and etching of the formed magnetic nanocylinders ("magnetization-alignment-demagnetization" process) can be broadened as a general method to align non-magnetic 1-D nanostructures assisted by an external magnetic field.

.

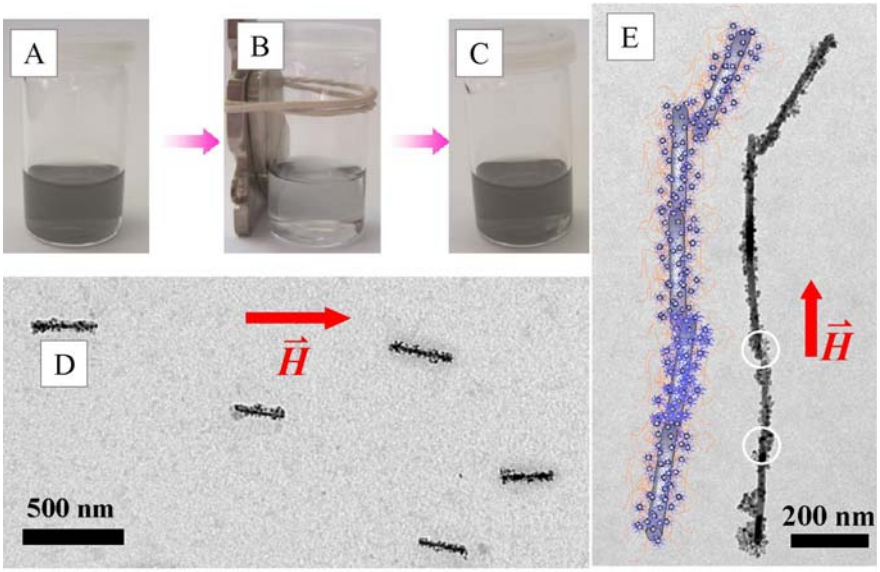

Figure 2-9. (A), the magnetic Te (2) nanocylinder solution in THF; (B), when close to a magnet; (C), after leaving the magnet and shaking; (D), TEM image of aligned magnetic nanocylinders when deposited from solution onto a carbon-coated TEM grid in the presence of an external magnetic field (0.3 T); (E), linear connection of aligned magnetic nanocylinders. The cartoon on the left side illustrates how this linear superstructure has been constructed.

2.6 Individual Contributions to Joint Publications

The results presented in this thesis were obtained in collaboration with others, and have been published or will be submitted to publication as indicated below. In the following, the contributions of all the coauthors to the different publications are specified. The asterisk denotes the corresponding author.

Chapter 3

This work is published in *Nature Materials* (**2008**, 7, 718) under the title:

"Water-Soluble Organo-Silica Hybrid Nanowires"

by Jiayin Yuan, Youyong Xu, Andreas Walther, Sreenath Bolisetty, Manuela Schumacher, Holger Schmalz, Matthias Ballauff, and Axel H. E. Müller*

I conducted all experiments and wrote the publication.

Exceptions are stated in the following:

Y. Xu was involved in discussion.
A. Walther performed some cryo-TEM measurements and analysis.
S. Bolisetty did the polarized optical microscopy measurements and interpreted the results.
M. Schumacher was involved in discussion.
H. Schmalz performed the anionic polymerization of the PBIEM backbone.
M. Ballauff and A. H. E. Müller were involved in scientific discussion and correcting this manuscript.

Chapter 4

This work is published in *Polymer* (**2008**, 49**,** 1547) under the title:

"Cadmium Selenide Nanowires within Core-Shell CPBs: Synthesis, Characterization and the Double-Loading Process"

by Jiayin Yuan, Markus Drechsler, Youyong Xu, Mingfu Zhang, and Axel H. E. Müller*

I conducted all experiments and wrote the publication.

Exceptions are stated in the following:

M. Drechsler performed some TEM measurements and interpreted the results.

Y. Xu was involved in discussion.
M. Zhang was involved in discussion.
A. H. E. Müller was involved in scientific discussion and corrections of this manuscript.

Chapter 5

This work has been submitted to *Chemistry of Materials* under the title:

"Template-directed Synthesis of Titania Hybrid Nanowires within Core-Shell Cylindrical Polymer Brushes"

by Jiayin Yuan, Yan Lu, Felix Schacher, Thomas Lunkenbein, Stephan Weiss, Holger Schmalz, and Axel H. E. Müller*

I conducted all experiments and wrote the publication.

Exceptions are stated in the following:

Y. Lu was involved in discussion and performed the SEM measurements.
F. Schacher performed the DLS measurements.
T. Lunkenbein performed the XRD measurements.
S. Weiss performed part of the NMR measurements.
H. Schmalz performed the anionic polymerization of the PBIEM backbone.
A. H. E. Müller was involved in scientific discussion and corrections of this manuscript.

Chapter 6

This work is published in *Advanced Materials* (**2008**, 20, 947) under the title:

"Room-temperature Growth of Uniform Tellurium Nanorods and the Assembly of Tellurium or Fe_3O_4 Nanoparticles on the Nanorods"

by Jiayin Yuan, Holger Schmalz, Youyong Xu, Nobuyoshi Miyajima, Markus Drechsler, Michael W. Möller, Felix Schacher, and Axel H. E. Müller*

I conducted all experiments and wrote the publication.

Exceptions are stated in the following:

H. Schmalz was involved in discussion and performed the anionic polymerization.
Y. Xu was involved in discussion.

N. Miyajima performed the high-resolution TEM and electron diffraction.

M. Drechsler performed some TEM measurements.

M. W. Möller performed the XRD measurements.

F. Schacher performed the synthesis of the P*t*BMA polymer with high molecular weight.

A. H. E. Müller was involved in scientific discussion and corrections of this manuscript.

Chapter 7

This work has been submitted to *ACS Nano* under the title:

"Alignment of Tellurium Nanorods via a Magnetization-Alignment-Demagnetization ("MAD") Process assisted by an External Magnetic Field"

by Jiayin Yuan, Haitao Gao, Felix Schacher, Youyong Xu, Reinhard Richter, Wolfgang Tremel and Axel H. E. Müller*

I conducted all experiments and wrote the publication.

Exceptions are stated in the following:

H. Gao was involved in discussion and performed the SQUID measurements.

F. Schacher was involved in discussion and performed the synthesis of the P*t*BMA polymer.

Y. Xu was involved in discussion.

R. Richter was involved in discussion and the setup of the magnetic field.

W. Tremel and A. H. E. Müller were involved in scientific discussion and corrections of this manuscript.

2.7 References

1. Zhang, M.; Drechsler, M.; Müller, A. H. E. *Chem. Mater.* **2004,** 16, (3), 537-543.
2. Murray, C. B.; Norris, D. J.; Bawendi, M. G. *J. Am. Chem. Soc.* **1993,** 115, (19), 8706-15.
3. O'Regan, B.; Graetzel, M. *Nature* **1991,** 353, (6346), 737-40.
4. Zheng, Q.; Zhou, B.; Bai, J.; Li, L.; Jin, Z.; Zhang, J.; Li, J.; Liu, Y.; Cai, W.; Zhu, X. *Adv. Mater.* **2008,** 20, (5), 1044-1049.
5. Bach, U.; Lupo, D.; Comte, P.; Moser, J. E.; Weissortel, F.; Salbeck, J.; Spreitzer, H.; Gratzel, M. *Nature* **1998,** 395, (6702), 583-585.
6. Kim, D. H.; Kim, S. H.; Lavery, K.; Russell, T. P. *Nano Lett.* **2004,** 4, (10), 1841-1844.
7. Cozzoli, P. D.; Kornowski, A.; Weller, H. *J. Am. Chem. Soc.* **2003,** 125, (47), 14539-14548.
8. Foerster, S.; Abetz, V.; Müller, A. H. E. *Adv. Polym. Sci.* **2004,** 166, (Polyelectrolytes with Defined Molecular Architecture II), 173-210.

Chapter 3

Water-Soluble Organo-Silica Hybrid Nanowires

Abstract

The anisotropic nature of cylindrical polymer brushes (CPBs) has been applied to template one-dimensional nanostructured materials, such as metal, semiconductor or magnetic nanowires. Here, by constructing the CPBs themselves with a precursor-containing monomer, we successfully synthesized hybrid nanowires with a silsesquioxane core and a shell made up from oligo(ethylene glycol) methacrylate units, which are soluble in many solvents, like water, methanol, THF and benzene. They were characterized by AFM, TEM, SEM, and cryo-TEM. The length and diameter of these rigid wires are tunable by the degrees of polymerization of both the backbone and the side chain. They show lyotropic liquid-crystalline behavior and can be pyrolyzed to silica nanowires. This approach provides a new route to the controlled fabrication of inorganic or hybrid silica nanostructures by living polymerization techniques.

* The results of this chapter have been published as

"Water-Soluble Organo-Silica Hybrid Nanowires"

by Jiayin Yuan, Youyong Xu, Andreas Walther, Sreenath Bolisetty, Manuela Schumacher, Holger Schmalz, Matthias Ballauff, and Axel H. E. Müller*

Nature Materials, **7**, 718-722 (2008)

3.1 Introduction

Great efforts have been made for exploring techniques to develop unique 1D structures, including laser-assisted catalytic growth,[1] vapor-liquid-solid[2] or solution-liquid-solution techniques,[3] template directed synthesis,[4] and others.[5] Cylindrical polymer brushes (CPBs), i.e. molecular brushes carrying linear or dendritic side chains densely grafted from a linear main chain, exhibit extended chain conformations ("bottle brushes").[6, 7] We used core-shell superstructured CPBs with a hydrophilic core to align in-situ generated nanoparticles, like γ-Fe_2O_3, CdS, or CdSe.[8-10] The superior control of anionic polymerization and atom transfer radical polymerization (ATRP) of molecular weight distribution of the backbone and side chains, respectively, enables the precise design of the structure as well as the function of the CPB. The core governs the nanowire dimension and the shell protects the nanowires from agglomeration and precipitation in solution.

Herein, we demonstrate that we can employ CPBs as robust tools for the synthesis of soluble organo-silica nanowires with a silsesquioxane (R-$SiO_{1.5}$) core, and a corona made up of oligo(ethylene glycol) methacrylate (OEGMA). These nanowires serve as in-situ template for the pyrolytic formation of purely inorganic silica nanowires. They can also construct lyotropic liquid-crystalline phase.

3.2 Experimental section

All chemicals were of analytical grade and used as received without further purifications, except that APTS (95%, ABCR) and OEGMA (M_n ~ 475 g mol^{-1}, 8.5 EO units, Aldrich) were filtered over an alumina column shortly before polymerization. The synthesis of the CPBs via the combination of anionic polymerization of the backbone and atom transfer radical polymerization (ATRP) of the side chains was reported earlier.[11] The DP of the backbone was determined to be 3,200 via characterizing the poly(2-bromoisobutyryloxyethyl methacrylate) (PBIEM) polyinitiator by *gel permeation chromatography* (GPC) (eluent: tetrahydrofuran with 4% tetra-*n*-butylammonium bromide, standard: polystyrene) and *static light scattering* (SLS). The DP of side chains was calculated from monomer conversion in polymerization by *nuclear magnetic resonance* (^{1}H-NMR). In order to avoid the hydrolysis of the trimethoxysilyl groups of the polymer brushes, all ATRP polymerizations were conducted in benzene at 80 °C and the reaction mixtures were purified under nitrogen via ultrafiltration in benzene as well.

The condensation of the trimethoxysilyl moieties inside the core-shell polymer brushes proceeded as follows. First 445 mg of the core-shell CPB [$APTS_{20}$-*b*-$OEGMA_{57}$]$_{3200}$ (containing 0.278 mmol of triemthoxysilyl groups) in 20 ml of benzene, was dialyzed against pure methanol. Then the brush solution was diluted to 200 ml with methanol, and 20 ml of aqueous ammonia solution (12 % wt) was added under stirring. After 24 hours, the excess ammonia and water in the polymer brush solution were removed by dialysis against methanol. The solvent can be changed by further dialysis against other solvents, like benzene, dioxane or water.

Atomic force microscopy (AFM) images were recorded on a Digital Instruments Dimension 3100 microscope operated in tapping mode. The samples were prepared by dip-coating from dilute solutions of the polymer brushes in benzene or methanol onto freshly cleaved mica to form a monomolecular film of the brushes.

Thermogravimetric analysis (TGA) measurements were carried out on a Mettler Toledo TGA/SDTA 851. The measurements were performed under airflow of 50 ml min^{-1} with heating from 30 °C to 700 °C (rate: 10 °C min^{-1}). Before TGA measurements, samples were collected from the brush solution with a rotary evaporator and dried in vacuum oven at 50 °C at least one day. For the preparation of silica nanowires on mica, the hybrid brushes were dip-coated onto

mica substrate, which was heated to and maintained at 700°C for half an hour in the presence of air.

Transmission electron microscopy (TEM) images were taken on a Zeiss EM EF-TEM instrument operated at 200 kV. A 5μL droplet of a diluted solution (~0.01 g L^{-1}) in benzene or methanol, was dropped onto a copper grid (200 mesh) coated with carbon film, followed by drying at room temperature for a short time. For *cryogenic transmission electron microscopy* (Cryo-TEM) studies, a drop of the aqueous dilute solution (0.02 g L^{-1}) was placed on a hydrophilized Lacey TEM grid, where most of the liquid was removed with blotting paper, leaving a thin film stretched over the grid holes. The specimens were shock frozen by rapid immersion into liquid ethane and cooled to approximately 90K by liquid nitrogen in a temperature-controlled freezing unit (Zeiss Cryobox, Zeiss NTS GmbH, Oberkochen, Germany). After the specimens were frozen, the remaining ethane was removed using blotting paper. The specimen was inserted into a cryo-transfer holder (CT3500, Gatan, München, Germany) and transferred to a Zeiss EM922 EF-TEM instrument operated at 200 kV.

Scanning electron microscopy (SEM) was performed using a Zeiss 1530 Gemini instrument equipped with a field emission cathode with a lateral resolution of approximately 2 nm. The AFM sample was taken for the SEM measurement after sputtering a thin layer (1~2 nm) of Pt.

Statistical analysis of the size distribution of the cylindrical objects (polymer brushes, hybrid nanowires and silica nanowires) in Fig. 3-3 and Fig. 3-4 was performed using the UTHSCSA ImageTool program (University of Texas). In each sample between 95 to 105 objects were measured to define the dimension, except in Fig. 3-4C, where 68 objects were collected for the analysis.

The polarized optical microscope measurements were carried out using Leica DMXRE optical microscope having crossed polarizers. It is further equipped with Leica DC300 digital camera, having different standard magnification ranges. The samples were prepared by formation of thin liquid film on glass surface, further concentrated by slow solvent evaporation of part of the solvent.

3.3 Results and discussion

As an exemplary system, illustrated in Fig. 3-1, we first synthesized an ATRP polyinitiator, poly(α-bromoisobutyryloxyethyl methacrylate) (PBIEM) with 3200 initiating sites. This was used to grow block copolymer chains with 20 units of 3-acryloylpropyl trimethoxysilane (APTS) and 57 units of OEGMA, leading to a core-shell CPB, $[APTS_{20}$-*b*-$OEGMA_{57}]_{3200}$. Hydrolysis of the trimethoxysilyl moieties and subsequent condensation led to a crosslinked silsesquioxane core, solubilized by the poly(OEGMA) (POEGMA) shell. Pyrolysis at 700 °C can be used to generate inorganic silica nanowires.

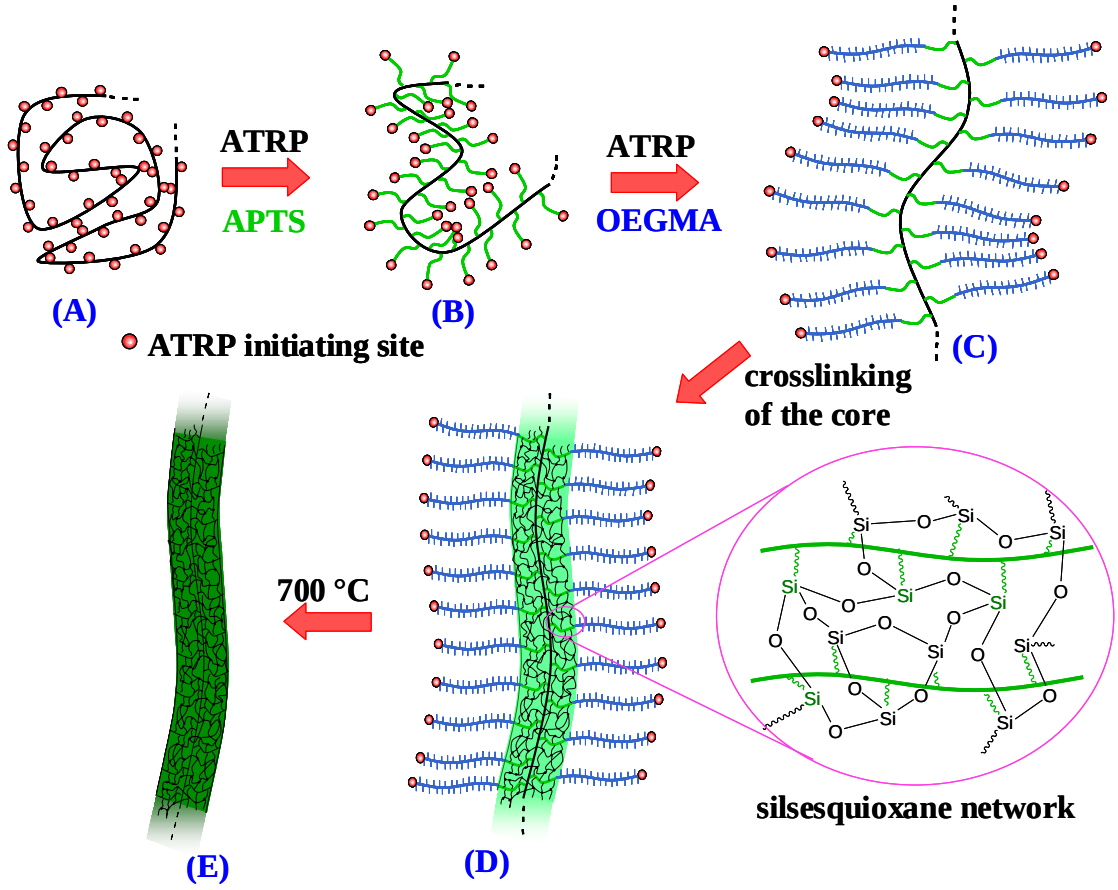

Figure 3-1. Synthesis of soluble organo-silica and inorganic silica nanowires. (A) ATRP polyinitiator PBIEM with DP = 3200; (B) cylindrical polymer brush (CPB) with side chains of 20 APTS units; (C) core-shell CPB with additional 57 OEGMA units; (D) soluble organo-silica hybrid nanowires with crosslinked silsesquioxane network in the core; (E) inorganic silica nanowires after pyrolysis. For details, see Fig. 3-2.

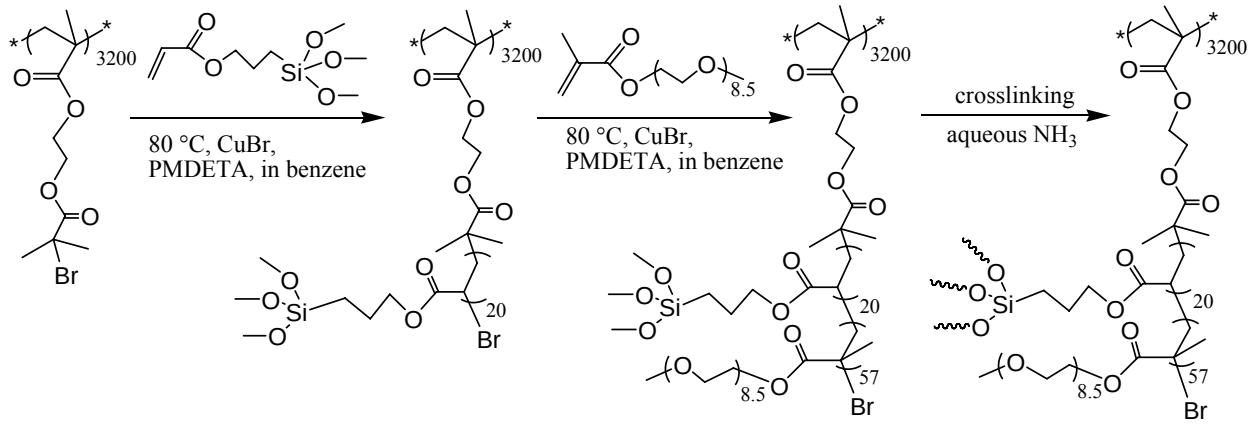

Figure 3-2. Synthetic route to soluble organo-silica hybrid nanowires via ATRP using CuBr as catalyst and N,N,N′,N",N"-pentamethyldiethylenetriamine (PMDETA) as ligand. (A) ATRP polyinitiator PBIEM; (B) $[APTS_{20}]_{3200}$ CPB; (C) $[APTS_{20}$-*b*-$OEGMA_{57}]_{3200}$ core-shell CPB; (D) soluble organo-silica hybrid nanowires $[(SiO_{1.5})_{20}$-*b*-$OEGMA_{57}]_{3200}$.

Molecular visualization of the products at each step, i.e., polymerization, condensation and pyrolysis, was undertaken by AFM on mica to verify the success of the synthetic strategy. In all cases, AFM revealed individual wormlike / wirelike structures lying flat on the substrate. Fig. 3-3A and 3-3B show height images of the $[APTS_{20}]_{3200}$ and $[APTS_{20}$-*b*-$OEGMA_{57}]_{3200}$ CPBs, respectively. In the case of $[APTS_{20}$-*b*-$OEGMA_{57}]_{3200}$ the wormlike structures are much more stretched, due to the bulky POEGMA blocks. Individual objects, indicated by white arrows in each AFM image in Fig. 3-3A-D, were subjected to cross-section analysis (Fig. 3-3E, all widths not deconvoluted for tip size[12]). The typical $[APTS_{20}]_{3200}$ brush (green) is 1.4 nm high in its center and 35 nm in width. Growth of the POEGMA block strongly increases the center height to 4.4 nm and width to 76 nm. The regular cylindrical shape of the $[APTS_{20}$-*b*-$OEGMA_{57}]_{3200}$ CPBs in Fig. 3-3B enables a statistical analysis of their length. The number- and weight-average lengths are L_n = 322 nm and L_w = 355 nm, respectively, giving a polydispersity L_w/L_n = 1.10, which agrees well with that of the PBIEM backbone (M_w/M_n = 1.14).

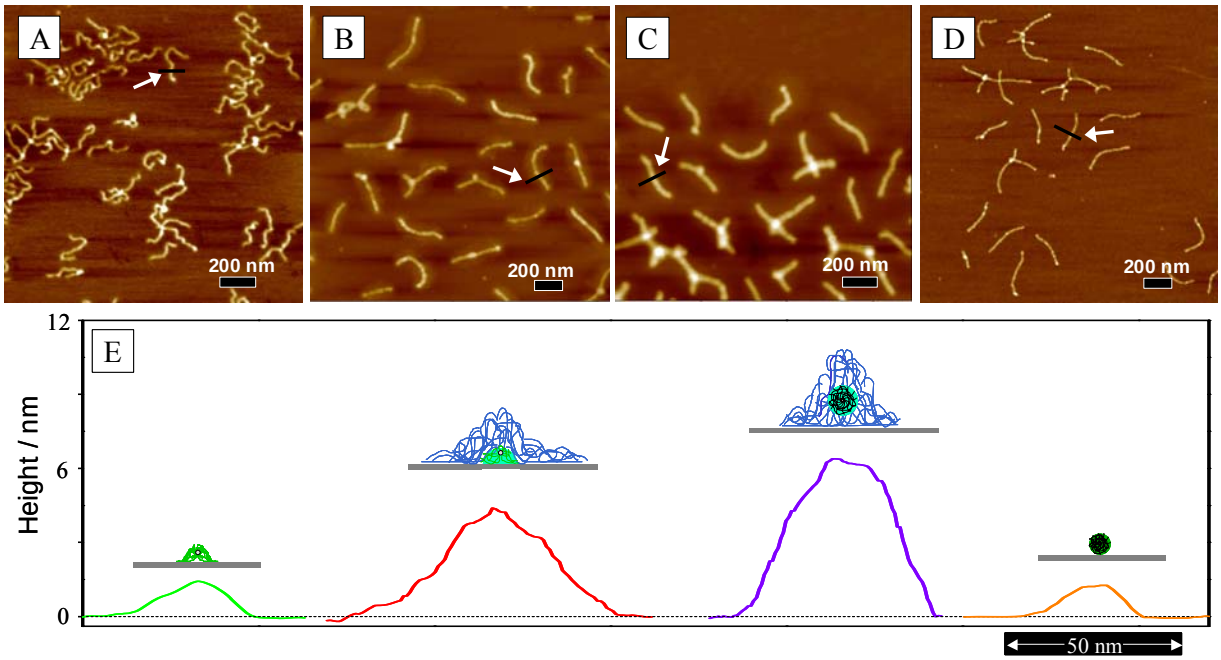

Figure 3-3. AFM height images on mica: (A) $[APTS_{20}]_{3200}$ CPBs (z range, 4 nm), (B) $[APTS_{20}$-*b*-$OEGMA_{57}]_{3200}$ core-shell CPBs (z range, 15 nm), (C) soluble organo-silica hybrid nanowires $[(SiO_{1.5})_{20}$-*b*-$OEGMA_{57}]_{3200}$ (z range, 20 nm), (D) inorganic silica nanowires (z range, 4 nm). (E) cross-sectional analysis of objects marked with an arrow.

The condensation of the APTS units, catalyzed by ammonia in a methanol/water mixture via the Stöber method,[13] introduced a continuous silsesquioxane network in the core, which is protected and solubilized by the POEGMA shell. Analysis of Fig. 3-3C indicates that the hybrids have L_n = 283 nm, 39 nm (12%) shorter than before condensation. The width decreases by 24% from 76 nm to 58 nm. The lateral and longitudinal contraction reveals the successful cleavage of the methoxyl protecting groups followed by condensation, which shrinks the core size. In contrast, the height of the hybrid nanowires increases by 45% from 4.4 nm to 6.4 nm (Fig. 3-3E). We assume that the crosslinked poly(APTS) (PAPTS) block can no longer spread to be flatly adsorbed on mica surface. CPBs with POEGMA, PAPTS and PAPTS-*b*-POEGMA side chains are soft materials at room temperature (glass transition temperature, T_g < -45 °C; see Supporting Information Fig. 3-6). Obviously, the silsesquioxane network hardens the core and reduces the penetration of the AFM tip into the CPB.

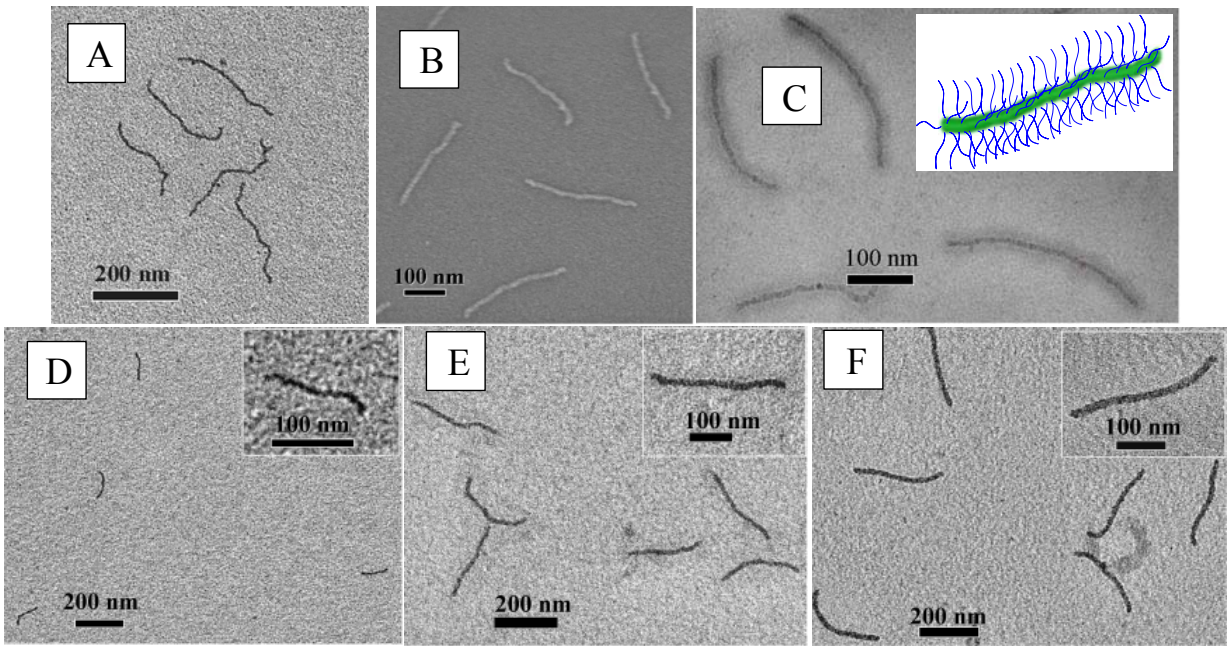

Figure 3-4. Electron microscopy characterization of soluble organo-silica hybrid nanowires. (A) non-stained TEM image of $[(SiO_{1.5})_{20}$-*b*-$OEGMA_{57}]_{3200}$; (B) its SEM image and (C) its non-stained cryo-TEM image in water. (D), (E) and (F) are non-stained TEM images of $[(SiO_{1.5})_{21}$-*b*-$OEGMA_{58}]_{1500}$, $[(SiO_{1.5})_{41}$-*b*-$OEGMA_{68}]_{3200}$, and $[(SiO_{1.5})_{72}$-*b*-$OEGMA_{95}]_{3200}$ respectively.

The absolute dimensions of the organo-silica hybrid nanowires in the dry state and in solution were determined by scanning electron microscopy (SEM), transmission electron microscopy (TEM) and cryogenic TEM (cryo-TEM), respectively. Fig. 3-4A shows a non-stained TEM image of the hybrid nanowires. The characteristic, wire-like dark domains represent the silsesquioxane core, whereas the organic corona is not visible due to low contrast. The number-average length of these dark objects is L_n = 276 ± 29 nm (close to the AFM value) and the diameter is 9 nm, giving an aspect ratio of 30. The SEM image (Fig. 3-4B) shows the collapsed POEGMA shell. Here, L_n = 280 ± 30 nm and d = 21 ± 3 nm are observed, leading to an aspect ratio of 13. Thus, the thickness of POEGMA shell is 6~7 nm. The structure of the hybrid nanowires in water was identified by cryo-TEM measurements, as shown in Fig. 3-4C. The dark line represents the nanowire core, and the gray corona stands for the POEGMA shell. The inset illustrates the compact superstructure of a single hybrid nanowire in solution. The size of the nanowire core (L_n = 285 ± 40 nm, d = 9.5 ± 1 nm) remains the same as that in Fig. 3-4A, while

the diameter, including the solvent-swollen corona, has dramatically expanded to 45 ± 5 nm, leading to a thickness of the swollen corona of ~18 nm.

To demonstrate the structural control of the shape, different-sized nanowires were prepared and compared with the $[APTS_{20}$-*b*-$OEGMA_{57}]_{3200}$ in Fig. 3-4 D-F and Table 3-1. As expected, a decrease of the backbone DP from 3200 to 1500 with constant DPs of the side-chain blocks decreases the nanowire length from 276 to 138 nm, while the diameter kept constant (Fig. 3-4D). At constant DP of the backbone we increased the PATPS block DP from 20 to 41 and 72, respectively, and the diameter increased from 9 nm to 15 and 21 nm, respectively (Fig. 3-4 E,F). Here the length increased very slightly (3% and 7%, respectively), due to the stronger repulsion of the enlarged side chains. The variation in the length as well as the diameter clearly verifies that the nanowire dimension can be designed by the living polymerization techniques like anionic polymerization and ATRP, which easily control and govern the precise DP of the polymers.

Table 3-1 TEM characterization of the length and the $SiO_{1.5}$ core diameter of organo-silica hybrid nanowires with various DPs of the backbone and PAPTS side chain block.

Hybrid Nanowire	Length (nm)	Diameter (nm)	Aspect Ratio
$[APTS_{20}$-*b*-$OEGMA_{57}]_{3200}$	276 ± 29	9	30
$[APTS_{21}$-*b*-$OEGMA_{58}]_{1500}$	138 ± 25	9	15
$[APTS_{41}$-*b*-$OEGMA_{68}]_{3200}$	285 ± 45	15	19
$[APTS_{72}$-*b*-$OEGMA_{95}]_{3200}$	295 ± 45	21	14

The hybrid nanowires were converted to inorganic silica nanowires by a pyrolysis process at 700 °C, which has been often adopted to generate template-free 1D nanostructures.[14, 15] Fig. 3-3D shows the AFM image of the obtained uniform silica nanowires from $[APTS_{20}$-*b*-$OEGMA_{57}]_{3200}$ on mica. Obviously the nanowires are thinner than the hybrid nanowires, resulting from the loss of the POEGMA shell during the pyrolysis. The width and height of the nanowires obtained by cross-section analysis in Fig. 3-3E are 31 nm and 1.3 nm, respectively. The difference in width with respect to the TEM image (31 - 9 nm = 22 nm) corresponds to the non-deconvoluted

contribution of the tip size. The dimensions are very close to those of the $[APTS_{20}]_{3200}$ CPB (35 nm and 1.4 nm). Only the number-average length is 276 nm, 14 % smaller. The silica content in the hybrid nanowires was determined to be 3.53% (theoretical amount: 3.95%) by thermogravimetric analysis (TGA), and the residue was proven to be pure silica.(see Supporting Information Fig. 3-7 and 3-8) Although the POEGMA shell is removed during pyrolysis, it is essential in the condensation process, as it screens the intermolecular crosslinking, stretches the backbone, and most importantly, solubilizes the hybrid nanowires in methanol, in which the condensation reaction takes place. Additionally, the biocompatibility of the POEGMA shell may bring the soluble hybrid nanowires into bio-related potential applications, such as biosensors.

Very recently, 1D silica structures templated by polysaccharide derivatives or Magnus salt have been reported.[16, 17] In these strategies, either linear cellulose backbones carrying amino groups or Pt salt nanofibers were exploited to direct the condensation of the tetraethyl orthosilicate. However, great care has to be taken to suppress or avoid the homogenous nucleation of silica nanoparticles in the solution, which causes difficulties in the purification step. In our approach, the silica precursor is directly incorporated within the APTS monomer, acting as the building component of the CPBs rather than being added. Thus, the formation of free silica nanoparticles in the solution is totally excluded in this process. The integration of the silica precursor into the template greatly simplifies the reaction system, and is the great advantage of our method. Although an isocyanate-derived monomer containing the triethoxylsilyl group has been reported to polymerize via anionic polymerization at –78 °C to build a patterned surface,[18] the approach with APTS is superior, as acrylates can be polymerized not only by ionic, but also controlled/living radical polymerization under mild conditions. After this paper was submitted, the construction of spherical hybrid micelles by the use of 3-methacryloylpropyl trimethoxysilane, an analogue of APTS, was reported. However, the uncontrolled free-radical polymerization leads to a rather broad distribution of the micelle sizes.[19]

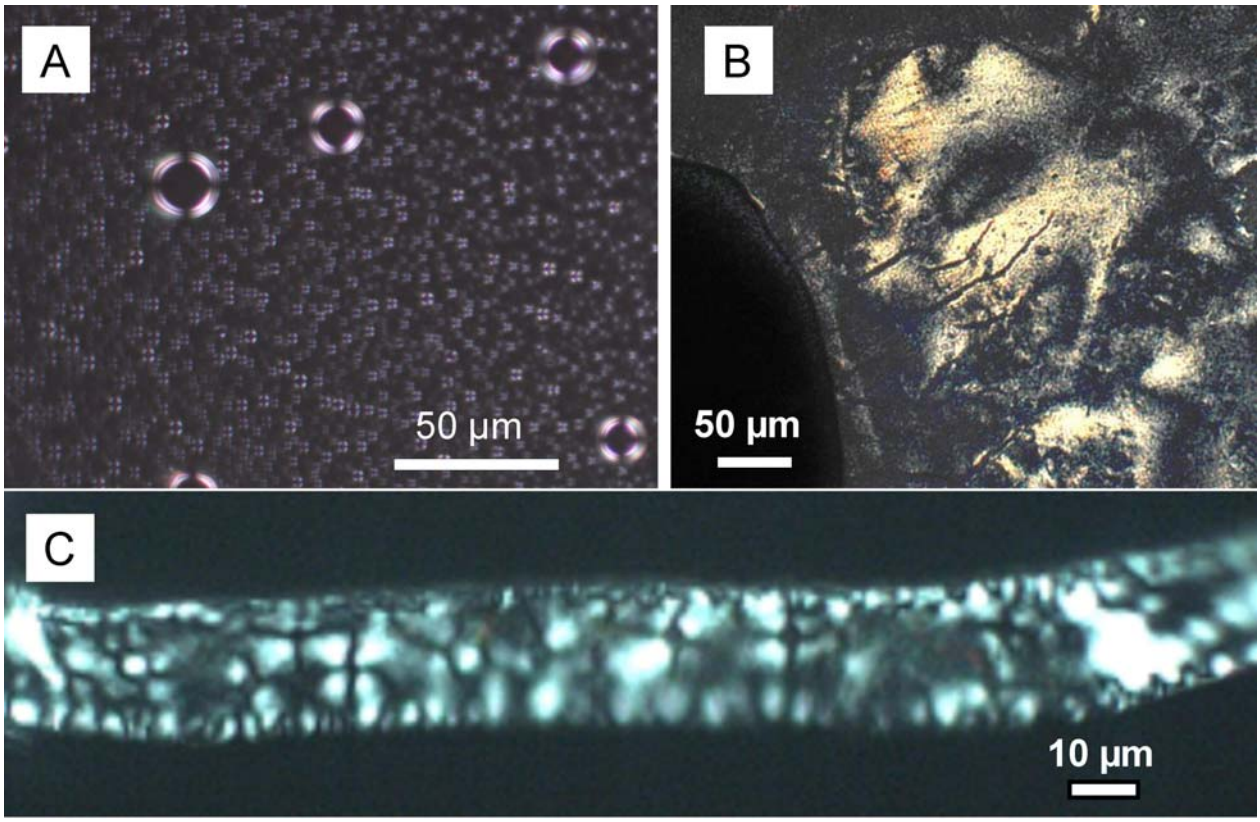

Figure 3-5. Lyotropic liquid-crystalline phase of organo-silica hybrid nanowires $[(SiO_{1.5})_{20}$-*b*-$OEGMA_{57}]_{3200}$. (A) Droplets (tactoids) formed from the isotropic phase during slow evaporation of a thin film of the methanolic hybrid nanowire solution on glass surface, (B) Schlieren texture at a later stage. (C) Schlieren texture of the lyotropic phase confined in a capillary.

As frequently reported, 1D nanostructures can assemble into ordered superstructures.[20-22] In our case, the soluble organo-silica hybrid nanowires were investigated by optical microscopy with crossed polarizers, to probe for the existence of a lyotropic liquid-crystalline phase, which may occur due to a competition of orientational entropy and excluded volume interaction of stiff CPBs.[23, 24] The formation of the lyotropic liquid crystalline phase, stemming from the ordering of hybrid nanowires at higher concentration, can be verified by the birefringence patterns emerging from the solution. Fig. 3-5A shows the typical birefringence patterns obtained from hybrid nanowires $[APTS_{20}$-*b*-$OEGMA_{57}]_{3200}$ by formation of a thin film through slowly evaporating the nanowire solution (~ 1g L^{-1}) in methanol on glass substrate. The coexistence of an isotropic and a nematic phase is revealed by the observation of tactoids, i.e. nematic droplets floating in the

isotropic phase. At a later stage, a fully developed liquid-crystalline phase, showing a Schlieren texture, was observed as shown in Fig. 3-5B, characteristic of a nematic phase. The Schlieren texture is also observed in a capillary,(Fig. 3-5C) where the disclinations are clearly visible. The flowability and deformability of the birefringent phase were easily confirmed by the movement of the capillary under the polarized optical microscope. Such kind of nematic liquid-crystalline behavior was also reported for the CdSe nanorod solutions.[25, 26]

3.4 Conclusions

In conclusion, we have described a new concept to design soluble organo-silica hybrid nanowires by the use of core-shell cylindrical polymer brushes. The hybrid nanowires are size-controllable and can be employed to generate inorganic silica nanowires or to construct lyotropic phases. The integration of the silica precursor into the APTS monomer is rather helpful in the synthesis, and in fact, it could be extended to other commercial analogous monomers. Moreover, the shape dependence of the organo-silica hybrid nanostructures on the manner how the precursors (namely APTS monomer) have been spatially arranged, makes it possible to configure various hybrid nanostructures based on polymeric superstructures, which have been widely studied and show many topologies, not only cylindrical or micellar, but also vesicular, tubular and lamellar. The strategy described here would also be useful to coat various nanostructures with silica by functionalizing their surface with ATRP initiators.

Acknowledgements. This work was supported by the Deutsche Forschungsgemeinschaft (grant Mu896/22). We thank Dr. Markus Drechler, Violetta Olszowka, Markus Hund, Benjamin Goßler, Christina Löffler, and Jérôme Crassous for their kind help in TEM, AFM, SEM, TGA and polarized optical microscopy measurements. We also thank Dr. Günter Lattermann for the helpful discussions on polarized optical microscopy.

3.5 References

1. Duan, X.; Lieber, C. M. *Adv. Mater.* **2000,** 12, (4), 298-302.
2. Ma, C.; Wang, Z. L. *Adv. Mater.* **2005,** 17, (21), 2635-2639.
3. Grebinski, J. W.; Richter, K. L.; Zhang, J.; Kosel, T. H.; Kuno, M. *J. Phys. Chem. B* **2004,** 108, (28), 9745-9751.
4. Adelung, R.; Aktas, O. C.; Franc, J.; Biswas, A.; Kunz, R.; Elbahri, M.; Kanzow, J.; Schuermann, U.; Faupel, F. *Nat. Mater.* **2004,** 3, (6), 375-379.
5. Milenkovic, S.; Hassel Achim, W.; Schneider, A. *Nano Lett.* **2006,** 6, (4), 794-9.
6. Zhang, M.; Müller, A. H. E. *J. Polym. Sci. Part A: Polym. Chem.* **2005,** 43, (16), 3461-3481.
7. Dziezok, P.; Sheiko, S. S.; Fischer, K.; Schmidt, M.; Möller, M. *Angew. Chem. Int. Ed.* **1998,** 36, (24), 2812-2815.
8. Zhang, M.; Estournes, C.; Bietsch, W.; Müller, A. H. E. *Adv. Funct. Mater.* **2004,** 14, (9), 871-882.
9. Zhang, M.; Drechsler, M.; Müller, A. H. E. *Chem. Mater.* **2004,** 16, (3), 537-543.
10. Yuan, J.; Drechsler, M.; Xu, Y.; Zhang, M.; Müller, A. H. E. *Polymer* **2008,** 49, (6), 1547-1554.
11. Zhang, M.; Breiner, T.; Mori, H.; Müller, A. H. E. *Polymer* **2003,** 44, (5), 1449-1458.
12. Berdyyeva, T.; Woodworth, C. D.; Sokolov, I. *Ultramicroscopy* **2005,** 102, (3), 189-198.
13. Stoeber, W.; Fink, A.; Bohn, E. *J. Colloid Int. Sci.* **1968,** 26, (1), 62-9.
14. Wang, X.; Guerin, G.; Wang, H.; Wang, Y.; Manners, I.; Winnik, M. A. *Science* **2007,** 317, (5838), 644-647.
15. Wang, X.; Liu, K.; Arsenault, A. C.; Rider, D. A.; Ozin, G. A.; Winnik, M. A.; Manners, I. *J. Am. Chem. Soc.* **2007,** 129, (17), 5630-5639.
16. Zollfrank, C.; Scheel, H.; Greil, P. *Adv. Mater.* **2007,** 19, (7), 984-987.
17. Ren, L.; Wark, M. *Chem. Mater.* **2005,** 17, (24), 5928-5934.
18. Park, J. W.; Thomas, E. L. *J. Am. Chem. Soc.* **2002,** 124, (4), 514-515.
19. Wei, H.; Cheng, C.; Chang, C.; Chen, W. Q.; Cheng, S. X.; Zhang, X. Z.; Zhuo, R. X. *Langmuir* **2008**.
20. Hermanson, K. O.; Lumsdon, S. O.; Williams, J. P.; Kater, E. W.; Velev, O. D. *Science* **2001,** 294, (5544), 1082-1086.
21. Huang, Y.; Duan, X.; Wei, Q.; Lieber, C. M. *Science* **2001,** 291, (5504), 630-3.

22. Elbahri, M.; Paretkar, D.; Hirmas, K.; Jebril, S.; Adelung, R. *Adv. Mater.* **2007,** 19, (9), 1262-1266.

23. van der Schoot, P. *J. Phys. Chem. B* **1996,** 104, (3), 1130-9.

24. Wintermantel, M.; Fischer, K.; Gerle, M.; Ries, R.; Schmidt, M.; Kajiwara, K.; Urakawa, H.; Wataoka, I. *Angew. Chem. Int. Ed.* **1995,** 34, (13/14), 1472-4.

25. Li, L.-S.; Alivisatos, A. P. *Adv. Mater.* **2003,** 15, (5), 408-411.

26. Li, L.-S.; Walda, J.; Manna, L.; Alivisatos, A. P. *Nano Lett.* **2002,** 2, (6), 557-560.

3.6 Supporting Information

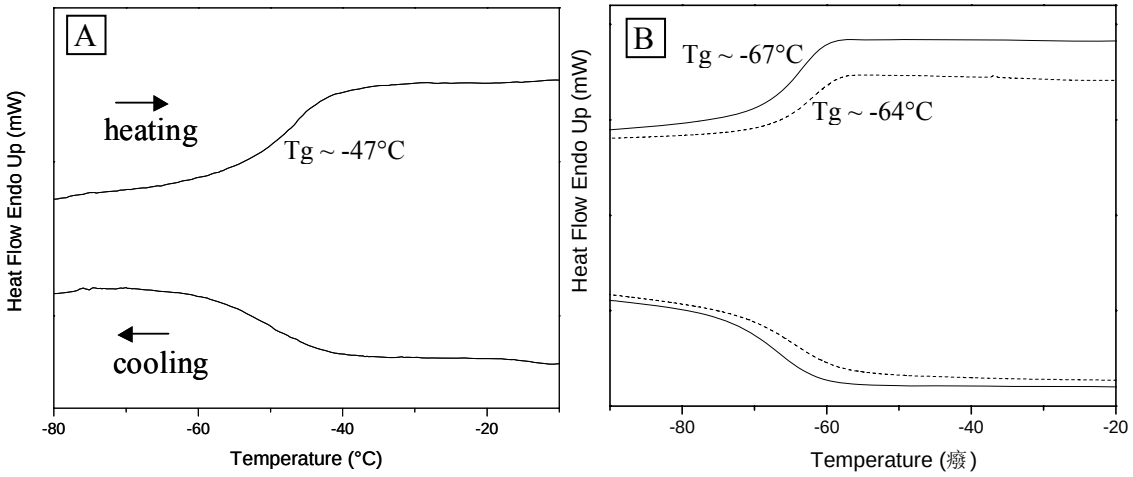

Figure 3-6. DSC curves of $[APTS_{20}]_{3200}$ CPB in (A), $[OEGMA_{67}]_{3200}$ CPB in (B) (solid line) and $[APTS_{20}$-*b*-$OEGMA_{57}]_{3200}$ in (B) (dashed line). All show rather low Tg, which indicates that the polymer chains are not frozen at RT and soft.

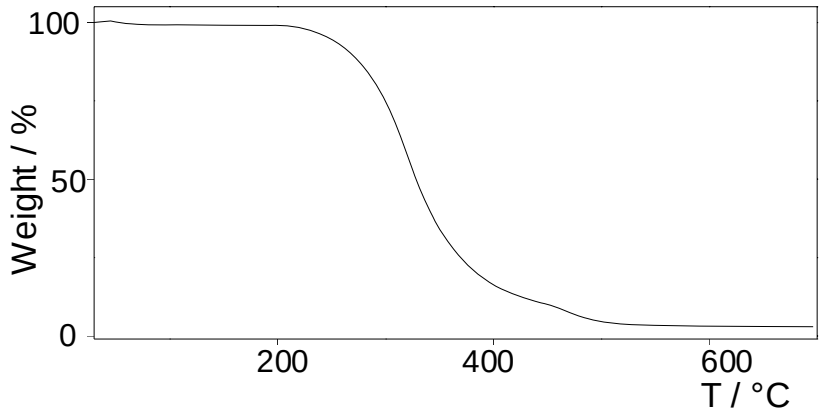

Figure 3-7. TGA curve of bulk organo-silica hybrid nanowires. The measurements were carried out under air flow of ~50 ml min^{-1} with a heating rate of 10 K min^{-1}. The weight loss remains constant above 530 °C, leaving a residue of 3.53%, very close to the theoretical calculated SiO_2 amount of 3.95%.

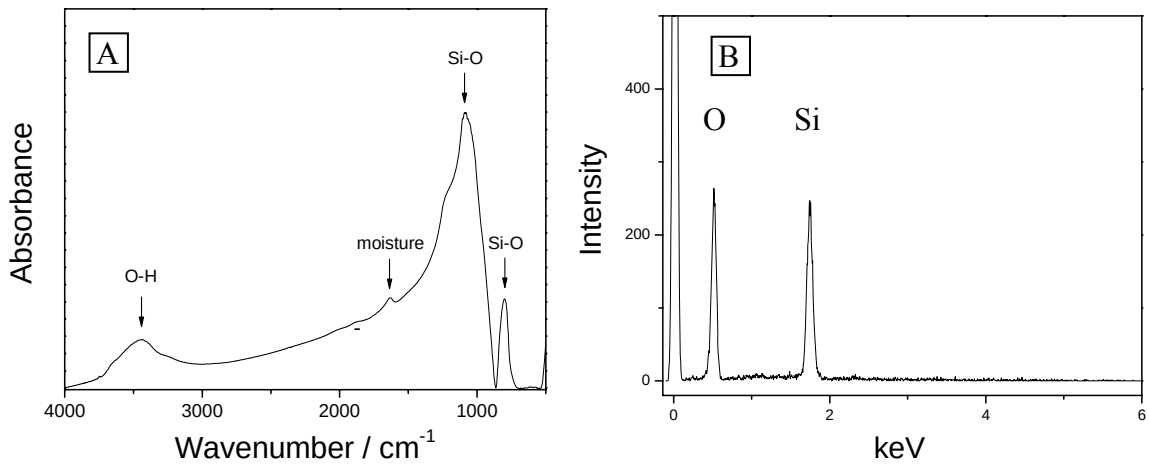

Figure 3-8. (A) Fourier transform infrared spectrum of the residue of the organo-silica hybrid nanowires after TGA. It only shows the stretching and deformation of O–H bond in the Si–O–H group (3500–3100 cm^{-1}) and the asymmetric stretching vibration of the Si-O-Si group (1130-1040 cm^{-1}), which are typical bonds from pure silica. Meanwhile, the typical C-H bond representing the organic moiety disappears from the region between 2800 and 3000 cm^{-1}, proving that all polymer part is removed. (B) Energy dispersive X-ray analysis of the residue of bulk silica hybrid nanowires after TGA measurement. It reveals that the residue is pure silica with a Si/O ratio of 1:1.93. By combination of the Fourier transform infrared spectrum and energy dispersive X-ray analysis, the residue after the pyrolysis is verified to be pure inorganic silica.

Chapter 4

Cadmium Selenide Nanowires within Core-Shell Cylindrical Polymer Brushes: Synthesis, Characterization and the Double-Loading Process

Abstract

Cadmium selenide (CdSe) nanowires were successfully in situ fabricated, utilizing amphiphilic core-shell cylindrical polymer brushes (CPB) as well-defined unimolecular template. The hydrophilic CPB core acts as the nanoreactor for generating and shaping CdSe nanoparticles into nanowires via the coordination of cadmium ions by carboxylate groups into the core and the subsequent introduction of H_2Se gas; the hydrophobic polymer brush shell protects the nanowires from agglomeration and render the hybrid a soluble material. The formation of 170 nm-long CdSe nanowires proceeds simultaneously with the nucleation, growth and combination of CdSe nanoparticles. After the introduction of CdSe nanowires, the recuperated chemical structure of CPB facilitates a double-loading process, broadening the CdSe nanowire from 7.5 to 9.3 nm on an average. Both hybrids are soluble and stable in organic solvents for one year and a potential candidate of the nanoscale optic and electric devices.

***** The results of this chapter have been published as:

"Cadmium Selenide Nanowires within Core-Shell Cylindrical Polymer Brushes: Synthesis, Characterization and the Double-Loading Process"

by Jiayin Yuan, Markus Drechsler, Youyong Xu, Mingfu Zhang, and Axel H. E. Müller*

Polymer **49**, 1547 (2008)

4.1 Introduction

Semiconductor nanowires[1-6] are considered as the prospective building blocks, interconnects and functional components for assembling nanosized photonic, electronic and optical devices and sensors.[7-14] Among them, cadmium selenide (CdSe) nanowires are promising candidates to build up optoelectronic devices, such as solar cells, and have received steadily growing interest. This has benefited from intensive studies on CdSe quantum dots.[15-17] In the last decade, there have been many efforts to develop CdSe nanowires utilizing a variety of techniques. For instance, direct-current electrodeposition in porous anodic aluminum oxide templates has been used by the groups of Guo[18] and Peng[19] to generate CdSe nanowire with well-controlled crystalline and polycrystalline structure. Lieber and co-workers reported a laser-assisted catalytic growth method to fabricate CdSe nanowires.[4] A surfactant-assisted solution synthesis of CdSe nanowires was published by Rao et al.[20] The group of Kuno has grown straight and branched CdSe nanowires with lengths between 1 μm and 10 μm by a solution-liquid-solution technique using gold/bismuth core-shell nanoparticles as seeds.[21-23] Chen and co-workers fabricated single-crystalline CdSe nanowires by a chemical vapor deposition method assisted with laser ablation.[24] Xia and co-workers employed the cation-exchange reaction between Ag^{+} and Cd^{2+} to transform single-crystal Ag_2Se nanowires into single-crystal CdSe nanowires.[25] A vapor-phase growth of CdSe nanowires assisted with silicon powder was achieved by the group of Zhang.[26] Wang and co-workers provided a systematic study on the growth of 1-dimensional CdSe nanostructures by a vapor-liquid-solid process.[27] Great progress until now have been reached, however the generation of well-distributed and aligned semiconductor nanowires is still challenging in this field.

In addition, polyelectrolytes and biopolymers, like DNA and viruses, have been widely exploited as templates for mineralization and fabrication of various inorganic nanowires due to the mild synthetic conditions.[28-32] However only a few reports were related to the polymer template-directed synthesis of semiconductor nanowires, with notable examples including micro channels within a thin polymer film,[33] a polymer-assisted solvothermal process,[34-36] mesoscale structures self-assembled from AB or ABC block copolymers,[37, 38] and biopolymers such as DNA strains.[39, 40]

Recently, we reported the formation of worm-like cadmium sulfide (CdS) nanowires within well-defined amphiphilic core-shell cylindrical polymer brushes (CPB).[41] In this paper, extending

this technique, we accomplished the synthesis of CdSe semiconductor nanowires and carried out a double-loading process to broaden these nanowires. Comparing the rigorous conditions such as high temperature, high pressure, toxic organometallic precursors, this facile and environmentally benign synthesis using nontoxic reactants appears to be superior.

4.2 Experimental Section

Materials. All chemicals were of analytical grade and used as received without further purifications. Cadmium acetate dihydrate ($CdAc_2 \cdot 2H_2O$) was purchased from Merck. Selenium powder (<325 mesh, 99.7%) and chloroform (>99.8%, stabilized with amylene) were purchased from Acros. Methanol (>99.8%) and paraffin oil were purchased from Fluka. The CPB $[AA_{25}\text{-}b\text{-}n BA_{61}]_{1500}$ (1500 side chains, each consisting of 25 acrylic acid units and 61 *n*-butyl acrylate units, L_n = 169 nm, L_w = 180 nm) that we used as template was synthesized as reported earlier.[42]

Synthesis of the hybrid of polymer brush and CdSe nanoparticles. 40.0 mg of the polymer brush, $[AA_{25}\text{-}b\text{-}nBA_{61}]_{1500}$ (containing 0.102 mmol of carboxylic acid groups) was dissolved in 40 mL of a mixture of methanol and chloroform (v/v = 1/1). Then 0.097 mmol of NaOH (0.128 M solution in methanol) was added to neutralize 95% of the carboxylic acid groups. After stirring for 6 h, 0.051 mmol of $CdAc \cdot 2H_2O$ (0.0720 M solution in methanol) was injected and the reaction mixture was stirred for 12 h.

To remove the uncoordinated Cd^{2+} ions, continuous dialysis was carried out in a mixture of methanol and chloroform (v/v = 1/1) using PVDF membrane tubes (MWCO = 500,000, SpectraPor). The process was monitored by the conductivity change of the dialyzate measured with an automatic titration system (Titrando 809, Metrohm) and ended when an almost constant conductivity was obtained during the dialysis.

The formation of CdSe particles was carried out under argon atmosphere. A 3-neck round bottle glass charged with a stirring bar, thermometer, condenser, 2.0 g of selenium powder and 50 ml of paraffin oil was bubbled by argon for half an hour and then heated to 300 °C under vigorous stirring.[43] The mixture became a dark red clear solution above 220 °C due to the melting of Se powder (mp = 217 °C). The released H_2Se gas was distributed by argon flow through the glass pipeline into the polychelate solution. The reaction mixture turned red instantly, signifying the formation of CdSe nanoparticles. After 1 hour the obtained transparent dark red solution was bubbled with Ar for one hour, degassed by three cycles of freeze-pump-thaw process and diluted to 100 ml. This solution was ready for double-loading process in an analogous procedure.

Characterization. *Atomic force microscopy* (AFM) images were recorded on a Digital Instruments Dimension 3100 microscope operated in tapping mode with minimum amplitude setpoint to avoid strong deformation of the objects. The samples were prepared by dip-coating

from dilute sample solutions in a mixture of methanol/chloroform (v/v = 1/1) onto freshly cleaved mica. The height profile analysis was conducted with Nanoscope III and Uthscsa Image Tool software.

Transmission electron microscopy (TEM) images were taken on a Zeiss/LEO 922 OMEGA microscope operated at 200 kV, or a Zeiss CEM 902 microscope operated at 80 kV. To prepare the samples, 1 μL of a dilute solution of 0.01 g/L (polymer content) was put onto a copper grid (300 mesh, Plano) coated with a SiO_x film and dried in the saturated solvent vapor at ambient temperature. Energy-dispersive X-ray (EDX) analysis was performed on a LEO 1530 field emission scanning electron microscope using an X-ray detector. The samples were obtained similarly except onto a silicon wafer.

UV-vis absorption spectra of samples in methanol / chloroform (v/v = 1/1) were recorded on a Perkin-Elmer Lambda 15 UV-vis spectrophotometer. Photoluminescence spectra of samples were collected on a Shimadzu RF-5301 PC spectrofluorometer.

4.3 Results and discussion

A general approach employing CPBs as templates to fabricate CdSe nanowires includes three steps as shown in Scheme 4-1, similar as we reported before. In the first step (a to b), the carboxylic groups in the poly(acrylic acid) (PAA) core were neutralized by NaOH. Via ion exchange, Cd^{2+} ions replace Na^{+} ions (step 2: b to c), forming a polychelate.[44] The purified polychelate solution reacted with H_2Se gas to generate CdSe nanoparticles aligned within the cylindrical core (step 3: c to d). Simultaneously, the PAA core resumes the initial chemical structure (i.e., carboxylic acid functions) which enables the double-loading process by repeating steps 1 to 3.

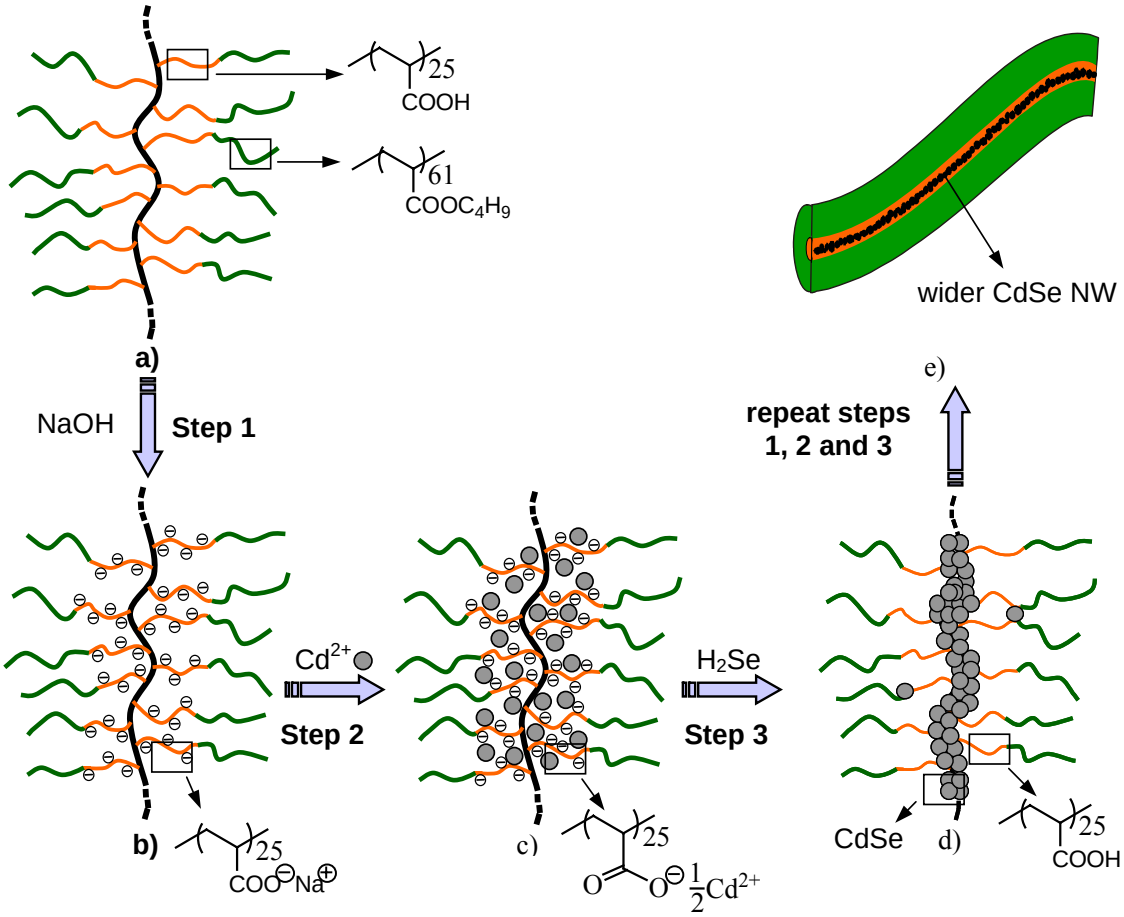

Scheme 4-1. Illustration of the CdSe nanowire synthesis inside the CPB. a) the core-shell CPB, $[AA_{25}\text{-}b\text{-}nBA_{61}]_{1500}$; b) neutralized polymer brush with poly(sodium acrylate) core; c) polychelate of the polymer brush and Cd^{2+}; d) 1st loaded hybrid of the CPB and CdSe nanowires; e) the 2nd loaded hybrid of the CPB and CdSe nanowires.

The CPB $[AA_{25}\text{-}b\text{-}nBA_{61}]_{1500}$ as a unimolecular template with a low length polydispersity (L_w/L_n = 1.08),[42] as visualized by AFM in Fig. 4-1A, defines both the dimension and size distribution of the CdSe nanowires within the core region. The wormlike cylinders are distinctly visible in the AFM height image, whereas the core-shell structure is seen in the phase image. After the uptake of Cd^{2+} the characteristic "pearl necklace"[45] morphology was identified by the AFM image in Fig. 4-1B due to the "cross-linking" of side chains initiated by the coordination between divalent Cd^{2+} ions and monovalent carboxylate groups from different side chains.[41] To elaborate this change, the longitudinal height profile of single brush is analyzed in Fig. 4-1, in which the CPB (Fig. 4-1C) possesses a relatively lower height and smoother contour in contrast to the polychelate (Fig. 4-1D). The results from the height profile analysis, as summarized in Table 4-1, ensures that the chelation of Cd^{2+} ions and carboxylic groups remarkably increases the average height from 0.71 nm of the CPB to 2.40 nm of the polychelate, and the standard deviation reflecting the inhomogeneity in the brush height shifts from 0.20 of the CPB to 1.00 of the polychelate.

Table 4-1. Height profile analysis of single brushes in AFM images of A) the core-shell CPB, $[AA_{25}\text{-}b\text{-}nBA_{61}]_{1500}$; B) the polychelate; C) the 1st loaded hybrid; D) the hybrid polychelate; and E) the double-loaded hybrid.

Sample	Average height /nm	Standard deviation /nm
A	0.71	0.20
B	2.40	1.00
C	2.00	0.64
D	3.30	0.90
E	2.66	1.44

Transmission electron microscopy (TEM) does not give a clear image of the pure polymer brushes due to the rather low contrast. The chelation with Cd^{2+} enhances the visibility. Fig. 4-2 shows wormlike dark grains (7~13 nm) oriented within the CPB. An enlarged view (on the right) portrays a string of dark dots, which supports the "pearl necklace" structure of the polychelate verified by AFM in Fig. 4-1B. The "pearl necklace" structure vanishes after the reaction of H_2Se

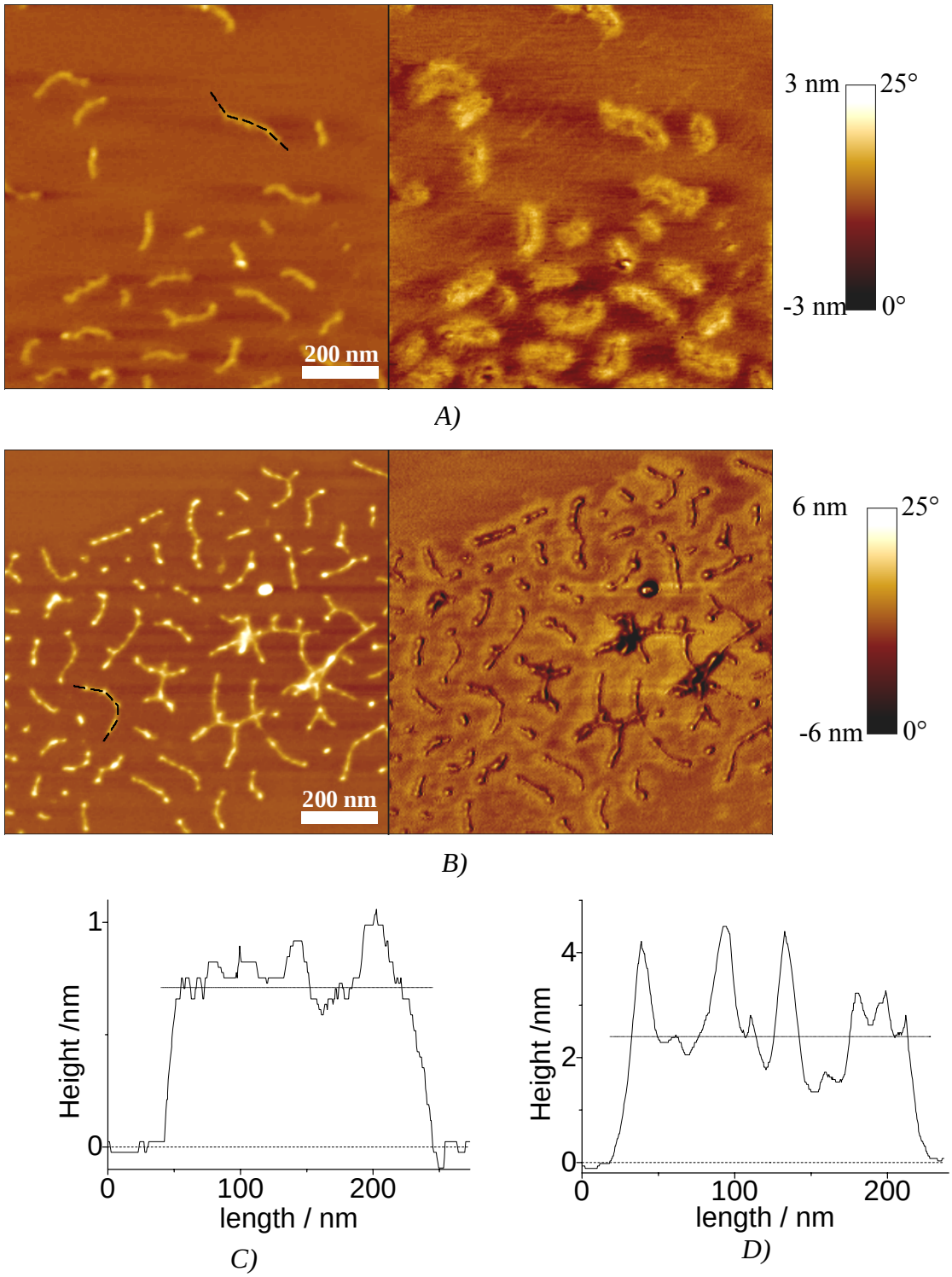

Figure 4-1. Tapping mode AFM images (left, height; right, phase) of the core-shell CPB [AA_{25}-*b*-*n*BA_{61}]$_{1500}$ (A) and the polychelate of the CPB and Cd^{2+} ions (B). Their corresponding height profiles (single brush marked by black dash line) are shown in C) and D). (average height is indicated by the dashed line)

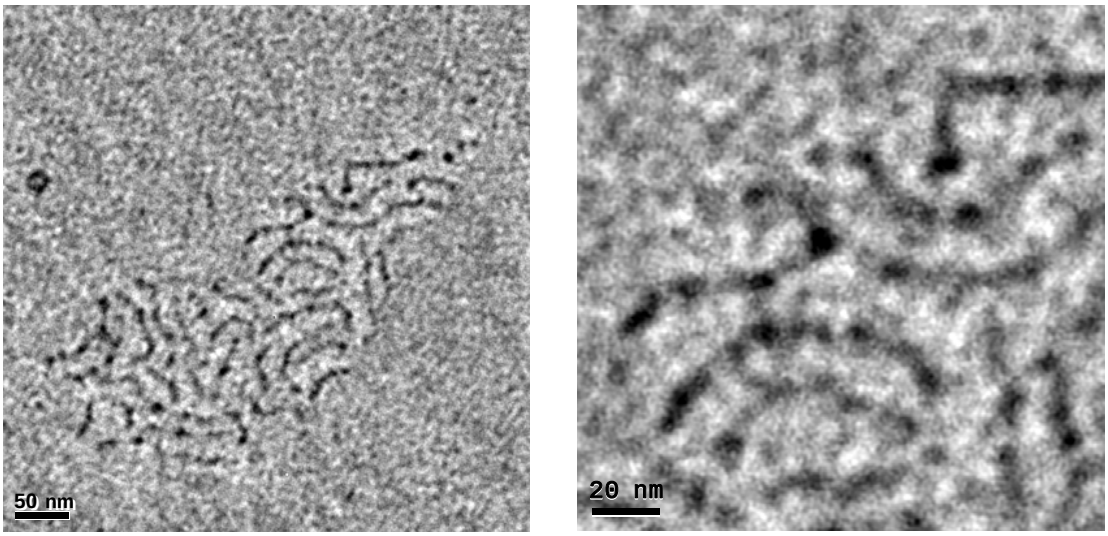

Figure 4-2. Nonstained TEM images of the polychelate of the core-shell CPB $[AA_{25}$-*b*-*n*$BA_{61}]_{1500}$ and Cd^{2+} ions. The right image is the enlarged view of the left one.

with Cd^{2+}, forming the hybrid, as shown in the AFM image in Fig. 4-3A. The reason is that although the coordinated Cd^{2+} ions in the polychelate are confined separately, in-situ produced CdSe can diffuse, form nuclei and grow into a continuous phase due to the forfeit of the strong ionic bond between Cd^{2+} and the carboxylic acid groups. As shown in Table 4-1, the average height of the polychelates (2.40 nm) retracts to 2.00 nm of the hybrid brush, but still 1.30 nm higher than that of the pure CPB. Meanwhile the standard deviation of the hybrid decreases from 1.00 of the polychelate to 0.64, but remains higher than 0.20 of the CPB. Thus, the hybrid molecules are relatively "flatter" than the polychelate, but rougher than the CPB. Since the carboxylic acid coordination sites after the formation of CdSe nanowires were resumed, the reloading of CdSe nanoparticles was subsequently carried out in the same manner. The hybrid polychelate, named after the combination of the hybrid and the coordinated Cd^{2+} ions exhibits again the "pearl-necklace" morphology in the AFM images in Fig. 4-3B, although not as obvious as that in the polychelate. Its height average (see Table 4-1) increases from 2.0 nm of the hybrid, to 3.3 nm, and is 0.9 nm higher than that of the polychelate, because of the overlapped size-expansion effects from the formed CdSe nanowires and the crosslinking caused by newly introduced Cd^{2+}. The standard deviation of the hybrid polychelate increases to 0.90, a little lower

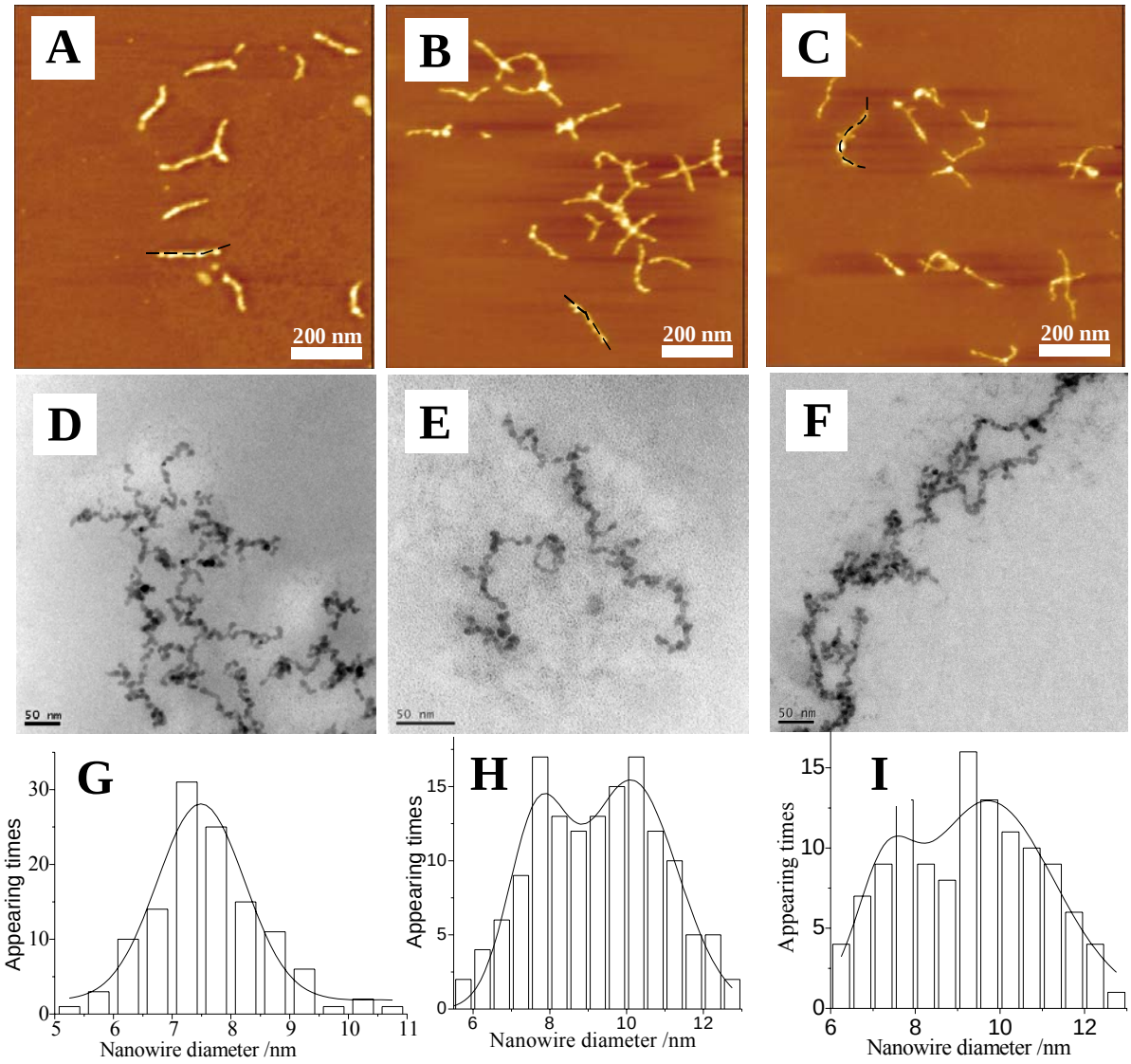

Figure 4-3. A-C) Tapping mode AFM height images of A) the 1st loaded hybrid of the core-shell CPB $[AA_{25}\text{-}b\text{-}nBA_{61}]_{1500}$ and CdSe nanowires (Z range: 6 nm), B) the hybrid polychelate of the 1st loaded hybrid and Cd^{2+} ions (Z range: 12 nm), and C) the double-loaded hybrid of the polymer brush and CdSe nanowires (Z range: 12 nm). The single polymer brushes/hybrids in each image marked with a black dash line were used for the height analysis in Table 4-1. E-G) are the corresponding non-stained TEM images. G-I) are the corresponding statistic width distribution of the nanowires in the above TEM images.

that 1.00 of the polychelate, since the deformation caused by the coordination is partially prevented by the solid CdSe nanowire inside the brush core. After reaction of the reloaded Cd^{2+}

with H_2Se, the double-loaded hybrid shrinks to 2.66 nm, higher than 2.00 of the first loaded one, which insinuates a further size expansion of the polymer brush as a result of the double-loading. Yet it unexpectedly shows the highest standard deviation, which may indicate that the new CdSe nanoparticles render the shape of the nanowires more irregular.

Fig. 4-3D shows a representative TEM image of the 1st loaded hybrid of the polymer brush and the CdSe nanowires. In contrast to the polychelate in Fig. 4-2, a higher contrast was attained due to the formation of CdSe nanoparticles. To characterize the width of the CdSe nanowires, a statistical calculation was performed by measuring the nanowire width at different locations away from the distorted joins. The result in Fig. 4-3G stands for a quasi-Gaussian monomodal distribution curve where the widths range from 5 to 11 nm with an average value of 7.6 nm. After reloading Cd^{2+} ions into the hybrid to form the hybrid polychelate, the nanowires show big "knobs" along their backbone, as shown in Fig. 4-3E. As we have discussed above, in the polychelate Cd^{2+} ions coordinate with the carboxylic groups on different side chains to form the separated necklace-like spheres; in the case of the hybrid polychelates, the already existing CdSe nanowire connects the isolated necklace-like spheres after the reloading of Cd^{2+} ions. In the corresponding width distribution curve (Fig. 4-3H), the hybrid polychelates show a bimodal distribution. The first peak between 7 and 8 nm stands at the same position as the peak in Fig. 4-3G, while the second peak appears around 10 nm standing for the protrusion due to the spheres along the nanowires. The reloading of CdSe nanoparticles to CdSe nanowires is completed by bubbling H_2Se to the hybrid polychelate solution. Fig. 4-3F shows a TEM image of the double-loaded hybrid, in which the linear CdSe nanowires are clear to see. The statistic width calculation in Fig. 4-3I demonstrates a bimodal quasi-Gaussian distribution and an average of 9.3 nm similar to that of the hybrid polychelate, which reveals that the newly formed CdSe nanoparticles in the spheres of the hybrid polychelate almost directly attached to the nearby CdSe nanowire surface.

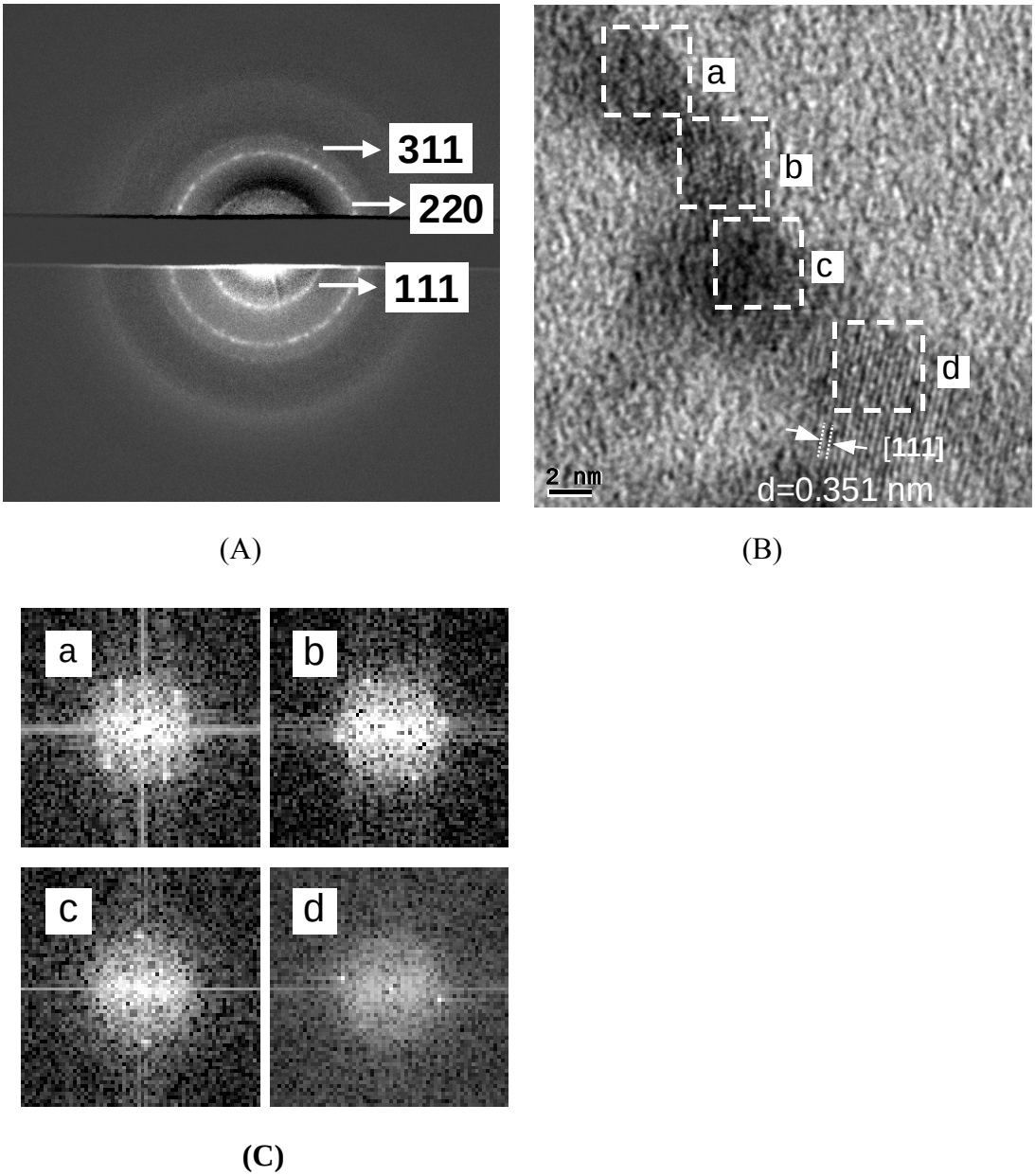

Figure 4-4. A) SAED pattern of the 1st loaded hybrid of the core-shell CPB $[AA_{25}$-*b*-*n*$BA_{61}]_{1500}$ and CdSe nanowires (image subtracted by the blank grid), B) HRTEM image of the crystals aligned along the CdSe nanowires, and C) Fast Fourier Transform (FFT) pattern corresponding to the white squares in HRTEM image in B).

In order to understand the crystalline structure, selected area electron diffraction (SAED) was applied to the 1st loaded hybrid, the hybrid polychelates and the double-loaded hybrid, all of

which show a polycrystalline behavior. The SAED rings of the 1st loaded hybrid were presented in Fig. 4-4A. It supports the presence of polycrystalline particles, as often appearing in template-directed methods. The d spacings calculated from the rings are 3.51, 2.15, and 1.83 Å, which correspond to the lattice planes [111], [220], and [311] of the cubic (zinc blende) phase of CdSe. (Joint Committee on Powder Diffraction Standards file No. 19-0191). Since the SAED pattern represents the collective behavior of the crystallites, the intrinsic structure of the CdSe nanowire is further examined by high resolution TEM (HRTEM) in Fig. 4-4B. The lattice plane with an interplane distance of 0.351 nm corresponding to the [111] plane was directly observable in square d. The same lattice planes in other areas of the nanowires (squares a, b and c) are somewhat smeared but can be detected by the FFT pattern, as shown in Fig. 4-4C. Every two symmetric and opposite white points define a line, which is perpendicular to the lattice plane. In this way, the differently oriented crystals were found along the nanowires, indicating that the polycrystallinity of the hybrid material actually results from the intrinsic polycrystallinity of each nanowire itself.

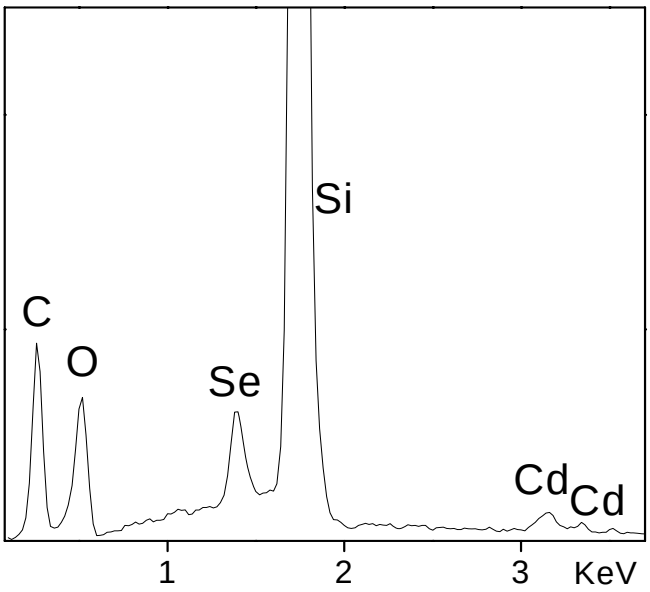

Figure 4-5. EDX spectrum of the double-loaded hybrid of the polymer brush and CdSe nanowires.

Table 4-2. EDX results of the amount of Cd and Se in the1st loaded and double-loaded hybrids.

Sample	1st loading	2nd loading
Cd / Se	1.18	1.08
CdSe	21.9 ± 5.9 %	38.2 ± 7.2 %

Elemental analysis of the hybrids was achieved by the energy-dispersive X-ray (EDX) analysis of a scanning electron micrograph. Fig. 4-5 shows the EDX spectrum of the 2nd loaded hybrid of the polymer brush and CdSe nanowires on a silicon wafer, which confirms the presence of cadmium and selenium. The collected EDX results of the two hybrids in Table 2 present the ratios of Cd to Se close to the theoretical value. If the carbon content is transferred to the corresponding amount of the polymer brush and the sum of the Cd and Se content as the approximate loaded CdSe nanowires, 21.9 ± 5.9% content of CdSe for the first loaded hybrid and 38.2 ± 7.2% for the second one were calculated. Since there is a high deviation due to the weak signals in EDX analysis, in order to verify the successful introduction of more CdSe nanoparticles during the double-loading process, UV-vis spectroscopy measurements were further performed.

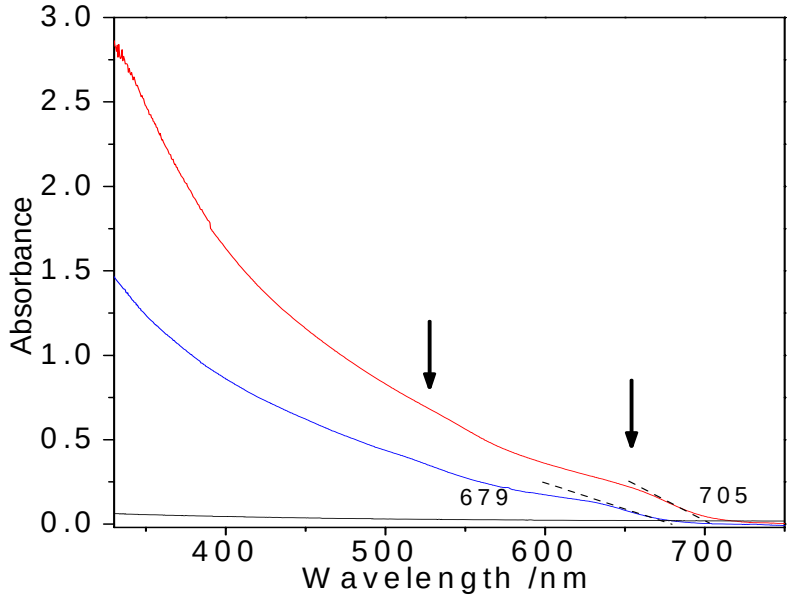

Figure 4-6. UV–vis spectra of the polychelate (black line), 1st loaded hybrid (blue line) and double-loaded hybrid (red line), the concentration for all is 0.4 g/L (polymer content).

In Fig. 4-6, the weak UV-vis absorption of the polychelate supports that the strong absorption of the two hybrids comes exclusively from the CdSe nanowires. Apparently, the double-loaded hybrid shows stronger absorption than the 1st loaded hybrid, which confirms the increase of the CdSe amount during the double-loading process. It is known that bulk CdSe starts to absorb at about 716 nm.[15] The 1st loaded hybrid shows an absorption onset at 679 nm and the double-loaded one at 705 nm. Both display a blue-shift relative to that of bulk CdSe, indicating the existence of the quantized transition. According to Murray's empirical curve,[15] the threshold corresponds to CdSe nanoparticles with a rough size of 7 nm and 10 nm, respectively, which proves the growth of CdSe nanowires by width during the double-loading process. These values are close to the nanowire average width values of 7.6 and 9.3 nm as obtained by TEM, which indicates that the quantized effect of the nanowire detected according to the blue-shift of the absorption edge most probably arises from the width of the nanowires. Besides, a weak transition for both hybrids at around 550 nm is observed, corresponding to a nanoparticle size of roughly 3nm, which becomes more obvious at higher concentration. The existence of multi-absorption transitions confirms the TEM analysis because the nanowires are constructed by a linear interconnection of differently sized CdSe nanocrystals, which are probably a fusion of two or more even smaller nanoparticles during the nanowire formation process. AFM images support this because the height of the CdSe nanowires is limited to the maximum height of the hybrid molecules in Table 4-1. The first loaded hybrid showed a maximum height of 3.38 nm and the second one of 7.30 nm, both are smaller than the width of the nanowires and the nanoparticle size deduced from the UV threshold absorptions. This, in essence, leads to the flat shape of the nanowires, which are around 2 nm high and 7.5 nm wide for the first loaded hybrid, and 2.66 nm high and 10.5 nm wide for the second one. Besides, partial CdSe nanoparticles which were in situ formed in the polymer brush core and failed to reach the CdSe nanowires also contribute to the absorption at higher energies.

The photoluminescence (PL) behavior of both hybrids shows an unusual dependence on the excitation wavelength For example, a lower excitation wavelength results in a blue-shifted wide emission. This can be understood, since the whole nanowire is created by the alignment and connection of different sized and random orientated CdSe nanocrystals, thus a lower excitation wavelength is able to excite smaller sized nanocrystals. Moreover the aligned CdSe nanocrystals are more similar to the close-packed quantum dots rather than the usual isolated nanocrystals

embedded in polymer matrix. In such case, the electronic energy transfer between the small and large quantum dots is involved through the dipole-dipole interdot interactions.[46-51] Furthermore, very recently the PL intensity heterogeneity along the length of individual nanowires due to all kinds of disorder like surface/interface roughness and so on, was also reported by Kuno et al[52], which suggests that the photoluminescence of the nanowires is governed not only by the building block like nanocrystals, but also by the disorder caused fluctuations of the exciton potential along the nanowire.

4.4 Conclusions

CdSe nanowires were successfully fabricated using well-defined core-shell amphiphilic cylindrical polymer brushes with PAA core and P*n*BA shell as unimolecular templates under mild solution conditions. The products were characterized by AFM, TEM, EDX, UV-Vis and photoluminescence spectroscopy. A double-loading of CdSe nanoparticles into the polymer brush core was carried out and its influence was examined in detail. The double-loading presents the unique advantage of the polymer brushes as both nanoreactor and template. The hybrids from both loadings showed good solubility and stability (one year without any precipitation) in a concentration below 0.4 g/L. The single CdSe nanowires protected by the polymer brush shell can be handled in solution and serve as a candidate for electric nanoscale devices.

Acknowledgement. This work was financially supported by Deutsche Forschungsgemeinschaft (DFG) within Priority Program SPP 1165 (Mu896/22-2). We thank Ms. Violetta Olszowka and Mr. Markus Hund due to the help in AFM analysis.

4.5 References

1. Lieber, C. M. *MRS Bulletin* **2003,** 28, (7), 486-491.
2. Yang, P. *MRS Bulletin* **2005,** 30, (2), 85-91.
3. Teo, B. K.; Sun, X. H.; Hung, T. F.; Meng, X. M.; Wong, N. B.; Lee, S. T. *Nano Lett.* **2003,** 3, (12), 1735-1737.
4. X. Duan, C. M. L. *Adv. Mater.* **2000,** 12, (4), 298-302.
5. Li, Q.; Gong, X.; Wang, C.; Wang, J.; Ip, K.; Hark, S. *Adv. Mater.* **2004,** 16, (16), 1436-1440.
6. Hu, J.; Bando, Y.; Liu, Z.; Sekiguchi, T.; Golberg, D.; Zhan, J. *J. Am. Chem. Soc.* **2003,** 125, (37), 11306-11313.
7. Kim, H.-M.; Cho, Y.-H.; Lee, H.; Kim, S. I.; Ryu, S. R.; Kim, D. Y.; Kang, T. W.; Chung, K. S. *Nano Lett.* **2004,** 4, (6), 1059-1062.
8. Johnson, J. C.; Choi, H.-J.; Knutsen, K. P.; Schaller, R. D.; Yang, P.; Saykally, R. J. *Nat. Mater.* **2002,** 1, (2), 106-110.
9. Greytak, A. B.; Barrelet, C. J.; Li, Y.; Lieber, C. M. *Appl. Phys. Lett.* **2005,** 87, (15), 151103/1-3.
10. Huang, Y.; Duan, X.; Lieber, C. M. *Small* **2005,** 1, (1), 142-147.
11. Sirbuly, D. J.; Law, M.; Yan, H.; Yang, P. *J. Phys. Chem. B* **2005,** 109, (32), 15190-15213.
12. Holmes, J. D.; Johnston, K. P.; Doty, R. C.; Korgel, B. A. *Science* **2000,** 287, (5457), 1471-1473.
13. Wang, Z. L. *Adv. Mater.* **2003,** 15, (5), 432-436.
14. Li, S. Y.; Lee, C. Y.; Lin, P.; Tseng, T. Y. *J. Vac. Sci. Technol. B Microelectron Nanometer Struct-Process Meas. Phenom.* **2006,** 24, (1), 147-151.
15. Murray, C. B.; Norris, D. J.; Bawendi, M. G. *J. Am. Chem. Soc.* **1993,** 115, (19), 8706-15.
16. Peng, X.; Schlamp, M. C.; Kadavanich, A. V.; Alivisatos, A. P. *J. Am. Chem. Soc.* **1997,** 119, (30), 7019-7029.
17. Landes, C.; Burda, C.; Braun, M.; El-Sayed, M. A. *J. Phys. Chem. B* **2001,** 105, (15), 2981-2986.
18. Xu, D.; Shi, X.; Guo, G.; Gui, L.; Tang, Y. *J. Phys. Chem. B* **2000,** 104, (21), 5061-5063.

19. Peng, X. S.; Zhang, J.; Wang, X. F.; Wang, Y. W.; Zhao, L. X.; Meng, G. W.; Zhang, L. D. *Chem. Phys. Lett.* **2001,** 343, (5,6), 470-474.
20. Rao, C. N. R.; Govindaraj, A.; Deepak, F. L.; Gunari, N. A.; Nath, M. *Appl. Phys. Lett.* **2001,** 78, (13), 1853-1855.
21. Khandelwal, A.; Jena, D.; Grebinski, J. W.; Hull, K. L.; Kuno, M. K. *J. Electron. Mater.* **2006,** 35, (1), 170-172.
22. Grebinski, J. W.; Richter, K. L.; Zhang, J.; Kosel, T. H.; Kuno, M. *J. Phys. Chem. B* **2004,** 108, (28), 9745-9751.
23. Grebinski, J. W.; Hull, K. L.; Zhang, J.; Kosel, T. H.; Kuno, M. *Chem. Mater.* **2004,** 16, (25), 5260-5272.
24. Venugopal, R.; Lin, P. I.; Liu, C. C.; Chen, Y. T. *J. Am. Chem. Soc.* **2005,** 127, (32), 11262-11268.
25. Jeong, U.; Xia, Y.; Yin, Y. *Chem. Phys. Lett.* **2005,** 416, (4-6), 246-250.
26. Wang, Z. Y.; Zhang, L. D.; Ye, C. H.; Fang, X. S.; Xiao, Z. D.; Kong, M. G. *J. Nanosci. Nanotechnol.* **2005,** 5, (12), 2088-2092.
27. Ma, C.; Wang, Z. L. *Adv. Mater.* **2005,** 17, (21), 2635-2639.
28. Thurn-Albrecht, T.; Schotter, J.; Kastle, G. A.; Emley, N.; Shibauchi, T.; Krusin-Elbaum, L.; Guarini, K.; Black, C. T.; Tuominen, M. T.; Russell, T. P. *Science* **2000,** 290, (5499), 2126-2129.
29. Cornelissen, J. J. L. M.; Van Heerbeek, R.; Kamer, P. C. J.; Reek, J. N. H.; Sommerdijk, N. A. J. M.; Nolte, R. J. M. *Adv. Mater.* **2002,** 14, (7), 489-492.
30. Cavalli, S.; Popescu, D. C.; Tellers, E. E.; Vos, M. R. J.; Pichon, B. P.; Overhand, M.; Rapaport, H.; Sommerdijk, N. A. J. M.; Kros, A. *Angew. Chem. Int. Ed.* **2006,** 45, (5), 739-744.
31. Muniz, G.; Banerjee, I. A.; Yu, L.; Djalali, R.; Chen, Y.-f.; Matsui, H. *PMSE Preprints* **2005,** 92, 590-591.
32. Djalali, R.; Chen, Y.-F.; Matsui, H. *J. Am. Chem. Soc.* **2002,** 124, (46), 13660-13661.
33. Adelung, R.; Aktas, O. C.; Franc, J.; Biswas, A.; Kunz, R.; Elbahri, M.; Kanzow, J.; Schuermann, U.; Faupel, F. *Nat. Mater.* **2004,** 3, (6), 375-379.
34. Yang, Q.; Tang, K.; Wang, C.; Qian, Y.; Zhang, S. *J. Phys. Chem. B* **2002,** 106, (36), 9227-9230.

35. Zhan, J.; Yang, X.; Wang, D.; Li, S.; Xie, Y.; Xia, Y.; Qian, Y. *Adv. Mater.* **2000,** 12, (18), 1348-1357.

36. Xie, Y.; Qiao, Z. P.; Chen, M.; Liu, X. M.; Qian, Y. T. *Adv. Mater.* **1999,** 11, (18), 1512-1515.

37. Niu, H.; Zhang, L.; Gao, M.; Chen, Y. *Langmuir* **2005,** 21, (9), 4205-4210.

38. Yang, C.-S.; Awschalom, D. D.; Stucky, G. D. *Chem. Mater.* **2002,** 14, (3), 1277-1284.

39. Zhang, X.-D.; Jin, J.; Yang, W.-S.; Fu, L.-S.; Zhang, H.-J.; Li, T.-J. *Huaxue Xuebao* **2002,** 60, (3), 532-535.

40. Tian, M.; Li, P.-c.; Yang, W.-s. *Fenzi Kexue Xuebao* **2002,** 18, (2), 75-78.

41. Zhang, M.; Drechsler, M.; Müller, A. H. E. *Chem. Mater.* **2004,** 16, (3), 537-543.

42. Zhang, M.; Breiner, T.; Mori, H.; Müller, A. H. E. *Polymer* **2003,** 44, (5), 1449-1458.

43. Deng, Z.; Cao, L.; Tang, F.; Zou, B. *J. Phys. Chem. B* **2005,** 109, (35), 16671-16675.

44. Clay, R. T.; Cohen, R. E. *Supramol. Sci.* **1998,** 5, (1-2), 41-48.

45. Zhang, M.; Teissier, P.; Krekhova, M.; Cabuil, V.; Müller, A. H. E. *Prog. in Colloid Polym. Sci.* **2004,** 126, 35-39.

46. Achermann, M.; Petruska, M. A.; Crooker, S. A.; Klimov, V. I. *J. Phys. Chem. B* **2003,** 107, (50), 13782-13787.

47. Artemyev, M. V.; Woggon, U.; Jaschinski, H.; Gurinovich, L. I.; Gaponenko, S. V. *J. Phys. Chem. B* **2000,** 104, (49), 11617-11621.

48. Artemyev, M. V.; Bibik, A. I.; Gurinovich, L. I.; Gaponenko, S. V.; Woggon, U. *Phys. Rev. B Condens. Matter* **1999,** 60, (3), 1504-1506.

49. Kagan, C. R.; Murray, C. B.; Nirmal, M.; Bawendi, M. G. *Phys. Rev. Lett.* **1996,** 76, (9), 1517-20.

50. Kagan, C. R.; Murray, C. B.; Bawendi, M. G. *Phys. Rev. B Condens. Matter* **1996,** 54, (12), 8633-8643.

51. Scholes, G. D. *Ann. Rev. Phys. Chem.* **2003,** 54, 57-87.

52. Hull, K.; Grebinski, J.; Protasenko, V.; Kuno, M. Abstracts of Papers, 229th ACS National Meeting, San Diego, CA, United States, March 13-17, **2005**, PHYS-227.

Chapter 5

Template-directed Synthesis of Titania Hybrid Nanowires within Core-Shell Cylindrical Polymer Brushes

Abstract

Well-defined core-shell bishydrophilic cylindrical polymer brushes (CPBs) with a poly(2-hydroxyethyl methacrylate) (PHEMA) core and a poly(oligo(ethylene glycol) methacrylate) (POEGMA) shell were synthesized via combination of anionic polymerization and atom transfer radical polymerization. They were used as unimolecular cylindrical template for the controlled fabrication of linear assemblies of titania nanoparticles, because PHEMA can coordinate with the titanium ions via a transalcoholysis reaction and attach them to the cylindrical core. The formed titania-CPB hybrid nanowires are amorphous and soluble in organic solvents as well as water. A phase transition from amorphous titania to anatase titania was found by refluxing the hybrid nanowire solution for 5 days in a mixture of water/dioxane (vol. ratio = 1/3). They could also serve as in-situ template for the pyrolytic formation of inorganic crystalline titania nanowires at 550 °C.

* The results of this chapter have been submitted to *Chemistry of Materials* as:

"Template-directed Synthesis of Titania Hybrid Nanowires within Core-Shell Cylindrical Polymer Brushes"

by Jiayin Yuan, Yan Lu, Felix Schacher, Thomas Lunkenbein, Stephan Weiss, Holger Schmalz and Axel H. E. Müller*

5.1 Introduction

Cylindrical polymer brushes (CPBs), which possess linear side chains or high-generation dendritic side groups densely grafted from a linear main chain, have attracted considerable experimental and theoretical attention over the past decade, owing to the possibility of forming extended chain conformations and their peculiar solution and bulk properties.[1, 2] Among various structures, the core-shell CPBs with diblock copolymer side chains are of great interest. They are architecturally very attractive to both polymer and material scientists. When the diblock copolymer side chains include block segment combinations of soft-hard, hydrophilic-hydrophobic and crystalline-amorphous, the core-shell CPBs resemble intramolecular phase-separated cylindrical micelles.[3-8] Practically they have been used as unimolecular template for the fabrication of one-dimensional (1D) inorganic nanostructures, such as gold[9], CdS[10], CdSe[11], SiO_2[12] and γ-Fe_2O_3[13] nanowires. Generally, the dimension of the incorporated 1D inorganic nanostructures can be strictly controlled by the CPBs. For example, the diameter depends on the length of the block in the CPB core, and the length is largely determined by the degree of the polymerization (DP) of the backbone. Furthermore, the solubility and biocompatibility of the inorganic nanowires can be achieved by the design of the shell block.

Titanium dioxide (titania) with a controlled morphology has tremendous practical applications in many different fields such as photocatalysis, gas sensors, dye-sensitized solar cells, optics, etc.[14-16] The functions of these materials are dominated by interfacial processes, where the nanoscale titania structures are of huge significance. Numerous reports have described the synthesis of titania nanomaterials with different morphologies, templated by small surfactants or amphiphilic block copolymers.[17, 18] However, most of the conventional micellar structures from the self-assembly of surfactant or block polymer are dynamically stable and could collapse upon a small disturbance in the external environments such as solvent, temperature, concentration, or pH.[19] Herein, we demonstrate that we can use core-shell CPBs as robust tools for the controlled fabrication of linear assemblies of titania nanoparticles, forming a kind of titania-CPB hybrid nanowires. They serve as in situ template for the pyrolytic formation of inorganic crystalline titania nanowires.

5. 2 Experimental section

5.2.1 Synthesis of titania-CPB hybrid nanowires and inorganic titania nanowires

All chemicals were of analytical grade and used as received without further purifications, except that 2-(trimethysilyloxy)ethyl methacrylate (TMS-HEMA, >96%, Aldrich) and oligo(ethylene glycol) methacrylate (OEGMA, M_n ~ 475 g mol^{-1}, 8.5 EO units, Aldrich) were filtered over an alumina column shortly before polymerization.

Core-shell CPB [$HEMA_{85}$-*b*-$OEGMA_{200}$]$_{3200}$ The typical synthesis of the CPBs via the combination of anionic polymerization of the backbone and atom transfer radical polymerization (ATRP) of the side chains was reported by us earlier.[3] The DP of the backbone was determined to be 3,200 via characterizing the poly(2-bromoisobutyryloxyethyl methacrylate) (PBIEM) polyinitiator by gel permeation chromatography (GPC) (eluent: tetrahydrofuran with 4% tetra-*n*-butylammonium bromide, standard: polystyrene) and static light scattering (SLS). The DP of side chains was calculated from monomer conversion in polymerization by proton nuclear magnetic resonance (^{1}H-NMR). All ATRP polymerizations were conducted in benzene at 60 °C and the reaction mixtures were purified under nitrogen via ultrafiltration using benzene as the eluent.

For the cleavage of the trimethysilyl moieties, 1.05 g of the core-shell [TMS-$HEMA_{85}$-*b*-$OEGMA_{200}$]$_{3200}$ CPB in 58 ml of benzene was dialyzed against dioxane for one week. Then the solution was diluted to 500 ml with dioxane. 80 ml of water and 2 ml of 32 % aqueous HCl solution were added under strong stirring. After 2 days, the solution was purified by ultrafiltration using dioxane as the eluent.

Titania-CPB hybrid nanowires [($HEMA_{85}$+*n*TiO_2)-*b*-$OEGMA_{200}$]$_{3,200}$ To introduce the titanium precursor, 1.3 g of $Ti(OC_4H_9)_4$ was added to 0.50 g of core-shell CPB [$HEMA_{85}$-*b*-$OEGMA_{200}$]$_{3200}$ in 300 ml dioxane under vigorous stirring. After 1 day, the solution was purified by ultrafiltration using dioxane as the eluent under nitrogen. The formation of titania-CPB hybrid nanowires was conducted simply by adding 25 vol. % of water in the Ti^{4+}-doped CPB hybrid solution in dioxane. The solution was kept stirring for 5 days. To improve the crystallinity, refluxing at 100 °C for 5 days was performed. The final products were purified by ultrafultration using dioxane as the eluent.

Inorganic titania nanowires The bulk samples were prepared by removing the dioxane solvent from the titania-CPB hybrid nanowire solution and dried by high vacuum for one day.

The samples on silicon wafer or mica was prepared by dip-coating from the titania-CPB hybrid nanowire solution in dioxane and dried in air. Both samples were then heated to 550 °C at a heating rate of 10 K/min and then kept at 550 °C for half an hour in the presence of air.

5.2.2 Characterization methods

Atomic force microscopy (AFM) images were recorded on a Digital Instruments Dimension 3100 microscope operated in tapping mode. The samples were prepared by dip-coating from dilute solutions (0.02 g/L) of the polymer brushes or hybrid nanowires in dioxane onto freshly cleaved mica to form a monomolecular film.

Thermogravimetric analysis (TGA) measurements were carried out on a Mettler Toledo TGA/SDTA 851. The measurements were performed under airflow of 50 ml/min with heating from 30 °C to 550 °C (rate: 10 K /min), and then kept at 550 °C for half an hour in the presence of air. Before TGA measurements, samples were collected from the solution with a rotary evaporator and dried in vacuum oven at least one day.

Transmission electron microscopy (TEM) images were taken on a Zeiss EM EF-TEM instrument operated at 200 kV. A 5μL droplet of a dilute solution (0.02 g/L) in dioxane was dropped onto a copper grid (200 mesh) coated with carbon film, followed by drying at room temperature for a short time.

Scanning electron microscopy (SEM) and the *energy dispersive X-ray* (EDX) analysis was performed using a Zeiss 1530 Gemini instrument equipped with a field emission cathode with a lateral resolution of approximately 2 nm. The sample was measured after sputtering a thin layer (1~2 nm) of Pt.

The *X-ray diffraction* (XRD) measurement was performed at 25 °C on a Panalytical XPERT-PRO diffractometer in reflection mode using CuK_{α} radiation.

Dynamic light scattering (DLS) measurements were performed on an ALV DLS/SLS-SP 5022F compact goniometer system with an ALV 5000/E correlator and a He-Ne laser. CONTIN analysis of the obtained autocorrelation functions was carried out.

5.3 Results and discussion

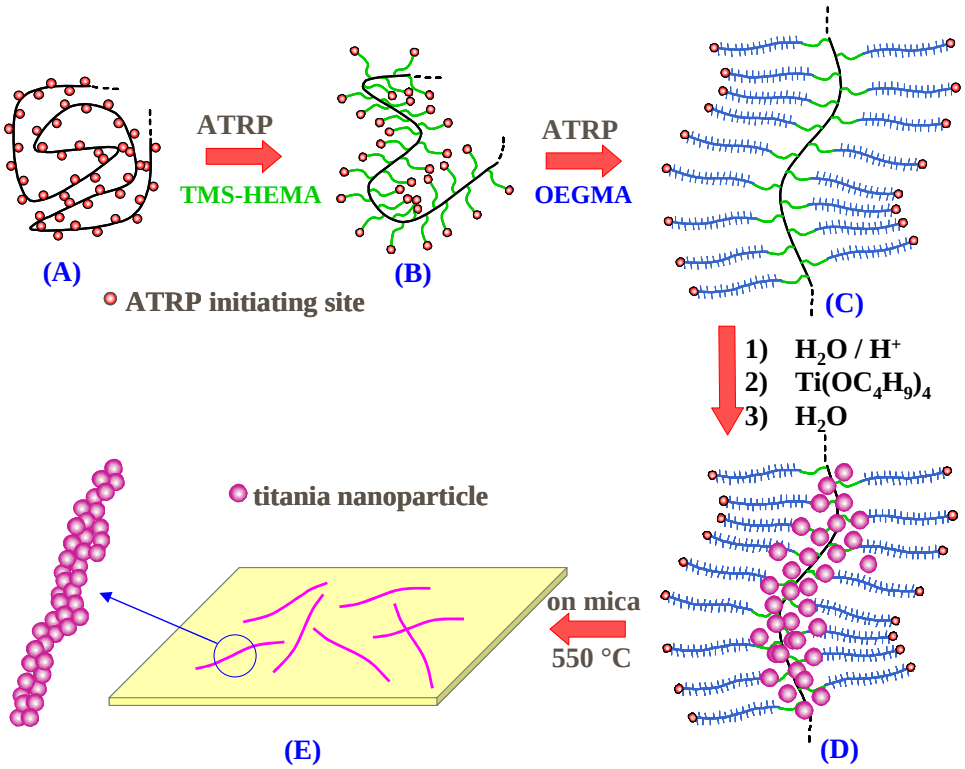

Figure 5-1. Synthesis of titania-CPB hybrid nanowires and inorganic titania nanowires. A), ATRP polyinitiator PBIEM with DP =3,200; B), CPB with side chains of 85 TMS-HEMA units; C), core–shell CPB with an additional 200 OEGMA units; D), titania-CPB hybrid nanowires; E), inorganic titania nanowires after pyrolysis on mica. For details, see Fig. 5-2.

As an example illustrated in Figs 1 and 2, we first synthesized a polyinitiator, poly(2-bromoisobutyryloxyethyl methacrylate) (PBIEM), with 3,200 initiating sites by anionic polymerization of 2-(trimethysilyloxy)ethyl methacrylate (TMS-HEMA) followed by an ether cleavage and esterification with α-bromoisobutyryl bromide. This was then used to grow diblock copolymer side chains via sequential ATRP of TMS-HEMA (85 units) and oligo(ethylene glycol) methacrylate (OEGMA) (200 units), leading to a core–shell superstructured CPB, [TMS-$HEMA_{85}$-*b*-$OEGMA_{200}$]$_{3,200}$. The poly(TMS-HEMA) (PTMS-HEMA) block in the core was then hydrolyzed into polyHEMA (PHEMA) via the removal of the trimethoxysilyl (TMS) moieties under acidic conditions. Through complexation, the PHMEA core could locally confine the titania precursor, $Ti(OC_4H_9)_4$, into a 1D manner. Via hydrolysis, wormlike linear assemblies of

titania nanoparticles were formed within the core-shell CPB, leading to soluble titania-CPB hybrid nanowires. At the end, uniform crystalline titania nanowires were obtained by the simultaneous removal of the template via pyrolysis. Because of the living/controlled character of anionic polymerization and ATRP, the length as well as the diameter of the brush core, which directly determines the size of the titania nanowire, are well-defined.

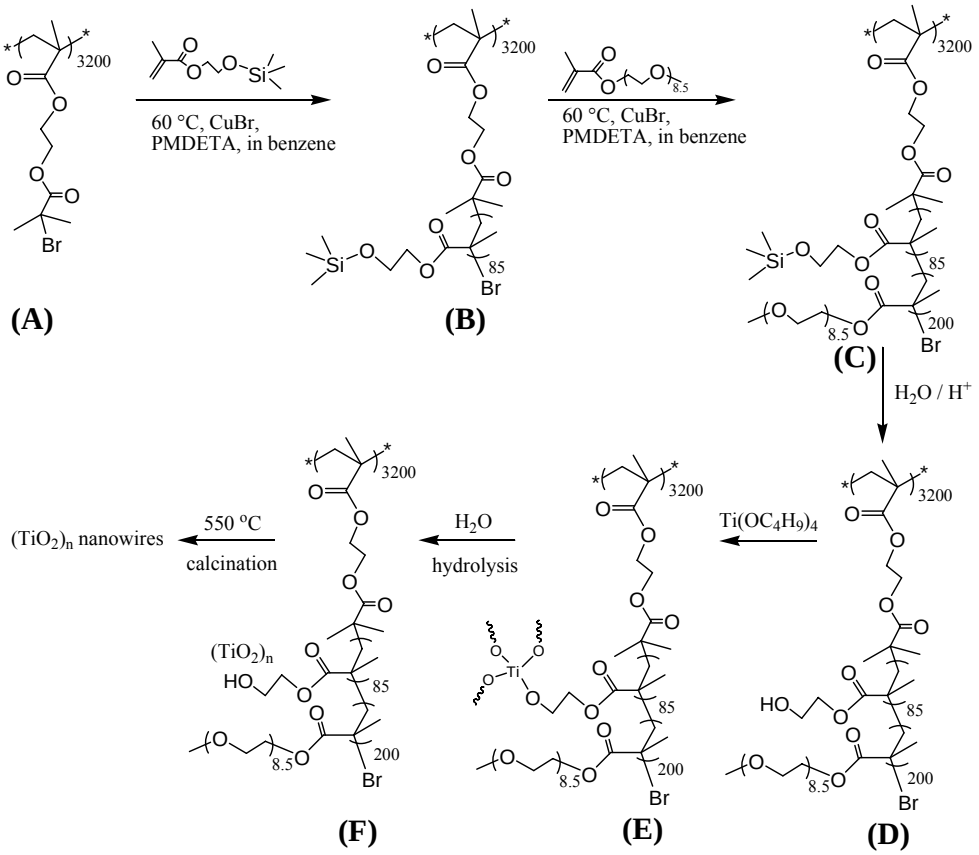

Figure 5-2. Synthetic route for titania-CPB hybrid nanowires. A), ATRP polyinitiator PBIEM; B), $[TMS\text{-}HEMA_{85}]_{3,200}$ CPB; C), $[TMS\text{-}HEMA_{85}\text{-}b\text{-}OEGMA_{200}]_{3,200}$ core–shell CPB; D), $[HEMA_{85}\text{-}b\text{-}OEGMA_{200}]_{3,200}$ core–shell CPB; E) Ti^{4+}-doped CPB hybrids $[(HEMA_{85}+n Ti^{4+})\text{-}b\text{-}OEGMA_{200}]_{3,200}$; F), titania-CPB hybrid nanowires $[(HEMA_{85}+n TiO_2)\text{-}b\text{-}OEGMA_{200}]_{3,200}$.

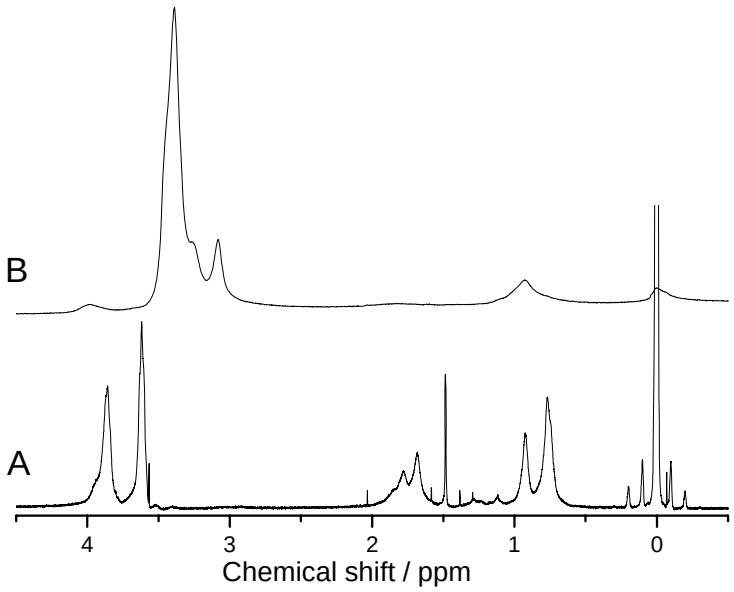

Figure 5-3. ^{1}H-NMR spectra of [TMS-HEMA$_{85}$]$_{3,200}$ CPB (A, in $CDCl_3$) and [TMS-HEMA$_{85}$-*b*-OEGMA$_{200}$]$_{3,200}$ CPB (B, in C_6D_6). The sharp peak at 1. 5 ppm in (A) is from residual water.

Since the protons in the PTMS-HEMA and POEGMA blocks have their corresponding chemical shift, the existence of each block can be easily identified by the ^{1}H-NMR spectra. Fig. 5-3 A shows the spectrum of [TMS-HEMA$_{85}$]$_{3,200}$ CPB, in which the protons of the trimethysilyl groups (-Si*(CH$_3$)$_3$*) show up at 0.05 ppm. The methylene protons (O-*CH$_2$*-*CH$_2$*-O) appear as two peaks at 3.77 ppm. After the introduction of the second block, it shows a POEGMA-dominated spectrum (Fig. 5-3 B), due to the larger OEGMA units in the side chains (200 units) compared to the TMS-HEMA units (85 units). Here, the trimethylsilyl protons, characteristic of the PTMS-HEMA block, become very weak but still visible at 0.05 ppm. The deduction of the ^{1}H-NMR spectra verifies the sequential growth of PTMS-HEMA and POEGMA blocks into the side chains of CPB.

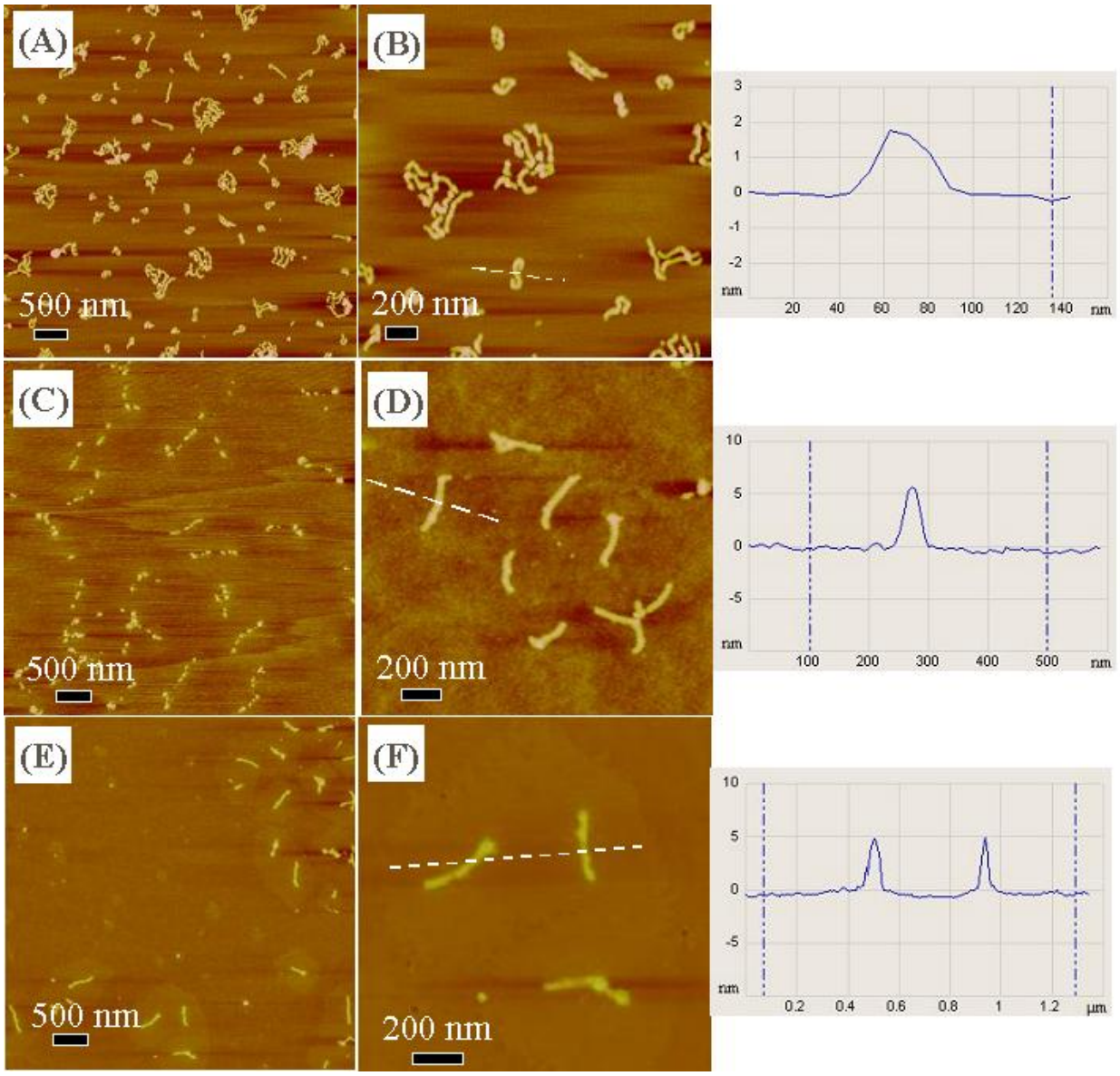

Figure 5-4. A-F), AFM height images of $[TMS\text{-}HEMA_{85}]_{3200}$ (A&B), $[TMS\text{-}HEMA_{85}\text{-}b\text{-}OEGMA_{200}]_{3200}$ (C&D), and $[HEMA_{85}\text{-}b\text{-}OEGMA_{200}]_{3200}$ (E&F) CPBs dip-coated from dilute solutions in dioxane onto mica surface except (D) on a silica wafer. The height scales are 5 nm (A&B) and 20 nm (C-F) respectively. The curves on the right of (B), (D) and (F) are the cross-section analysis of the corresponding wormlike objects, indicated by the white dashed line in the AFM images.

A molecular visualization of the pure CPBs by AFM was undertaken after the growth of each block in the side chains as well as the hydrolysis step to verify the successful synthesis of the

polymeric template. An overview of the [TMS-HEMA$_{85}$]$_{3200}$ CPBs on mica is displayed in Fig. 5-4A. Wormlike as well as irregular shaped objects were observed. The enlarged view in Fig. 5-4B shows that the irregular shaped objects are also CPBs which are strongly twisted. Some are even curved into spheres. In the cross-section analysis, they are typically 1.7 nm high in their center.

To generate a more extended conformation of the backbone, POEGMA was chosen as the second block in the side chains, as we expected that the long and bulky POEGMA chains will introduce a strong repulsion among the side chains to stretch the backbone. Against our expectation, the AFM characterization of the [TMS-HEMA$_{85}$-*b*-OEGMA$_{200}$]$_{3200}$ CPBs on mica gives only linear dots instead of worms (Fig. 5-4C), indicating the breaking of CPBs.[20] We further conducted DLS measurements of both CPBs. The [TMS-HEMA$_{85}$-*b*-OEGMA$_{200}$]$_{3200}$ CPBs have a hydrodynamic radius of 280 nm in dioxane, significantly higher than 81 nm of the [TMS-HEMA$_{85}$]$_{3200}$ CPBs, which hints to a scission of the CPBs occurring when dried on mica. This is supported by AFM measurements on a silica wafer, on which the [TMS-HEMA$_{85}$-*b*-OEGMA$_{200}$]$_{3200}$ CPBs still keep their wormlike morphology (Fig. 5-4D). They are more cylindrical and well-defined. The height dramatically increases to 5.2 nm, three times that of the [TMS-HEMA$_{85}$]$_{3200}$ CPB (1.7 nm). The unexpected scission on mica surface could result from the different response of the hydrophobic PTMS-HEMA and hydrophilic POEGMA blocks to the hydrophilic and negatively charged mica surface. The former tries to minimize the contact with mica surface, while the latter makes totally opposite efforts. Through the covalent bonds, both blocks in the side chains pass and focus their stress onto the backbone, causing its breaking. This mechanism is supported in the following hydrolysis step.

After the removal of the TMS groups, namely turning the hydrophobic PTMS-HEMA block into hydrophilic PHEMA, the newly formed [HEMA$_{85}$-*b*-OEGMA$_{200}$]$_{3200}$ CPBs are stable on mica (Fig. 5-4E). The height is slightly below 5 nm (Fig. 5-4F), due to the loss of the TMS groups. Their regular cylindrical shape facilitates a statistical analysis of their length. The number- and weight-average lengths are L_n = 308 nm and L_w = 340 nm, respectively, giving a polydispersity L_w/L_n = 1.10, which agrees well with that of the PBIEM backbone (M_w/M_n = 1.14). By monitoring the evolution of the CPB morphologies at different stages, one can easily prove the synthetic strategy, as the morphological changes stem from the structural variation in the side.

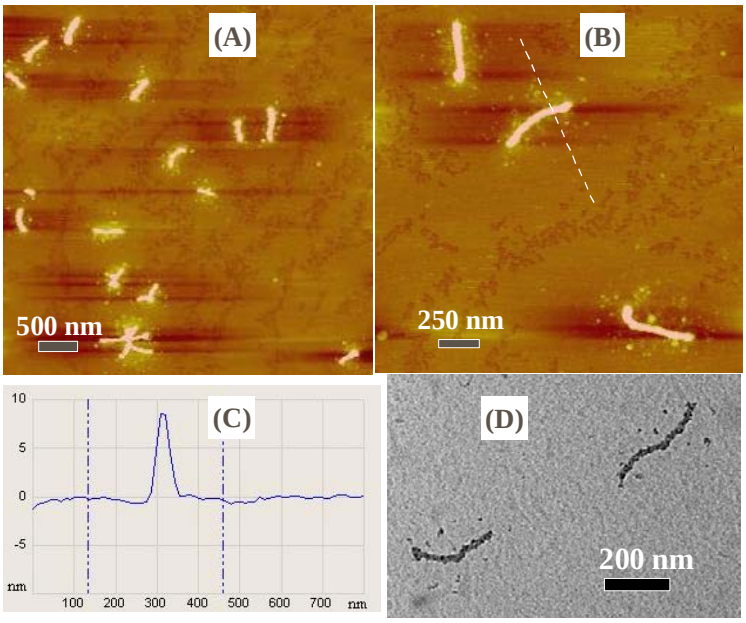

Figure 5-5. A-B), AFM height images of Ti^{4+}-doped CPB hybrids, [($HEMA_{85}$-*n*Ti^{4+})-*b*-$OEGMA_{200}$]$_{3200}$, on mica; C), the cross-section analysis of a single object (white dashed line) in B); D), the corresponding TEM image on carbon coated grid.

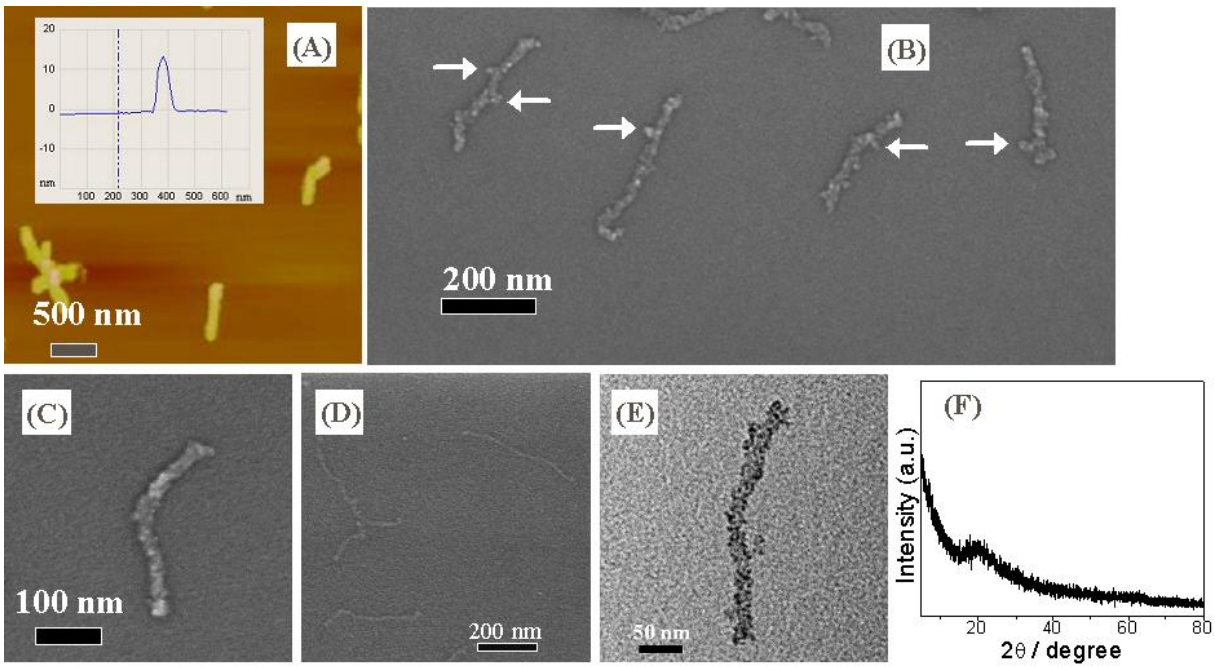

Figure 5-6. A), AFM height image of titania-CPB hybrid nanowires, the insert shows the cross-section analysis of a single hybrid nanowire; B-C), SEM images of titania-CPB hybrid nanowires; D), SEM image of pure CPBs as a comparison; E), TEM image of a single titania-CPB hybrid nanowire; F), XRD pattern of the obtained titania-CPB hybrid nanowires.

It has been reported that the transalcoholysis reaction between titanium tetraalkoxide and 2-hydroxyethyl methacrylate takes place instantaneously at room temperature without catalyst.[21, 22] We made use of this reaction to fix the titanium precursors onto the PHEMA core of the core-shell $[HEMA_{85}$-*b*-$OEGMA_{200}]_{3200}$ CPBs. Aiming at a high content of titanium precursor in the core, a large excess of $Ti(OC_4H_9)_4$ (molar ratio: Ti^{4+}/hydroxyl = 10) was adopted in the present work. Excess $Ti(OC_4H_9)_4$ was removed by ultrafiltration using pure dioxane as eluent. The Ti^{4+}-doped CPB hybrids were characterized by AFM and TEM. A representative AFM image (Fig. 5-5A) shows that the wormlike morphology remains together with small round dots. A close view in Fig. 5-5B indicates that these dots are exclusively located around the worms. TEM characterization gives a further clue to understand this peculiar morphology. Without staining, the contrast for the CPBs is too weak to render an image via TEM. However, a good contrast was achieved when Ti^{4+} ions were loaded, as shown in Fig. 5-5D. The wormlike dark domains in the bright-field TEM image represent the position of Ti^{4+} ions. This directly proves the successful coordination of Ti^{4+} ions into the PHEMA core block. The diameter of the wormlike objects is about 20 nm. The dark dots are also observed around each worm, similar to the AFM observation in Fig. 5-5A and 5-5B, indicating that they contain Ti^{4+} ions. As reported, oxygen atoms in the PEG chains weakly coordinate with Ti^{4+}.[23] We believe that the dots around the Ti^{4+}-doped CPB hybrids come from the Ti^{4+}-mediated crosslinking of oligo(ethylene glycol) chains in the POEGMA shell. The amount of Ti^{4+} ions in the shell is significantly less than that in the PHEMA core, since the main black objects stay in the core (Fig. 5-5D). Due to the introduction of a new component, the Ti^{4+} ions, into the CPB, the height increases from 5 nm to 8.7 nm.

Titania-CPB hybrid nanowires were generated when the Ti^{4+}-doped CPB hybrids reacted with water. To ensure the complete hydrolysis, the reaction mixture was stirred for 5 days. Fig. 5-6A shows the AFM image of the titania-CPB hybrid nanowires. The wormlike shape was maintained which demonstrates the high stability of the CPBs. The cross-section analysis indicates a further increase of the height to 11.5 nm, due to the formation of titania nanoparticles in the CPB core. To achieve their absolute dimensions, the sample was further subjected to SEM characterization. Figs. 5-6B shows the SEM image of titania-CPB hybrid nanowires well-dispersed on mica. The high self-dispersibility of the hybrid nanowires is rendered by the large POEGMA shell, which screens the fusion and agglomeration of the titania nanoparticles among different CPBs. The hybrid nanowires are 290 ± 36 nm in length and 29 ± 8 nm in diameter, giving an aspect ratio of

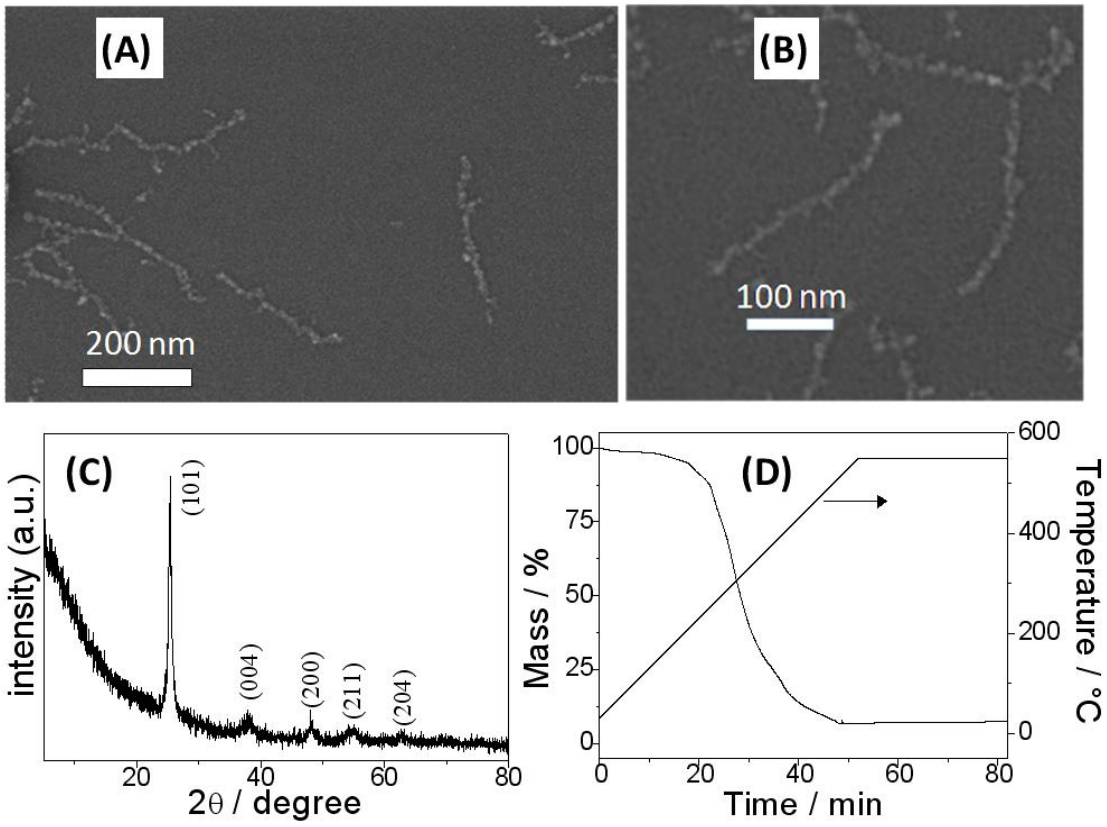

Figure 5-7. A-B), SEM image of titania nanowires after calcination at 550 °C; C), XRD pattern of the titania nanowires; D), TGA curve of the titania-CPB hybrid nanowires.

10. Fig. 5-6C is an enlarged view of a single hybrid nanowire. Here, lighter dots are distributed along the grey cylinder, i.e. the hybrid nanowire. Compared with the pure CPB in Fig. 5-6D, the light dots only appear after the titania nanoparticles were introduced. We assume that these dots represent larger titania nanoparticles which can hardly be encapsulated within the CPB in the solid state (shrinking of the CPB during the drying process). Interestingly, we did not observe isolated dots around these nanowires, but several protrusions (indicated by the white arrows in Fig. 5-6B). We assume that the TiO_2 molecules formed by the Ti^{4+} ion in the POEGMA shell may diffuse close to the core region and attach to the nanoparticles there. To have a deep view of the intrinsic structures of titania nanoparticles within the CPB, TEM characterization was performed. As shown in Fig. 5-6E, the black dots, namely titania nanoparticles with a diameter of 2-7 nm are confined into a linear manner. This is the solid proof that the strategy of using CPB as cylindrical template to fabricate titania nanoparticles is successful. Here, the diameter of the hybrid nanowires is ~19 nm, similar as the precursors. The XRD measurement of the titania-CPB

hybrid nanowires (Fig. 5-6F) indicates an amorphous phase of the titania at this step. The broad peak at $2\theta = 20°$ comes from the solid CPBs.

The titania-CPB hybrid nanowires were converted to inorganic crystalline titania nanowires by a pyrolysis process at 550 °C. Fig. 5-7A shows SEM images of the obtained uniform titania nanowires on mica. They appear thinner compared to the hybrid nanowires because of the width shrinkage from 29 nm of the hybrid nanowires to only 14 nm now due to the decomposition of the whole CPB during the pyrolysis. A close view of these nanowires (Fig. 5-6B) further indicates that individual nanowires actually consist of the linearly aligned titania nanoparticles.(also seen in the TEM image in Fig. 5-6E) The rough contour and the inhomogeneous brightness along the nanowires result from the nonuniformity of the nanoparticles´ size and the different contrast between the nanoparticle center and the boundary. The inorganic titania nanowires were proven to be crystalline by XRD measurement. The corresponding diffraction peaks in Fig. 5-7C match well with that of anatase phase[24], confirming the phase transformation in the calcination process. In the EDX analysis only oxygen and titanium elements were detected, proving the complete removal of the organic moieties. The titania content in the hybrid nanowires was determined to be 8.05% by thermogravimetric analysis, 34% higher than the theoretical amount, 6.02%, when each HEMA unit in the core was considered to bind one titanium atom. The difference here comes from the additional Ti^{4+} ions fixed in the CPB shell, as discussed before.

Further efforts were made to improve the crystallinity of the titania phase within the hybrid CPB, as they are important for photocatalytic applications in solution. Here we refluxed the titania-CPB hybrid nanowires in a mixture of water/dioxane (vol. ratio: 1/3) at 100 °C. No phase transformation of titania occurred after one day. However after 5 days, anatase phase are found. An overview in Fig. 5-7A shows the characteristic wormlike shape, verifying the existence of the CPBs. An enlarged view of a single object (Fig. 5-7B) shows that the titania nanoparticles become irregular in their shape and more discontinuous after refluxing 5 days. At room temperature, the mobility of the titania nanoparticles is largely hindered by the interaction with the compact PHEMA chains in the CPB core; however at reflux conditions, the polymer chains may relax, which partially undermines the interaction with nanoparticles. Some nanoparticles were found to be released from the CPB matrix to the solution during the refluxing process. As compensation, the crystallinity of the titania nanoparticles was improved. As indicated by the

high-resolution TEM in Fig. 5-8C, the crystalline phase of the titania nanoparticles can be easily observed. A lattice spacing of 3.52 Å was determined corresponding to the lattice spacing of the [101] plane of the anatase phase. It should be mentioned that amorphous phase was still detected. We expect that with a longer term of refluxing, titania nanoparticles could be completely transferred into anatase phase.

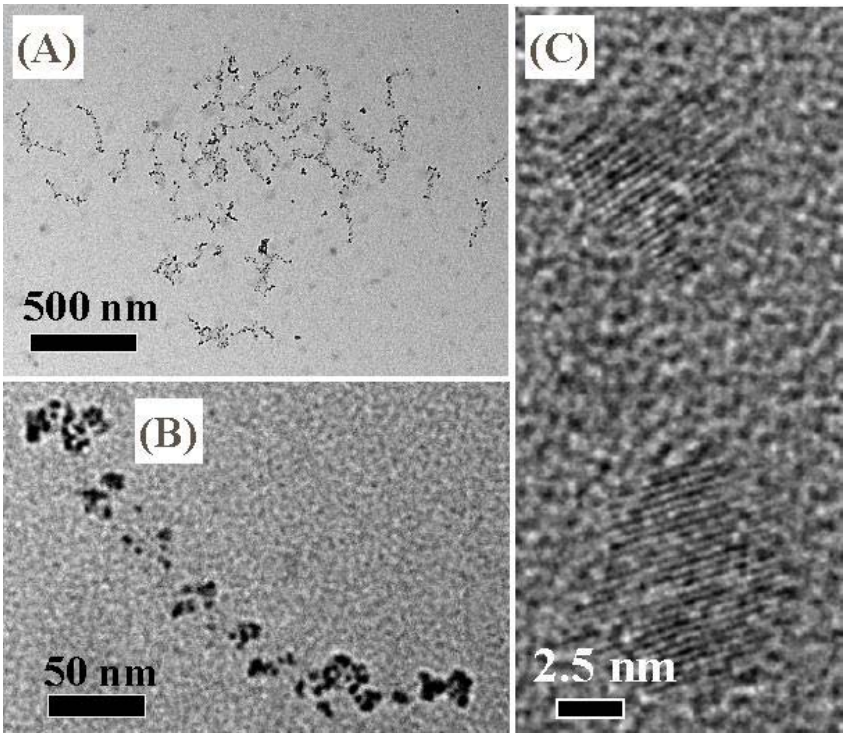

Figure 5-8. TEM images of titania-CPB hybrid nanowires after reflux for 5 days. A), the overview; B), a single hybrid nanowires; C), the high-resolution TEM image of the titania crystals.

5.4 Conclusions

We have described a new concept to generate uniform, soluble titania-polymer hybrid nanowires by using core-shell superstructured bishydrophilic CPBs as the template. The titania-CPB hybrid nanowires can form pure inorganic titania nanowires by pyrolysis at 550 °C. XRD measurement showed the amorphous phase of the titania nanoparticles in the titania-CPB hybrid nanowires but anatase phase in the pure titania nanowires. The crystallinity of the titania-CPB hybrid nanowires was improved by reflux for 5 days with a compromise of a partial loss of nanoparticles. Further improvement could be obtained by using a stronger polyacid, e.g., poly(styrenesulfonic acid) to firmly immobilize the titania nanoparticles in the CPB. These hybrid nanowires are potentially useful as photocatalyst.

Acknowledgements. This work was supported by the Deutsche Forschungsgemeinschaft (SPP 1165, grant Mu896/22). We thank Christina Löffler for the kind help in TGA measurements.

5.5 References

1. Sheiko, S. S.; Sumerlin, B. S.; Matyjaszewski, K. *Prog. Polym. Sci.* **2008,** 33, (7), 759-785.
2. Zhang, M.; Müller, A. H. E. *J. Polym. Sci. Part A: Polym. Chem.* **2005,** 43, (16), 3461-3481.
3. Zhang, M.; Breiner, T.; Mori, H.; Müller, A. H. E. *Polymer* **2003,** 44, (5), 1449-1458.
4. Djalali, R.; Hugenberg, N.; Fischer, K.; Schmidt, M. *Macromol. Rapid Comm.* **1999,** 20, (8), 444-449.
5. Börner, H. G.; Beers, K.; Matyjaszewski, K.; Sheiko, S. S.; Moeller, M. *Macromolecules* **2001,** 34, (13), 4375-4383.
6. Lee, H.; Jakubowski, W.; Matyjaszewski, K.; Yu, S.; Sheiko, S. S. *Macromolecules* **2006,** 39, (15), 4983-4989.
7. Cheng, G.; Böker, A.; Zhang, M.; Krausch, G.; Müller, A. H. E. *Macromolecules* **2001,** 34, (20), 6883-6888.
8. Cheng, C.; Qi, K.; Khoshdel, E.; Wooley, K. L. *J. Am. Chem.Soc.* **2006,** 128, (21), 6808-6809.
9. Djalali, R.; Li, S.-Y.; Schmidt, M. *Macromolecules* **2002,** 35, (11), 4282-4288.
10. Zhang, M.; Drechsler, M.; Müller, A. H. E. *Chem. Mater.* **2004,** 16, (3), 537-543.
11. Yuan, J.; Drechsler, M.; Xu, Y.; Zhang, M.; Müller, A. H. E. *Polymer* **2008,** 49, (6), 1547-1554.
12. Yuan, J.; Xu, Y.; Walther, A.; Bolisetty, S.; Schumacher, M.; Schmalz, H.; Ballauff, M.; Müller, A. H. E. *Nat. Mater.* **2008,** 7, (9), 718-722.
13. Zhang, M.; Estournes, C.; Bietsch, W.; Müller, A. H. E. *Adv. Funct. Mater.* **2004,** 14, (9), 871-882.
14. O'Regan, B.; Graetzel, M. *Nature* **1991,** 353, (6346), 737-40.
15. Zheng, Q.; Zhou, B.; Bai, J.; Li, L.; Jin, Z.; Zhang, J.; Li, J.; Liu, Y.; Cai, W.; Zhu, X. *Adv. Mater.* **2008,** 20, (5), 1044-1049.
16. Bach, U.; Lupo, D.; Comte, P.; Moser, J. E.; Weissortel, F.; Salbeck, J.; Spreitzer, H.; Gratzel, M. *Nature* **1998,** 395, (6702), 583-585.
17. Kim, D. H.; Kim, S. H.; Lavery, K.; Russell, T. P. *Nano Lett.* **2004,** 4, (10), 1841-1844.

18. Cozzoli, P. D.; Kornowski, A.; Weller, H. *J. Am. Chem. Soc.* **2003,** 125, (47), 14539-14548.

19. Förster, S.; Abetz, V.; Müller, A. H. E. *Adv. Polym. Sci.* **2004,** 166, (Polyelectrolytes with Defined Molecular Architecture II), 173-210.

20. Sheiko, S. S.; Sun, F. C.; Randall, A.; Shirvanyants, D.; Rubinstein, M.; Lee, H.-i.; Matyjaszewski, K. *Nature* **2006,** 440, (7081), 191-194.

21. Kameneva, O.; Kuznetsov, A. I.; Smirnova, L. A.; Rozes, L.; Sanchez, C.; Alexandrov, A.; Bityurin, N.; Chhor, K.; Kanaev, A. *J. Mater. Chem.* **2005,** 15, (37), 4078.

22. Kuznetsov, A. I.; Kameneva, O.; Rozes, L.; Sanchez, C.; Bityurin, N.; Kanaev, A. *Chem. Phys. Lett.* **2006,** 429, (4-6), 523-527.

23. Yu, K.; Zhao, J.; Zhao, X.; Ding, X.; Zhu, Y.; Wang, Z. *Mater. Lett.* **2005,** 59, (21), 2676-2679.

24. Tahir, M. N.; Eberhardt, M.; Theato, P.; Faiss, S.; Janshoff, A.; Gorelik, T.; Kolb, U.; Tremel, W. *Angew. Chem. Int. Ed.* **2006**, 45, (6), 908-912.

Chapter 6

Room-temperature growth of uniform tellurium nanorods and the assembly of tellurium or Fe_3O_4 nanoparticles on the nanorods

Abstract

Uniform and single-crystalline tellurium (Te) nanorods with high aspect ratio (20) are prepared via a cylindrical polymer brush-assisted method in THF at room temperature. The experiment was simply conducted by purging in-situ generated H_2Te gas into the CPB solution in THF. These formed rods are well dispersed and long-term stable in solution due to the polymers on their surface. Te nanorods prepared by this method were successfully used to assemble inorganic (Te or Fe_3O_4) nanoparticles on the nanorod surface via the hydrophobic interactions. The prepared Te nanorod / Te or Fe_3O_4 nanoparticle complex structures were characterized by TEM and SEM.

***** The results of this chapter have been published as:

"Room-temperature growth of uniform tellurium nanorods and the assembly of tellurium or Fe_3O_4 nanoparticles on the nanorods"

by Jiayin Yuan, Holger Schmalz, Youyong Xu, Nobuyoshi Miyajima, Markus Drechsler, Michael W. Möller, Felix Schacher, and Axel H. E. Müller*

Advanced Materials, **20**, 947 (2008)

6.1 Introduction

Significant attention has been directed towards one-dimensional (1D) semiconductor nanostructures in the last decade, such as nanorods, nanowires, due to their potential application as building blocks, interconnects and functional components for assembling nanodevices.[1-4] A variety of techniques and methods to create such structures have been developed, including laser-assisted catalytic growth (LCG),[5] vapour-liquid-solid (VLS),[6] and solution-liquid-solution (SLS) techniques,[7] chemical vapour deposition (CVD),[8] inorganic or polymer template directed synthesis,[9, 10] surfactant assisted process,[11] and others[12, 13]. To date, great progress has been made, however, exploring various routes to obtain defined size and shape for semiconductor 1D structures is still a challenge in this field.

Recently, 1D tellurium (Te) nanostructures attracted much interest due to their unique properties, like being an elemental semiconductor with a narrow bandgap (direct bandgap energy of 0.35 eV),[14] helical conformation and lack of centrosymmetry in its crystal structure,[15] which lead to the prospective use in light detectors, switching devices, integrated photonic circuits or near-field imaging.[16, 17] Many active efforts to achieve 1D Te nanostructures have been already reported.[18-22] For example, Qian et al.[18-20] prepared single-crystal Te nanowires from polycrystalline powder; Xia et al.[21] grew Te nanotubes through a nucleation-induced concentration depletion. Nevertheless, the room temperature synthesis of Te nanorods so far is seldomly reported due to the difficult control of the size and shape of 1D structures at low temperature. [22-24]

On the other hand, cylindrical polymer brushes (CPB) as novel polymer 1D structures have been exploited to fabricate 1D inorganic nanostructures more recently.[25-27] In all cases, core-shell structured CPB were used as a "scaffold", in which the functional core loads metal ions and the shell confines a 1D domain. After the chemical reaction, the metal ions were converted to nanocrystals, which were aligned into a quasi-continuous 1D structure within the CPB. In general, such 1D nanostructures are polycrystalline, because each consists of differently oriented nanocrystals. As a result, no single crystalline 1D structure has ever been synthesized so far when CPB was employed.

In this communication we report a room temperature solution preparation of single-crystalline Te nanorods by a CPB-assisted method and the assembly of Te or Fe_3O_4 nanoparticles on the Te nanorods. The macromolecule CPB ($[t\text{BMA}_{90}]_{3200}$) used in this research has a backbone of

poly(2-hydroxyethyl methacrylate) (DP=3,200) and poly(*tert*-butyl methacrylate) (P*t*BMA) side chains which consist of 90 repeating units and were grown from each unit of the backbone via the "grafting from" technique[28] (see Supporting Information). Uniform Te nanorods were achieved by simply introducing H_2Te gas into the solution of CPB in organic solvent. It is found that the aspect ratio (AR), defined as the ratio of the lengths of the major and minor axes, of the Te nanorods varies from 2.7 to 22 depending on the reaction medium. Besides, a strong dependence of the nanorod formation on the CPB concentration has been also observed. Our primary results demonstrate that the CPBs not only act as the capping agents for the formation of Te nanorods, but also react with H_2Te to chemically attach the nanorod, which assembles Te or Fe_3O_4 nanoparticles onto the nanorods.

6.2 Experimental section

The experiments were carried out under a gentle argon flow at room temperature (21°C). A three-necked flask with magnetic stirrer, 1.25 g of aluminium telluride (99.5% pure, Gerac) and 60 ml of dioxane (analytical grade, Acros) were equipped with a bubble counter and connected to a short manifold with 4 branch ends which insert into 4 parallel identical flasks. In a typical procedure, the dispersion of aluminium telluride in dioxane and the CPB solutions (40 ml) in tetrahydrofuran (THF) or other solvents in flasks were bubbled with argon for 30 minutes. Then 10 ml of oxygen-free H_2SO_4 solution (0.5 M) was added dropwise by syringe in a controlled manner in portions of 2ml, 3ml, 3ml and 2ml every 30 minutes to produce H_2Te gas. H_2Te gas was distributed via argon flow into the 4 reaction flasks. At the end, argon was further bubbled for 30 min and the flasks were opened to air for several minutes. Then each flask containing 5 ml reaction solution was sealed and saved under argon in dark for two weeks to check the aging effect. The rest was refilled with solvent to 60 ml and refluxed under argon for one day. Magnetic nanoparticles (~ 10 nm) capped with oleic acid were synthesized by the conventional coprecipitation method[29, 30] and redispersed in THF. TEM images were taken on a ZEISS EM922 OMEGA electron microscope operated at 200 kV. A 2 µl droplet of the solution was dropped onto a carbon-coated copper grid (Fig. 6-1 a-d and f-h, Fig. 6-2 a-b and Fig. 6-3 a-h) or a lacey carbon grid (Fig. 6-2e). HRTEM and its *selected area electron diffraction* (SAED) measurements were carried out on a Philips CM20FEG TEM operated at 200 kV. The FTIR spectra were taken on a Bruker EQUINOX 55/S infrared spectrometer. The XRD measurement was performed at 25 °C on a Panalytical XPERT-PRO diffractometer in reflection mode using CuK_α radiation.

6.3 Results and discussion

The typical Te nanorods synthesized with this method are summarized in Table 6-1.

Table 6-1. Summary of Te nanorods (NRs) prepared by the CPB-assisted method.

Exp.	CPB conc. (g/L)	Solvent	Structure[a]
1	0.5	THF	NRs (AR =21)
2	0.5	acetone	NRs (AR =2.7)
3	0.5	dioxane	submicron-sized particles
4	0.5	chloroform	no reaction
5	0.5	toluene	no reaction
6	0.5	chloroform/methanol (v/v=1:1)	NRs
7	5	THF	NRs (AR = 22)
8	0.05	THF	NRs and particles

[a] the aspect ratio (AR) is given only for uniform Te nanorods.

Similar to the common chemical routes to 1D nanostructures,[31, 32] the present approach proceeds through nucleation and growth steps as well. The transmission electron microscopy (TEM) images in Fig.6-1a to 6-1d clearly indicate the formation of Te nanoseeds and subsequent growth into nanorods at different stages in experiment 1. Well-dispersed Te nanoseeds with a uniform size of 22 ± 3 nm in Fig. 6-1a were identified after 10 min bubbling H_2Te gas through the CPB solution. The high-resolution transmission electron microscopy (HRTEM) image in Fig. 6-1b indicates a trigonal Te single-crystalline structure of the nanoseed, which is the same for different nanoseeds. They originate from the homogeneous nucleation process of Te atoms, which were transformed from the absorbed H_2Te gas in the solution. Xia et al.[21] also reported that the Te nanotubes grew from single-crystalline nanoseeds. Fig. 6-1c and 6-1d show samples that were taken after 30 min and 2.5 hours at the end of the reaction, respectively. Only Te nanorods were observed instead of nanoseeds. The diameter of the nanorods is 35.6 ± 4.1 and 36.1 ± 7.9 nm for the former and latter, which are quite identical within the limits of error. In contrast, the average length (L_n) of the nanorods increases from 346 ± 17 to 741 ± 37.8 nm (AR = 21). This indicates that the Te nanorods grew along the longitudinal direction, while their lateral dimensions were in fact maintained all over the whole process.[21] Moreover, the length of the Te nanorods could be simply controlled by the reaction time and cutting off the H_2Te flow. A close view of the TEM images in Fig. 6-1c and 6-1d shows that the Te nanorods are homogeneously

distributed. This is in good accordance with the high stability of the obtained Te nanorod solution, in which no precipitation was detected for days even without stirring. The length distribution histogram according to 137 Te nanorods is given in Fig. 6-1e, showing an extremely low polydispersity (L_w/L_n=1.003). Its narrow range of variation in the longitudinal size implies that the Te nanorods grew simultaneously from the monodisperse nanoseeds, which is confirmed in Fig. 6-1a.

Fig. 6-1f shows a representative TEM image of a single Te nanorod. The straight nanorod possesses a uniform diameter along its entire length. Its HRTEM image in Fig. 6-1g proves that the Te nanorod is structurally single-crystalline with a periodic fringe spacing of 5.92 Å along the longitudinal axis (c axis), which corresponds to the interplanar spacing between the (001) planes of the hexagonal lattice of Te and agrees with the results obtained from Te 1D structures prepared in other groups[33, 34]. The corresponding electron diffraction pattern (Fig. 6-1h) was obtained by aligning the nanorod with the $[1\bar{1}0]$ zone axis, which can be indexed to the hexagonal crystalline structure (space group: $P3_121$ (no.152)). This is consistent with the HRTEM result in Fig. 6-1g. This demonstrates that due to the highly anisotropic structure of trigonal single-crystalline Te, the growth direction was basically confined to the (001) direction[21], in which Te preferentially grew into a 1D structure[35]. Te nanorods with high aspect ratio of 18 were also synthesized by Xia et al.[22] In that case, refluxing (178°C) ethylene glycol (EG) with 1.5% of water is required in order to achieve a fast reduction of orthotelluric acid by adding hydrazine. In contrast, our method avoids both heating and adding of any reductant, and the Te atoms actually originate from the disproportionative decomposition of H_2Te rather than the reduction of Te precursors. Besides, the dimension (length and diameter) of the Te nanorods prepared by the CPB-assisted method are much smaller, only half of that by reducing orthotelluric acid. In their method, the reduction of orthotelluric acid by hydrazine in water was also tried at room temperature (20 °C), however, the full conversion of the amorphous Te colloids to s-whisker-shaped nanowires took several months.[22]

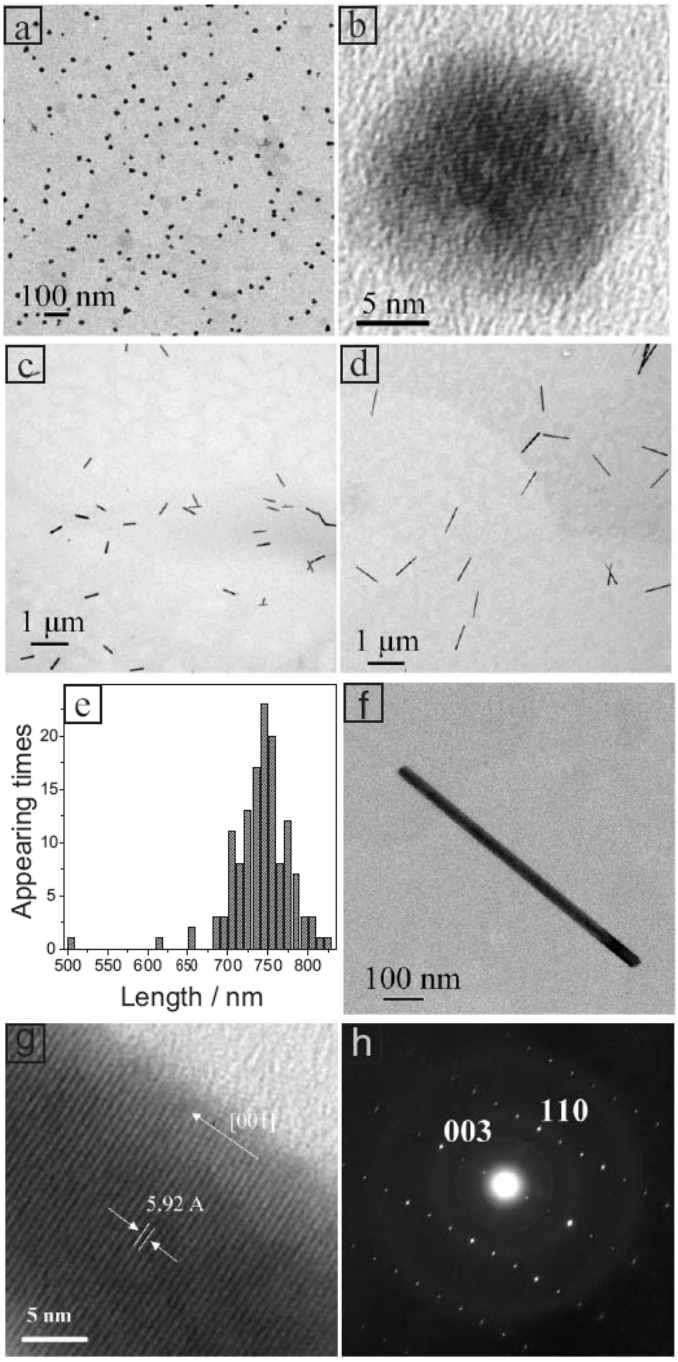

Figure 6-1. a-d) TEM images of Te nanoseeds and nanorods in experiment 1 which were synthesized by introducing H_2Te gas into a CPB $[t\text{BMA}_{90}]_{3200}$ solution in THF for a)10 min, c)30 min, and d) 2.5 h, respectively. b) a HRTEM image of a single seed; e) the length distribution histogram of 137 Te nanorods; f) a single Te nanorod in (d), its HRTEM image in (g) and the corresponding electron diffraction pattern in (h).

Interestingly, the freshly prepared Te nanorods were found to change their morphology when the nanorod solution was shortly exposed to air and then refluxed or aged under argon. Fig. 6-2a shows the Te nanorod/nanoparticle complex, which is formed directly after refluxing the Te nanorod solution for one day. Instead of the straight and smooth surface of the nanorods, a cylindrical nanorod/nanoparticle complex structure was observed. A close view of a single Te nanorod/nanoparticle complex in Fig. 6-2b shows that spherical Te nanoparticles were enriched and assembled on the nanorod surface. The same phenomenon was also found when the freshly prepared sample was aged for two weeks (see Supporting Information), and is attributed to a nanoparticle formation stage during the post-treatment. Since H_2Te is quite hydrophilic and hardly removed from the solution by bubbling argon for half an hour, the residual amount was rapidly oxidized to elemental Te when the solution was open to air.[24] The sudden increase of the Te atom concentration supersaturated the solution and initiated nanoparticle formation. The Te nanoparticles in the complex generated from refluxing are 15~30 nm in size, and mostly amorphous. The XRD pattern of the complex is shown in Fig. 6-2c, which confirms that the whole complex is a single phase of elemental Te. The measured lattice constants are a= 4.462Å and c=5.930 Å, which are consistent with the reported data (a= 4.457 Å, c=5.927 Å, JCPDS file no.361452). To study its structure, the Te nanorod/nanoparticle complex was purified by ultracentrifugation and washing with THF several times. Fig. 6-2d shows the FTIR spectra of the pure CPB and the complex. A characteristic carbonyl absorption at 1721 cm^{-1} stemming from the CPB was clearly observed in the complex spectrum, which demonstrates that the CPB coexists with the complex. Meanwhile, its intensity dramatically decreases, and there is a significant difference from 1300 to 500 cm^{-1} between these two spectra, which indicates a chemical change of the CPB. Besides, a new intensive absorption at 627 cm^{-1} attributed to the Te-O vibration[36] strongly suggests a covalent bonding of the CPB to the Te nanorod/nanoparticle complex via a Te-O bridge. Considering the strong reducibility of H_2Te,[37] the CPB in fact was partially reduced and chemically attached to Te nanorods via a Te-O covalent bond during the reaction. Additionally, the Te nanorod/nanoparticle complex was measured by TEM on an empty hole of a lacey carbon grid in order to detect the CPBs, which have a low contrast. In the TEM image of Fig. 6-2e, a thin layer of ca. 4 nm thickness (indicated by the black arrow), was found on part of the complex surface. This layer exhibits a weaker contrast than both the nanorod and the nanoparticles. Our previous atomic force microscopy (AFM) investigation suggests that on solid surface like mica and silicon wafer, the CPBs typically possess a thickness of 3~4 nm (see

Supporting Information), which implies that this thin layer is a monolayer of CPBs. According to the results above, a structure model of the Te nanorod/nanoparticle complex and CPB hybrid is proposed in Fig. 6-2f, in which both Te nanoparticles and CPB are tightly attached on the nanorod surface. It should be mentioned that after refluxing, the solution was stable and only few free Te nanoparticles (< 3%) were observed.

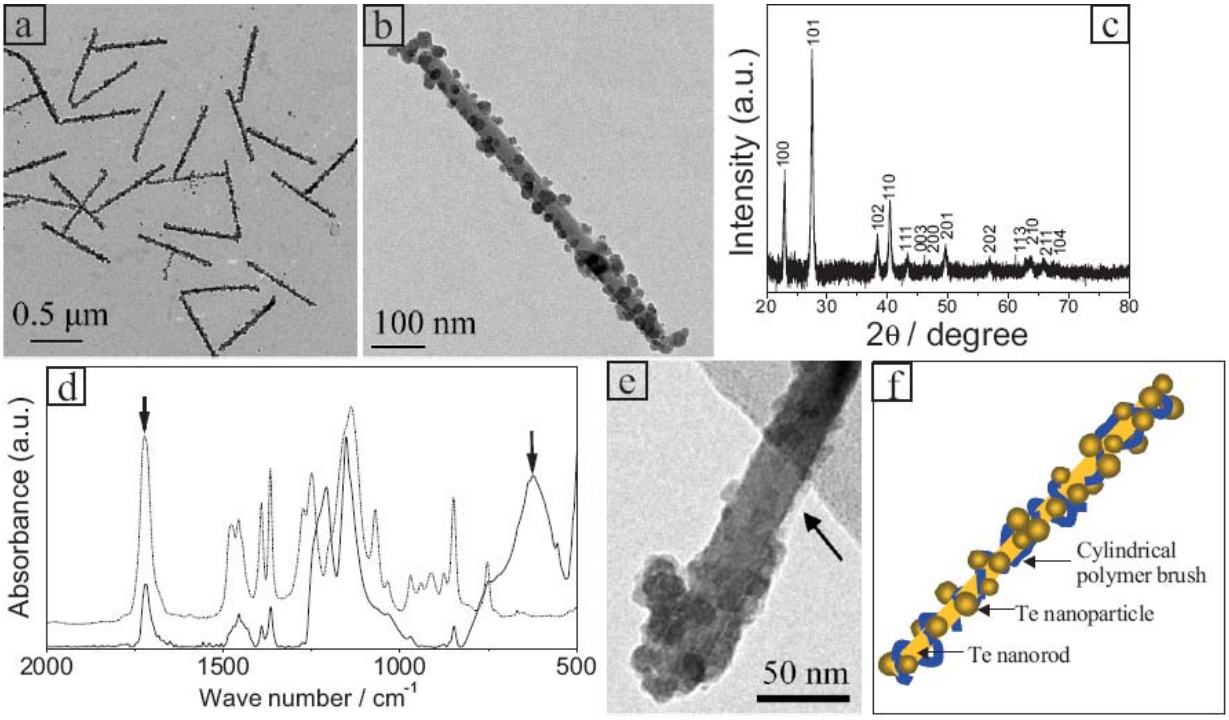

Figure 6-2. a) TEM images of Te nanorod/nanoparticle complex obtained by refluxing the freshly prepared Te nanorod solution under argon in experiment 1, and a single Te nanorod/nanoparticle complex in b), c) XRD pattern of Te nanorod/nanoparticle complex; d) FTIR spectra of CPB (dotted line) and the Te nanorod/nanoparticle complex (full line); e) TEM image of a single Te nanorod/nanoparticle complex on the empty hole of a lacey carbon grid; (f) proposed model for Te nanorod/nanoparticle complex and CPB hybrid.

Our proposed mechanism of the formation of Te nanorods and the assembly of Te nanoparticles on the nanorods is related to the special properties of H_2Te, which is highly instable, decomposing into Te and H_2 even at room temperature,[38, 39] and able to reduce organic carbonyl compounds.[37] In our experiments, H_2Te gas was introduced by a gentle stream of argon saturating the solution throughout the reaction period. Te atoms, which stemmed from the

decomposition of H_2Te, were concentrated and supersaturated the solution until Te nuclei were formed and grew into trigonal single-crystalline nanoseeds. Since H_2Te was introduced throughout the reaction, Te atoms were continuously supplied and deposited preferentially onto the (001) facet of the nanoseeds due to the difference of free energies of the various surfaces.[21, 22] The CPBs improve the preferential growth along the (001) facet by capping and chemically attaching other circumambient surfaces of the nanorod. As each CPB possesses ca. 288,000 *t*BMA units, it can act as a powerful capping agent, which largely confines the growth direction. On the other hand, a normal linear P*t*BMA polymer with less *t*BMA units, as a "mild" capping agent, can assist the growth of shorter Te nanorods. This is verified by repeating the reaction in linear P*t*BMA (M_w=95,000 g/mol) solution (0.5 g/L) in THF, in which shorter Te nanorods (410 ± 64 nm) with a smaller aspect ratio of 8 were generated, as shown in the TEM image in Fig. 6-3a. This shows that the CPB-assisted method can be applied to produce shorter Te nanorods, by employing linear and commercial P*t*BMA polymer.

It should be pointed out, for the purpose of only Te nanorods, the CPB-assisted method does not need further purification step unless keeping the reaction flasks simply closed for additional several hours to completely decompose H_2Te. The assembly process of Te nanoparticles on the nanorods took place only when the reaction flasks were shortly opened to air after bubbling argon, and refluxed or aged under argon. The formed Te nanoparticles were stabilized by polymer and stuck to the Te nanorods via a hydrophobic interaction between the polymers on both surfaces. Similar hydrophobic interactions between the surfactant capping agents have been recently reported to assist the self-assembly of small TiO_2 nanoparticles onto larger Co_3O_4 nanocubes.[40] It is worth pointing out that in our case the polymers on the nanorod surface get immobilized via Te-O covalent bonding, which prevents them from leaving the nanorods into the solution and assists the assembly process. The special feature to assemble inorganic nanoparticles was further proven by the assembly of oleic acid-capped Fe_3O_4 nanoparticles on Te nanorods, which generates a novel kind of Te nanorod-based magnetic nanocylinders (Te nanorod/Fe_3O_4 nanoparticle complexes). The TEM image of such magnetic nanocylinders is shown in Fig. 6-3b, in which all Fe_3O_4 nanoparticles in solution were enriched on Te nanorods to leave a nanoparticle-free solution. An enlarged TEM image in Fig. 6-3c clearly shows the densely packed magnetite nanoparticles on the nanorod surface. The hydrophobic interaction, which facilitates the assembly of Fe_3O_4 nanoparticles on the nanorods, results from the polymer layer on Te nanorod and the long alkyl chains of oleic acid on the magnetite nanoparticle surface. To the

best of our knowledge, this is the first time that Te nanorods serve as a template to form magnetic nanocylinders by the assembly of the Fe_3O_4 nanoparticles on the nanorods, which is actually the unique property of the Te nanorods prepared in our method. The controlled assembly and tuning the number of the Fe_3O_4 nanoparticles per Te nanorod is beyond the scope of this paper and will be published elsewhere.

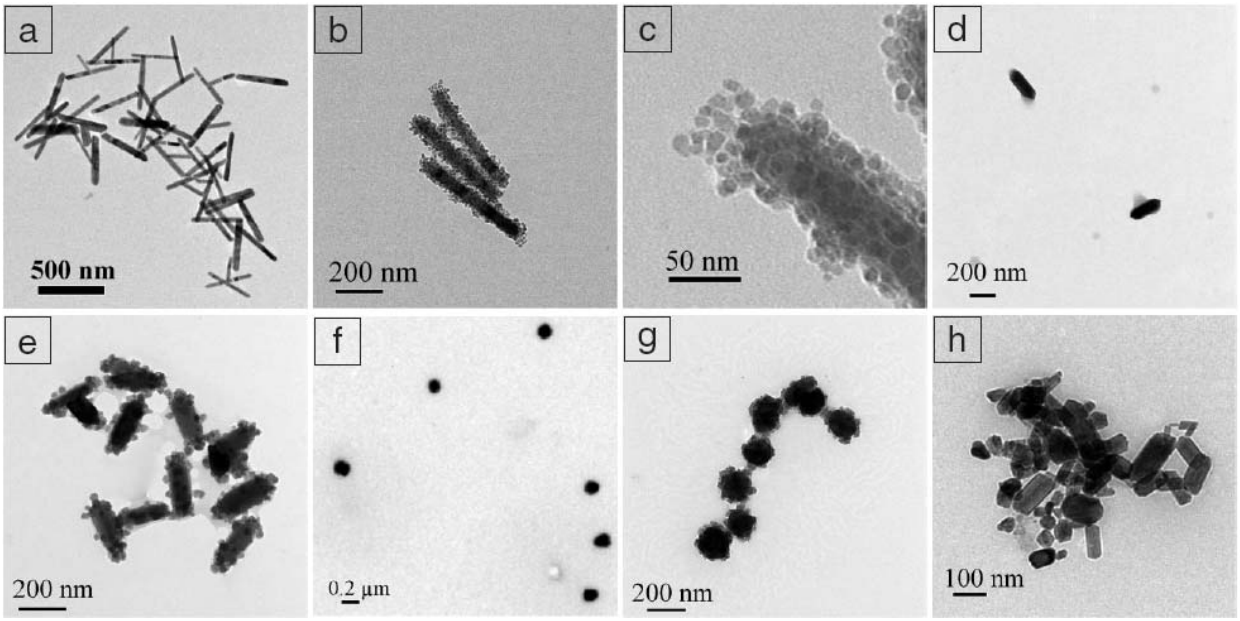

Figure 6-3. TEM images of a) Te nanorods prepared via CPB-assisted method using normal linear P*t*BMA (M_w = 95,000 g/mol) polymer solution (0.5 g/L) in THF, b-c) Te nanorod/Fe_3O_4 nanoparticle complex prepared by the assembly of Fe_3O_4 nanoparticles on the nanorods in a), d) Te nanorods prepared from CPB solution in acetone in the experiment 2, e) Te nanorod/nanoparticle complex obtained by refluxing the freshly prepared Te nanorod solution in d), f) Te submicron-sized particles prepared from CPB solution in dioxane in experiment 3, g) Te submicron-sized particle/nanoparticle complex obtained by refluxing the freshly prepared Te submicron-sized particle solution in f), h) Te irregular structures obtained in the blank experiment without polymer in THF.

As it was reported that the solvent can influence the growth of the Te nanostructures,[22] we also found the analogous dependence of the nanorod formation on the reaction media. For example, when acetone was used as the solvent, bulky Te nanorods with an average length of 281

nm and width of 105 nm were prepared (Fig. 6-3d); and in dioxane only submicron-sized particles (~167nm) were obtained (Fig. 6-3f). Similarly, in both reactions, refluxing or aging can modify the morphologies of the obtained nanorods (Fig. 6-3e) and submicron-sized particles (Fig. 6-3g). It is worth noting that highly hydrophobic solvents like chloroform or toluene, which were used as the reaction solvents, prevent the formation of Te nanostructures. This indicates that in order to grow Te nanostructures in hydrophobic solvents, the presence of a miscible hydrophilic solvent is necessary. For instance, when methanol was added into chloroform to form a 50/50 volume mixture, differently sized Te nanorods were generated (see Supporting Information).

Another key factor of this method is the CPB concentration. Increasing the CPB concentration from 0.5 g/L to 5 g/L in THF leads to the increase of nanorod length from 741 ± 37.8 nm (AR = 21) to 822 ± 107 nm (AR = 22) (see Supporting Information). However, at a lower CPB concentration of 0.05 g/L, irregular Te nanorods with a small amount of submicron-sized particles were generated (see Supporting Information). When pure THF was used in a control experiment, only aggregates of irregular shaped Te particles were found (Fig. 6-3h). From this, it can be concluded that not only the solvent but also the CPB concentration are essential to prepare uniform Te nanorods.

6.4 Conclusions

In summary, we have developed a simple solution approach for the synthesis of uniform single-crystalline Te nanorods at room temperature via a CPB-assisted method. This approach can prepare Te nanorods with high aspect ratio and avoids high temperature, purification steps and adding of reducing agent. Due to the high similarity of the crystal structure, the CPB assisted method may also be extended to synthesize other elemental nanostructures, like Se. Furthermore, the unique property of the prepared Te nanorods to assemble inorganic nanoparticles is quite useful to generate various Te nanorod-based complex structures.

Acknowledgement: The authors acknowledge the Deutsche Forschungsgemeinschaft (SPP 1165) for financial support. We thank Dr. Wolfgang Milius for the help with JCPDS files and Dr. Mingfu Zhang and Dr. Saikat Mandal for helpful discussions.

6.5 References

1. Kim, H.-M.; Cho, Y.-H.; Lee, H.; Kim, S. I.; Ryu, S. R.; Kim, D. Y.; Kang, T. W.; Chung, K. S. *Nano Lett.* **2004,** 4, (6), 1059-1062.
2. Huang, Y.; Duan, X.; Lieber, C. M. *Small* **2005,** 1, (1), 142-147.
3. Johnson, J. C.; Choi, H.-J.; Knutsen, K. P.; Schaller, R. D.; Yang, P.; Saykally, R. J. *Nat. Mater.* **2002,** 1, (2), 106-110.
4. Wang, Z. L. *Adv. Mater.* **2003,** 15, (5), 432-436.
5. X. Duan, C. M. L. *Adv. Mater.* **2000,** 12, (4), 298-302.
6. Ma, C.; Wang, Z. L. *Adv. Mater.* **2005,** 17, (21), 2635-2639.
7. Grebinski, J. W.; Richter, K. L.; Zhang, J.; Kosel, T. H.; Kuno, M. *J. Phys. Chem. B* **2004,** 108, (28), 9745-9751.
8. Fan, Z.; Dutta, D.; Chien, C.-J.; Chen, H.-Y.; Brown, E. C.; Chang, P.-C.; Lu, J. G. *Appl. Phys. Lett.* **2006,** 89, (21), 213110/1-213110/3.
9. Peng, X. S.; Zhang, J.; Wang, X. F.; Wang, Y. W.; Zhao, L. X.; Meng, G. W.; Zhang, L. D. *Chem. Phys. Lett.* **2001,** 343, (5,6), 470-474.
10. Adelung, R.; Aktas, O. C.; Franc, J.; Biswas, A.; Kunz, R.; Elbahri, M.; Kanzow, J.; Schuermann, U.; Faupel, F. *Nat. Mater.* **2004,** 3, (6), 375-379.
11. Rao, C. N. R.; Govindaraj, A.; Deepak, F. L.; Gunari, N. A.; Nath, M. *Appl. Phys. Lett.* **2001,** 78, (13), 1853-1855.
12. Elbahri, M.; Paretkar, D.; Hirmas, K.; Jebril, S.; Adelung, R. *Adv. Mater.* **2007,** 19, (9), 1262-1266.
13. Milenkovic, S.; Hassel Achim, W.; Schneider, A. *Nano Lett.* **2006,** 6, (4), 794-9.
14. Araki, K.; Tanaka, T. *Jpn. J. Appl. Phys.* **1972,** 11, (4), 472-9.
15. Zhu, Y.-J.; Wang, W.-W.; Qi, R.-J.; Hu, X.-L. *Angew. Chem. Int. Ed.* **2004,** 43, (11), 1410-1414.
16. Lu, Q.; Gao, F.; Komarneni, S. *Adv. Mater.* **2004,** 16, (18), 1629-1632.
17. Zhao, A.; Zhang, L.; Pang, Y.; Ye, C. *Applied Physics A: Materials Science & Processing* **2005,** 80, (8), 1725-1728.
18. Gautam, U. K.; Rao, C. N. R. *J. Mater. Chem.* **2004,** 14, (16), 2530-2535.
19. Mayers, B.; Gates, B.; Yin, Y.; Xia, Y. *Adv. Mater.* **2001,** 13, (18), 1380-1384.
20. Chen, X.; Wang, Z.; Wang, X.; Wan, J.; Qian, Y. *Appl. Phys. A* **2005,** 80, (7), 1443-1445.

21. Mayers, B.; Xia, Y. *Adv. Mater.* **2002,** 14, (4), 279-282.
22. Mayers, B.; Xia, Y. *J. Mater. Chem.* **2002,** 12, (6), 1875-1881.
23. Tang, Z.; Wang, Y.; Sun, K.; Kotov, N. A. *Adv. Mater.* **2005,** 17, (3), 358-363.
24. Zheng, R.; Cheng, W.; Wang, E.; Dong, S. *Chem. Phys. Lett.* **2004,** 395, (4-6), 302-305.
25. Djalali, R.; Li, S.-Y.; Schmidt, M. *Macromolecules* **2002,** 35, (11), 4282-4288.
26. Zhang, M.; Estournes, C.; Bietsch, W.; Müller, A. H. E. *Adv. Funct. Mater.* **2004,** 14, (9), 871-882.
27. Zhang, M.; Drechsler, M.; Müller, A. H. E. *Chem. Mater.* **2004,** 16, (3), 537-543.
28. Zhang, M.; Breiner, T.; Mori, H.; Müller, A. H. E. *Polymer* **2003,** 44, (5), 1449-1458.
29. Kang, Y. S.; Risbud, S.; Rabolt, J. F.; Stroeve, P. *Chem. Mater.* **1996,** 8, (9), 2209-2211.
30. Yang, S.; Liu, H. *J. Mater. Chem.* **2006,** 16, (46), 4480-4487.
31. Yu, H.; Gibbons, P. C.; Buhro, W. E. *J. Mater. Chem.* **2004,** 14, (4), 595-602.
32. Sun, Y.; Gates, B.; Mayers, B.; Xia, Y. *Nano Lett.* **2002,** 2, (2), 165-168.
33. Liu, Z.; Hu, Z.; Liang, J.; Li, S.; Yang, Y.; Peng, S.; Qian, Y. *Langmuir* **2004,** 20, (1), 214-218.
34. He, Z.; Yu, S.-H.; Zhu, J. *Chem. Mater.* **2005,** 17, (11), 2785-2788.
35. Mohanty, P.; Kang, T.; Kim, B.; Park, J. *J. Phys. Chem. B* **2006,** 110, (2), 791-795.
36. Weng, L.; Hodgson, S. N. B.; Ma, J. *J. Mater. Sci. Lett.* **1999,** 18, (24), 2037-2039.
37. Petragnani, N.; Lo, W.-L. *J. Am. Chem. Soc.* **1998,** 9, (5), 415-425.
38. Dennis, L. M.; Anderson, R. P. *J. Am. Chem. Soc.* **1914,** 36, 882-909.
39. Kambe, N.; Kondo, K.; Morita, S.; Murai, S.; Sonoda, N. *Angew. Chem.* **1980,** 92, (12), 1041-2.
40. Li, J.; Tang, S.; Lu, L.; Zeng, H. C. *J. Am. Chem. Soc.* **2007,** 129, (30), 9401-9409.

6.6 Supporting Information

The CPB [*t*BMA$_{90}$]$_{3200}$ was synthesized via the combination of anionic polymerization of the poly(2-hydroxyethyl methacrylate) (poly(HEMA)) backbone and atom transfer radical polymerization (ATRP) of the poly(*tert*-butyl methacrylate) (P*t*BMA) side chain.[28] The poly(HEMA) backbone was synthesized via anionic polymerization of 2-(trimethylsilyloxy)ethyl methacrylate and its following hydrolysis. The ATRP macroinitiator poly(2-bromoisobutyryloxyethyl methacrylate) (PBIEM) was obtained by the esterification of the poly(HEMA) backbone and its polydispersity was determined to be 1.14 via gel permeation chromatography (GPC) (eluent: tetrahydrofuran with 4% tetra-n-butylammonium bromide, standard: polystyrene). The degree of polymerization (DP) of the macroinitiator PBIEM was calculated to be 3,200 according to its polydispersity (1.14) in GPC and the absolute weight-averaged molecular weight achieved by static light scattering (SLS) measurement. The CPB side chains were prepared via ATRP of *tert*-butyl methacrylate (*t*BMA) by the "grafting from" technique. The initiation efficiency of the macroinitiator was determined to be 0.84 by the solvolysis via base(sodium methoxide)-catalyzed transesterification reaction in methanol, which cleaves the P*t*BMA side chains from the backbone and compare their molecular weight from GPC (eluent: tetrahydrofuran, standard: poly(tert-butyl methacrylate)) with that calculated from the conversion of ATRP polymerization. The formed CPB [*t*BMA$_{90}$]$_{3200}$ has a polydispersity of 1.36 (GPC, eluent: tetrahydrofuran, standard: polystyrene) and can be visualized by atomic force microscopy as shown in Fig. 6-4.

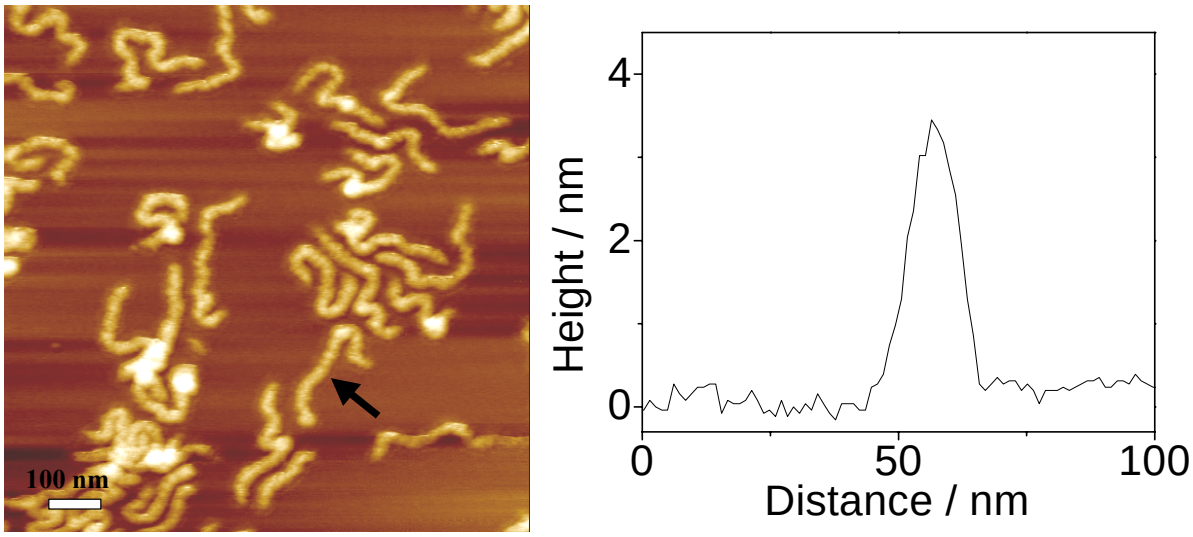

Figure 6-4. AFM image of CPB $[t\text{BMA}_{90}]_{3200}$ on mica surface (height: 8 nm), and a height section profile of a single CPB indicated by the black arrow. The sample was prepared by dip-coating from dilute CPB solution in $CHCl_3$ with concentration of ~0.01 g/L, onto freshly cleaved mica surface. The AFM images were taken with a Digital Instruments Dimension 3100 microscope operated in Tapping Mode (free amplitude of the cantilever <30 nm, set point ratio <0.90). The section of a single CPB $[t\text{BMA}_{90}]_{3200}$ on mica surface was analyzed by using the software "Nanoscope III" (Version 5.13) and "UTSCSA Imagetool". The height profile (on the right side) indicates that the single CPB in its center is 3.5 nm high.

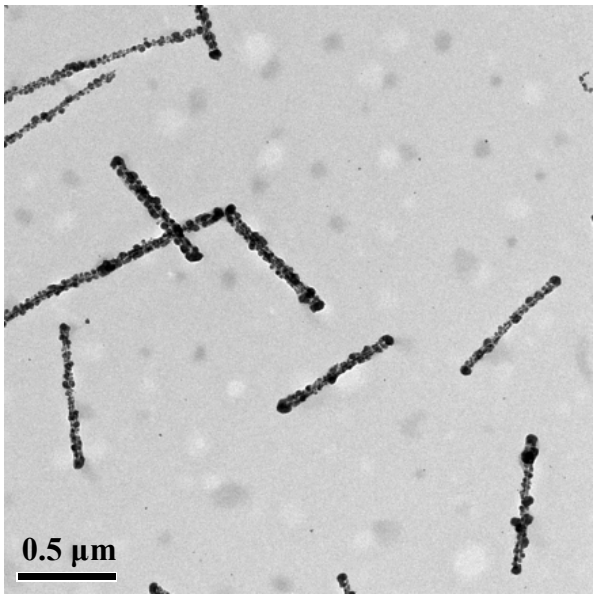

Figure 6-5. TEM image of Te nanorod/nanoparticle complex obtained by aging under argon in dark for 2 weeks in experiment 1.

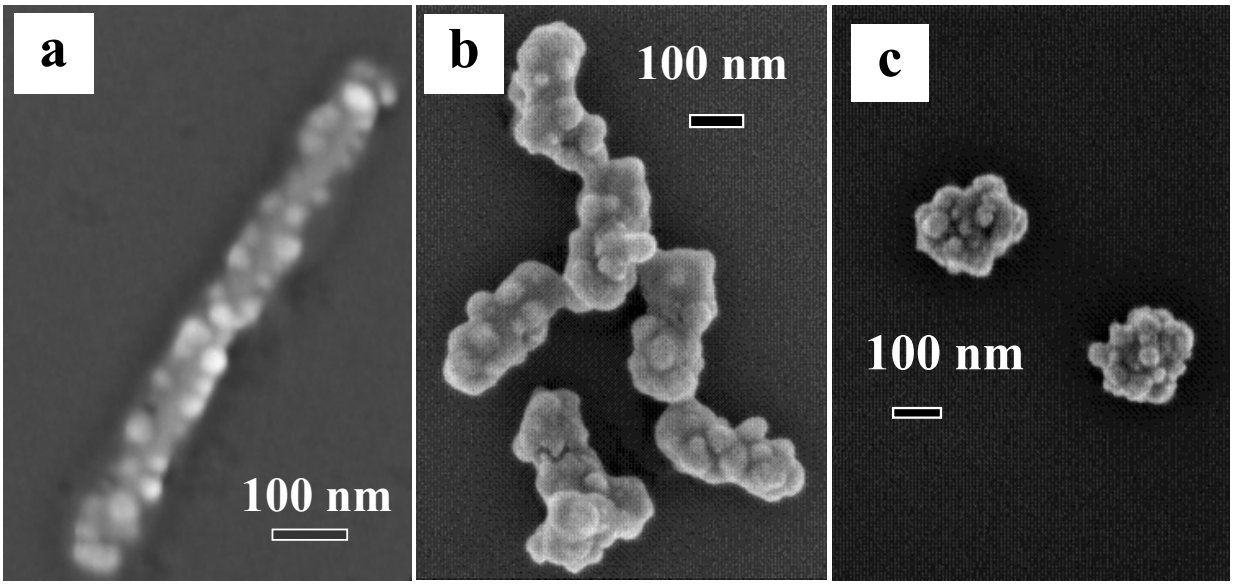

Figure 6-6. Field-emission Scanning Electron Microscopy (FESEM) images of the Te nanorod/nanoparticle complex prepared from CPB solution in THF in experiment 1 (a) and in acetone in experiment 2 (b). (c) is the FESEM image of the Te submicron-sized particle/nanoparticle complex prepared from CPB solution in dioxane in experiment 3.

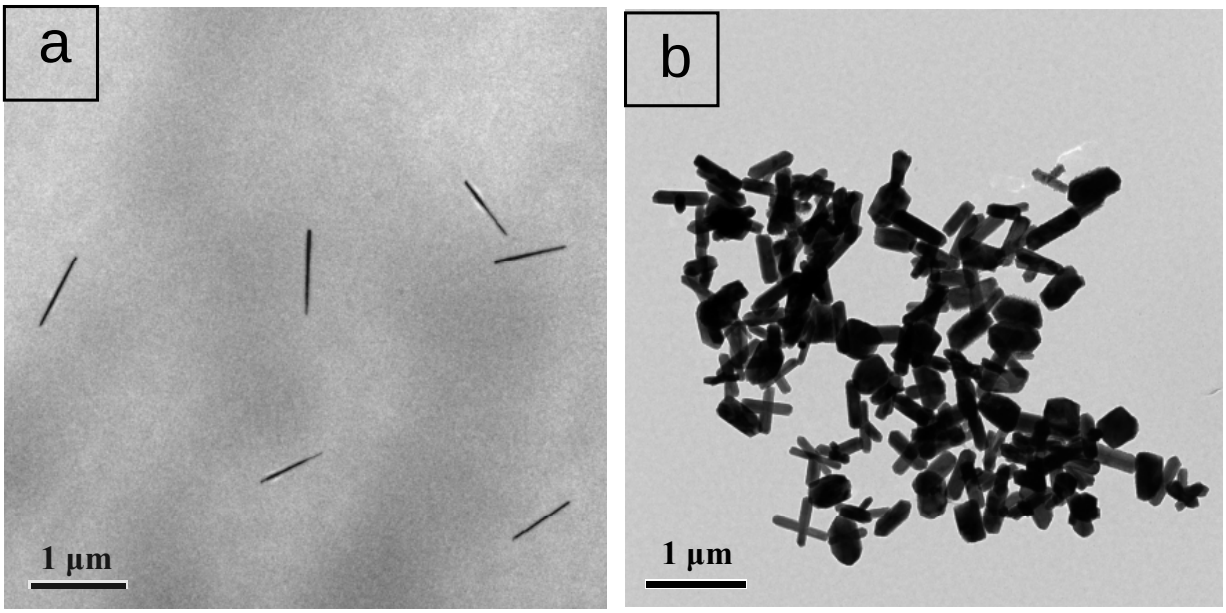

Figure 6-7. a) TEM image of the Te nanorods prepared with CPB concentration of 5 g/L in THF in experiment 7. b) TEM image of the Te nanostructures obtained with CPB concentration of 0.05 g/L in THF in experiment 8.

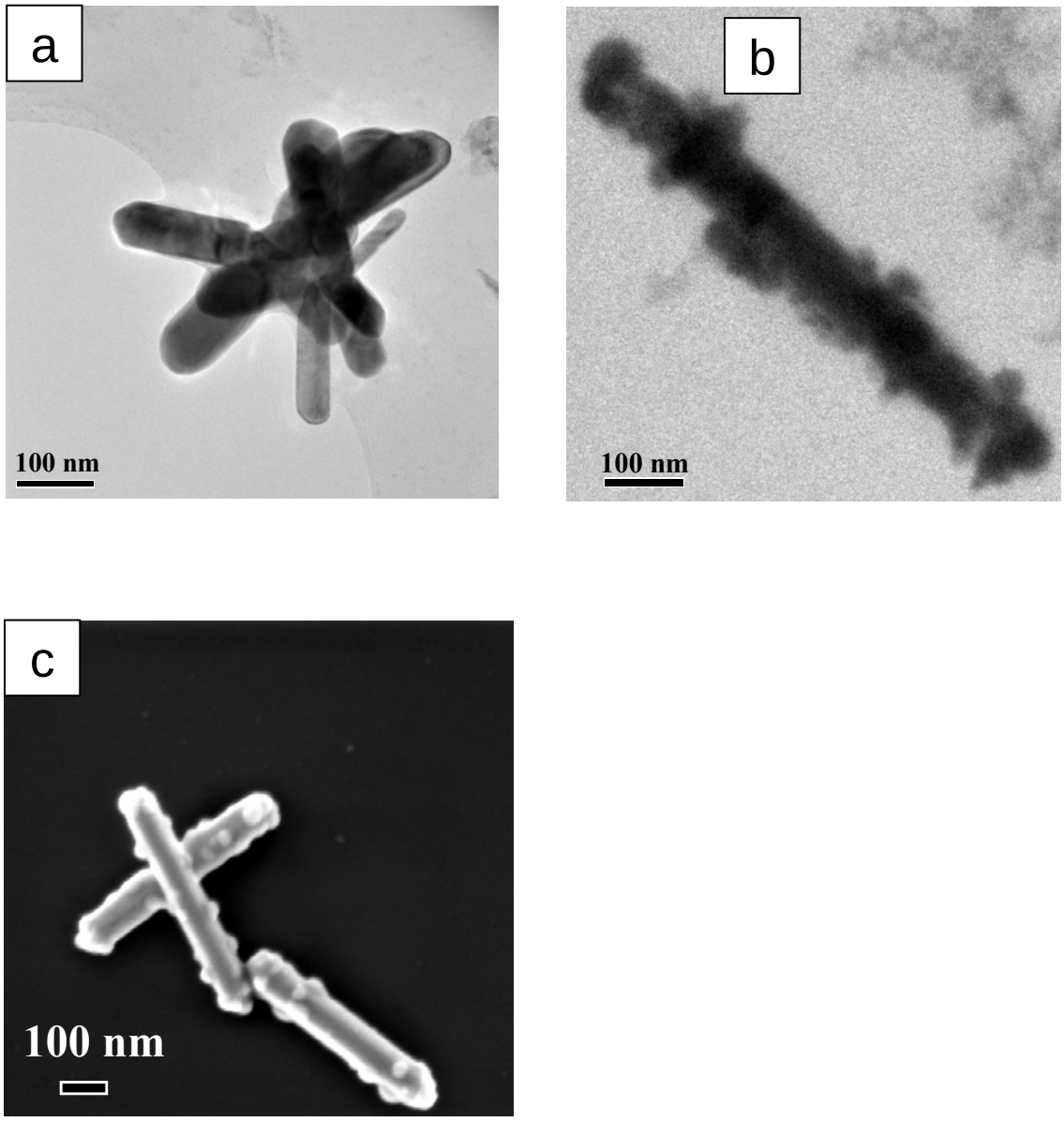

Figure 6-8. TEM images of Te nanorods (a), the nanorod/nanoparticle complex (b) and FESEM image of the Te nanorod/nanoparticle complex (c) formed in a chloroform/methanol mixture (v/v=1:1) in experiment 6. The TEM image (a) demonstrates that in the presence of CPB, Te nanorods, although with different size, were generated in the mixture solvent of chloroform and methanol (v/v=1:1). The refluxing under argon converted the Te nanorods to Te nanorod/nanoparticle complex structure, as shown in TEM (b) and FESEM (c) images.

Chapter 7

Alignment of Tellurium Nanorods via a Magnetization-Alignment-Demagnetization ("MAD") Process assisted by an External Magnetic Field

Abstract

Tellurium (Te) nanorods have been successfully aligned on a solid substrate via a "magnetization-alignment-demagnetization" ("MAD") process in the presence of an external magnetic field. Te nanorods carrying a poly(*tert*-butyl methacrylate) shell were first converted into magnetic nanocylinders by assembling magnetite nanoparticles on their surface via a hydrophobic interaction in THF. We demonstrate that below a critical concentration of the nanoparticles, this assembly process is able to quantitatively tune the magnetite nanoparticles´ density on the nanorods in terms of their stoichiometric ratio. Due to the polymer and surfactant on their surface, the formed magnetic nanocylinders are soluble in THF, and aligned when dried on a solid substrate in the presence of an external magnetic field. The demagnetization of the pre-aligned nanocylinders was achieved via an acid-etching process, leaving Te nanorods in an aligned state. This "MAD" process can be extended as a general procedure for other non-magnetic 1-D nanostructures. Additionally, the non-etched magnetic nanocylinders can be potentially applied in field of magnetorheology.

* The results of this chapter have been submitted to *ACS Nano* as:

"Alignment of Tellurium Nanorods via a Magnetization-Alignment-Demagnetization ("MAD") Process assisted by an External Magnetic Field"

by Jiayin Yuan, Haitao Gao, Felix Schacher, Youyong Xu, Reinhard Richter, Wolfgang Tremel and Axel H. E. Müller*

7.1 Introduction

There has been expanding interest in one-dimensional (1-D) nanostructures in the last decade, such as nanorods, nanotubes, or nanowires, due to a range of size- and geometry-dependent properties[1-4] and potential applications in optical and electronic devices,[5–7] sensing and imaging,[8, 9] gene delivery,[10, 11] etc. So far, great progress has been achieved in developing numerous 1-D nanostructures through various techniques and methods.[12-17] Currently, the organization and manipulation of these 1-D nanostructures have attracted a lot of attention, as further scientific and technological advances in the application of 1-D nanostructures in functional nanodevices depend strongly on the ability to assemble them into ordered and complex architectures. To date, only a few techniques exist that allow the organization of 1-D nanostructures with notable examples of using binding of ligands that stabilize anisotropic nanoparticles[18-21], biorecognition[22], template-directed self-assembly of nanorods,[23-25] external electric or magnetic field introduced alignment,[26-29] interactions between segmented polymer–metal rods in selective solvents[30], etc. In general, most of these methods are limited and available only for certain specific 1-D nanomaterials with corresponding required physical properties.

Very recently, we observed that tellurium (Te) nanorods covered by a layer of poly(*tert*-butyl methacrylate) (P*t*BMA) could assemble inorganic (Te or magnetite) nanoparticles onto their surface via a hydrophobic interaction.[31] This interesting finding leads to continuing research on the Te nanorods functionalized with magnetite nanoparticles, named as magnetic nanocylinders, which combine the uniform geometry of the Te nanorods and the magnetic function of the magnetite nanoparticles. In this paper, we report a facile and unique process, named as "magnetization-alignment-demagnetization" ("MAD") process to align Te nanorods on a solid substrate, as illustrated in Scheme 7-1. In this process, we demonstrate for the first time the quantitative control of magnetite nanoparticles' density on the nanorods, supported by mathematic calculations, the aligning behavior of the formed magnetic nanocylinders, and the stepwise etching of pre-aligned magnetic nanocylinders into Te nanorods. In fact, to the best of our knowledge this is the first example of a general approach to align non-magnetic nanorods in the magnetic field by decorating their surface with magnetite nanoparticles followed by selective removal of these nanoparticles.

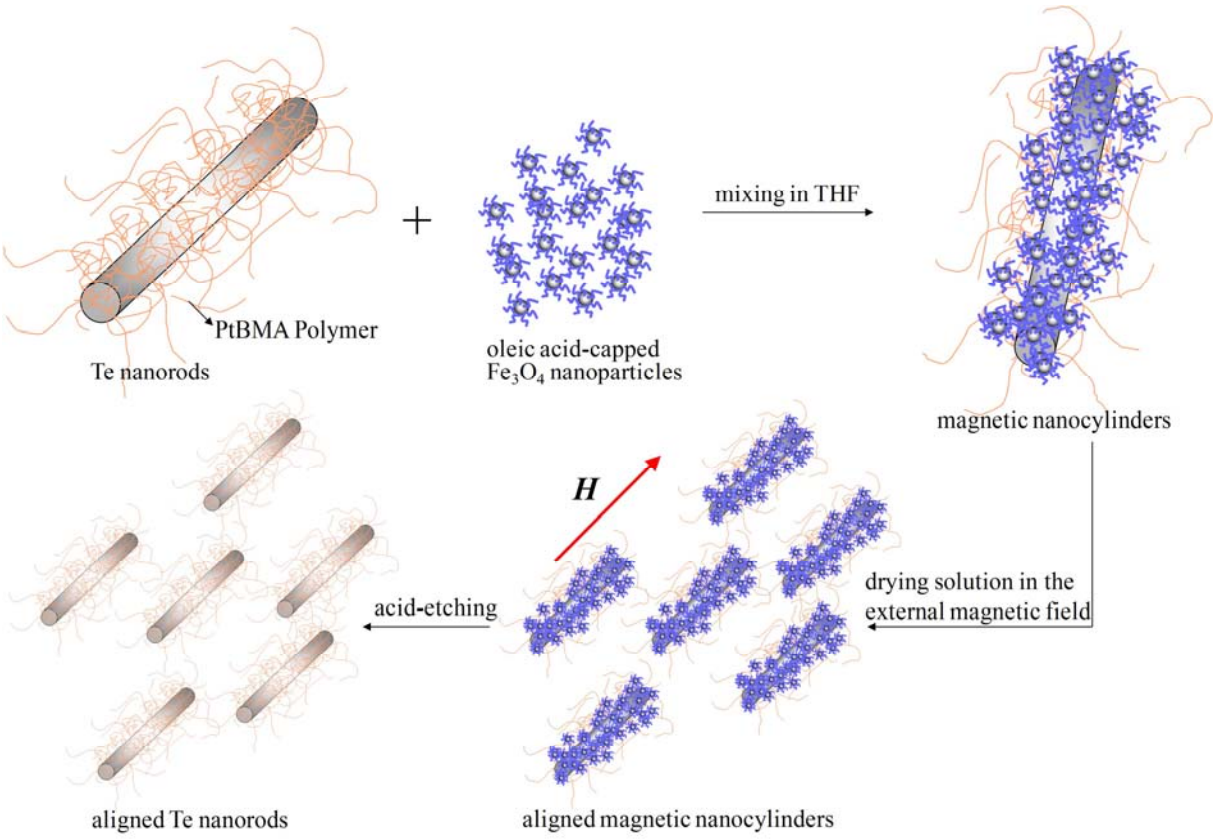

Scheme 7-1. Illustration of the alignment of Te nanorods via a "MAD" process assisted by an external magnetic field.

1-D magnetic nanostructures have been the constant pursuit of researchers[32] due to their expected utilizations as sensors, magnetic recording and spintronic devices.[33-35] Here, as a coexistent advantage of the versatile "MAD" process, magnetic nanocylinders are constructed more easily compared to other synthetic methodologies. Although the coating of gold nanorods with magnetic nanoparticles has been reported very recently[36], our synthetic strategy is obviously superior with four-fold advantages: 1) no purification is required after mixing the nanoparticles and nanorods in THF, as all nanoparticles statistically attach to the nanorods below a critical concentration; 2) the magnetic property of nanocylinders is quantitatively tunable by varying the stoichiometric ratio of these two components; 3) the size and aspect ratio of the magnetic nanocylinders stems from the Te nanorods, which can be effectively controlled[32]; 4) due to the protective polymer and surfactant layer on their surface, these nanocylinders are well-dispersed in organic solvents, which facilitates the further processing.

7.2 Experimental section

Preparation of linear poly(*tert*-butyl methacrylate) (P*t*BMA). P*t*BMA with high molecular weight was synthesized by atom transfer radical polymerization (ATRP). Briefly, 0.049 g (0.5 mmol) of CuCl catalyst with 0.086 g (0.5 mmol) of N,N,N′,N′′,N′′-pentamethyldiethylenetriamine in 10 mL of toluene, 0.095 g (0.5 mmol) of the initiator *p*-toluenesulfonyl chloride in 4 mL of toluene, and 42.66 g (0.3 mol) purified *t*BMA in 40 mL of toluene were first prepared and bubbled with argon for 10 min in 3 separated screw cap glasses. After transferring the catalyst and initiator to *t*BMA monomer with nitrogen-flashed syringe, the solution was stirred in an oil bath at 90 °C for 26 hours. Then the mixture was cooled to room temperature, and filtered through an Al_2O_3 column. After precipitation in water, the product was freeze-dried from dioxane. The number-averaged molecular weight is 95,000 g/mol and the polydispersity is 1.09, measured from a conventional GPC using THF as eluent and P*t*BMA as standard.

Preparation of magnetite nanoparticles. The oleic acid-capped magnetite nanoparticles were prepared by the co-precipitation method.[34,35] Briefly, 28.1 g of $FeCl_3 \cdot 6H_2O$ in 550 mL of water and 10.9 g of $FeCl_2 \cdot 4H_2O$ in 30 mL H_2O (with 4 drops of fuming HCl) were mixed and kept at 60°C. A black precipitate appeared when 90 mL of aqueous NH_4OH (25%) was added to the solution. After stirring for 10 minutes, the black precipitate was separated by magnet and washed with H_2O till pH 9. To cap the surface with oleic acid, the mixture of 300 mL of water and 32 mL of 10 wt% oleic acid in paraffin oil was added. After heating at 80 °C for 1 h, the oleic acid-capped nanoparticles were separated by magnet, and the black oil phase was washed with water and ethanol to remove the excess oleic acid. Further filtration through glass fiber was carried to remove any agglomerates and the mixture was centrifuged for 1 h (4000 rms, 30°C).

Preparation of Te nanorods. The Te nanorods were prepared from the room-temperature decomposition of H_2Te gas in a P*t*BMA solution in THF.[15] As an example, the synthesis of Te (1) nanorods was carried out under a gentle argon flow at room temperature. A three-necked flask with magnetic stirrer, 1.25 g of aluminum telluride (Al_2Te_3, 99.5 % pure, Gerac) and 60 mL of dioxane, was equipped with a bubble counter and connected to a pipeline inserted into a 250 mL reaction flask containing 200 mL of P*t*BMA solution (0.5 g/L) in THF. The dispersion of Al_2Te_3 in dioxane and the P*t*BMA solution in THF were bubbled with argon for 30 minutes. Then 10 mL

of oxygen-free H_2SO_4 solution (0.5 M) was added dropwise by a syringe pump within 2 hours. The generated H_2Te gas was distributed via argon flow into the reaction flask. At the end, argon was further bubbled for 30 min and the reaction flask was further stirred overnight. For the synthesis of Te (2) nanorods, 2 g of Al_2Te_3 and 1 g/L of P*t*BMA in THF were used; in the case of Te (3) nanorods, 1.6 g of Al_2Te_3 and 0.5 g/L of P*t*BMA in THF were used.

Preparation and alignment of magnetic nanocylinders. The assembly of magnetite nanoparticles on the Te nanorod surface was achieved by adding different amounts of magnetite nanoparticle solution into the Te nanorod solution in THF under strong mechanical shaking under argon for 2 hours. The magnetic nanocylinders were aligned in a magnetic field of 0.3 T. The sample was prepared by placing one drop of the magnetic nanocylinder solution in THF on a carbon-coated TEM grid and immediately inserted into the magnetic field, which was parallel to the TEM grid surface.

Demagnetization process. The acid-etching process was carried out in an aqueous HCl solution (pH = 1) under an argon atmosphere to avoid the oxidation of the Te nanorods. The aligned magnetic nanocylinders on a carbon-coated copper TEM grid were immersed into the aqueous HCl solution for a desired period. To monitor the etching process, the sample was taken out after 20, 40, 60 and 80 min respectively, and rinsed by pure water before subjected to the TEM investigation.

Transmission electron microscopy (TEM). TEM images and the electron diffraction patterns were taken on a Zeiss EM EF-TEM instrument operated at 200 kV. For each sample, a 2 µl droplet of the solution was deposited onto a carbon-coated copper TEM grid.

Scanning electron microscopy (SEM). (SEM) was performed using a Zeiss 1530 Gemini instrument equipped with a field emission cathode with a lateral resolution of approximately 2 nm. The sample was prepared by placing one drop of the solution onto a purified silicon wafer.

Superconducting quantum interference device (SQUID) measurement. Magnetic properties of the samples were studied with a Quantum Design MPMS-XL superconducting quantum interference device magnetometer between 300 and 5 K, with a maximum applied field of 50 kOe (= 5 T). The magnetization was also measured as a function of temperature at a given applied field in the field cooled (FC) and zero field cooled (ZFC) modes. For the ZFC measurements, the sample was first cooled down to 5 K in zero magnetic field. Subsequently, a

magnetic field of 100 Oe (10 mT) was applied and the magnetization was measured while the temperature was increased up to 300 K. Afterwards, the magnetization of the sample under a magnetic field of 100 Oe as a function of decreasing temperature (down to 5 K) was measured as the FC magnetization.

Size distribution analysis. The statistical analysis of the size distribution of the nanoparticles and nanorods was performed using the UTHSCSA ImageTool program (University of Texas). In each sample 100 ± 10 objects were measured to define the dimension.

7.3 Results and discussion

Synthesis and characterization of magnetite nanoparticles and Te nanorods. As the basic components to build the magnetic nanocylinders, magnetite nanoparticles and Te nanorods were separately prepared first. Fig. 7-1A shows a representative transmission electron microscopy (TEM) image of the magnetite nanoparticles produced through the conventional co-precipitation method.[37, 38] Since the nanoparticles are capped with oleic acid molecules and possess an alkyl layer on the surface, they are soluble in most organic solvents, like cyclohexane, benzene and also in THF. The crystallinity of the nanoparticles was checked by high-resolution TEM (Fig. 7-1B). There is clear evidence of lattice planes corresponding to the (220) planes of magnetite with 0.2967 nm interplanar spacing. Their size distribution histogram in Fig. 7-1C, which resembles a Gaussian curve, shows that the nanoparticles studied in this article are averagely 9.6 nm in diameter with a standard deviation of 21%. Electron diffraction measured from a large zone (Fig. 7-1D), presents the distinct rings that can be indexed to the magnetite structure. The Mössbauer spectrum (see Supporting Information) further confirms the phase to be magnetite Fe_3O_4, which is typical for the magnetic nanoparticles obtained through the co-precipitation method.[39, 40]

The Te nanorods were prepared by purging in-situ generated H_2Te gas into a P*t*BMA polymer solution in THF at room temperature, as we reported earlier.[31] In this research, three types of Te nanorods with different aspect ratios were synthesized for the study of the magnetic nanocylinders. Their dimensions are listed in Table 7-1. As an example, a typical TEM image of the Te (1) nanorods is shown in Fig. 7-1E. Due to the P*t*BMA polymer attached to the surface, the nanorods are well soluble and form a clear blue solution in THF. The TEM image in Fig. 7-1F with a higher magnification exhibits the smooth surface of the nanorods. These nanorods are averagely 422 ± 48 nm long and 47 ± 11 nm in diameter, giving an aspect ratio of 9. The length distribution histogram is present in Fig. 7-1G, which matches a Gaussian distribution as well. The high-resolution TEM (Fig. 7-1H) and its electron diffraction pattern (Fig. 7-1I) proves that the Te nanorod is structurally single-crystalline along the longitudinal axis (c axis), corresponding to the interplanar spacing between the (001) planes of the hexagonal lattice. From the above characterizations, both nanoparticles and nanorods as the constructing units are single crystalline with a narrow size distribution in their dimension, and soluble in THF.

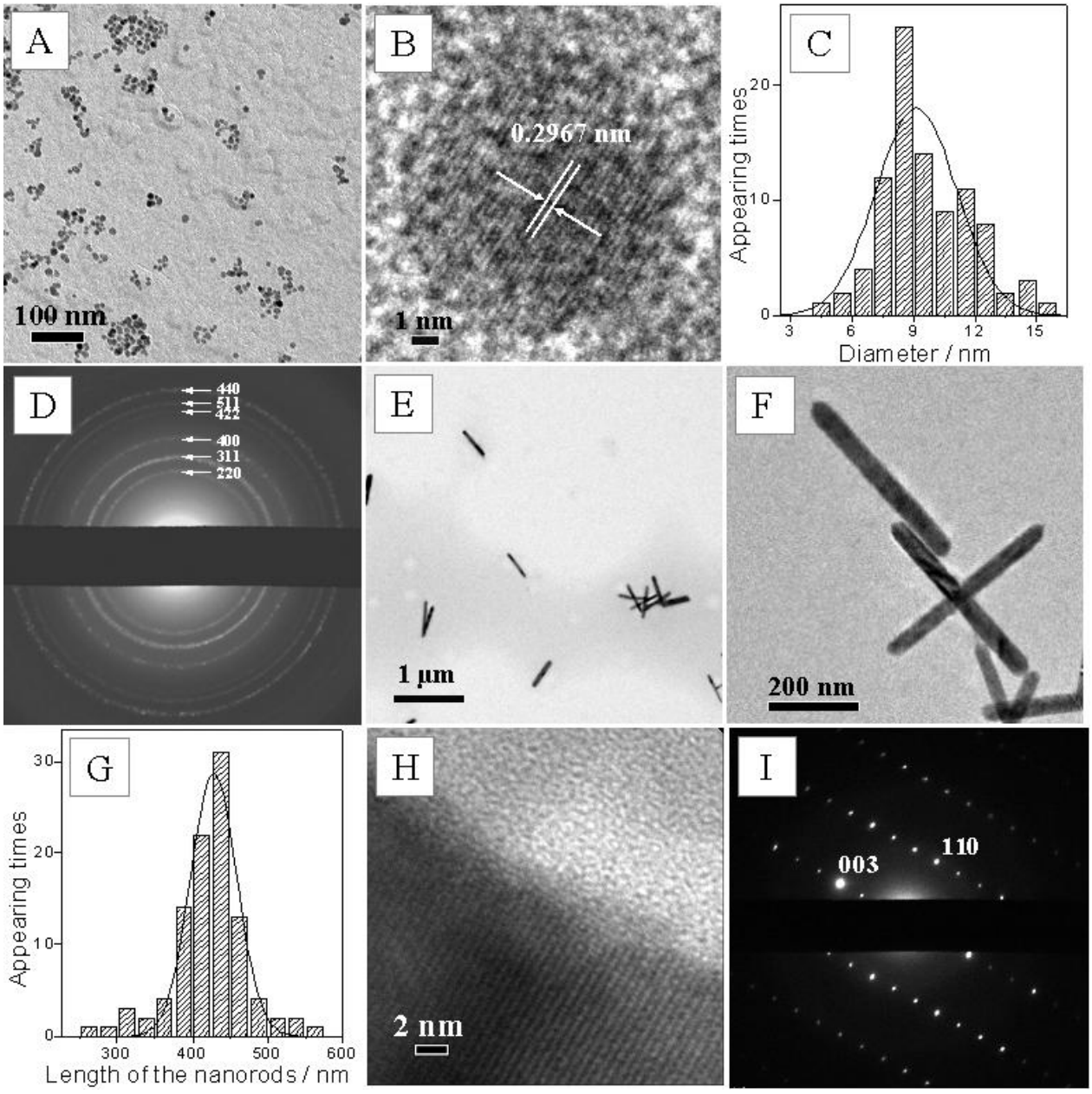

Figure 7-1. (A), TEM image of the as-synthesized magnetite nanoparticles; (B), high-resolution TEM image of a single nanoparticle; (C), size distribution histogram of the nanoparticles (black curve is the Gaussian fit); (D), selected area electron diffraction pattern of the nanoparticles; (E), TEM image of the Te (1) nanorods; (F), their enlarged view; (G), their length distribution histogram (black curve is the Gaussian fit); (H) high-resolution TEM image of a single nanorod; and (I), its corresponding electron diffraction pattern.

Table 7-1. Three types of Te nanorods with different lengths and diameters obtained via TEM investigation.

Sample	Length /nm	Diameter /nm	Aspect Ratio
Te (1)	422 ± 48	47 ±11	9
Te (2)	295 ± 47	21 ± 5	14
Te (3)	473 ± 46	155 ± 32	3

Controlled assembly of magnetite nanoparticles on Te nanorods. The magnetic nanocylinders were produced by mixing the Te nanorod solution and magnetite nanoparticle solution in THF under strong mechanical shaking. During this process, the magnetite nanoparticles assembled onto the nanorod surface via the hydrophobic interaction[41] between the P*t*BMA layer on the nanorods and the alkyl chains on the nanoparticles. Fig. 7-2A-D shows various TEM images of the magnetic Te (1) nanocylinders that were prepared with constant Te (1) nanorod concentration (60 mg/L) and decreasing concentration of nanoparticles from 50.6 mg/L (Fig. 7-2A) to 1.87 mg/L (Fig. 7-2D) in THF solution. All TEM images reveal that the nanoparticles tend to adhere onto the nanorod rather than stay in THF. By carefully examining the TEM images, the free nanoparticles, indicated by a white arrow, become evidently less and less from Fig. 7-2A to 7-2B until totally vanishing in Fig. 7-2C and 7-2D. Due to the large gap between the nanoparticle concentrations in Fig. 7-2B and 7-2C, an additional sample was prepared in the same way with only 6.5 mg/L of magnetite nanoparticles in THF solution, which showed the existence of free nanoparticles in the TEM investigation. Thus we define the concentration of the magnetite nanoparticles in Fig. 7-2C, 5.2 mg/L as the critical concentration. Above it (Fig. 7-2A-B), free nanoparticles exist in the THF solution; in contrast, below it all nanoparticles will sit on the nanorods (Fig. 7-2C-D), which leads to pure magnetic nanocylinders in THF.

A close view of the magnetic nanocylinders in Fig. 7-2C and 7-2D indicates a statistical distribution of the nanoparticles on all Te nanorods. Since a triple amount of magnetite nanoparticles was introduced in Fig. 7-2C compared to Fig. 7-2D, the magnetic nanocylinders in Fig. 7-2C have a higher density of nanoparticles. A calculation based on the concentrations of Te nanorods and Fe_3O_4 nanoparticles proves that each nanocylinder in Fig. 7-2C carries ca. 167

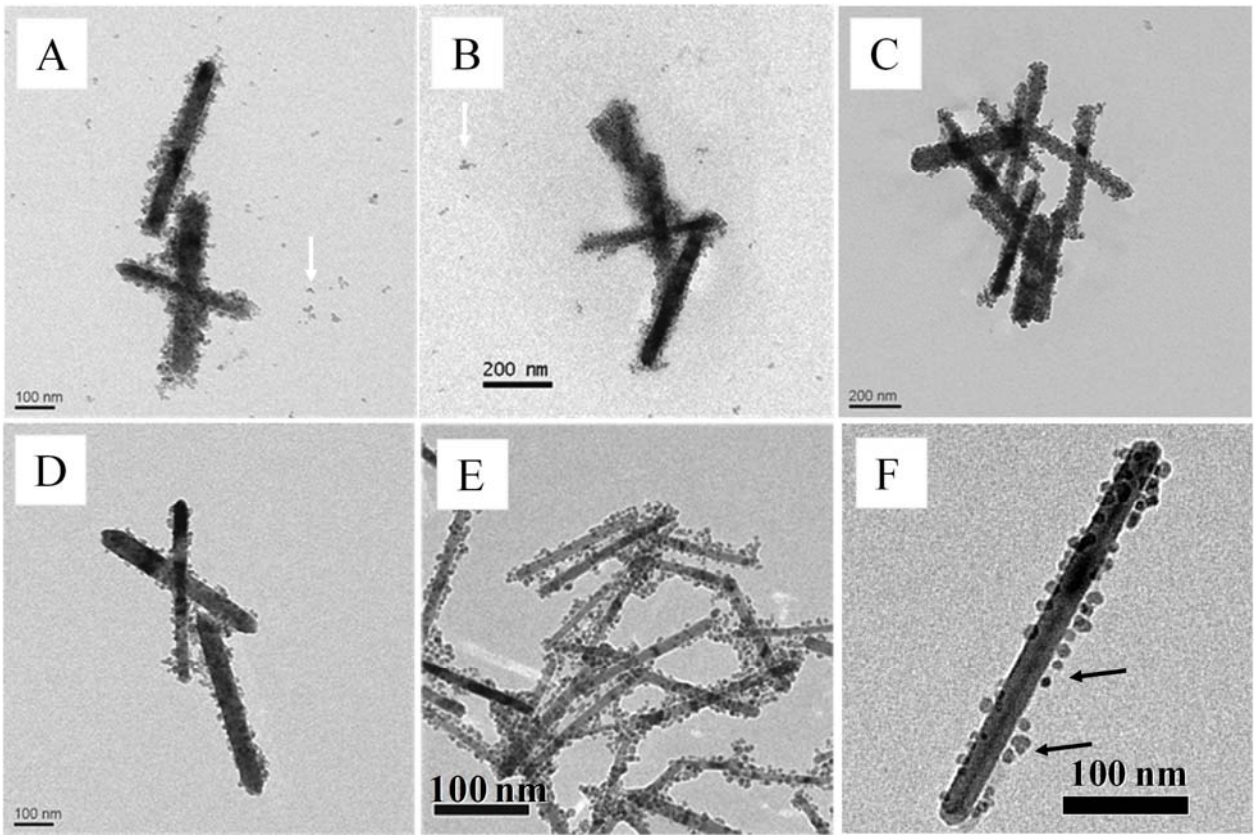

Figure 7-2. (A)-(D), magnetic Te (1) nanocylinders prepared from Te (1) nanorods (60 mg/L) and different concentrations of magnetite nanoparticles: (A) 50.6 mg/L, (B) 16.8 mg/L, (C) 5.2 mg/L, and (D) 1.87 mg/L in THF. The stoichiometric ratios (nanoparticles to nanorods) are (A) 1625, (B) 539, (C) 167 and (D) 60, respectively. (E), magnetic Te (2) nanocylinders prepared from Te (2) nanorods (33.7 mg/L) and magnetite nanoparticles (8.65 mg/L) with a stoichiometric ratio of 69. (F), a single Te (2) magnetic nanocylinder with ca. 50 nanoparticles.

nanoparticles, and in Fig. 7-2D only 60 (see Supporting Information). As the magnetic cylinders are based on the nanoparticles, their magnetic properties can be quantitatively tuned by loading different amounts of nanoparticles below the critical concentration. In the same manner, the critical concentration of the nanoparticles on Te (2) nanorods (33.7 mg/L) was determined to be 8.65 mg/L. The corresponding TEM image is shown in Fig. 7-2E. Here, according to the stoichiometric ratio, each Te (2) nanorod carries only 69 magnetite nanoparticles, much less than the Te (1) nanorod in Fig. 7-2C due to its smaller size and less surface, although both are under their own critical concentration of the nanoparticles, respectively. In order to illustrate the

hydrophobic interaction between the oleic acid-capped nanoparticles and P*t*BMA polymer protected Te nanorods, a single Te (2) magnetic nanorod carrying ca. 50 nanoparticles is enlarged in Figure 7-2F, where the spacing between the nanoparticles and Te nanorod is clearly visible. Here, the strong hydrophobic interaction fixes and "suspends" the nanoparticles in the dense polymer matrix on the nanorod surface.

Characterization of magnetic nanocylinders. To detail the assembly of magnetite nanoparticles, the formed magnetic Te (1) nanocylinders at the critical concentration of nanoparticles are subjected to further investigations. Fig. 7-3A displays a TEM image of a single magnetic Te (1) nanocylinder. An enlarged view of its end (the inset in Fig. 7-3A) reveals a dense layer of nanoparticles on the nanorod surface. At several sites on the nanorod (indicated by black arrows), packing with double layers of nanoparticles is also detected. The electron diffraction pattern of the single magnetic nanocylinder is displayed in Fig. 7-3B. As expected, both dotted and ring-shaped patterns appear simultaneously. The dotted pattern represents the single-crystalline Te nanorod, as the "backbone" of the nanocylinder, and the ring-shaped pattern for the randomly oriented nanoparticles on the nanorod. In fact, the whole pattern resembles a simple overlap of the diffraction patterns of magnetite nanoparticles (Fig. 7-1D) and a single Te nanorod (Fig. 7-1I).

The morphological change of the Te nanorods before and after covering with nanoparticles can be easily observed in their scanning electron microscopy (SEM) images. In Fig. 7-3C, the pure Te nanorods exhibit rigid and homogenous surface. The mean diameter is 50.9 ± 6.6 nm, 4 nm wider than that from TEM analysis, since the P*t*BMA layer on the nanorods are visible in SEM. The decoration with magnetite nanoparticles roughens the smooth surface of the nanorods, as shown in Fig. 7-3D. Instead of a flat surface, bright dots appear all over the nanorods. The enlarged view is shown in Fig. 7-3E. Differently from the TEM analysis of the individual magnetic nanocylinders, the SEM image offers direct evidence on how nanoparticles pack on the nanorod surface. It is found that although congested with the bright dots (the oleic acid-capped magnetite nanoparticles), some space of the nanorod surface remains unoccupied by nanoparticles. Free space between the nanoparticles is frequently observed, and a monolayer close-packing does not exist. This is in accordance with a theoretical calculation, where we found

that each nanorod could hold 660 magnetite nanoparticles on its surface by monolayer close-packing (see Supporting Information), much more than the observed 167 nanoparticles. We believe that the sites on the nanorods, which were occupied by P*t*BMA polymers, introduce a spatial repulsion and eventually prevent magnetite nanoparticles on the nanorod surface from packing closely with each other. Fig. 7-3F is the result obtained from the energy-dispersive X-ray (EDX) analysis of the magnetic nanocylinders. Only the signals of carbon, oxygen, iron and Te are detected (Si signal from the substrate.). They are the exact constructing elements of the oleic acid-capped magnetite nanoparticles, and the P*t*BMA attached Te nanorods. Despite of the rough baseline, we still calculate a weight ratio of 1:8.1 (12 %) for Fe_3O_4 : Te, which is close to the theoretical value, 1: 11 (9 %).

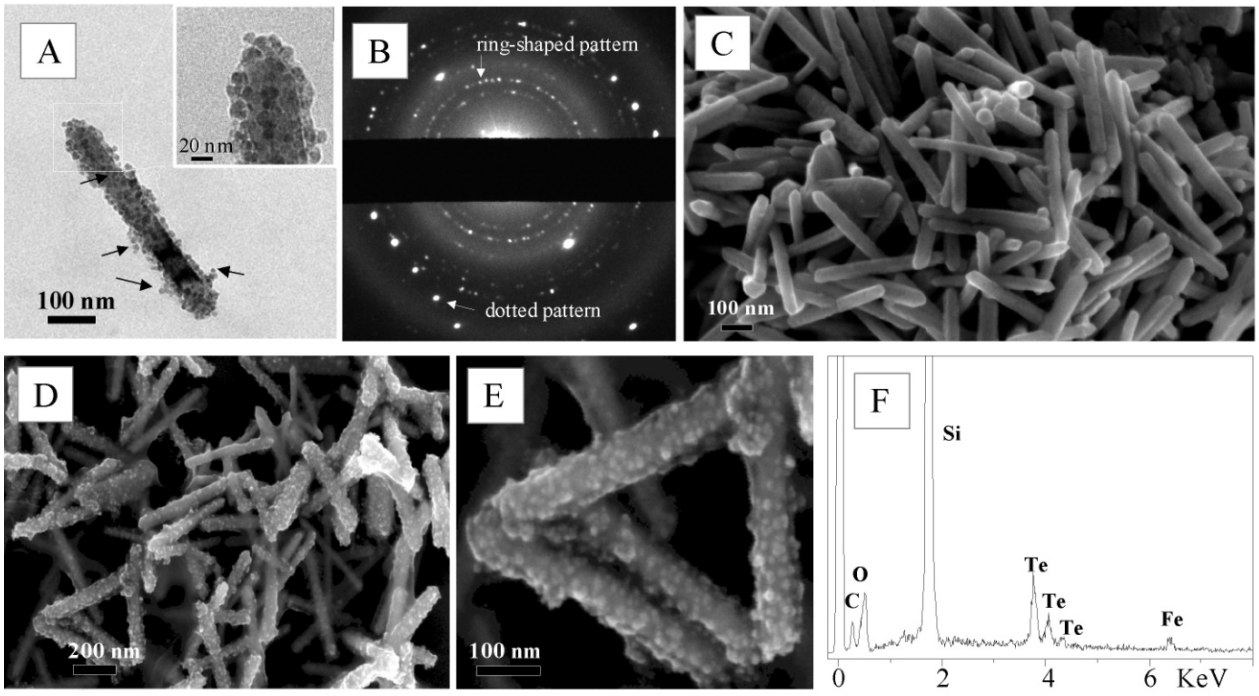

Figure 7-3. Electron microscopy analysis of the magnetic Te (1) nanocylinders prepared by Te (1) nanorods (60 mg/L) and magnetite nanoparticles at the critical concentration (5.2 mg/L). (A), TEM image of a single magnetic nanocylinder; (B), its electron diffraction pattern; (C), the SEM image of the pure Te nanorods; (D), SEM image of the magnetic nanocylinders; (E), its enlarged view; and (F), the corresponding elemental analysis.

Magnetic nanocylinders with overloaded magnetite nanoparticles. Our further effort was aimed to exceed the limitation of loading magnetite nanoparticles onto the nanorods. Here, a concentration of magnetite nanoparticles of 300 mg/L, well above the critical concentration (5.2 mg/L), was used to form the magnetic Te (1) nanocylinders. The excessive nanoparticles were removed by sonication and then ultrafiltration using a PTFE membrane with a pore size of 200 nm. The TEM images of the magnetic Te (1) nanocylinders before and after purification are shown in Fig. 7-4. In Fig. 7-4A, the nanoparticles, although enriched on the Te nanorods, spread all over the space. The loosely attached nanoparticles were firstly dissociated from the nanocylinders by sonication and then filtered away by ultrafiltration. Fig. 7-4B shows an individual purified magnetic nanocylinder, where more nanoparticles were evidently found on the nanorod than that formed at the critical concentration (Fig. 7-3A). Due to the over-saturation with the nanoparticles on the surface, the contour shape of the nanorod can hardly be distinguished. The nanorod is completely covered with almost two layers of nanoparticles. Its structure was further investigated at a high magnification on its top, as shown in the inset in Fig. 7-4B. It is easy to see that the nanoparticles even pile up on some sites of nanorod surface to form protrusions. The overloading enables a high content of magnetite nanoparticles in the nanocylinders.

To estimate the amount of the magnetite nanoparticles in such overloaded nanocylinders, superconducting quantum interference device (SQUID) measurements were performed for both the magnetite nanoparticles and the purified magnetic nanocylinders. Fig. 7-4C presents the hysteresis curves M(H) of the nanoparticles at 300 K and 5 K. The magnetite nanoparticles are superparamagnetic at 300 K and ferromagnetic at 5 K, which is typical for magnetite nanoparticles.[42, 43] The remancence, coercivity and saturation magnetization at 5 K are 13.3 emu/g, 229 Oe, and 69 emu/g , respectively. The blocking temperature is determined as 160 K from the zero field cooling (ZFC) and field cooling (FC) curves in Fig. 7-4D. In the case of magnetic nanocylinders, whose magnetic properties are exclusively arising from the magnetite nanoparticles, the shape of the M(H) curve is rather similar to that of the magnetite nanoparticles. At 5 K, the coercivity is 259 Oe, very close to that of the pure nanoparticles, since the physical properties (size, crystallinity, capping-agent, etc.) of the spherical and isotropic nanoparticles were maintained during the assembly process. The only significant difference lies in the remancence and saturation magnetization, which are 13.3 emu/g and 69 emu/g for nanoparticles,

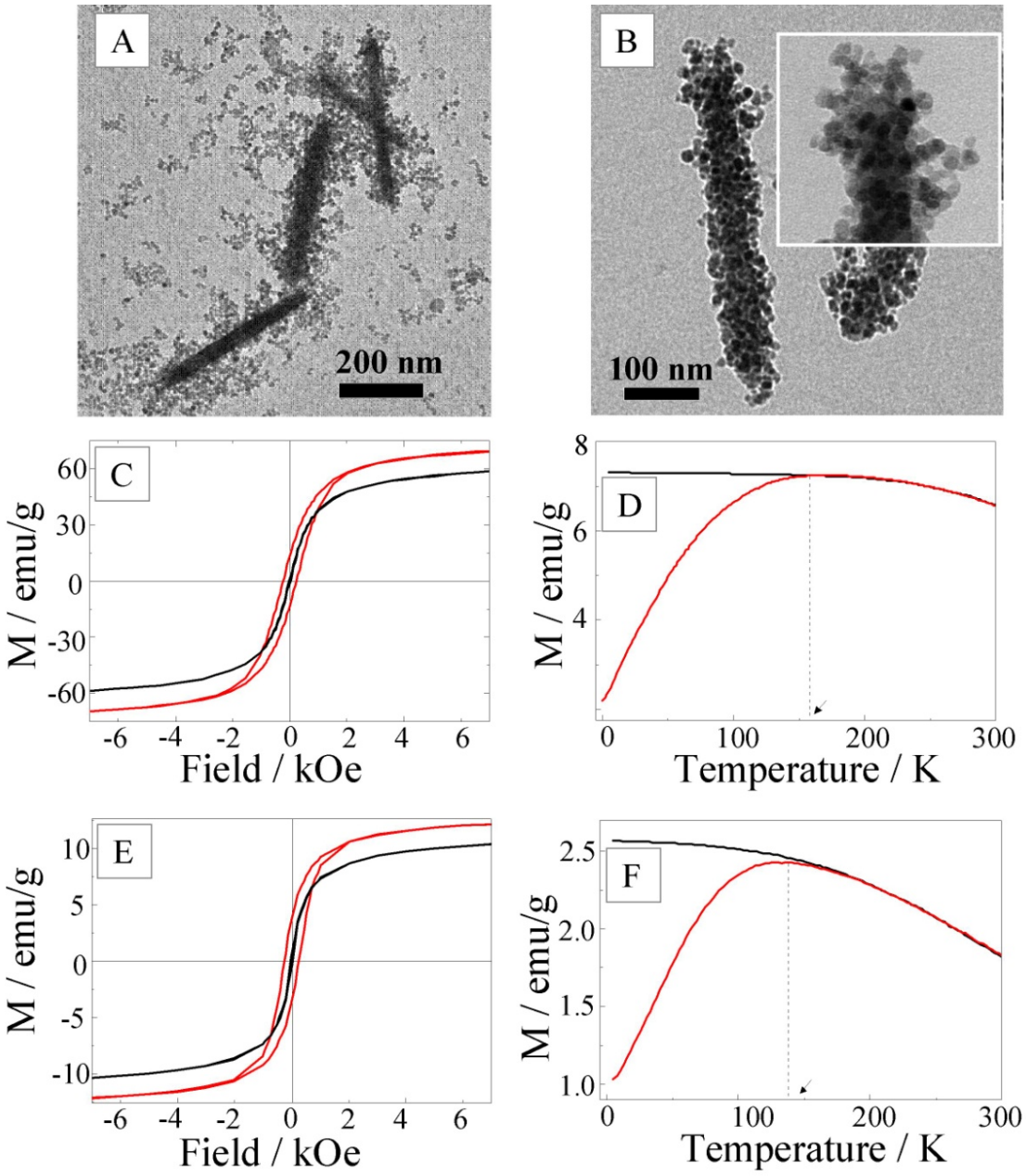

Figure 7-4. (A) and (B), the TEM images of magnetic Te (1) nanocylinders formed with 300 mg/L of magnetite nanoparticles and 60 mg/L of Te (1) nanorods before and after purification (sonication and ultrafiltration); (C), magnetization curves M(H) for the magnetite nanoparticles at 300 K (black line) and 5 K (red line); (D), ZFC (red line) and FC (black line) curves with the temperature ranging from 5 K to 300 K; (E), magnetization curves M(H) for the magnetic nanocylinders at 300 K (black line) and 5 K (red line); and (F), ZFC (red line) and FC (black line) curves of the magnetic nanocylinders with the temperature ranging from 5 K to 300 K.

but only 3.7 emu/g and 12 emu/g for nanocylinders at 5 K. Such difference is commonly caused by the volume-dilution effect of magnetite nanoparticles in the formed nanocylinder structure. According to the saturation magnetization of the nanoparticles before and after assembly on Te nanorods, 15 wt% of magnetite nanoparticles on the nanocylinders is calculated,[44] which is almost twice as high as the 8 wt% calculated from the nanocylinders formed at the critical concentration. The blocking temperature of the magnetic nanocylinders slightly shifted to 140 K in Fig. 7-4F, 20 K lower than the pure magnetite nanoparticles. The small difference could come from the assembly process. We assume that in the presence of excessive nanoparticles, small ones are easier to be inserted into the P*t*BMA polymer matrix on the nanorod surface than the large ones. Thus, the nanoparticles that have been assembled on the nanorods contain a larger fraction of small nanoparticles, which decreases the average size of the assembled magnetite nanoparticles. As reported, the change in the size of the magnetic nanoparticles is reflected in the blocking temperature.[45-47] It is worth noting that the magnetic nanocylinders based on the immobilization of magnetite nanoparticles on the Te nanorods remain superparamagnetic at room temperature, whereas single-phase magnetite nanorods with the same size (422 nm long, 47 nm wide) would exhibit ferromagnetic behaviour because of the transition of superparamagnetism to ferromagnetism for magnetite nanoparticles above ~25 nm at room temperature.[48, 49] In the field of magnetorheology, superparamagnetic nanorods are of great interest because after the removal of external magnetic field they do not retain any magnetism (coercivity), which avoids additional magnetic forces among nanorods and the corresponding agglomeration in solution.

Alignment of the magnetic nanocylinders in an external magnetic field. The magnetic Te (2) nanocylinders shown in Fig. 7-2E were further checked with respect to their response to a magnetic field. It was first visualized by responding to an external magnet, as shown in Fig. 7-5A-C. The responsive behavior of the magnetic nanocylinders in solution to the magnetic field can be utilized to align the nanocylinders on a solid substrate. To prepare the sample, the magnetic nanocylinder solution, was dropped on a carbon-coated cupper TEM grid fixed on the tip of a plastic sample holder, which was immediately inserted into a magnetic field of 0.3 T parallel to the TEM grid surface. Fig. 7-5D shows the aligned magnetic nanocylinders on TEM grid. Due to the magnetic nanoparticles on the surface, the longitudinal axis of all Te nanorods is almost parallel to the magnetic field, quite different from the randomly oriented Te nanorods. A

similar ordering of 1-D magnetic nanostructures (nickel or nickel-based alloy nanowires) in an external magnetic field has also been reported.[28, 29] The structure of the nanocylinders shows high stability in the strong magnetic field, only very few magnetite nanoparticles were dissociated from the nanocylinders during the alignment as shown in Fig. 7-5D.

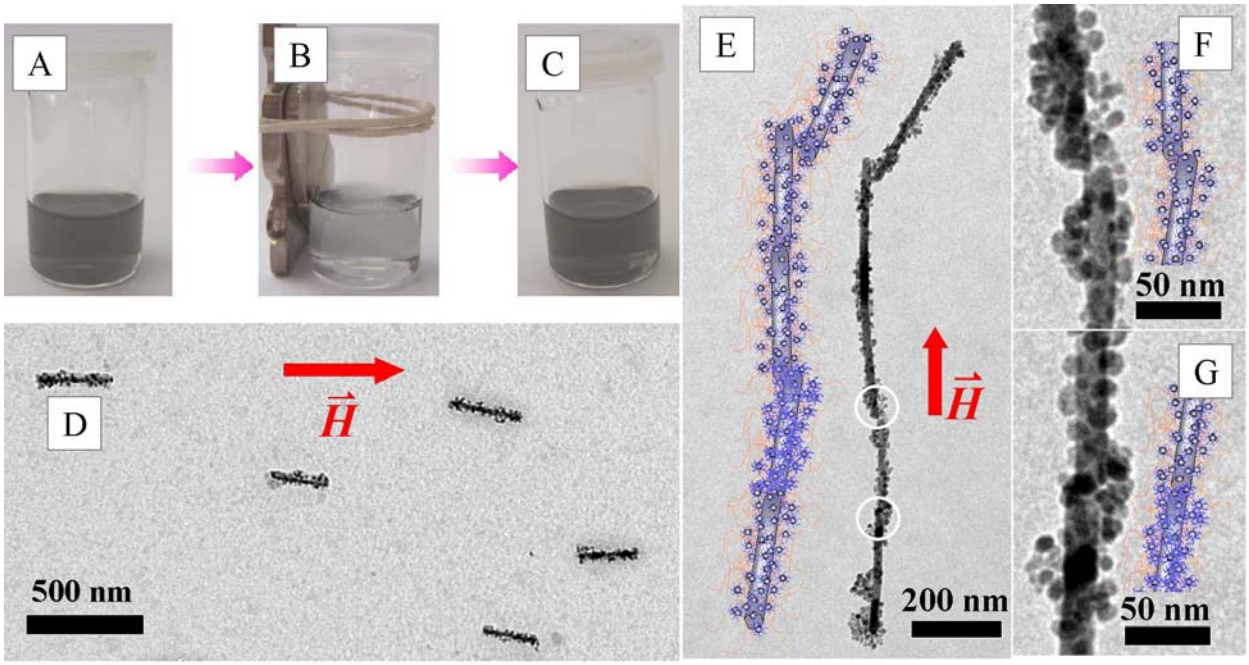

Figure 7-5. (A), the magnetic Te (2) nanocylinder solution in THF; (B), when close to a magnet; (C), after leaving the magnet and shaking; (D), TEM image of aligned magnetic nanocylinders when deposited from solution onto a carbon-coated TEM grid in the presence of an external magnetic field (0.3 T); (E), linear connection of aligned magnetic nanocylinders. The cartoon on the left side illustrates how this linear superstructure has been constructed. F) and (G) are the enlarged views of the junctions of the magnetic nanocylinders indicated by the white circles in Fig. 7-5E.

Very interestingly, a linear connection of the nanocylinders was often found in the TEM images. Fig. 7-5E presents an example of this elongated superstructure, which is made up of 5 individual magnetic nanocylinders via end-to-end junction. This behavior resembles that of macroscopic magnetic rods, which are connected at the ends via magnetic dipolar interaction. The whole linear superstructure points to the same direction as the magnetic field. These ordered superstructures were not observed in the absence of the external magnetic field in our studies. To

detail how the nanocylinders are connected at both ends, two junctions were enlarged in Fig. 7-5F and 5G. In Fig. 7-5F, the two nanocylinders are combined by a small joint at both ends, but the two faces of the ends are nearly mismatched. Differently in Fig. 7-5G, the two nanocylinders are parallel to each other and connected directly face-to-face at both ends despite of a rather small translation perpendicular to the longitudinal axis of the nanorods.

Demagnetization of pre-aligned magnetic nanocylinders. The oriented nanocylinders, whose magnetic properties originate from the magnetite nanoparticles, can be readily demagnetized by a selective etching process in an aqueous acid solution, namely dissolving the magnetite nanoparticles from the nanorods. Very significantly, the etching will keep the Te nanorods in an aligned state, as the hydrophobic polymer shell on the nanorod in the aqueous solution acts as a cage, fixing and "freezing" the nanorods on the substrate. Figures 7-6A-D show the original and stepwise HCl-etched magnetic nanocylinders after 20, 40, and 60 min, which present a clear trend of decreasing population and size of nanoparticles on the nanorod. Unexpectedly, a few magnetite particles were still observed anchoring the nanorod surface after 60 min etching (indicted by the white circle in Fig. 7-6D). The unusual stability of magnetite nanoparticles against strong HCl acid (pH = 1) is owed to the hydrophobic alkyl chains of oleic acid on the nanoparticle surface that are further immobilized in the hydrophobic polymer matrix on the nanorod. In such intensive hydrophobic environment, the diffusion of HCl molecules to the magnetite nanoparticles is retarded.

The etching process was accomplished after 80 minutes. Figure 7-6E shows a representative TEM image of the aligned Te nanorods after etching away the nanoparticles (more images in Fig. 7-10, Supporting Information). The longitudinal axis of these nanorods points to the same direction as the external magnetic field. In the enlarged view (inset in Fig. 7-6E) of a single nanorod, the nanorod surface is clearly flat and free of nanoparticles, indicating the successful demagnetization of the Te nanorod. It should be mentioned that although hydrochloric acid is not able to attack Te,[50] some nanorods were spotted becoming thinner specifically in the center during the etching process (Figures 7-6C, 7-6D and 7-10) due to the rather vigorous corrosiveness of HCl.

The methodology of decorating nanorods with magnetite nanoparticles, aligning and etching of the formed magnetic nanocylinders ("MAD" process), can be broadened as a general method to align non-magnetic 1-D nanostructures assisted by an external magnetic field. The type of 1-D nanostructures, polymer layers, magnetic nanoparticles and surfactants can be specially combined and designed for a specific application. For example, the polymeric layer on the nanostructures can be created either during the formation of the 1-D nanostructures like in our case, or more commonly via surface-initiated polymerization techniques[51, 52] and "grafting onto" methods[53].

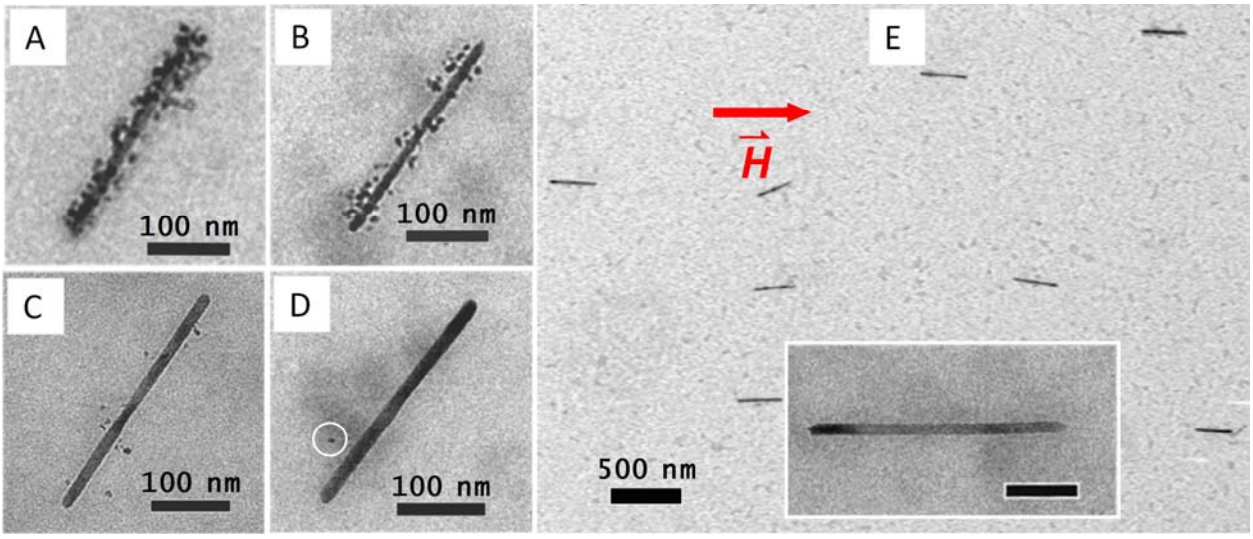

Figure 7-6. (A)-(D), TEM images of the original Te (2) magnetic nanocylinders, and the stepwise HCl-etched ones after 20, 40 and 60 min; (E), Te (2) nanorods after the complete etching of nanoparticles (80 min) from the nanorod surface. The inset in (E) is an enlarged view of a single rod.

7.4 Conclusions

In conclusion, we have successfully aligned Te nanorods via an interesting magnetization-alignment-demagnetization ("MAD") process assisted by an external magnetic field. The assembly of magnetite nanoparticles onto Te nanorods in THF solution can be quantitatively controlled in terms of their stoichiometric ratio below a critical concentration of the nanoparticles. Due to the polymer and surfactant on their surface, the formed magnetic nanocylinders are soluble in THF, which enables the alignment of these nanocylinders on a solid substrate in the presence of an external magnetic field. Via an acid-etching process, they were

demagnetized into Te nanorods in an organized manner. This "MAD" process can be extended as a general procedure for the alignment of non-magnetic 1-D nanostructures. Additionally, the magnetic nanocylinders based on the Te nanorods and magnetite nanoparticles can be potentially applied in field of magnetorheology, where the ordering of magnetic nanocylinders by an external field may record the signals or change the fluid viscosity.

Acknowledgements. This work was financially supported by the Deutsche Forschungsgemeinschaft (SPP1165, grant Mu896/22). We thank Benjamin Goßler for the kind help in SEM measurements. The authors would like to thank Verena Jung and Dr. Vadim Ksenofontov for the Mössbauer measurements and discussions.

7.5 References

1. Xia, Y.; Yang, P.; Sun, Y.; Wu, Y.; Mayers, B.; Gates, B.; Yin, Y.; Kim, F.; Yan, H. One-Dimensional Nanostructures: Synthesis, Characterization, and Applications. *Adv. Mater.* **2003**, 15, 353-389.

2. Wang, X.; Song, J.; Liu, J.; Wang, Z. L. Direct-Current Nanogenerator Driven by Ultrasonic Waves. *Science* **2007**, 316, 102-105.

3. Dai, H.; Hafner, J. H.; Rinzler, A. G.; Colbert, D. T.; Smalley, R. E. Nanotubes as Nanoprobes in Scanning Probe Microscopy. *Nature* **1996**, 384, 147-150.

4. Jain, P. K.; Eustis, S.; El-Sayed, M. A. Plasmon Coupling in Nanorod Assemblies: Optical Absorption, Discrete Dipole Approximation Simulation, and Exciton-Coupling Model. *J. Phys. Chem. B* **2006**, 110, 18243-18253.

5. Murphy, C. J.; Sau, T. K.; Gole, A. M.; Orendorff, C. J.; Gao, J.; Gou, L.; Hunyadi, S. E.; Li, T. Anisotropic Metal Nanoparticles: Synthesis, Assembly, and Optical Applications. *J. Phys. Chem. B* **2005**, 109, 13857-13870.

6. Hu, J.; Li, L.; Yang, W.; Manna, L.; Wang, L.; Alivisatos, A. P. Linearly Polarized Emission from Colloidal Semiconductor Quantum Rods. *Science* **2001**, 292, 2060-2063.

7. Huynh Wendy, U.; Dittmer Janke, J.; Alivisatos, A. P. Hybrid Nanorod-Polymer Solar Cells. *Science* **2002**, 295, 2425-2427.

8. Sudeep, P. K.; Joseph, S. T. S.; Thomas, K. G. Selective Detection of Cysteine and Glutathione Using Gold Nanorods. *J. Am. Chem. Soc.* **2005**, 127, 6516-6517.

9. Huang, X.; El-Sayed, I. H.; Qian, W.; El-Sayed, M. A. Cancer Cell Imaging and Photothermal Therapy in the Near-Infrared Region by Using Gold Nanorods. *J. Am. Chem. Soc.* **2006**, 128, 2115-2120.

10. Gorelikov, I.; Field, L. M.; Kumacheva, E. Hybrid Microgels Photoresponsive in the Near-Infrared Spectral Range. *J. Am. Chem. Soc.* **2004**, 126, 15938-15939.

11. Salem Aliasger, K.; Searson Peter, C.; Leong Kam, W. Multifunctional Nanorods for Gene Delivery. *Nat. Mater.* **2003**, 2, 668-671.

12. Duan, X.; Lieber, C. M. General Synthesis of Compound Semiconductor Nanowires. *Adv. Mater.* **2000**, 12, 298-302.

13. Ma, C.; Wang, Z. L. Road Map for the Controlled Synthesis of CdSe Nanowires, Nanobelts, and Nanosaws-A Step towards Nanomanufacturing. *Adv. Mater.* **2005**, 17, 2635-2639.

14. Grebinski, J. W.; Richter, K. L.; Zhang, J.; Kosel, T. H.; Kuno, M. Synthesis and Characterization of Au/Bi Core/Shell Nanocrystals: A Precursor toward II-VI Nanowires. *J. Phys. Chem. B* **2004**, 108, 9745-9751.

15. Adelung, R.; Aktas, O. C.; Franc, J.; Biswas, A.; Kunz, R.; Elbahri, M.; Kanzow, J.; Schuermann, U.; Faupel, F. Strain-Controlled Growth of Nanowires within Thin-Film Cracks. *Nat. Mater.* **2004**, 3, 375-379.

16. Milenkovic, S.; Hassel Achim, W.; Schneider, A. Effect of the Growth Conditions on the Spatial Features of Re Nanowires Produced by Directional Solidification. *Nano Lett.* **2006**, 6, 794-799.

17. Yuan, J.; Xu, Y.; Walther, A.; Bolisetty, S.; Schumacher, M.; Schmalz, H.; Ballauff, M.; Müller, A. H. E. Water-Soluble Organo-Silica Hybrid Nanowires. *Nat. Mater.* **2008**, 7, 718-722.

18. Thomas, K. G.; Barazzouk, S.; Ipe, B. I.; Joseph, S. T. S.; Kamat, P. V. Uniaxial Plasmon Coupling through Longitudinal Self-Assembly of Gold Nanorods. *J. Phys. Chem. B* **2004**, 108, 13066-13068.

19. Joseph, S. T. S.; Ipe, B. I.; Pramod, P.; Thomas, K. G. Gold Nanorods to Nanochains: Mechanistic Investigations on Their Longitudinal Assembly Using α,ω-Alkanedithiols and Interplasmon Coupling. *J. Phys. Chem. B* **2006**, 110, 150-157.

20. Nie, Z.; Fava, D.; Kumacheva, E.; Zou, S.; Walker, G. C.; Rubinstein, M. Self-Assembly of Metal-Polymer Analogues of Amphiphilic Triblock Copolymers. *Nat. Mater.* **2007**, 6, 609-614.

21. Khanal Bishnu, P.; Zubarev Eugene, R. Rings of Nanorods. *Angew. Chem. Int. Ed.* **2007**, 46, 2195-2198.

22. Caswell, K. K.; Wilson James, N.; Bunz Uwe, H. F.; Murphy, C. J. Preferential End-to-End Assembly of Gold Nanorods by Biotin-Streptavidin Connectors. *J. Am. Chem. Soc.* **2003**, 125, 13914-13915.

23. Dujardin, E.; Mann, S.; Hsin, L.-B.; Wang, C. R. C. DNA-Driven Self-Assembly of Gold Nanorods. *Chem. Comm.* **2001**, 14, 1264-1265.

24. Zhang, Q.; Gupta, S.; Emrick, T.; Russell, T. P. Surface-Functionalized CdSe Nanorods for Assembly in Diblock Copolymer Templates. *J. Am. Chem. Soc.* **2006**, 128, 3898-3899.

25. Correa-Duarte Miguel, A.; Perez-Juste, J.; Sanchez-Iglesias, A.; Giersig, M.; Liz-Marzan, L. M. Aligning Au Nanorods by Using Carbon Nanotubes as Templates. *Angew. Chem. Int. Ed.* **2005**, 44, 4375-4378.

26. Gupta, S.; Zhang, Q.; Emrick, T.; Russell, T. P. "Self-Corralling" Nanorods under an Applied Electric Field. *Nano Lett.* **2006**, 6, 2066-2069.

27. Ryan Kevin, M.; Mastroianni, A.; Stancil Kimani, A.; Liu, H.; Alivisatos, A. P. Electric-Field-Assisted Assembly of Perpendicularly Oriented Nanorod Superlattices. *Nano Lett.* **2006**, 6, 1479-1482.

28. Hangarter, C. M.; Rheem, Y.; Yoo, B.; Yang, E.-H.; Myung, N. V. Hierarchical Magnetic Assembly of Nanowires. *Nanotechnology* **2007**, 18, 205305.

29. Hangarter, C. M.; Myung, N. V. Magnetic Alignment of Nanowires. *Chem. Mater.* **2005**, 17, 1320-1324.

30. Park, S.; Lim, J.-H.; Chung, S.-W.; Mirkin, C. A. Self-Assembly of Mesoscopic Metal-Polymer Amphiphiles. *Science* **2004**, 303, 348-351.

31. Yuan, J.; Schmalz, H.; Xu, Y.; Miyajima, N.; Drechsler, M.; Möller, M. W.; Schacher, F.; Müller, A. H. E. Room-Temperature Growth of Uniform Tellurium Nanorods and the Assembly of Tellurium or Fe_3O_4 Nanoparticles on the Nanorods. *Adv. Mater.* **2008**, 20, 947-952.

32. Zhang, M.; Estournes, C.; Bietsch, W.; Müller, A. H. E. Superparamagnetic Hybrid Nanocylinders. *Adv. Funct. Mater.* **2004**, 14, 871-882.

33. Sellmyer, D. J.; Zheng, M.; Skomski, R. Magnetism of Fe, Co and Ni Nanowires in Self-assembled Arrays. *J. Phys.: Condens. Matter* **2001**, 13, R433-R460.

34. Fert, A.; Piraux, L. Magnetic Nanowires. *J. Magn. Magn. Mater.* **1999**, 200, 338-358.

35. Tonucci, R. J.; Justus, B. L.; Campillo, A. J.; Ford, C. E. Nanochannel Array Glass. *Science* **1992**, 258, 783-785.

36. Gole, A.; Stone, J. W.; Gemmill, W. R.; zur Loye, H.-C.; Murphy, C. J. Iron Oxide Coated Gold Nanorods: Synthesis, Characterization, and Magnetic Manipulation. *Langmuir* **2008**, 24, 6232-6237.

37. Yang, S.; Liu, H. A Novel Approach to Hollow Superparamagnetic Magnetite/Polystyrene Nanocomposite Microspheres via Interfacial Polymerization. *J. Mater. Chem.* **2006**, 16, 4480-4487.

38. Kang, Y. S.; Risbud, S.; Rabolt, J. F.; Stroeve, P. Synthesis and Characterization of Nanometer-Size Fe_3O_4 and γ-Fe_2O_3 Particles. *Chem. Mater.* **1996**, 8, 2209-2211.

39. Lee, H. S.; Lee, W. C.; Furubayashi, T. A Comparison of Coprecipitation with Microemulsion Methods in the Preparation of Magnetite. *J. Appl. Phys.* **1999**, 85, 5231-5233.

40. Gee, S. H.; Hong, Y. K.; Erickson, D. W.; Park, M. H.; Sur, J. C. Synthesis and Aging Effect of Spherical Magnetite (Fe_3O_4) Nanoparticles for Biosensor Applications. *J. Appl. Phys.* **2003**, 93, 7560-7562.

41. Li, J.; Tang, S.; Lu, L.; Zeng, H. C. Preparation of Nanocomposites of Metals, Metal Oxides, and Carbon Nanotubes via Self-Assembly. *J. Am. Chem. Soc.* **2007**, 129, 9401-9409.

42. Woo, K.; Hong, J.; Choi, S.; Lee, H. W.; Ahn, J. P.; Kim, C. S.; Lee, S. W. Easy Synthesis and Magnetic Properties of Iron Oxide Nanoparticles. *Chem. Mater.* **2004**, 16, 2814-2818.

43. Lee, D. K.; Kang, Y. S.; Lee, C. S.; Stroeve, P. Structure and Characterization of Nanocomposite Langmuir-Blodgett Films of Poly(maleic monoester)/Fe_3O_4 Nanoparticle Complexes. *J. Phys. Chem. B* **2002**, 106, 7267-7271.

44. Galindo-Gonzalez, C.; De Vicente, J.; Ramos-Tejada, M. M.; Lopez-Lopez, M. T.; Gonzalez-Caballero, F.; Duran, J. D. G. Preparation and Sedimentation Behavior in Magnetic Fields of Magnetite-Covered Clay Particles. *Langmuir* **2005**, 21, 4410-4419.

45. Bodker, F.; Morup, S. Size Dependence of the Properties of Hematite Nanoparticles. *Europhys. Lett.* **2000**, 52, 217-223.

46. Hanson, M.; Johansson, C.; Pedersen, M. S.; Morup, S. The Influence of Particle Size and Interactions on the Magnetization and Susceptibility of Nanometer-size Particles. *J. Phys.: Condens. Matter* **1995**, 7, 9269-9277.

47. Thakur, M.; De, K.; Giri, S.; Si, S.; Kotal, A.; Mandal, T. K. Interparticle Interaction and Size Effect in Polymer Coated Magnetite Nanoparticles. *J. Phys.: Condens. Matter* **2006**, 18, 9093-9104.

48. Liu, X.; Kaminski, M. D.; Guan, Y.; Chen, H.; Liu, H.; Rosengart, A. J. Preparation and Characterization of Hydrophobic Superparamagnetic Magnetite Gel. *J. Magn. Magn. Mater.* **2006**, 306, 248-253.

49. Yang, T.-I.; Brown, R. N. C.; Kempel, L. C.; Kofinas, P. Magneto-Dielectric Properties of Polymer-Fe_3O_4 Nanocomposites. *J. Magn. Magn. Mater.* **2008**, 320, 2714-2720.

50. Budavari, S.; O'Neil, M.; Smith, A.; Heckelman, P. The Merck Index, Eleventh Edition. **1989**, 9026.

51. Tang, C.; Bombalski, L.; Kruk, M.; Jaroniec, M.; Matyjaszewski, K.; Kowalewski, T. Nanoporous Carbon Films from "Hairy" Polyacrylonitrile-grafted Colloidal Silica Nanoparticles. *Adv. Mater.* **2008**, 20, 1516-1522.

52. Duan, H.; Kuang, M.; Wang, D.; Kurth Dirk, G.; Mohwald, H. Colloidally Stable Amphibious Nanocrystals Derived from Poly{[2-(dimethylamino)ethyl] methacrylate} Capping. *Angew. Chem. Int. Ed.* **2005**, 44, 1717-1720.

53. Tahir Muhammad, N.; Zink, N.; Eberhardt, M.; Therese Helen, A.; Faiss, S.; Janshoff, A.; Kolb, U.; Theato, P.; Tremel, W. Hierarchical Assembly of TiO_2 Nanoparticles on WS_2 Nanotubes Achieved through Multifunctional Polymeric Ligands. *Small* **2007**, 3, 829-834.

7.6 Supporting Information

1. Mössbauer spectrum of the magnetite nanoparticles

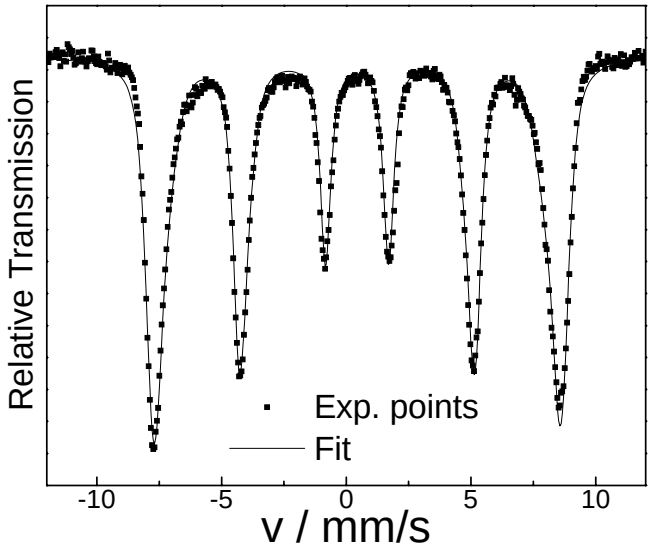

Figure 7-7. ^{57}Fe Mössbauer spectrum of the magnetite nanoparticles. The spectra were recorded using a constant-acceleration conventional spectrometer and a helium bath cryostat. The partly resolved two sextets at 85 K confirm the phase to be magnetite Fe_3O_4.

2. Details of Te (2) and Te (3) nanorods and their assembly with magnetite nanoparticles

Beside Te (1), the Te (2) and Te (3) nanorods were also used for the synthesis of magnetic nanocylinders to verify this robust strategy. Fig. 7-8A shows the TEM image of Te (2) nanorods before decorated with nanoparticles. The average length and diameter are 295 ± 47 nm and 21 ± 5 nm (aspect ratio = 14). When magnetite nanoparticles were added into the Te (2) nanorod solution above the critical concentration (here defined as 8.65 mg/L), the nanoparticles are found everywhere in the TEM grid (Fig. 7-8B). At the critical concentration, as shown in Fig. 7-8C, all nanoparticles stick on the Te nanorods and leave no free nanoparticle in the solution. Through the calculation, the population of nanoparticles per nanorod here is 69 (253 by theoretical calculation, see following Supporting Information). Below the critical concentration, less nanoparticles are attached on the Te nanorods, as shown in Fig. 7-8D (only 17 nanoparticles per Te nanorod by calculation).

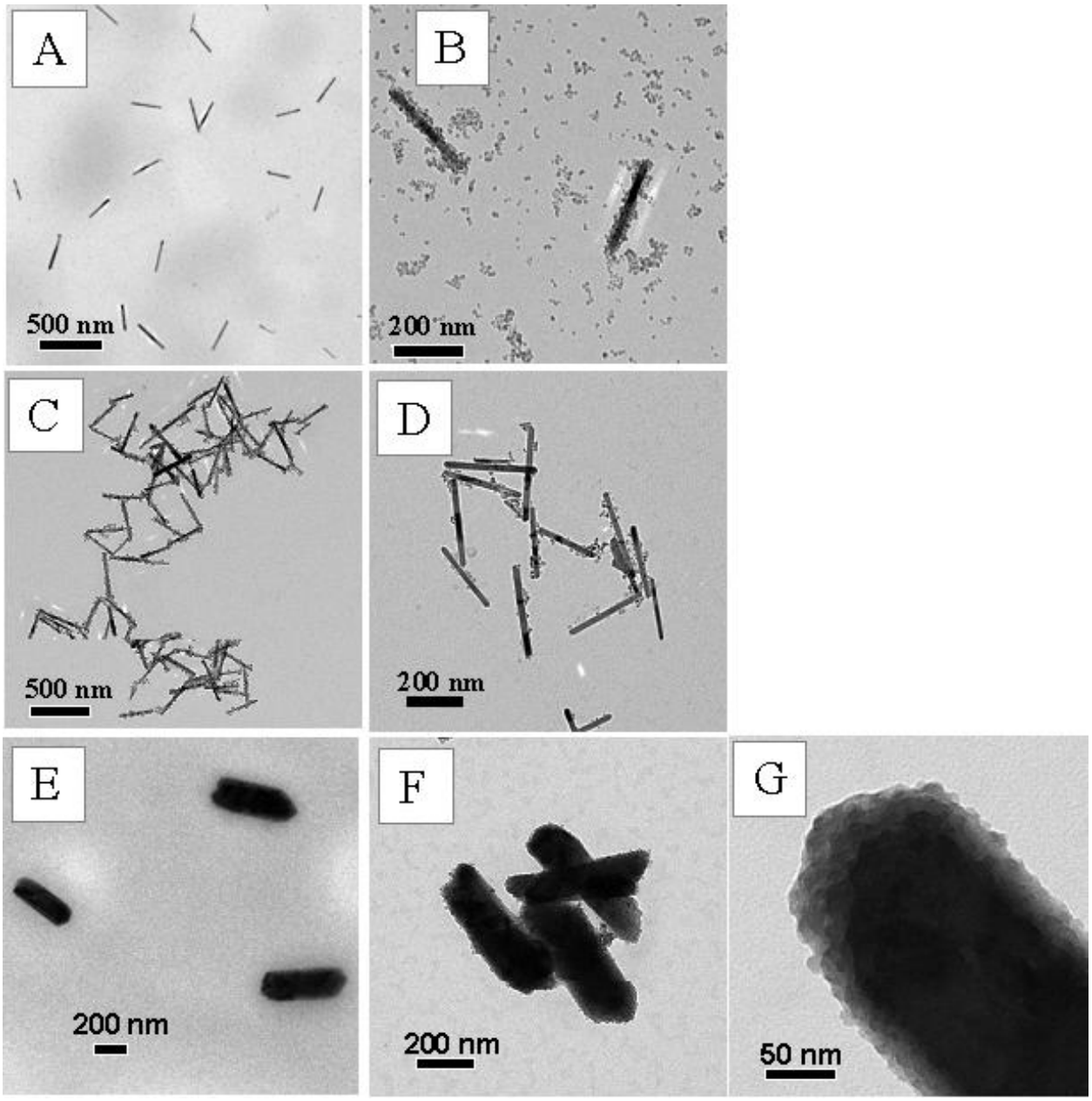

Figure 7-8. (A), TEM image of Te (2) nanorods; (B)-(D), magnetic Te (2) nanocylinders formed by Te (2) nanorods (33.7 mg/L) and different concentrations of magnetite nanoparticles: (B) 25 mg/L, (C) 8.65 mg/L, and (D) 2.15 mg/L in THF; (E), TEM image of Te (3) nanorods; (F), magnetic nanocylinders formed by Te (3) nanorods (71 mg/L) and magnetite nanoparticles (1.8 mg/L) at the critical concentration; and (G), enlarged view of the magnetic Te (3) nanocylinders at the critical concentration.

The Te (3) nanorods with a rather low aspect ratio of 3 are shown in the TEM image in Fig. 7-8E. They also show the ability of assembling magnetite nanoparticles. The magnetic Te (3) nanocylinders at the critical concentration are shown in the TEM image in Fig. 7-8F. Each nanocylinder contains 597 nanoparticles (2121 by theoretical calculation, see following Supporting Information). Fig. 7-8G shows its enlarged view, where the dense nanoparticles are clearly visible on the nanorod edge.

3. Calculation of the population of magnetite nanoparticles per Te nanorod according to their concentrations in THF.

In order to simplify the calculation, several assumptions are made as follows.

(1) Both Te nanorods and magnetite nanoparticles are considered as rigid objects regardless of polymer or surfactant on their surface.

(2) The Te nanorods and magnetite nanoparticles are considered uniform. The dimensional parameters, like radius and length, are taken from their average values. The polymer layer on Te nanorods and the oleic acid layer on magnetite nanoparticles are neglected with regard to the weight.

The mass of individual Te nanorod is expressed as below:

$$m_{Te,NR} = \rho_{Te} \cdot V_{Te,NR} = \rho_{Te} \cdot \pi \cdot R_{Te,NR}{}^2 \cdot L_{Te,NR} \quad (1)$$

$m_{Te,NR}$: Mass of a single Te nanorod

ρ_{Te} : Density of tellurium at 25 °C, 6.24 g/cm^3.

$V_{Te,NR}$: Volume of a single Te nanorod

$R_{Te,NR}$: Radius of the Te nanorod section

$L_{Te,NR}$: Length of the Te nanorod

The mass of a single nanoparticle is expressed as below:

$$m_{Fe_3O_4,NP} = \rho_{Fe_3O_4} \cdot V_{Fe_3O_4,NP} = \rho_{Fe_3O_4} \cdot \frac{4}{3} \cdot \pi \cdot R_{Fe_3O_4,NP}{}^3 \quad (2)$$

$m_{Fe_3O_4,NP}$: Mass of a single magnetite nanoparticle

$\rho_{Fe_3O_4}$: Density of magnetite at 25 °C, 5.1 g/cm^3.

$V_{Fe_3O_4,NP}$: Volume of a single magnetite nanoparticle

$R_{Fe_3O_4,NP}$: Radius of the magnetite nanoparticles

$$\begin{aligned} n_{real} &= \frac{N_{Fe_3O_4,NP}}{N_{Te,NR}} = \frac{\frac{M_{Fe_3O_4,NP}}{m_{Fe_3O_4,NP}}}{\frac{M_{Te,NR}}{m_{Te,NR}}} \\ &= \frac{M_{Fe_3O_4,NP}}{M_{Te,NR}} \cdot \frac{m_{Te,NR}}{m_{Fe_3O_4,NP}} \\ &= \frac{C_{Fe_3O_4,NP}}{C_{Te,NR}} \cdot \frac{\rho_{Te} \cdot \pi \cdot R_{Te,NR}{}^2 \cdot L_{Te,NR}}{\rho_{Fe_3O_4} \cdot \frac{4}{3} \cdot \pi \cdot R_{Fe_3O_4,NP}{}^3} \\ &= \frac{C_{Fe_3O_4,NP}}{C_{Te,NR}} \cdot \frac{\rho_{Te} \cdot R_{Te,NR}{}^2 \cdot L_{Te,NR}}{\rho_{Fe_3O_4} \cdot \frac{4}{3} R_{Fe_3O_4,NP}{}^3} \end{aligned} \quad (3)$$

The population of nanoparticles per nanorod is calculated from the equation below.

$N_{Fe_3O_4,NP}$: Total population of magnetite nanoparticles.

$N_{Te,NR}$: Total population of Te nanorods.

$M_{Fe_3O_4,NP}$: Mass of all magnetite nanoparticles.

$M_{Te,NR}$: Mass of all Te nanorods.

$C_{Fe_3O_4,NP}$: Concentration of magnetite nanoparticles in THF.

$C_{Te,NR}$: Concentration of Te nanorods in THF.

Table 7-2. Population of magnetite nanoparticles per Te nanorod according to their concentrations in THF.

	Fig. 7-2C	Fig. 7-2D	Fig. 7-2E	Fig. 7-8D	Fig. 7-8F
$C_{Te,NR}$ (mg /L)	60	60	33.7	33.7	71
$C_{Fe_3O_4,NP}$ (mg /L)	5.2	1.87	8.65	2.15	1.8
$R_{Te,NR}$ (nm)	23.45	23.45	10.5	10.5	77.5
$L_{Te,NR}$ (nm)	422	422	295	295	473
n_{real}	167	60	69	17	597

4. Calculation of the population of nanoparticles per Te nanorod by monolayer close-packing from their dimension.

The assumptions here are made as follows.

(1) Both Te nanorods and magnetite nanoparticles are considered as rigid objects.

(2) The Te nanorods and magnetite nanoparticles are considered uniform. The dimensional parameters, like radius and length, are taken from their average values, except in the case of magnetite nanoparticles, the radius is set to 5.8 nm (1 nm thickness of oleic acid layer) since the layer of oleic acid on their surface cannot be neglected in solution with regard to the volume.

In Fig. 7-9C, the following equation is valid,

$$\sin\frac{\alpha}{2}=\frac{R_{Fe_3O_4,NP}}{R_{Te,NR}+R_{Fe_3O_4,NP}}$$

$$\alpha=2\cdot\arcsin(\frac{R_{Fe_3O_4,NP}}{R_{Te,NR}+R_{Fe_3O_4,NP}})$$

In Fig. 7-9E, the d is calculated from the Pythagorean theorem

$$d=\sqrt{(R_{Fe_3O_4,NP}+R_{Fe_3O_4,NP})^2-R_{Fe_3O_4,NP}{}^2}=\sqrt{3}R_{Fe_3O_4,NP}$$

The population of nanoparticles per Te nanorod can be calculated from the equation below.

$$n_{theo.} = \frac{2\pi}{\alpha} \cdot \frac{L_{Te,NR}}{d} = \frac{2\pi}{2 \cdot \arcsin\left(\frac{R_{Fe_3O_4,NP}}{R_{Te,NR} + R_{Fe_3O_4,NP}}\right)} \cdot \frac{L_{Te,NR}}{\sqrt{3} R_{Fe_3O_4,NP}}$$

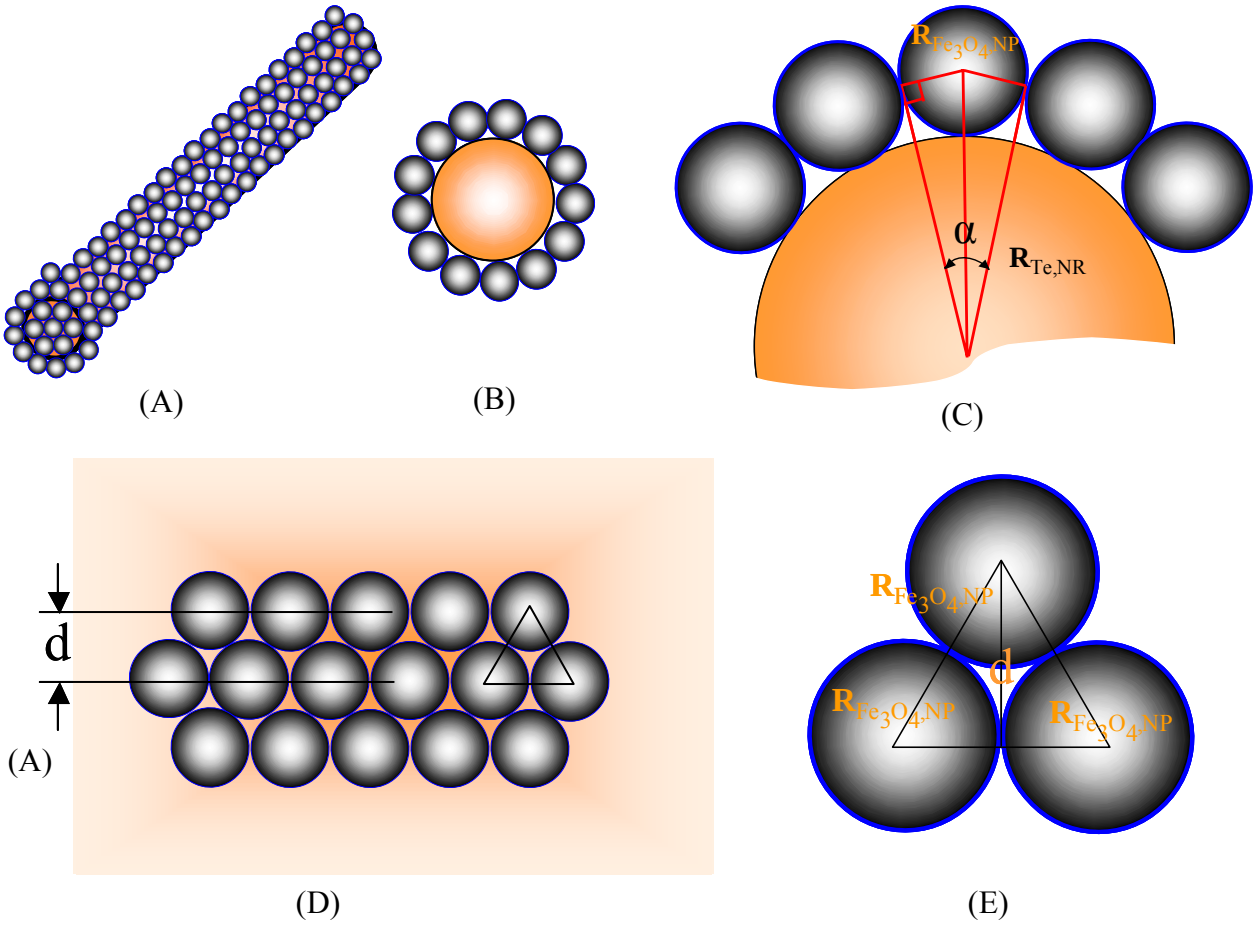

Figure 7-9. (A) Illustration of magnetic nanocylinders with monolayer of magnetite nanoparticles close-packed on a single Te nanorod. (B) Cross-section view of the magnetic nanocylinders. (C) Mathematic relation between the cross-sections of the nanoparticles and the Te nanorod. (D) Vertical view of monolayer close-packing of nanoparticles on Te nanorod surface. (E) Mathematic relation between the monolayer of nanoparticles closed packed on the Te nanorod surface.

Table 7-3. Population of nanoparticles per Te nanorod by monolayer close-packing from their dimension.

	Te (1)	Te (2)	Te (3)
$R_{Fe_3O_4,NP}$ (nm)	5.8	5.8	5.8
$R_{Te,NR}$ (nm)	23.45	10.5	77.5
$L_{Te,NR}$ (nm)	422	295	473
$n_{theo.}$	660	253	2121

5. Aligning Te nanorods via etching the magnetite nanoparticles away from the nanorods.

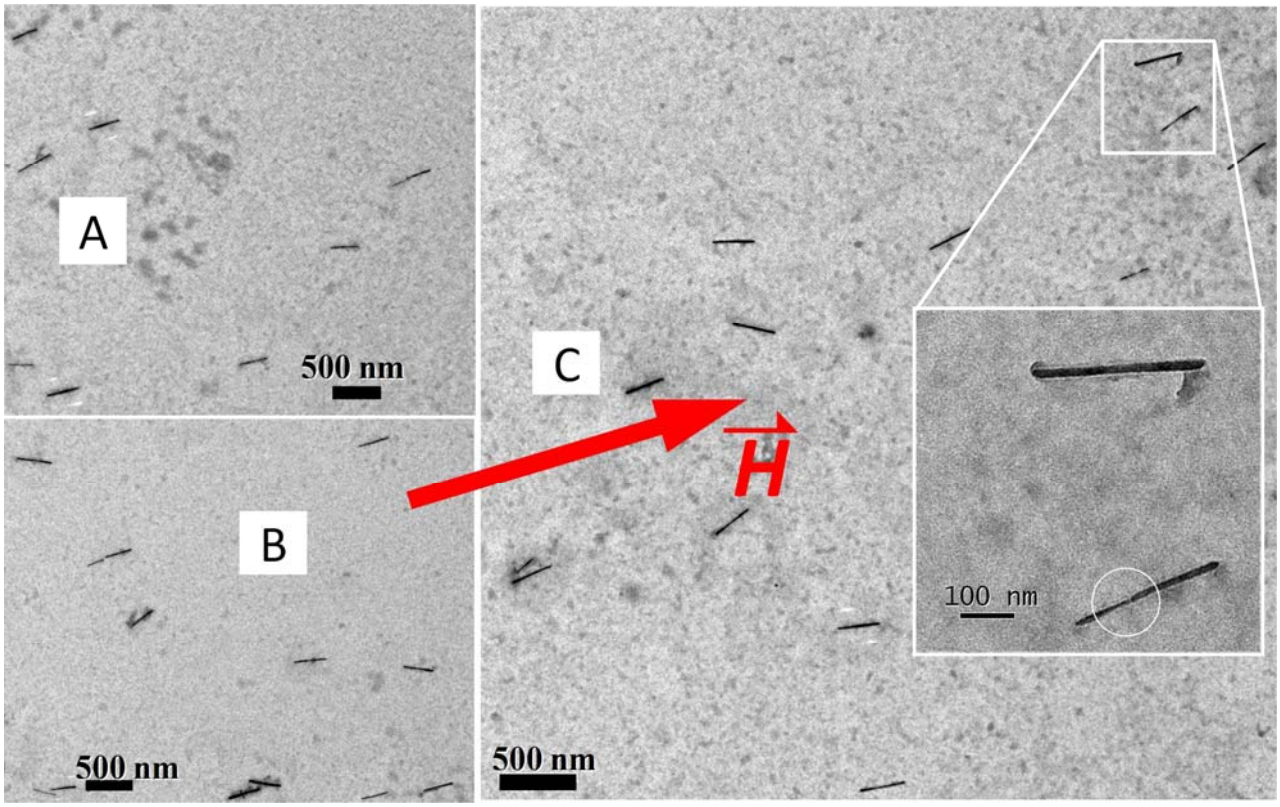

Figure 7-10. (A)-(C), TEM images of aligned Te (2) nanorods on the carbon-coated TEM grid after the complete etching of magnetite nanoparticles from the nanorod surface in aqueous HCl solution (80 min). The inset in (C) is an enlarged view of two nanorods; the white circle indicates a slightly deformed area (thinner diameter) of a nanorod after etching due to the corrosiveness of HCl.

Chapter 8 Summary

Cylindrical polymer brushes (CPBs) have been synthesized via the combination of anionic polymerization (for the backbone) and atom transfer radical polymerization (for the side chains) via the "grafting from" technique to achieve a narrow molecular weight distribution in both the backbone and the side chains. They were employed as template for the preparation of various types of one-dimensional (1D) polymer-inorganic hybrid nanomaterials.

In the case of well-defined core-shell superstructured CPBs, depending on the aimed functional 1D hybrid nanostructures, different combinations of core and shell have been chosen. CPBs with a poly(3-acryloylpropyl trimethoxysilane) core and a poly(oligo(ethylene glycol) methacrylate) (POEGMA) shell were hydrolyzed by aqueous ammonia to produce water-soluble organosilica hybrid nanowires. Since the trimethoxysilyl group was directly incorporated into the structure of the CPB, the addition of an external inorganic precursor in this case is avoided. These hybrid nanowires can form a lyotropic phase and serve as in-situ template for the pyrolytic formation of inorganic silica nanowires.

Amphiphilic CPBs with a hydrophilic poly(acrylic acid) (PAA) core and a hydrophobic poly(*n*-butyl acrylate) (P*n*BA) shell were used as cylindrical templates and nanoreactors for the fabrication of CdSe semiconductor nanowires, due to the coordination ability of PAA with Cd^{2+} ions. Since the chemical structure of the PAA core was resumed, a double-loading process was carried out to load more CdSe nanoparticles into the CPB. AFM, TEM and UV-Vis characterizations have proven the increasing amount of CdSe in the hybrids.

Bishydrophilic CPBs with a poly(2-hydroxyethyl methacrylate) (PHEMA) core and a POEGMA shell were employed for the fabrication of a wormlike assembly of TiO_2 semiconductor nanoparticles, forming a kind of titania-CPB hybrid nanowires. The titanium alkoxide precursor was introduced into the CPB via a transalcoholysis reaction between $Ti(OC_4H_9)_4$ and the PHEMA block. The titania-CPB hybrid nanowires were used to generate anatase titania nanowires via pyrolysis at 550 °C.

In general, all these inorganic nanowires templated by the core-shell CPB showed very uniform size in length as well as diameter, due to the low molecular weight distribution of the CPB backbone and the side chains. The shell of the CPBs protects the fabricated inorganic nanowires

from agglomeration, and in addition, renders the hybrid nanomaterials soluble in various solvents, including water.

Poly(*tert*-methyl methacrylate) (P*t*BMA) homopolymer CPBs were used to support the formation of uniform single-crystalline tellurium nanorods (length up to 822 nm, D ~ 36.1 ± 7.9 nm, aspect ratio from 2.7 to 22) at room temperature in THF. These rods with polymer attached on their surface are very stable in THF, and able to assemble tellurium or magnetite (Fe_3O_4) nanoparticles on the Te nanorods. The strategy to synthesize the Te nanorods was further extended to linear P*t*BMA polymers with high molecular weight. The assembly of Fe_3O_4 nanoparticles on these Te nanorods was controlled by the stoichiometric ratio of the nanoparticles and nanorods. The Fe_3O_4-decorated Te nanorods are superparamagnetic. They were aligned in the presence of an external magnetic field when deposited from THF solution on a solid substrate.

These novel one-dimensional hybrid nanomaterials based on CPBs can have many potential applications due to their electronic, optical, catalytic, semiconducting, and magnetic properties.

Zusammenfassung

Durch Kombination von anionischer Polymerisation (für das Rückgrat) und ATRP (für die Seitenketten) wurden zylindrische Polymerbürsten mittels der „grafting from“ Technik hergestellt. Auf diese Weise konnten enge Molekulargewichtsverteilungen sowohl im Rückgrat als auch bei den Seitenketten gewährleistet werden. Ausgehend von diesen Polymerbürsten konnten dann verschiedene eindimensionale (1D) polymer-anorganische Hybridmaterialien im Nanometer-Maßstab dargestellt werden.

Im Falle der wohldefinierten Polymerbürsten mit Kern-Schale Struktur wurden, je nach Art der gewünschten eindimensionalen Hybridstruktur, verschiedene Kombinationen von Kern und Schale ausgewählt. Zylindrische Polymerbürsten mit einem Kern aus Poly(3-acryloylpropyl trimethoxysilan) und einer Schale aus Poly(oligoethylenglykol)methacrylat wurden in wässriger Ammoniak-Lösung hydrolysiert um wasserlösliche Polymer-Silizium Hybride zu erhalten. Der Vorteil bei dieser Methode ist, dass die Trimethoxysilyl-Gruppe kovalent und damit direkt an die Polymerbürste gebunden ist und damit die Zugabe einer zusätzlichen anorganischen Siliziumquelle vermieden werden kann. Diese Hybrid-Nanodrähte können flüssigkristalline lyotrope Phasen ausbilden und ausserdem als Vorstufen für die pyrolytische Bildung von Silizium-Nanodrähten dienen.

Weiterhin wurden amphiphile zylindrische Polymerbürsten mit einem hydrophilen Kern aus Polyacrylsäure und einer hydrophoben Schale aus Poly(*n*-butylacrylat) als Template und gleichzeitig Nanoreaktoren benutzt. Durch die Möglichkeit der Polyacrylsäure, Cd^{2+} Kationen zu komplexieren, konnten zylindrische CdSe-Halbleiterstäbchen hergestellt werden. Da durch die Koordination die chemische Struktur der Polyacrylsäure nicht verändert wurde, konnte der Beladungsprozess wiederholt werden und somit die Dichte an CdSe Nanopartikeln in der Hybridstruktur erhöht werden. Dies konnte durch AFM, TEM und UV-Vis eindrucksvoll belegt werden.

Doppelt hydrophile Polymerbürsten mit einem Poly(2-hydroxyethylmethacrylat)-Kern und einer Poly(oligoethylenglykol)methacrylat-Schale wurden für die Darstellung von wurmähnlichen TiO_2 Halbleiter-Nanopartikeln und somit einer Polymer-Titandioxid-Hybridstruktur verwendet. Als Titanquelle hierbei diente eine in-situ durchgeführte Transalkoholyse zwischen dem Kern der Polymerbürste und zugeführtem $Ti(OC_4H_9)_4$. Die

Polymer-Titandioxid-Hybriddrähte wurden dann zur Bildung von Anatas-Nanodrähten bei 550 °C pyrolysiert.

Alle bislang vorgestellten anorganischen Nanodrähte weisen einheitliche Längen und Dicken auf. Dies wird auf die niedrige Molekulargewichtsverteilung der Polymerbürsten zurückgeführt, die in allen Fällen als Vorstufen verwendet wurden. Außerdem diente die Schale der Polymerbürsten zur Abschirmung der anorganischen Nanodrähte untereinander. Hierdurch konnte eine weitere Aggregation verhindert werden und die Polymer-Metall-Hybridstrukturen konnten in verschiedenen Medien, inklusive Wasser, in Lösung gehalten werden.

Bei einer leicht abgeänderten Strategie wurden zylindrische Homopolymerbürsten aus Poly(*tert*-butylmethacrylat) benutzt um einheitliche einkristalline Tellur-Nanodrähte (Länge bis zu 822 nm, Durchmesser ca. 36 nm, Aspektverhältnis von 2.7 bis 22) bei Raumtemperatur in THF herzustellen. Diese Stäbchen sind löslich in THF und weisen adsorbiertes Polymer auf der Oberfläche auf. Weiterhin konnten zusätzliche Tellur- oder Magnetit (Fe_3O_4)-Nanopartikel darauf abgelegt werden. Dieselbe Methode wurde auch für lineare P*t*BMA-Polymere mit sehr hohen Molekulargewichten verwendet. Die Darstellung von Magnetit auf diesen Tellurstäben konnte durch das stöchiometrische Verhältnis von Nanopartikeln und Stäbchen kontrolliert werden. Die Tellurstäbe mit Magnetitpartikeln zeigen superparamagnetisches Verhalten und konnten in Anwesenheit eines externen Magnetfeldes auf Oberflächen ausgerichtet werden.

All diese neuartigen, eindimensionalen und auf Polymerbürsten basierenden Hybridstrukturen zeigen faszinierende elektronische, optische, katalytische, halbleitende und magnetische Eigenschaften und sind dadurch im Rahmen verschiedenster Anwendungen von Interesse.

Chapter 9 List of Publications

During the course of this thesis the following papers have been published (or to be submitted):

1. **Yuan, J.**; Xu, Y.; Walther, A.; Bolisetty, S.; Schumacher, M.; Schmalz, H.; Ballauff, M.; Müller, A. H. E., *Water-soluble Organo-Silica Hybrid Nanowires.* ***Nature Materials*** 2008, 7, (9), 718-722.
2. **Yuan, J.**; Schmalz, H.; Xu, Y.; Miyajima, N.; Drechsler, M.; Möller, M. W.; Schacher, F.; Müller, A. H. E., *Room-Temperature Growth of Uniform Tellurium Nanorods and the Assembly of Tellurium or Fe_3O_4 Nanoparticles on the Nanorods.* ***Advanced Materials*** 2008, 20, (5), 947-952.
3. **Yuan, J.**; Drechsler, M.; Xu, Y.; Zhang, M.; Müller, A. H. E., *Cadmium Selenide Nanowires within Core-Shell Cylindrical Polymer Brushes: Synthesis, Characterization and the Double-Loading Process.* ***Polymer*** 2008, 49, (6), 1547-1554.
4. **Yuan, J.**; Lu, Y.; Schacher, F.; Lunkenbein, T.; Weiss, S.; Schmalz H.; Müller, A. H. E., *Template-directed Synthesis of Titania Hybrid Nanowires within Core-Shell Cylindrical Polymer Brushes.* 2009, submitted to ***Chemistry of Materials***.
5. **Yuan, J.**; Gao, H.; Schacher, F.; Xu, Y.; Richter, R.; Tremel, W.; Müller, A. H. E., *Synthesis and Alignment of Magnetic Nanocylinders Based on Tellurium Nanorods and Magnetite Nanoparticles.* 2009, submitted to ***ACS Nano***.
6. **Yuan, J.**; Xu, Y.; Schumacher, M.; Schmalz, H.; Müller, A. H. E., *Core-shell Cylindrical Polymer Brushes with Silica Nanowires.* ***Polymer Preprint*** *(Am. Chem. Soc., Div. Polym. Chem.), 2008, 49(1), 21-22.*
7. Xu, Y.; Drechsler, M.; **Yuan, J.**; Müller, A. H. E., *Hybrids of Magnetic Nanoparticles with Double-hydrophilic Core-shell Cylindrical Polymer Brushes.* ***Polymer Preprint*** *(Am. Chem. Soc., Div. Polym. Chem.), 2008, 49(1), 338-339.*
8. Petrov, P.; **Yuan, J.**; Yoncheva, K.; Müller, A. H. E.; Tsvetanov, C. B., *Wormlike Morphology Formation and Stabilization of "Pluronic P123" Micelles by Solubilization of Pentaerythritol Tetraacrylate.* ***Journal of Physical Chemistry B*** 2008, 112, (30), 8879-8883.

9. Walther, A.; **Yuan, J.**; Abetz, V.; Müller, A. H. E.; *Structure-Tunable Bidirectional Hybrid Nanowires Templated by Polymeric Multicompartment Cylinders.* 2009, ***Nano Lett.*** DOI: 10.1021/nl9002975.

10. Xu, Y.; Becker, H.; **Yuan, J.**; Burkhardt, M.; Zhang, Y.; Walther, A.; Bolisetty, S.; Ballauff, M.; Müller, A. H. E., *Double-Grafted Cylindrical Brushes: Synthesis and Characterization of Poly(lauryl methacrylate) Brushes.* ***Macromolecular Chemistry and Physics*** 2007, 208, (15), 1666-1675.

11. Schumacher, M., Ruppel, M., **Yuan, J.,** Schmalz, H., Colombani, O., Drechsler, M., Müller, A. H. E., *Smart Oorganic-Inorganic Nanohybrids Based on Amphiphilic Block Copolymer Micelles and Silsesquioxane-Based Nanoparticles.* ***Langmuir*** 2009, 25(6), 3407-3417.

12. Schmalz, H.; Schmelz, J.; Drechsler, M.; **Yuan, J.**; Walther, A.; Schweimer, K.; Mihut, A. M., *Thermo-Reversible Formation of Wormlike Micelles with a Microphase-Separated Corona from a Semicrystalline Triblock Terpolymer*. ***Macromolecules*** 2008, 41, (9), 3235-3242.

13. Gao, C.; Muthukrishnan, S.; Li, W.; **Yuan, J.**; Xu, Y.; Müller, A. H. E., *Linear and Hyperbranched Glycopolymer-Functionalized Carbon Nanotubes: Synthesis, Kinetics, and Characterization.* ***Macromolecules*** 2007, 40, (6), 1803-1815.

14. Xu, Y.; Drechsler, M.; Bolisetty, S.; Fang, B.; **Yuan, J.**; Ballauff, M.; Müller, A. H. E., *Manipulating Charged Bottlebrush Polymers on the Nanoscale by Counterions: Collapse Transition to Helical Structures.* ***Soft Matter*** 2009, 5, 379 - 384.

15. Xu, Y.; Bolisetty, S.; Drechsler, M.; Fang, B.; **Yuan, J.**; Ballauff, M.; Müller, A. H. E., *pH and Salt Responsive Poly(N,N-dimethylaminoethyl Methacrylate) Cylindrical Brushes and their Quaternized Derivatives.* ***Polymer*** 2008, 49, (18), 3957-3964.

16. Fang, B., Walther, A., Wolf, A., Xu, Y., Yuan, J., Han, Z., Müller, A. H. E., *Undulated Cylinders Stacked by Polymer Micelles with a Compartmentalized Corona.*, submitted to ***Angewandte Chemie International Edition*** 2009, 48, (16), 2877-2880.

Acknowledgements

The journey of pursuing a PhD degree is happier when you travel together. This thesis is the result of three and a half years of scientific work whereby I have been nicely accompanied and supported by many people. I am very glad to make use of this occasion to express my gratitude to all of them.

The first person I would like to thank is my supervisor, Prof. Dr. Axel H. E. Müller. The opportunity that he offered me to perform my PhD research in MCII has turned out to be the crucial issue in my life. His passions in the frontline of polymer science, his integral view on research, and his charming characters have imposed a strong impression on my mind. His careful supervision and constructive suggestions have become the strongest motivation of my productive research. I owe him lots of gratitude for encouraging me to present my work at various national and international conferences.

The MCII is a very marvelous, magic and “magnetic” group. The highly international atmosphere and the strong teamwork spirit have been the key factors to the fruitful results in my PhD. I have not only achieved the capability of carrying out scientific work independently, but also shared knowledge and made progress with colleagues together. Here I want to thank Youyong Xu, Andreas Walther, Felix Shacher, Manuela Schumacher, Dr. Holger Schmalz, Dr. Mingfu zhang, Dr. Markus Drechsler and Stephan Weiss for their close “Zusammenarbeit” in my publications during my PhD. I would also like to thank Sabine Wunder and André Gröschel for the GPC measurements, Annette Krökel and Andre Pfaff for the help in operating NMR and the freeze-dryer, Pierre Millard and Dr. Weian Zhang for introducing me RAFT technique, Evis Penott-Chang and Sharmila Muthukrishnan for the help in ATRP, Dr. Petar Petrov for introducing me the knowledge of polymer self-assembly, Felix Plamper, Alexander Schmalz and Hans-Joachim Voigtländer for their help in computer and network, and Susanne Erdinger and Melanie Förtsch for the labor routine.

I also want to thank all other colleagues - Anja Goldmann, Joachim Schmelz, Dr. Michael Witt, Sandrine Tea, Sergey Nosov, Andreas Hanisch, Markus Müllner, Alexandra Sperschneider, Annika Ochs, Stefan Reinicke, Thomas Ruhland, Andrea Wolf, Astrid Göldel, and Kerstin Matussek for the nice teamwork.

Of course, those who have given me many helps but already left MCII, should not be ignored. They are Denise Danz, Sergey Nosov, Dr. Xavier André, Dr. Alexandre Terrenoire, Harald Becker, Dr. Girish Ch. Behera, Dr. Markus Burkhardt, Bing Fang, Karina Möller, Dr. Chih-Cheng Peng, Markus Ruppel, and Dr. Saikat Mandal.

I had the pleasure to supervise and work with the students, Frank Polzer and Christian Bartz, who made the advanced lab course or bachelor thesis in our group.

During my study, I benefit a lot from the close collaborations in Bayreuth. I am grateful for Sreenath Bolisetty and Prof. Matthias Ballauff from Physikalische Chemie I for a joint research project, which led to a paper with the highest IF factor in my PhD. Many thanks are given to Thomas Lunkenbein and Michael W. Möller from Anorganische Chemie I for performing calcination and XRD measurements. Benjamin Gossler and Christina Löffler from Makromolekulare Chemie I, Carmen Kunert from Physikalische Chemie II, and Nobuyoshi Miyajima from Bayerisches Geoinstitut are grateful for their kind assistance in the TGA, SEM and HRTEM measurements, respectively.

This research has been financially supported by the DFG Schwerpunktprogramm (SPP) 1165. In this special research branch, all groups cooperated close with each other and tried all their best to achieve very small and tiny “worms” and “sticks”, which however have huge potential in solving various problems that we are facing. I give my special thanks to our cooperation partners, Thomas Lüdtke from Uni hannover, Haitao Gao from Uni Mainz and Hanne Scheel from Uni Erlangen-Nürnberg.

I deeply appreciate Gaby Rösner-Oliver for her great help in so many aspects. From the sophisticated German documents to the tips of enjoying the life in Bayreuth, her suggestions are of great importance.

I am very grateful for my wife Yan, for her love and patience during the PhD period. One of the best life experiences is the wedding-party organized by MCII, who lives in our memory forever.

Erklärung

Die vorliegende Arbeit wurde von mir selbstsändig verfasst und ich habe dabei keine anderen als die angegebenen Hilfsmittel und Quellen benutzt.

Ferner habe ich nicht versucht, anderweitig mit oder ohne Erfolg eine Dissertation einzureichen oder mich der Doktorprüfung zu unterziehen.

Bayreuth, den 07.01.2009

(Jiayin Yuan)